The Spatial Distribution of X-ray Clusters of Galaxies

Anita Katherine Romer

Degree of Doctor of Philosophy
University of Edinburgh
1994

Declaration

This thesis does not include work submitted for any other degree or professional qualification. The work presented in this thesis is of my own composition, except where clearly stated in the text, *e.g.* see § 6.5.

ABSTRACT

Clusters of galaxies are ideal probes of large-scale structure as they are rare objects; large volumes of the Universe can be mapped with relatively small (when compared to galaxies) numbers of clusters. Clusters are also bright, they are among the most luminous X-ray sources in the sky. The X-ray emission originates from hot, diffuse, intracluster gas. The distribution of the gas density follows that of the underlying (dark) mass potential. Consequently the cluster X-ray emission is concentrated towards the central core region of the cluster. In the past it was not possible to make large X-ray selected samples of clusters because the X-ray data suffered from either poor spatial resolution or inadequate areal coverage. Therefore, cluster samples have traditionally been developed by searching for projected galaxy enhancements in photographic or CCD surveys. However, such optically selected cluster samples have been shown to suffer from projection effects which bias their clustering properties and limit their use as diagnostic tools. The work described in this thesis concerns the development of the SGP RASS Cluster Sample (SRCS), the first truly X-ray selected sample of clusters, and its application to a quantitative study of large-scale structure.

The SRCS has been constructed from data acquired during the ROSAT All Sky Survey (RASS), where ROSAT is the German/UK/US X-ray satellite that was launched in 1990. The RASS, completed in 1992, was the first all sky survey made with an imaging X-ray telescope. Approximately 50,000 sources were detected during the RASS of which roughly 10% are clusters of galaxies. We have selected 345 cluster candidates from the RASS, to a limiting flux of $f_X \simeq 1 \times 10^{-12}\,\mathrm{erg\,s^{-1}\,cm^{-2}}$, from a 2800$\Box^\circ$ region centered around the South Galactic Pole (SGP). These candidates have been selected using both X-ray data from the RASS and digitised optical data from the COSMOS/UKST Object Catalogue (CUOC). Through a combination of optical spectroscopic data from our own observations and from the literature, we have been able to identify 154 of these candidates as clusters with redshifts. An additional 36 candidates have been identified with non-cluster X-ray sources that were contaminating the candidate list. The 154 RASS clusters in the SRCS constitute the largest X-ray selected cluster sample to date.

Our experience has provided us with a unique insight that will aid future searches for clusters in the RASS database. We have been found that a significant fraction, $\simeq 20\%$, of RASS clusters are *not* Abell optical clusters (Abell 1958, Abell *et al.* 1989). We have also shown that $\simeq 40\%$ of RASSclusters were not flagged as extended sources by the Standard Software Analysis System (SASS). We conclude, therefore, that it is not possible to make comprehensive identifications of RASS clusters by relying solely either on the

Abell catalogue or on existing SASS extent information. We also recommend that all candidates with a single galaxy in the X-ray error circle be followed up spectroscopically irrespective of whether the galaxy lies in a cluster with a known redshift. (This is due to the enhanced probability that such candidates are in fact X-ray bright AGN.) We note that planned changes to SASS may provide the means to identify contaminating objects without optical follow-up, by improving extent determinations. Such changes will also allow us to address one of the major drawbacks of the work presented in this thesis; that we have had to use unreliable source count rates.

Using the SRCS, we have been able to make the first determination of the spatial correlation function, ξ_{CC}, for an X-ray selected cluster sample. A reliable measurement of ξ_{CC}^{Xray} was long overdue, as it can provide important constraints on theories of large-scale structure formation. Constraints from ξ_{CC}^{Xray} are more robust than those derived from measurements of optical cluster clustering, $\xi_{CC}^{optical}$, because X-ray selected cluster samples do not suffer from the projection biases mentioned earlier. We hope to settle the controversy over the value of the cluster correlation length, r_0, using the SRCS. (Where r_0 is the separation at which $\xi_{CC} = 1$.)

We have found that the clustering patterns of the SRCS are similar, on all scales, to those of automated digitised optical cluster samples. In contrast, when we compare the SRCS to samples of Abell clusters, clusters which were selected by eye by Abell and co-workers from photographic plates, we measure a smaller correlation length ($r_0^{Xray} \lesssim 16\,h^{-1}\,\mathrm{Mpc}$ *cf.* $r_0^{Abell} \gtrsim 20\,h^{-1}\,\mathrm{Mpc}$) and less power on large ($r \gtrsim 40\,h^{-1}\,\mathrm{Mpc}$) scales. We attribute this difference to artificial clustering in the Abell catalogue, as evidenced by our comparisons of the two-dimensional clustering in our sample with that in Abell samples. The lack of anisotropy seen in the SRCS correlation function provides strong support for the claims of Sutherland 1988 that some of the clustering power seen in Abell cluster samples is due to projection effects. Alternative suggestions proposed to explain the line-of-sight anisotropy in the Abell catalogue, *e.g.* large peculiar velocities or supercluster elongations, are much less tangible in light of our results.

We have made comparisons between the SRCS correlation function and state of the art theoretical predictions. Our data seem to rule out a low density, positive cosmological constant, CDM model. However, they provide inadequate constraints to be able to distinguish between other, subtly different, models, *e.g.* standard CDM, mixed CDM and tilted CDM models. Larger X-ray cluster samples would be required to do so and it is planned to extend the project to produce a larger, more complete, SRCS in the near future.

Contents

Chapter 1

Introduction

1.1 Thesis Overview

Chapter 1; Introduction

This chapter describes the motivation behind the work described in this thesis. First, the role that large-scale structure observations, especially those of X-ray clusters of galaxies, can play in constraining cosmological models is described. Secondly, a critique is given of previous observations of the cluster correlation function. The motivation behind a new determination of the cluster spatial correlation function using an X-ray selected sample is then outlined.

Chapter 2; Selection of SGP RASS Cluster Candidates

The ROSAT All-Sky Survey (RASS) provides an ideal opportunity to create a large, uniform sample of X-ray clusters with which to study large-scale structure. The expectations for cluster detection in the RASS are described in the first section of this chapter. We then go on to discuss the development of a flux-limited sample of SGP RASS cluster candidates. (Where "SGP" denotes a 2800□° region centered on the South Galactic Pole). The selection methods used to derive this candidate sample utilize both the X-ray parameters available in the RASS database and digitised optical information.

Chapter 3; Spectroscopic Follow-Up of SGP RASS Cluster Candidates

The spectroscopic followup of the SGP RASS cluster candidate sample is described in this chapter. Details of the observing procedures, instruments used and reduction techniques employed are presented. The latter sections of this chapter describe the process of galaxy redshift determination and the methods employed to classify various galaxy types responsible for emission line spectra.

Chapter 4; The SGP RASS Cluster Sample

In this chapter an attempt is made to make fair identifications (as clusters or contaminating objects) of the SGP RASS cluster candidates. For this purpose, we utilize the spectroscopic information from our own observations and from the literature. These identifications have resulted in the SGP RASS Cluster Sample (SRCS), which comprises some 154 X-ray clusters with redshifts. Several subsamples of SGP RASS clusters are introduced at the end of the chapter, these subsamples represent a range of selection methods and flux limits. Estimates of the completeness of each subsample are presented.

Chapter 5; The X-ray Cluster Correlation Function

The methods by which the spatial correlation function was determined from the various subsamples of SRCS samples are described in this chapter. The results are presented in the form of tables and figures and are discussed in the context of a) previous results and b) theoretical models.

Chapter 6; Discussion

In this chapter the major conclusions of this thesis are re-iterated and suggestions are made for follow-up work in the area of X-ray cluster large-scale structure. Some of the other projects to which the ROSAT SGP cluster sample will be applied are also discussed.

Appendix A

The SGP RASS Cluster Candidate list is presented in this appendix. Candidate identifications and cluster redshifts are also given.

Appendix B

The results from the spectroscopic follow-up are presented in this appendix.

Appendix C

Finding charts produced from the COSMOS/UKST Object Catalogue are presented in this appendix. These finding charts illustrate the appearance on optical photographic plates of the regions surrounding 40 SGP RASS cluster candidates.

1.2 Physical and Observational Cosmology

1.2.1 The Standard Big Bang Model

The standard hot Big Bang model is a remarkably successful operating hypothesis describing the evolution of the Universe on the largest scales. In the Big Bang model, the Universe expands rapidly from a very hot, dense state at $t = 0$. It provides a framework for such observations as a) the Hubble law of recession of galaxies, interpreted in terms of the expansion of the universe, b) the abundances of light elements, in excellent agreement with the predictions of primordial nucleosynthesis and c) the thermal spectrum and isotropy of the cosmic microwave background radiation (CMBR), as expected from a hot, dense early phase of expansion.

The **Cosmological Principle** lies at the foundation of the standard cosmology, it states that the Universe, on average, is homogeneous and isotropic. There is growing evidence that these two assumptions are correct. The evidence for angular isotropy on large scales comes from the smallness, $\Delta T/T \simeq 5 \times 10^{-6}$, of the CMBR large–angle anisotropy detected by the COBE[1] satellite (Smoot *et al.* 1992). Additional evidence comes from the trend for the galaxy distribution to become homogeneous in deep redshift surveys, *e.g.* Fisher *et al.* (1993).

The geometrical expression of the cosmological principle is defined by the metric,

$$ds^2 = c^2dt^2 - a^2(t)\left[\frac{dr^2}{1-kr^2} + r^2(d\theta^2 + \sin^2\theta d\phi^2)\right], \qquad (1.1)$$

where $a(t)$ is the global scale factor which describes the overall expansion or contraction, r, θ, ϕ are the comoving coordinates of the galaxy and k defines the spatial curvature (the Friedmann-Robertson-Walker metric). The value of k is still an unknown, it defines whether the Universe is open & expand forever, $k = 0, -1$, or closed & eventually start to contract, $k = 1$. In the special case of $k = 0$ space-time can be described by Euclidean geometry and the Universe is said to be "flat"[2]. (Euclidean geometry is assumed throughout this thesis.)

The cosmological principle leads directly to Hubble's observation in 1929 that the recession velocity of a galaxy, $v(t)$, is proportional to its distance, $l(t)$, from us, see Mould *et al.* (1991) for a recent confirmation.

$$v(t) = H(t)l(t), \qquad (1.2)$$

where $H(t) = (\dot{a}/a)$ is the (slowly) time dependent Hubble's constant. Measurements of H_0, the present day value of $H(t)$ suggest that it value lies in the range $40 < H_0 <$

[1] COsmic Background Explorer

[2] N.B. The symbol k will be used hereafter to indicate wavenumber.

$100\,\mathrm{km\,s^{-1}Mpc^{-1}}$, *e.g.* Jacoby *et al.* (1992) , and throughout this thesis we adopt a value of $H_0 = 100h\,\mathrm{km\,s^{-1}Mpc^{-1}}$, where $h = 1$.

The consequence of the Hubble expansion on photons wavelength (λ_{rest}) radiated from an external galaxy and detected at our own is a Doppler shift,

$$\frac{\lambda_{obs}}{\lambda_{rest}} - 1 = \frac{v}{c} = z, \tag{1.3}$$

where v is the relative velocity of the galaxies, λ_{obs} is the observed wavelength and z is known as the *redshift*. Combining equations 1.1, 1.2 & 1.3, it is possible to relate the redshift to the luminosity distance, D,

$$D = \frac{c}{H_0 q_0^2}[zq_0 + (q_0 - 1)(\sqrt{2q_0 z + 1} - 1)], \tag{1.4}$$

where $q_0 = -(\frac{\ddot{a}a}{\dot{a}^2})_0$ is the present day "deceleration parameter" of the Universe, Weinberg (1972). We use equation 1.4 with $q_0 = \frac{1}{2}$ throughout this thesis to calculate distances to, and separations between, clusters of galaxies. An alternative expression of q_0 is,

$$q_0 = \frac{\Omega_0}{2} - \frac{\Lambda}{3H_0^2}, \tag{1.5}$$

where Λ is the cosmological constant in the solution of Einstein's equations and Ω_0 represents the present mass density relative to the density required to close a flat, $\Lambda = 0$ Universe,

$$\Omega_0 = \frac{8\pi G\rho_0}{3H_0^2}. \tag{1.6}$$

1.2.2 Inflation

There are certain observations that the standard Big Bang model cannot explain elegantly. For example the "horizon", and "flatness" problems which motivated the development of Inflation Theory, Guth (1981). The horizon problem relates to the fact that the CMBR is smooth on scales larger than a degree. The flatness problem refers to the fact that Ω_0 has been measured to be within one or two orders of magnitude of 1. (See Frieman 1994 for a discussion of the implications of these observations.) Inflation provides a context in which these problems are solved, by invoking an era, $t \approx 10^{-35}$ s, of very rapid expansion after which the Universe emerged homogeneous and flat.

An appealing aspect of Inflation is that it would imprint small scale perturbations in the primordial density field, *e.g.* Bardeen *et al.* (1983). It is generally accepted that galaxies, clusters and other large structures have developed via the gravitational evolution of such perturbations. (Note that Inflation is only one of several models of perturbation production, see Peebles 1993.) The perturbations produced by Inflation will

have a scale invariant, or Harrison-Zel'dovich, power spectrum; $P(k) \propto k$, where k is the wavenumber of the perturbation. Moreover, they will be governed by Gaussian statistics. This means that their statistical properties can be completely specified by the power spectrum or, equivalently, the two point correlation function (§1.2.6), see Efstathiou (1990) for a derivation.

Another prediction of Inflation is that the present day Universe has a mass density that must satisfy $\Omega = 1$. However, this requirement is not satisfied by the luminous matter in the Universe. An inventory of mass in stars, galaxies, X-ray gas *etc.* , pegs the luminous mass density at $\Omega_{lum} \sim 0.01$. In other words in a Big Bang+Inflation Universe, 99% of the mass in the Universe must be non-luminous 'dark matter'.

1.2.3 Dark Matter in the Universe

The existence of dark matter in the Universe was theorized long before the development of Inflation Theory. For example the "missing mass" problem discovered by Zwicky (1933) in clusters of galaxies. Zwicky showed that the summed mass of the galaxies, determined from the galaxy mass to light ratio, was an an order of magnitude less than the virial mass determined from the galaxy velocity dispersion, see White *et al.* (1993a) for a more up to date assessment. Other evidence for dark matter comes from flat spiral galaxy rotation curves, Fich & Tremaine (1991), and large-scale peculiar motions, Dekel (1994).

The nature of the dark matter is highly uncertain. There is evidence that at least some of the dark matter in galaxy halos is made up of degenerate brown dwarfs or MACHOS[3], substellar ($M < 0.08 M_{\odot}$) objects which did not reach sufficiently high temperatures to burn hydrogen, Alcock *et al.* (1993). However, there are two reasons why theories involving exotic, non-baryonic, dark matter have become popular. First, Big Bang primordial nucleosynthesis restricts the total, present epoch, baryon density to $0.010 < \Omega_B h^2 < 0.015$, Schramm (1990). Therefore, baryons could only account for 1% of the mass in an $\Omega_0 = 1$ Universe.

Secondly, if the Universe is dominated by baryons, it is very hard to reconcile the existence of galaxies and clusters with the observed smoothness of the CMBR. For these structures to have formed by the present epoch, the primordial density perturbations need to have evolved into enhancements where $\delta_\rho(r)/\rho_0 \sim 1$. (Where $\delta_\rho(r) = \rho(r) - \rho_0$, and ρ_0 is the average density of the Universe.) The background radiation was last in thermal contact with the baryonic matter at $z \simeq 1000$. The CMBR is, thus, engraved with a relic of the $z \simeq 1000$ baryonic density perturbations. The CMBR temperature

[3]MACHO is an acronym for massive compact halo objects

fluctuations, $\delta T/T \simeq 5 \times 10^{-6}$ (Smoot *et al.* 1992), are three orders of magnitude smaller than those required to produce $z \sim 0$ galaxies in a baryonic universe, Börner (1988). Alternatively, if the dominant type of matter was non-baryonic and, therefore, only weakly coupled to the background radiation, then it is possible to have large fluctuations in the $z \simeq 1000$ density field but not in the CMBR. In these scenarios, the fluctuations in the baryonic component were small at $z = 1000$, but grew later to the same size as the fluctuations in the non-baryonic component.

Despite many on-going searches, see Frieman (1994) for a review, the identity of the particle(s) responsible for the non-baryonic dark matter remains a mystery. In the absence of this information, it is possible to theorize particles that effect the primordial power spectrum in such a way as to mimic the observed large-scale structure observed in the Universe today. The relevant characteristic of these particles is the horizon scale of the Universe at which the particle velocity becomes non-relativistic. Density fluctuations with wave numbers smaller than this scale will be damped, because relativistic particles will stream away from regions of compression. For example hot dark matter (HDM, Shandarin *et al.* 1983), consisting of light particles such as neutrinos, would damp out any fluctuations smaller than a mass scale of a supercluster, $10^{15} M_{\odot}$. By contrast, cold dark matter (CDM, Blumenthal *et al.* 1984), consisting of heavy particles such as axions, would become non-relativistic very early and density fluctuations would be preserved on all scales.

1.2.4 The Cold Dark Matter Model

The previous sections have introduced a theoretical model, Big Bang+Inflation, from which we can begin to understand the observable Universe. However, a large piece of the puzzle remains unsolved; *i.e.* why is the Universe we observe today so clumpy, *e.g.* de Lapparent *et al.* (1986), when the CMBR is so smooth? To be able to answer this question we have to address several others, including; what is the nature of the matter in the Universe and what is the power spectrum of density fluctuations at the present and primaeval epochs? In the absence of definitive answers to these questions it is possible to theorize a multitude of models that could explain the process of large-scale structure formation. Only robust observations of the large-scale structure can prevent these models getting too far fetched. Observations, in effect, provide constraints on the palette of parameter space available to theorists.

As an example, let us review the present status of the Cold Dark Matter (CDM) model. This has proved to be a very popular model of large-scale structure formation theory, having the joint advantages of simplicity and the ability to predict, fairly

accurately, the observed galaxy clustering. In a standard CDM model the following assumptions are made; a) the Universe is dominated by weakly interacting massive particles, b) $\Omega_0 = 1$, $\Lambda = 0$, c) baryonic matter constitutes an insignificant fraction of the mass, d) there is biased galaxy and cluster formation, *i.e.* light does not trace mass in a linear fashion and e) the fluctuations in the early universe were adiabatic, governed by Gaussian statistics and scale-invariant, *i.e.* $P(k) \propto k$. In CDM universes, the present day power spectrum is modified from the primordial one; it tilts from $P(k) \propto k$ at small k to $P(k) \propto k^{-3}$ as $k \rightarrow \infty$, Blumenthal *et al.* (1984). The scale at which the power law slope changes sign corresponds to the horizon scale ($\sim ct$) at the transition between the radiation and matter dominated eras, $t \approx 5 \times 10^{11}$ s. (Before transition the growth of fluctuations smaller than the horizon scale is suppressed, afterwards all fluctuations grow at the same rate.)

The success of the CDM theory can be judged by comparing its predictions with observations. Figure 1.1 shows the power spectrum, $P(k)$, of density fluctuations as a function of wavenumber k corresponding to distance scales of order $10\,h^{-1}\,$Mpc to $3000\,h^{-1}\,$Mpc. This figure is a reproduction of Figure 1 in Lamb & Quashnock (1993). The shaded regions show the power spectrum of total mass-energy density fluctuations found from analysis of the COBE data (Smoot *et al.* 1992), and the power spectra of luminous matter density fluctuations found from analysis of the APM•optical (Peacock 1991) and the IRAS infrared (Fisher *et al.* 1993) galaxy survey data. The data points shown are from the analysis of surveys of faint radio galaxies (Peacock & Nicholson 1991), clusters of galaxies (Schectman 1985; Lahav *et al.* 1989) and from pencil beam surveys (Koo & Kron 1987; Broadhurst *et al.* 1990). The dashed line shows a typical power spectrum for the standard CDM model normalized to the COBE result. Note the 'knee' in the CDM spectrum at $k \approx 0.03\,h^{-1}\,$Mpc, which corresponds to the transition scale mentioned above.

It is apparent from Figure 1.1 that the CDM spectrum, when normalized to the COBE data at $k \lesssim 0.007\,h\,\mathrm{Mpc}^{-1}$ can provide a fair fit to the optical galaxy data for $k \gtrsim 0.1\,h\,\mathrm{Mpc}^{-1}$. However, for $0.06 \lesssim k \lesssim 0.1$ the observations begin to deviate wildly from the CDM prediction. The general interpretation of this deviation is that standard CDM underpredicts the power on these scales. It is possible to find non-standard CDM models that provide better fits to the observations; *e.g.* by reducing Ω_0, tilting the primordial power spectra away from $P(k) \propto k$, introducing a non zero cosmological constant, mixing some HDM in with the CDM *etc.* , Efstathiou *et al.* (1990). However, these non-standard models become increasingly less attractive as they gain complexity.

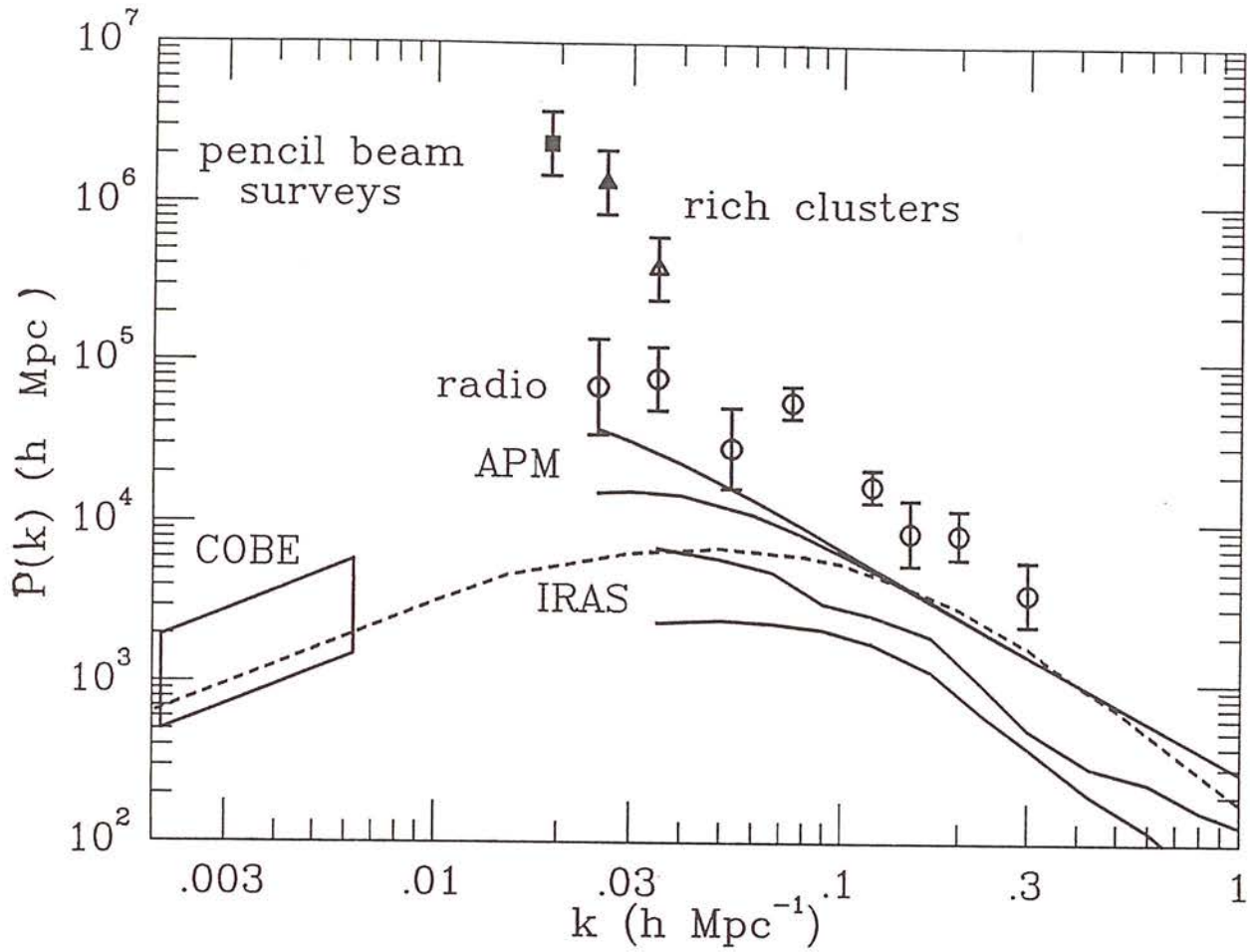

Figure 1.1: Power spectrum $P(k)$ of density fluctuations as function of wavenumber k corresponding to scales of $\sim 10 \rightarrow 3000\,h^{-1}\,\mathrm{Mpc}$. The dotted curve depicts a typical power spectrum for the cold dark matter model. The various data curves and points are described in the text. (Reproduction of Figure 1 in Lamb & Quashnock 1993)

1.2.5 Clusters as Probes of Large-Scale Structure

From Figure 1.1 it can be seen that observations of several types of object are required to measure the power spectrum on all scales. The limited size of present large area galaxy catalogues and the finite beam size of the COBE instrument (10°) means that a very interesting region of k space, that where the CDM spectral index[4], n, turns over from $n = 1$ to $n < 0$, cannot be accessed by existing observations of galaxies or the CMBR. Observations of clusters of galaxies, on the other hand, provide a very efficient way to probe fluctuations with wavelengths in this regime. Clusters are bright objects that can be observed to redshifts of $z \simeq 1$, Gunn *et al.* (1986), and have a very low space density; their typical separation is $\simeq 10\,h^{-1}\,\mathrm{Mpc}$. A volume complete all-sky sample of clusters to $z \simeq 0.1$ would contain several thousands of objects compared to the tens of millions of galaxies that occupy this volume[5]. This has the important practical benefit that far fewer redshift measurements are required to probe the same volume of the Universe if one uses clusters rather than galaxies.

A less obvious benefit of clusters is the fact that their distribution is easier to model, via analytical techniques, than that of galaxies. This is because clusters represent density enhancements that are only mildly "non-linear". In the linear regime, $\delta_\rho/\rho_0 \ll 1$, each Fourier mode[6] in the density field evolves independently. Coupling between modes is insignificant and all modes grow at the same rate as the scale factor, $a(t)$, see Efstathiou (1990) for a complete derivation. The density enhancements of galaxies are well outside this regime and the only way to model their large-scale structure accurately is using large n-body computer simulations, in which Newton's equations of motion are integrated numerically. By contrast, it is possible to study cluster large-scale structure analytically using the Zel'dovich (1970) approximation for the nonlinear evolution of structure. Recent progress in this area, *e.g.* Mann *et al.* (1993), means that observations of clusters can be compared against accurate theoretical predictions that are independent of n-body simulations. Although, there is also progress in the field of n-body simulations of cluster distributions, *e.g.* Croft & Efstathiou (1994), these are very time consuming calculations and a compromise has to be struck between the volume that is sampled and the spatial resolution of the simulation.

Despite the advantages of low spatial density and comparative ease of modelling, one caveat must be extended to the use of clusters of galaxies as probes of the large-scale structure; the cluster distribution may be unrepresentative of the mass distribution

[4] Where $P(k) \propto k^n$

[5] These figures assume that a galaxy richness limit ($RC \geq 0$) and a luminosity limit ($> L_*$) has been applied to the clusters and galaxies respectively.

[6] See § 1.2.6

in the Universe. (It is the mass distribution that we ultimately want to describe.) Kaiser (1984) suggested that clusters might form only in places where the primordial density enhancement was unusually large and thus give only a biased measure of the present day density fluctuation spectrum. If true then this means that there will be a more complicated relationship between cluster observations and analytical & n-body predictions than if the cluster distribution truly followed that of the mass.

1.2.6 The Spatial Correlation Function

Almost all studies of cluster large-scale structure, including that presented in this thesis, involve measurements of the spatial correlation function and not the power spectrum. Therefore, we define here the physical interpretation of the spatial correlation function and the relation between this statistic and the power spectrum of density fluctuations.

For any class of objects distributed in three dimensions throughout volume V with an average number density, n, the *two-point correlation function*, $\xi(r_{12})$, is defined by,

$$\delta P = n^2 \delta V_1 \delta V_2 [1 + \xi(r_{12})], \tag{1.7}$$

where δP is the joint probability that an object is found in both of the volume elements δV_1 and δV_2 separated by distance r_{12}. Equation 1.7 includes an assumption that the objects are distributed isotropically within the volume, reflected by the fact that ξ is only a function of separation and not of orientation. If the objects had a random distribution, the joint probability is simply proportional to the size of the volume elements, $\xi(r_{12}) = 0$ and equation 1.7 reduces to,

$$\delta P = n^2 \delta V_1 \delta V_2. \tag{1.8}$$

If, instead, the presence of an object in δV_1 increases the chance of finding an object in δV_2, the objects are said to be correlated and $\xi(r_{12}) > 0$. In the opposite case of anti-correlation, $-1 \leq \xi(r_{12}) \leq 0$. The amplitude of the correlations, or anti-correlations, is generally a function of the separation r. The *correlation length* is defined as the separation at which the correlation amplitude is equal to 1 and is usually assigned the symbol r_0. For example, in the case of galaxies, $r_0 \simeq 6\, h^{-1}$ Mpc, Maddox *et al.* (1990).

Let us now relate the correlation function to the power spectrum of density perturbations. The mass density contrasts can be described by a continuous function, $\delta_\rho(r)$. If we assume that $\delta_\rho(r)$ is periodic in some large volume V, then the density contrast can be expanded into its Fourier components,

$$\delta_\rho(r) = \frac{(2\pi)^{3/2}}{V^{1/2}} \sum \delta_k e^{ik.r}. \tag{1.9}$$

The Fourier transform of equation 1.9 is,

$$\delta_k = 2\pi^{-3/2}V^{-1/2}\int \delta_\rho(r)e^{-\,ik.r}\mathrm{d}^3r. \tag{1.10}$$

We now define the *autocorrelation function*, $\xi(r)$, of the density field,

$$\xi(r) = \langle \delta_\rho(r_1)\delta_\rho(r_1+r)\rangle \tag{1.11}$$

where $\delta_\rho(r_1)$ describes the density contrast at position r_1. (Equation 1.11 is the equivalent to equation 1.7 for a continuous distribution.) Combining equations 1.11, 1.9 and 1.10 we find that,

$$\xi(r) = 4\pi\int_0^\infty k^2\delta_k|\delta_k|^2\frac{sinkr}{kr}. \tag{1.12}$$

In other words, the autocorrelation function is the Fourier transform of the power spectrum,

$$P(k) = \langle|\delta_k|^2\rangle. \tag{1.13}$$

With regard to our previous comment about biasing in the cluster distribution, the relation between the spatial correlation function measured from observations of a sample of clusters, ξ_{CC}, and the autocorrelation function of the density field will be given, ξ_ρ, in the simplest case, by,

$$\xi_{CC}(r) = A\xi_\rho(r) \tag{1.14}$$

where A is a constant.

1.3 Observations of Cluster Spatial Correlation Function

In the previous section we attempted to explain why observations of the large-scale structure, and in particular that described by clusters of galaxies, are crucial to our understanding of the Universe. In this section we give a brief review of the progress that has been made in the specific study of the cluster spatial correlation function, $\xi_{CC}(r)$. We begin with a discussion of 5 different samples of clusters and the spatial correlation function results derived from them.

1.3.1 Five Determinations of ξ_{CC}

The results presented in table 1.1 represent five recent determinations of the spatial correlation function. In each case the observed correlation function has been found to follow a power law, parameterized by,

$$\xi_{CC}(r) = \left(\frac{r}{r_0}\right)^{-\gamma}, \tag{1.15}$$

where r_0 is the correlation length as defined in §1.2.6 (column 5) and γ is the power law slope (column 6). These five publications are highlighted because they represent real observational breakthroughs either in a) the number of clusters in the sample, b) the way the sample was selected or c) the methods used to obtain the cluster redshifts. We divide this discussion into three categories according to the selection method used to create each sample; A. visual inspection (samples I & II), B. plate digitisation (samples III & IV) or C. X-ray detection (sample V).

A. Samples produced by Visual Plate Inspection

The catalogues of optical clusters constructed by Abell (1958) and Abell, Corwin & Olowin (1989, hereafter ACO) remain the most complete sources of cluster information available in the literature. The catalogues were constructed by visually inspecting the Palomar Sky Survey Schmidt plates (northern sample, Abell 1958) and the United Kingdom Schmidt Telescope (UKST, § 2.2.1) IIIa-J survey plates (southern extension, ACO). This remarkable effort produced two catalogues comprising of more than 4000 clusters which sample the universe out to $z \approx 0.2$. The scheme used to classify galaxy enhancements on the photographic plates into clusters in both catalogues was as follows;

1. The cluster had to contain at least 30 galaxies within the magnitude range of $m_3 \rightarrow m_3 + 2$, where m_3 was the magnitude of the third brightest galaxy in the cluster. (The number of galaxies in this magnitude range is referred to as the cluster *richness.*)

2. The galaxies defining the cluster had to lie within $1.5\,h^{-1}$ Mpc of the cluster centre. The angular size of this radius is given by, $\theta = 150/cz_{est}$, where the approximate cluster redshift, z_{est}, was estimated using the magnitude, m_{10}, of the tenth brightest cluster galaxy.

3. The estimated redshift had to fall within the range $6000 < cz_{est} < 60000\,\mathrm{km\,s^{-1}}$.

The clusters were divided into richness and distance classes as shown in Table 1.2.

Sample I: Postman *et al.* (1992)

The best study of Abell cluster correlations, to date, was performed by Postman *et al.* 1992[7]. They performed a large area redshift survey of all 350 Abell clusters north of $\delta = -27°30'$, with $m_{10} \leq 16.5$. About half of the cluster redshifts were based on three or more independent galaxy spectra, with $\simeq 25\%$ being determined from only a single

[7]For an excellent review of the status of Abell ξ_{CC} measurements pre 1992, see Mann (1994)

Publication	No.	redshift source	Selection criteria	r_0 (h^{-1} Mpc)	γ	range (h^{-1} Mpc)
Measurements of ξ_{CC} from the Abell catalogue						
Postman *et al.* (1992) Sample I	351	own observations (33%) plus literature	$m_{10} < 16.5$, $\delta > -27°30'$, all α Abell $RC \geq 0$ clusters plus Virgo	$20^{+4.6}_{-4.0}$	$2.5^{\pm 0.2}$	$10 - 75$
Nichol *et al.* (1994a) Sample II	67	Huchra *et al.* (1990)	$10^h < \alpha < 15^h$ $58° < \delta < 78°$ $Lx > 10^{43}\,\mathrm{erg\,s^{-1}}, z \leq 0.24$	$16.1^{\pm 2.3}$	$1.9^{\pm 0.3}$	$6 - 30$
Measurements of ξ_{CC} from digitised cluster samples						
Nichol *et al.* (1992) Sample III	79	own observations (80%) plus literature	$21^h53^m < \alpha < 3^h35^m$ $-22°53' < \delta < -42°12'$, $R_{gal} \geq 22$	$16.4^{\pm 4.0}$	$2.1^{\pm 0.3}$	$3 - 35$
Dalton *et al.* (1992) Sample IV	190	own observations (83%) plus literature	$b \lesssim 40°$, $\delta < -20°$ $R_{gal} \geq 20$	$12.9^{\pm 1.2}$	2	$\approx 2 - 30$
Measurements of ξ_{CC} from X-ray selected cluster samples						
Lahav *et al.* (1989) Sample V	53	Struble & Rood (1987)	X-ray flux$> 1.7 \times 10^{-11}\,\mathrm{erg\,s^{-1}\,cm^{-2}}$ (all sky)	21	1.8	$\approx 3 - 100$

Table 1.1: Five recent determinations of the spatial cluster correlation function for Abell, digitised and X-ray samples of clusters. The number of clusters in the sample is listed in column 2, the source of redshift information in column 3 and the sample selection criteria in column 4 (including any angular, redshift or richness limits). The correlation length in h^{-1} Mpc, power law slope and the range of separations used to derive those values are given in columns 5, 6 & 7.

Richness Intervals (RC)					
Richness class	Galaxy counts	Richness class	Galaxy counts	Richness class	Galaxy counts
0	30 – 49	2	80 – 129	4	200 – 299
1	50 – 79	3	130 – 199	5	> 300
Distance Intervals (D)					
Distance class	m_r	Distance class	m_r	Distance	m_r
1	13.3-14.0	4	15.7-16.4	6	17.3-18.0
2	14.1-14.8	5	16.5-17.2	7	> 18.0
3	14.9-15.6				

Table 1.2: The richness and distance classes defined by Abell (1958).

galaxy spectrum. The mean redshift of their survey is $\bar{z} \approx 0.07$. They added the Virgo cluster (a nearby cluster not included in the Abell catalogue), thus producing a sample of 351 objects. They present estimates of $\xi_{CC}(r)$ over the range $10 \leq r \leq 75\,h^{-1}$ Mpc for various subsamples of the 351 clusters. They found that, after correcting for the influence of the Corona Borealis supercluster, all the samples had correlation lengths of $r_0 \simeq 20\,h^{-1}$ Mpc and power indices of $\gamma \simeq 2$.

Sample II: Nichol *et al.* (1994a)

Nichol *et al.* (1994a) have re-estimated the ξ_{CC} of the Abell cluster sample presented in Huchra *et al.* (1990). This sample included all 145 $RC \geq 0$, $D \geq 5$ Abell clusters in the region $10^h \leq \alpha \leq 15^h$ and $58° \leq \delta \leq 78°$. These clusters have accurate optical positions and spectroscopic redshifts. (The mean redshift of the sample is $\bar{z} = 0.16$). Briel & Henry (1993) analysed ROSAT All-Sky Survey (§ 2.1) data in regions around each of the 145 cluster positions and calculated source count rates and detection likelihoods. From this list, Nichol *et al.* (1994a) selected all 67 clusters with $z < 0.24$ and $L_X \geq 10^{43}\,\mathrm{erg\,s^{-1}}$ that were detected in X-rays at $\sigma > 2$, with which to perform a correlation function analysis. Over the range $6 \leq r \leq 40\,h^{-1}$ Mpc, they measured $r_0 = 16.1 \pm 3.4\,h^{-1}$ Mpc, and $\gamma = 1.9 \pm 0.3$. What is surprising about this result is that it differs form the findings of Huchra *et al.* (1990), $r_0 = 20.3^{+4.8}_{-5.1}$, for the whole sample of 145 clusters. This suggests that by imposing X-ray selection on a sample of optical clusters, the statistical properties of that sample may change.

B. Samples Produced by Plate Digitisation

Recently it has become technically possible to digitise photographic plates with sufficient resolution and speed that galaxy catalogues can be constructed over large areas

of the sky without the requirement of visual plate scanning. From these digitised galaxy samples, one can then produce cluster samples using computer algorithms with objective selection criteria. We describe here two cluster samples derived from plate scans of the UKST plates. (A third cluster sample, the ROE/NRL cluster catalogue, and the UKST survey is described in § 2.2.4.)

Sample III: Nichol *et al.* 1992

Nichol *et al.* (1992) presented the first $\xi_{CC}(r)$ for digitised clusters, based on a sample of 79 rich clusters taken from the Edinburgh/Durham Cluster Catalogue (EDCC). The EDCC contains 737 clusters or groups, Lumsden *et al.* 1992. It was developed from the Edinburgh/Durham Southern Galaxy Catalogue (EDSGC, Heydon-Dumbleton *et al.* 1989). The EDSGC was constructed using COSMOS scans of 60 UKST plates and covers an area of 0.5 steradians centered on the South Galactic Pole. The EDCC cluster-finding algorithm incorporates sophisticated background subtraction and deblending routines. Galaxy richness, R_{gal}, for EDCC clusters is defined in a similar way to that of Abell (1958), except that the counting radius was reduced to $1\,h^{-1}$ Mpc. The 79 clusters in the Nichol *et al.* (1992) analysis represent 90% of the $R_{gal} \geq 22$ EDCC clusters in the region $23^h53^m \leq \alpha \leq 3^h35^m$ and $-22°53' \leq \delta \leq -42°12'$. They measured $\xi_{CC}(r)$ for this sample over the range $3 \leq r \leq 35\,h^{-1}$ Mpc to have an $r_0 = 16.4 \pm 4.0\,h^{-1}$ Mpc and a slope of $\gamma = 2.1 \pm 0.3$. The unique characteristic of this sample is the large number of galaxy spectra, n_{gal}, used to determine the cluster redshift, *i.e.* $\bar{n}_{gal} = 10$.

Sample IV: Dalton *et al.* 1992

The Automatic Plate Measuring (APM) cluster sample (Dalton *et al.* 1992) covers $4300\square°$ ($\delta < -20°$, $b \lesssim 40°$) and was developed from the APM Galaxy Survey (Maddox *et al.* 1990). The APM galaxy survey contains $\sim$ 2 million galaxies with $b_j \leq 20.5$, and was constructed from the digitisation of 185 UKST plates, again centered on the South Galactic Pole, by the SERC APM machine at Cambridge University. Clusters of galaxies to $z_{est} \lesssim 0.1$ with $n_{gal} \geq 20$ were selected from the APM survey using surface density enhancement criteria. An iterative procedure was applied to define a characteristic magnitude and richness within $0.75\,h^{-1}$ Mpc of the cluster centre. The $\xi_{CC}(r)$ for 190 $R_{gal} \geq 20$ APM clusters, the largest digitised sample to date, was measured by Dalton *et al.* (1992) to have an $r_0 = 12.9 \pm 1.2$ for $\gamma = 2$.

C. An X-ray Selected Sample

The selection of the cluster samples I–IV relied on the detection of two-dimensional galaxy enhancements. An alternative approach is to select clusters by virtue of their

X-ray emission, § 2.1.2.

Sample V: Lahav *et al.* (1989)

Lahav *et al.* (1989) determined the only pre-ROSAT spatial correlation function for X-ray clusters, finding $r_0 = 21\,h^{-1}\,\mathrm{Mpc}$ for $\gamma = 1.8$. Their result was based on an all-sky sample of 53 X-ray clusters with (2–10 keV) fluxes greater than $1.7 \times 10^{-11}\,\mathrm{erg\,s^{-1}\,cm^{-2}}$. The majority of the clusters were selected from the all-sky HEAO I survey sample of Piccinotti *et al.* (1982). The list was supplemented with clusters from the ARIEL V survey (McHardy *et al.* 1981 & Warwick *et al.* 1981) and from EINSTEIN and EXOSAT observations. Accurate fluxes for 49 of these clusters were taken from EINSTEIN and EXOSAT observations. The authors claim that the sample is complete to $3 \times 10^{-11}\,\mathrm{erg\,s^{-1}\,cm^{-2}}$ and that the incompleteness at lower fluxes comes from a reduced cluster detection efficiency at low Galactic latitudes in the all-sky surveys. It should be noted that, when clusters at $b < 20°$ are removed, the measured correlation length of the remaining 45 clusters drops to $r_0 \approx 17\,h^{-1}\,\mathrm{Mpc}$

1.3.2 Motivation for a New Derivation of ξ_{CC}

Referring again to Figure 1.1, it can been seen that at $k \sim 0.03\,h\,\mathrm{Mpc}^{-1}$ there is a large discrepancy between the power measured from optical galaxies and from clusters. Any valid model of large-scale structure formation must be able to explain this discrepancy. To this end, various scenarios have been proposed. For example, suggestions that a) the primordial power spectrum had spikes in it, Dekel (1984), b) that clusters formed from only the largest primordial density enhancements, Kaiser (1984) and c) that there is a universal, richness dependent, correlation function, Bahcall & Burgett (1986).

However, there is a more obvious solution; perhaps the cluster observations are biased in some way so as to over predict the true clustering power. It can be seen from the discussion above that the cluster correlation length, r_0, is not a stable parameter between different cluster samples. It ranges from $13\,h^{-1}\,\mathrm{Mpc}$ (APM clusters, sample IV) to $\simeq 20\,h^{-1}\,\mathrm{Mpc}$ (Abell clusters, sample I). Admittedly these results are not enormously discrepant, given the size of the error bars in each case. However, in terms of finding a theoretical model of structure formation that can predict both galaxy and cluster clustering, this discrepancy is very important. Whereas a cluster correlation length of $r_0 \simeq 13\,h^{-1}\,\mathrm{Mpc}$ has been shown to be consistent with CDM models (albeit hybrid versions of the standard model mentioned in § 1.2.4, *e.g.* Croft & Efstathiou 1994), it is almost impossible to reconcile an $r_0 \simeq 20\,h^{-1}\,\mathrm{Mpc}$ with CDM models. Indeed, the extremely high values of $r_0 \sim 45\,h^{-1}\,\mathrm{Mpc}$ that have been measured for richness class

$RC > 2$ Abell clusters (Peacock & West 1992) would violate the fundamental assumption of CDM, and other models, that the primordial fluctuations were governed by Gaussian statistics.

Therefore, it is vital that we understand why the clustering measured from digitised cluster samples is consistently lower than that measured from raw samples of Abell clusters. (Where "raw" refers to samples that have had no additional X-ray selection applied.) Although the answer to that question seems clear, that the Abell catalogue suffers from inherent selection effects, this scenario is certainly not widely accepted. This is demonstrated by the following quotes made with regard to possible selection biases in sample I, the Postman *et al.* (1992) sample;

1) "The clustering properties of Abell clusters are robust and are not strongly dependent on selection or projection effects." (Postman *et al.* 1992)

2) "We use Postman *et al.* 's data to show that the clustering of Abell clusters is highly anisotropic in redshift space, providing clear evidence of artificial clustering." (Efstathiou *et al.* 1992)

The anisotropies that Efstathiou *et al.* (1992) are referring to are demonstrated in Figure 1.2. This is a reproduction of Figure 2 in their paper and shows contours of correlation amplitude as a function of angular (σ) and redshift (π) separation for the Postman *et al.* (1992) sample. (Where $r^2 = \sigma^2 + \pi^2$.) If the clustering properties of this sample were isotropic then the contours should be circular. They are clearly not circular, being stretched out along the redshift axis to $\pi \simeq 80\,h^{-1}$ Mpc. This effect was first noticed by Bahcall *et al.* (1986) and interpreted as evidence either for large peculiar velocities[8] of $\sim 2000\,\mathrm{km\,s^{-1}}$ or for preferential alignments of superclusters. Neither interpretation has been leant weight by subsequent observations, although a recent theoretical paper (Jing *et al.* 1992) did state that up to 30% of "possible universes" would show the same effect.

Efstathiou *et al.* (1992) prefer to interpret these anisotropies as evidence for projection effects in the Abell catalogue. These effects occur when galaxies are falsely associated with a cluster, because they happen to lie along the same line-of-sight. There are two manifestations of projection effects;

1) **The Sutherland effect**; "angular correlations that are not due to genuine clustering in redshift space", Sutherland (1988).

2) **Phantom clusters**; "A significant fraction of rich clusters identified in projection do not correspond to rich three-dimensional clusters", Frenk *et al.* (1990, also Lucey 1983).

The Sutherland effect occurs when two clusters lie along roughly the same line-of-sight and their halos overlap. Galaxies in the overlap regions boost the measured richness of

[8] Velocities in addition to the Hubble flow

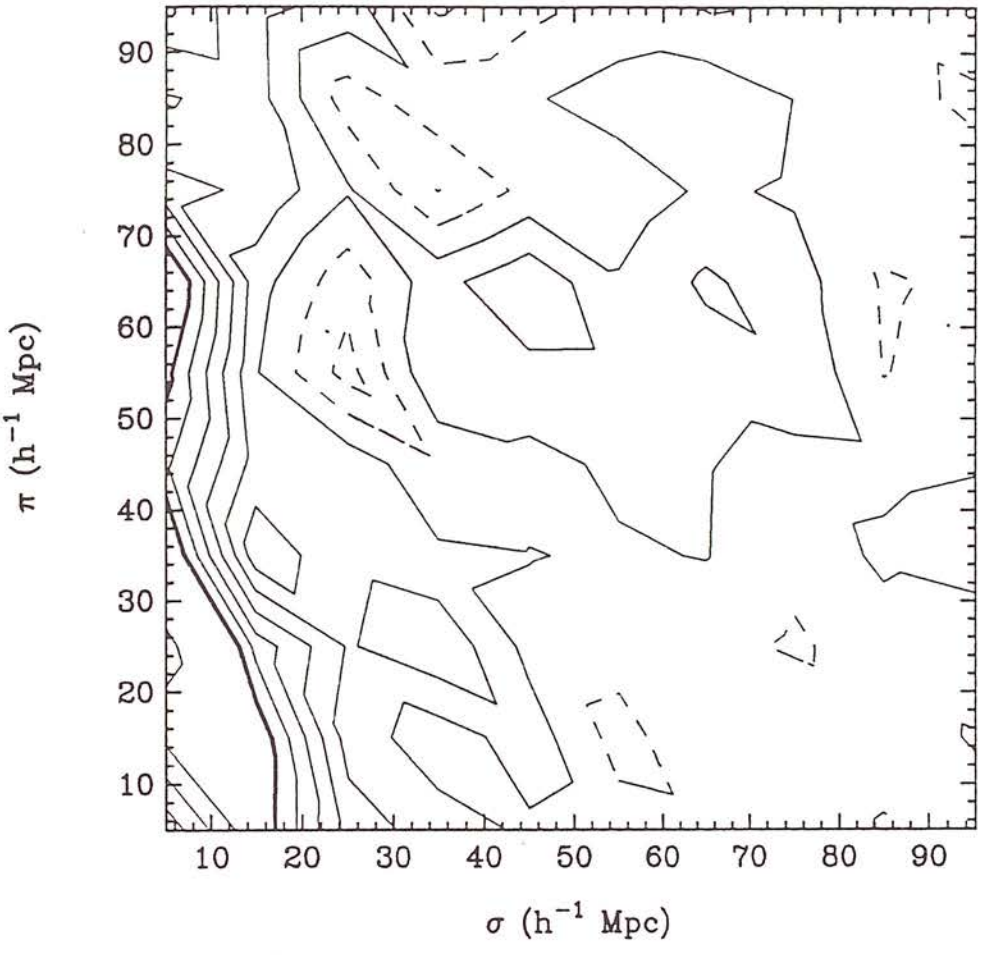

Figure 1.2: A contour plot of correlation amplitude as a function of angular and redshift distance, $\xi_{CC}(\sigma, \pi)$, for the Postman *et al.* (1992) sample, notice the large anisotropies in the π direction. The contour levels are at $-0.4 < \xi_{CC} < 4$, where the $\xi_{CC} = 1$ contour is shown in bold and the contour levels at negative values of ξ_{CC} are plotted as dashed lines. (Reproduction of Figure 2 in Efstathiou *et al.* 1992)

both clusters. Therefore, systems that are intrinsically quite poor will be included in a richness limited sample of optical clusters. The presence of these poor clusters artificially enhances the correlation amplitude and, because these clusters necessarily have a partner along the same line of sight, the enhancement will preferentially occur in the redshift direction. In several papers, Sutherland, Efstathiou and co-workers have attempted to correct for this effect in the Abell catalogue. They estimate the correlation length to be $r_0 = 14\,h^{-1}$ Mpc after performing this correction on the Postman *et al.* (1992) sample of Abell clusters, Efstathiou *et al.* (1992). The de-projection techniques they use have not been without criticism, however, *e.g.* Dekel *et al.* (1989).

It is possible to circumnavigate the Sutherland effect in optically selected cluster samples by selecting clusters with more rigorous criteria than Abell. Both the Nichol *et al.* (1992) and Dalton *et al.* (1992) samples (III & IV) employed smaller counting radii than Abell, in order to reduce the problems associated with overlapping clusters. Nichol (1992) states that, by choosing a selection radius of $1.0\,h^{-1}$ Mpc for EDCC clusters over the Abell radius ($1.5\,h^{-1}$ Mpc), the number of overlapping clusters is reduced from 30% to 8%. This is illustrated by the fact that the digitised correlation functions are much more isotropic in σ, π space than Figure 1.2. However, even these improved samples are not spared from the second variety of projection effects, that of phantom clusters. The only way to weed out phantom clusters from a sample is to take multiple galaxy spectra in the direction of the cluster candidate. (A real cluster will contain tens or hundreds of galaxies at the same redshift, whereas the galaxies around a phantom cluster will have a broad redshift range.) The detailed spectroscopic followup by Nichol *et al.* (1992) has shown that $\approx 10\%$ of EDCC clusters are in fact phantom projections.

Alternatively it is possible to remove **both** types of projection effects by selecting the cluster sample via the intense X-ray emission in the cluster core. The X-ray properties of clusters are described in § 2.1.2, but for now let us concentrate on the following salient features;

1) Clusters are highly luminous in X-ray emission, $L_X \sim 10^{43} \rightarrow 10^{45}\,\mathrm{erg\,s^{-1}}$, and can be detected in X-rays to $z \simeq 1$, Castander *et al.* (1994) & Nichol *et al.* (1994b).

2) The hot gas that is responsible for the emission is in hydrostatic equilibrium with the gravitational potential well of the cluster.

3) The X-ray emission is highly peaked towards the cluster core, with core radii of the X-ray emission varying between $0.1 - 0.9\,h^{-1}$ Mpc, Jones & Forman (1984).

From point 2), it is possible to confirm the presence of a three dimensional potential well from an X-ray detection of the intracluster gas. Thus the problem of phantom clusters is solved without having to take multiple galaxy spectra. The Sutherland effect does not

affect an X-ray selected sample because the core radii of the X-ray emission is smaller than the Abell radius. This has been shown to be true by Nichol *et al.* (1994a, sample II). Their correlation function has roughly symmetrical contours of $\xi_{CC}(\sigma, \pi)$, indicating that it is possible to weed out projection effects in the Abell catalogue by imposing an X-ray selection criterion. A final advantage of X-ray selection is that the comparison between observations and theoretical predictions is simpler for an X-ray selected sample of clusters than it is for an optically selected sample, Frenk *et al.* (1990). This is because there is a tighter relationship between the X-ray luminosity, L_X, and the cluster mass (via the cluster temperature, T; see David *et al.* 1993, for L_X to T relation) than there is between galaxy richness and cluster mass.

Despite these obvious advantages, previous studies of cluster large-scale structure have been the preserve, almost exclusively, of optically selected samples. The exceptions being the work by Lahav *et al.* (1989, sample V) and Nichol *et al.* (1994a). These two works are very important because they show that a) X-ray clusters cluster in the same way as optical clusters *i.e.* the correlation has a consistent power law form and b) (from sample II) that the differences between digitised clusters and raw Abell clusters have their origin in projection effects and not in a richness dependent correlation function. However, both of these studies have problems, the most important of which being that they include so few clusters. In addition the Lahav *et al.* sample is selected from a medley of satellite surveys which results in ambiguous completeness and homogeneity. The Nichol *et al.* sample has the advantage of being selected from only one survey, however, it is still biased by the intrinsic problems (especially incompleteness) of the Abell catalogue.

1.4 Summary

As the previous sections should have made clear, there is a real need for a new determination of ξ_{CC} using a large, representative sample of X-ray clusters that is wholly independent of the Abell catalogue. With such a sample it will be possible to probe present epoch large-scale structure in a fashion that transcends the problems of optical cluster samples. With the launch of ROSAT satellite in 1990 this goal is now possible to achieve. ROSAT performed the first all-sky survey with an imaging X-ray telescope and allows, for the first time, the development of homogeneous samples of X-ray clusters that are equivalent in size to the optical cluster catalogues.

The SGP RASS Cluster Project

The rest of this thesis describes the current status of the SGP RASS Cluster Project. This is an international collaboration that was set up to identify, and obtain redshifts for, all ROSAT All-Sky Survey (RASS) cluster sources in a 2800$\square^\circ$ region centered on the SGP. The institutions involved are the Royal Observatory Edinburgh, the Max Planck Institut für Extraterrestrische Physik in Gärching and the Naval Research Laboratory in Washington D.C. The primary scientific aim of this project was to study large-scale structure and measure ξ_{CC} from the largest and most homogeneous sample of X-ray clusters to date. The following chapters describe the development of that sample, the measurement of ξ_{CC} from it and finally how that measurement can help us understand the process of structure formation.

Chapter 2

Selection of SGP RASS Cluster Candidates

This chapter describes the sources of information and the methods used to construct a flux-limited list of ROSAT All-Sky Survey (RASS) cluster candidates from a 2800$\square^\circ$ region around the South Galactic Pole. The selection procedure draws on X-ray information from the RASS , §2.1, and on digitised optical information from the COSMOS/UKST Object Catalogue,§ 2.2.

2.1 The ROSAT All-Sky Survey

As X-rays are absorbed by the earths atmosphere, the development of cluster X-ray astronomy has followed that of X-ray instrumentation and satellite technology. (The earliest, confirmed, cluster detections were made in the early 1970's using the UHURU satellite, Gursky *et al.* 1971.) The launch of the ROSAT [1] satellite on June 1^{st} 1990 marked a landmark in that development. The goals of the ROSAT mission were to a) complete an all-sky survey with which to detect sources to a positional accuracy of $\lesssim 0.5'$ and provide broad-band spectra at X-ray ($0.07 \rightarrow 2.4$ keV, $\lambda = 100 \rightarrow 5$ Å) and XUV ($\lambda \leq 60$Å) wavelengths and b) study selected sources in more detail using pointing observations. The RASS (completed in August 1992) constitutes the first all-sky survey with an imaging X-ray telescope. The last all-sky X-ray survey, performed by the HEAO I satellite, featured position determination and sensitivity that were, respectively, 3 and 2 orders of magnitude worse than the ROSAT survey, Voges (1992). The improved sensitivity of the RASS means that $\simeq$ 50000 sources have been detected across the sky, compared to 842 detected during the HEAO I survey. The process of RASS source classification, as stars, AGN , clusters *etc.* , is several years from completion. However, pre-launch predictions, § 2.1.3, suggest that several thousand clusters will have been

[1] ROSAT is an acronym for the German word Röntgensatellit.

detected, thus increasing the number of known X-ray clusters by an order of magnitude.

In this section we describe the instruments used during the ROSAT All-Sky Survey (RASS), the processes of RASS data reduction, § 2.1.1, and the expectations for cluster detection in the RASS , § 2.1.3. We also introduce the salient features of cluster X-ray emission, § 2.1.2.

The X-ray telescope (XRT) on board ROSAT consists of the X-ray Mirror Assembly, the PSPC and the High Resolution Imager (HRI). The XRT is a grazing incidence four-fold nested Wolter type I configuration (Aschenbach 1988). The mirror shells are made out of a glass ceramic coated with a thin gold layer in order to increase X-ray reflectivity. One of the design advantages of the ROSAT mirror assembly is that scattering of X-rays by microroughness of the reflecting surfaces is negligible. The field of view of the telescope is 2° in diameter and the *geometric* collecting area is 1141 cm^2. (The *effective* collecting area is a decreasing function of energy and off-axis angle.) The telescope point spread function is $\sim 4.8''$ FWHM on-axis, increasing with off axis angle to several arc minutes. (Where the quoted values have been taken from the *UK ROSAT Announcement of Opportunity: AO2* 1991.)

The PSPC (Briel & Pfeffermann 1986) was used in conjunction with the XRT during the RASS . The PSPC consists of two identical proportional counters with a cathode grid readout scheme for position determination. X-rays penetrate into the counter volume through a 8 cm diameter polypropylene entrance window. The entrance window is supported by radial struts and a grid system and is additionally coated with carbon and lexan to decrease UV transmission. The average transmission of the window is 79% except in those regions blocked by struts. The PSPC is filled with a low pressure mixture of argon, methane and xenon. The field of view of the PSPC, like that of the XRT, is 2°. The gas has an almost 100% absorption efficiency for X-ray photons less than 2 keV in energy. The carbon coating means that the entrance window is basically opaque at energies just above the carbon edge at 0.28 keV.

The energy resolution is given by

$$\frac{\Delta E}{E} = 0.43 \left(\frac{E}{0.93}\right)^{-0.5}, \tag{2.1}$$

(FWHM). At 0.93 keV the position resolution of XRT+PSPC $\approx 25''$, which is achieved through a combination of a 0.5 mm spaced cathode grid wires and a sophisticated position determination procedure. The angular resolution is only a weak function of energy, however, it deteriorates rapidly with increasing off-axis angle due to the off-axis blur of the XRT. Particle background in the PSPC is very low, an anticoincidence counter rejects $\approx$ 99% of background events, with a resulting background of only 2.5×10^{-5}

counts s^{-1} $arcmin^{-2}$. (The three main background components are; scattered solar X-rays, high-energy charged particles and cosmic X-rays, Plucinsky *et al.* 1993, Snowden & Freyberg 1993, Snowden *et al.* 1992.)

The RASS was built up from scans in great circles through the ecliptic poles in the plane perpendicular to the earth-sun axis. With a PSPC+XRT field of view of 2° and a nominal survey rate of 1° per day, a celestial position in the plane of the ecliptic was visible for approximately two days. Due to the scanning method, the highest total exposure times, approximately 50,000 seconds was reached at the ecliptic poles, with the exposure decreasing gradually to $\approx$ 400 seconds at the ecliptic equator. During the penetration of the radiation belts around the magnetic poles and in the South Atlantic Anomaly the X-ray detector had to be switched off to prevent damage from a high flux of local charged particles. This has had the effect of decreasing the exposure over parts of the sky.

2.1.1 RASS Data Analysis

The data from the all-sky survey is processed at MPE by the ROSAT Standard Analysis Software System (SASS, Voges *et al.* 1992). For the purposes of SASS source detection and parameterization, the survey photon data are first collected into great circle strips 2° wide. The detection algorithm combines several complementary source detections techniques working on the raw photon data as well as on coarsely binned ($1.6' \times 1.6'$) images of the strips, Cruddace *et al.* (1991). The first step is a local detection (LDETECT) using square sliding windows. The window is moved across a binned representation of the raw data marking positions where the count rate in the central part of the window exceeds the value expected from the background – which is determined in the outermost regions of the window. The threshold for detection is set to a signal-to-noise value of 8. To account for extended sources, the process is repeated up to 4 times with different pixel sizes; $1.6', 3, 2', 4.8', 6.4'$. The window size consists of 5×5 pixels in each case. LDETECT has the inherent disadvantage that artificial parameters, such as bin sizes, window sizes and window geometries, will effect the decision as to whether a source detection is significant or not. This flaw is partially overcome by an additional detection algorithm called MDETECT ("map-detect"). This removes the LDETECT sources from the photon data and then computes a global background from a two-dimensional spline fit to the remainder. The sliding window procedure is then repeated using 3×3 pixels, whereby source counts inside the window are compared to the global background. Again a threshold of source detection is a signal-to-noise value of 8.

The final stage of the SASS processing is the determination of the best-fitting source

positions and fluxes using a maximum-likelihood (ML) routine. This analyses the raw, un-binned, photon data around each candidate source position flagged by either LDETECT or MDETECT. Only $\sim$ 15% of the candidates, those with a ML detection likelihood > 10, are retained in the source list after the ML analysis. This likelihood threshold was chosen to limit the number of spurious detections to $< 10\%$, Cruddace *et al.* (1991). For each RASS source accepted by ML, the following properties were calculated;

- The source position in celestial coordinates
- The exposure time
- The source and local background count rates
- The detection likelihood
- The hardness ratio (HR), which is defined as the difference between the hard ($0.4 - 2.4$ keV) and the soft counts ($0.07 - 0.4$ keV), divided by the total counts ($0.07 - 2.4$ keV). (The hard and soft bands are divide by the carbon edge mentioned in §2.1)
- The source extent and the corresponding likelihood, which are determined by fitting Gaussian profiles to the surface brightness and making a comparison to the point spread function.

The source information in each 2° strip is stored in Master Source Lists (MASOL files). Each source is given a unique, 7 digit identification number. These "MASOL numbers" are used throughout this thesis to refer to specific RASS sources, *e.g.* in table A.2 where the SGP RASS cluster candidates are listed. These MASOL numbers can be understood in the following manner; the first 3 digits refer to the RASS strip (1-90) in which the detection was made, the fourth digit indicates the quadrant of the detection and the last three digits identify the specific source in that quadrant. For example, the first source in table A.2 is 0011003, which is the third source detected in quadrant 1 of strip 1. The strip number is related to right ascension (α) in the following way;
In quadrants 2 & 3: α = strip no. $\times$ 4,
In quadrants 1 & 4: α = strip no. $\times$ 2.
Notice in table A.2 that a) the southern quadrants (3 & 4) are most commonly featured and b) any candidates with strip numbers '104', '105', '106' or '122' differ from those numbered '004', '005', '006' or '022' only in that they were processed by different versions of the SASS software. Note that the MASOL numbers will soon be abolished by

MPE, and replaced by source names that intrinsically include coordinate information. However, they are retained in this thesis for ease of cross referencing.

To date, the whole ROSAT survey has been processed once. SASS I, as this first processing run is known, has resulted in 49441 source detections, Ebeling *et al.* (1992). Detection of sources at the very edges of survey strips (a few % of the sky) is inhibited by SASS I. In the near future a re-analysis, SASS II, will take place in which the photons will be binned into smaller, slightly overlapping, fields allowing a 100% detection capability. The exposure of such fields will increase with ecliptic latitude, which will reduce the effective flux limit of the survey. Therefore, more sources will be identified by SASS II than by SASS I.

2.1.2 Cluster X-ray Properties

We present below a brief overview of the X-ray properties of clusters that are relevant to their detection and parameterization in the RASS , for a comprehensive review see Sarazin (1988).

Clusters are among the most luminous X-ray sources in the sky, $L_X \sim 10^{43} \rightarrow 10^{45}\,\mathrm{erg\,s^{-1}}$. Observations have shown that they are filled with a hot, diffuse intracluster plasma consisting of mostly ionized hydrogen and helium. Typical values are $2 \lesssim T \lesssim 10\,\mathrm{keV}$, $n \approx 10^{-4} - 10^{-2}\,\mathrm{cm^{-3}}$ and a $0.3\times$ solar heavy metal abundance (David *et al.* 1993, Sarazin 1992, Mushotzky 1992). The gas mass is typically $M_{gas} \sim 10^{14} M_{\odot}$ which is approximately $2 \rightarrow 10$ times that in the galaxies, and accounts for $\sim 10\% \rightarrow 20\%$ of the total mass. The gas was, probably, heated by infall and compression when it was first introduced into the cluster, Sarazin (1988). The gas is so rarified that it will not cool down after entering the cluster, except in the cores of some clusters where the density is high enough for the cooling time to be shorter than the Hubble time. Except in these cool cores, the gas is observed to be isothermal, *e.g.* Mushotzky 1994. The thermal energy of the gas is approximately equal to the gravitational potential, ϕ,

$$\frac{3k_B T_g}{2\mu m_p} \approx -\phi, \tag{2.2}$$

where T_g is the gas temperature, μm_p is the mean particle mass of the gas, Sarazin (1988).

The dominant emission process in the gas is thermal bremsstrahlung radiation, or free-free emission. For a gas temperature containing ions of charge Z, the emissivity (energy emitted per unit time, frequency and volume) at frequency ν is given approximately by,

$$\epsilon_\nu \propto T_g^{-1/2} Z^2 n_e n_i \exp(-h\nu/k_B T_g), \tag{2.3}$$

where n_e and n_i are the electron and ion number densities respectively, Ebeling (1994). The exact relation contains corrections for quantum mechanical effects, but from equation 2.3 we can see that, for a fixed gas temperature, the emissivity will be close to an exponential of the frequency, ν. Figure 2.1 is a reproduction of Figure 1 in Mushotzky (1992) and shows theoretical cluster X-ray emission as a function of energy for three different gas temperatures. Despite the wide variation of cluster X-ray spectra with gas temperature seen in this figure, the response of the PSPC to cluster emission is essentially independent of the gas temperature due to its limited spectral coverage. This is demonstrated in Figure 2.2, which shows predicted cluster spectra for various gas temperatures.

Figure 2.3 demonstrates the *spatial* distribution of cluster X-ray emission. It is a reproduction of Figure 1 in Burns *et al.* (1994) and shows a high quality ROSAT PSPC pointing observation of the Coma cluster ($z = 0.023$). There are two prominent features to note from this figure; (1) the almost circular contours in the main body of the cluster, which suggest that the cluster core is relaxed and (2) the protrusion in X-ray emission to the south west of the cluster centre which suggest that the cluster is in the process of a merger with the NGC 4839 galaxy group. These features, relaxed core and some degree of sub-clustering, are typical of X-ray clusters. The X-ray emission in Coma cluster has been observed, White *et al.* (1993a), to extend out to $2.5\,h^{-1}$ Mpc. The surface brightness, $I_X(r)$, in the Coma cluster core, $r \lesssim 0.5\,h^{-1}$ Mpc, is well fitted by the traditional King approximation to a self-gravitating isothermal sphere[2],

$$I_X(r) \propto \left[1 + \left(\frac{r}{r_c}\right)^2\right]^{-3\beta+1/2} \tag{2.4}$$

where r_c is the core radius of the galaxy distribution, $\beta \sim 1$ represents the ratio of the energy per unit mass in the galaxies to that in the gas. β is defined as,

$$\beta = \frac{\sigma_v^2}{k_B T/\mu m_p}, \tag{2.5}$$

where σ_v is the galaxy velocity dispersion. The Coma cluster is uncommon among bright, rich clusters in that it does not have a cooling flow at its centre, see *e.g.* Edge & Stewart (1991). (In cooling flow clusters the surface brightness profile is even more centrally peaked.)

2.1.3 Expectations for Cluster Detection

Prior to the satellite launch, several groups attempted to make realistic predictions of the cluster detection statistics for the ROSAT All-Sky Survey, *e.g.* Evrard & Henry (1991)

[2]See Bahcall & Lubin (1994) for a recent re-derivation of this profile.

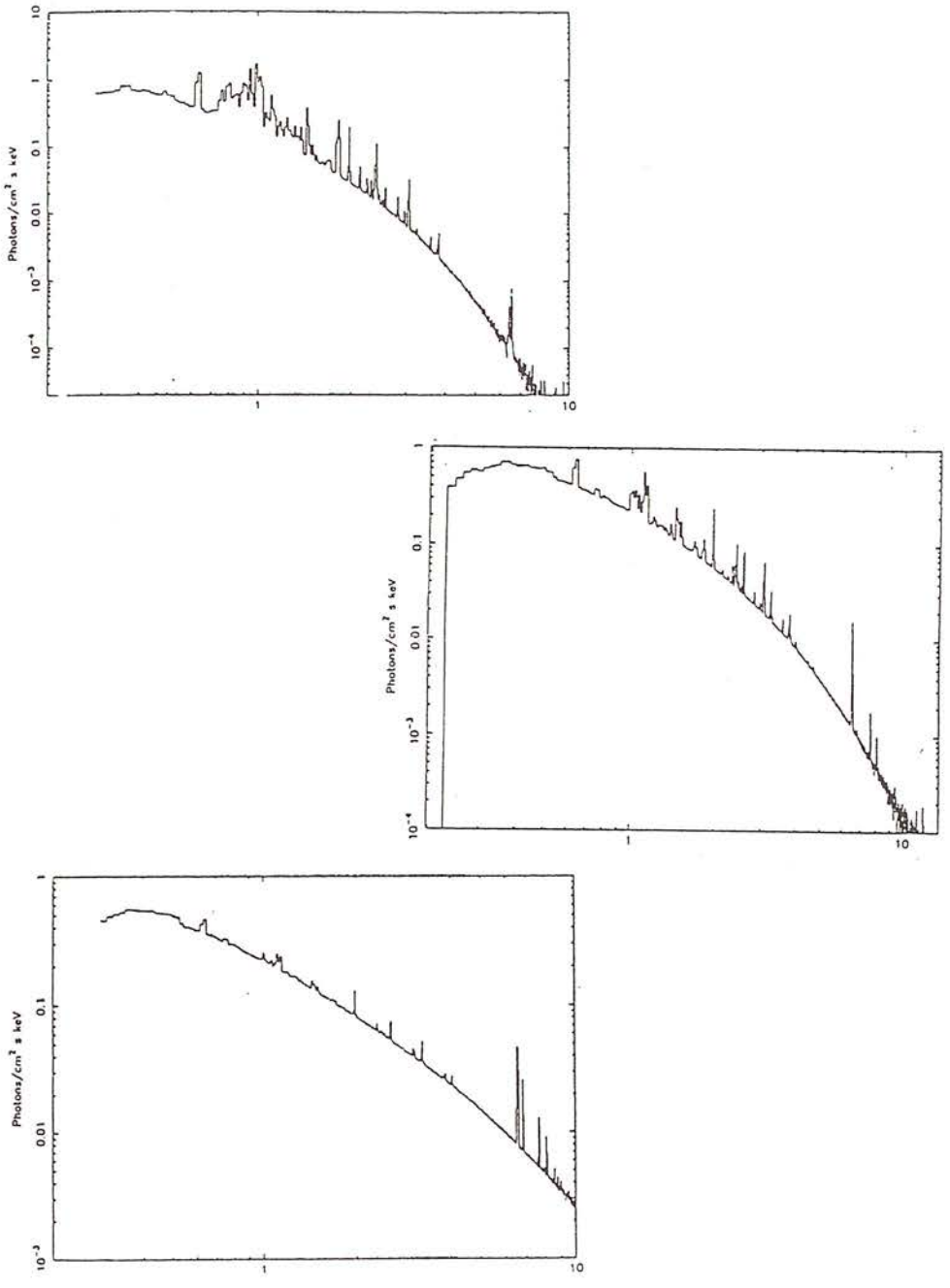

Figure 2.1: The predicted 0.3−10 keV emission from the intracluster gas at $k_BT = 1$ keV (top), 2 keV (middle) and 6 keV (bottom). Notice the strong changes in the spectrum as a function of temperature. (Reproduction of Figure 1 in Mushotzky 1992)

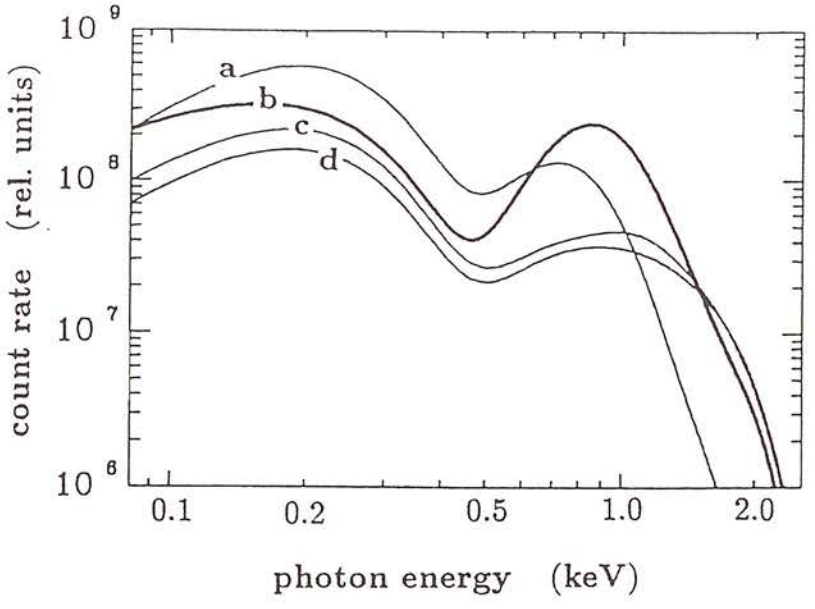

Figure 2.2: Projected PSPC cluster spectra for four different intracluster gas temperatures; (a) 1×10^7K, (b) $3 \times 10-^7$K, (c) 1×10^8K. (Reproduction of Figure 2 of Böhringer *et al.* 1992)

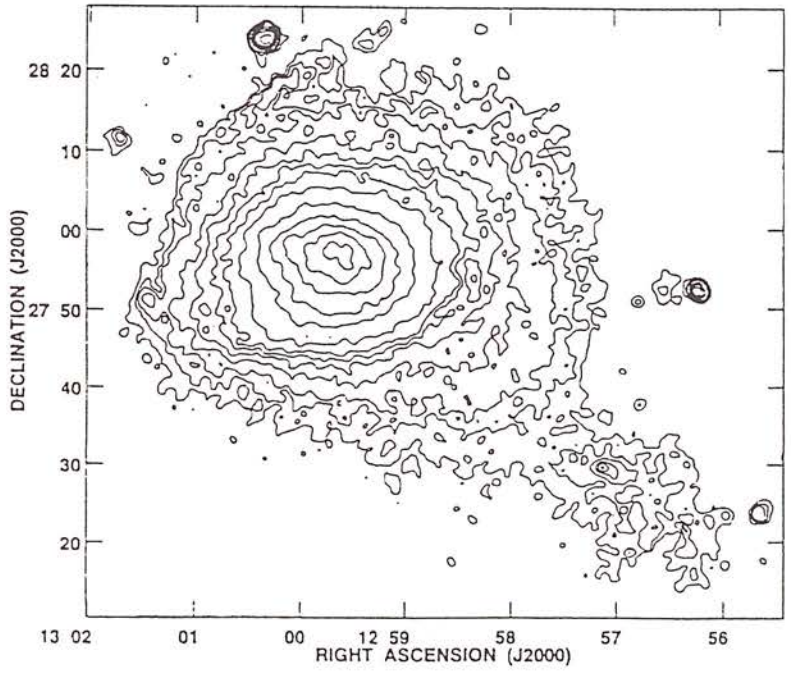

Figure 2.3: ROSAT PSPC X-ray image of the Coma cluster and NGC 4839 group. (Reproduction of Figure 1 in Burns *et al.* 1994.)

and Cruddace *et al.* (1991). These predictions involved many assumptions regarding the intrinsic distribution of clusters, the nature of the intracluster medium and the response of the ROSAT instruments. For example, to determine the distribution of fluxes received by the PSPC from clusters, one needs to assume a form for the cluster luminosity function. (The $0.1 - 2.4\,\mathrm{keV}$ flux is related[3] to its luminosity in that band by,

$$L_X = 4\pi F D^2, \tag{2.6}$$

where D is the luminosity distance to the object, equation 1.4.) Cruddace *et al.* (1991) adopted the luminosity function derived by Kowalski *et al.* (1984) and assumed evolution effects to be negligible. The Kowalski *et al.* result was based on the HEAO I observation of 202 Abell clusters and has the form,

$$n(dL_X) = 1.16 \times 10^{-7} exp\left(\frac{-L_X}{8.2}\right) L_X^{-1.5}, \tag{2.7}$$

where L_X is in units of $10^{44}\,\mathrm{erg\,s^{-1}}$ $(2 - 10\,\mathrm{keV})$ and $n(dL_X)$ is in units of $h^{-1}\,\mathrm{Mpc}^{-3}$. Conversely, Evrard & Henry used theoretical models, normalized to EINSTEIN and EXOSAT observations (Edge *et al.* 1990 & Gioia *et al.* 1990), that incorporated evolutionary effects. The general consensus was that several thousands of clusters would be detected in the survey, constituting $\sim 10 \rightarrow 15\%$ of all RASS sources, and that the redshift range of these detections will extend to $z = 0.5$ in the main survey and $z = 1.0$ in the ecliptic pole regions. The flux limit of the cluster detection was estimated by both groups to be $\approx 1 \times 10^{-12}\,\mathrm{erg\,s^{-1}\,cm^{-2}}$ over most of the sky and $\approx 1 \times 10^{-13}\,\mathrm{erg\,s^{-1}\,cm^{-2}}$ near the ecliptic poles.

Temperature determinations and spatial mapping of clusters detected in the RASS will only be possible for the very nearest and brightest objects, *e.g.* the Perseus and Virgo clusters (Böhringer *et al.* 1992). As stated in Henry (1992), approximately 5000 photons are required to make a cluster X-ray image like that shown in Figure 2.3. By contrast the majority of RASS clusters will feature only $20 - 500$ photons. (This prediction is based on typical count rates of $0.05 \rightarrow 1\,\mathrm{s^{-1}}$ and average RASS exposure times of $t_{exp} = 430 \pm 130$ s in the north and $t_{exp} = 324 \pm 118$ s in the south.) However, even with this limited number of photons, it is possible to utilize the energy discrimination of the PSPC detector to differentiate between the soft emission from stellar sources and the Galactic background and the hard emission from clusters of galaxies, Böhringer *et al.* (1992). This feature was exploited during the construction of an all-sky sample of 492 Abell RASS clusters by Ebeling *et al.* (1992).

[3] In practice Hydrogen column densities need to be taken into account, see § 2.4.1.

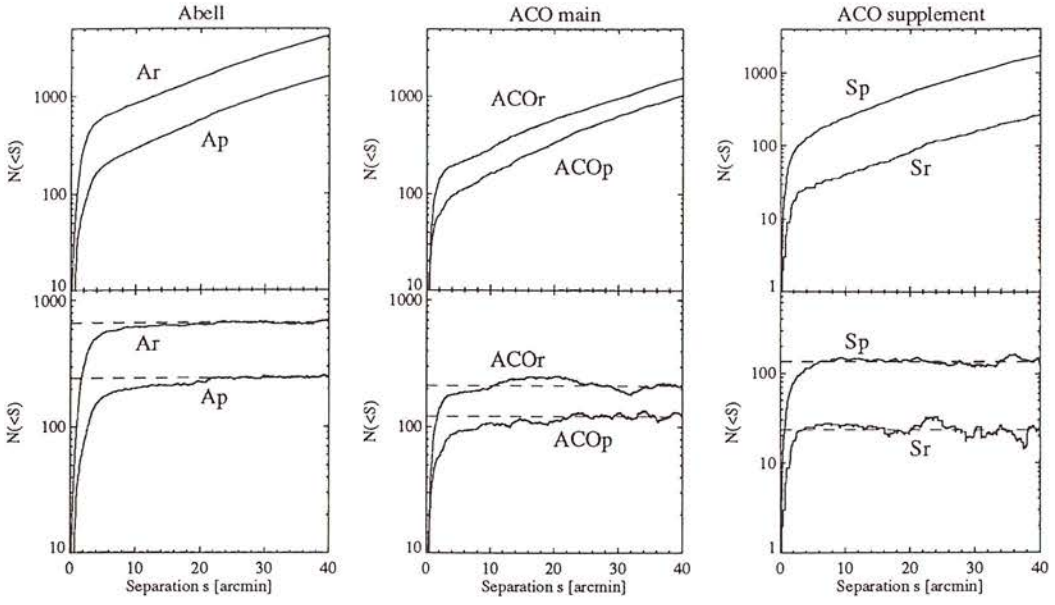

Figure 2.4: Cumulative number counts as a function of angular X-ray to optical source separation before (top) and after (bottom) background subtraction for six subsamples of the Abell catalogues. The subscripts 'p' and 'r' indicate the curves derived from correlations with the poor and rich samples respectively. (Reproduction of Figure 2 in Ebeling *et al.* 1992.)

Ebeling *et al.* (1992) identified X-ray bright Abell clusters by correlating the positions of clusters in the Abell & ACO catalogues with ROSAT all-sky survey source positions. This analysis was performed separately on the 2712 Abell (1958) clusters, 1364 ACO clusters and the 1174 southern "supplementary"[4] clusters. These three samples were further sub-divided into rich ($RC \geq 1$) and poor ($RC \leq 0$) clusters. The source positions and descriptions were generated by SASS I, § 2.1.

Figure 2.4 is a reproduction of Figure 2 of Ebeling *et al.* and shows the cumulative number counts $N(< s)$ for the six cluster samples as a function of angular distance s between optical and X-ray source position. The top half of the figure shows the raw distributions while the bottom plots depict the same data corrected for a contaminating background of chance coincidences obtained from a quadratic least squares fit in the $20' - 50'$ range of the distribution. The horizontal dotted line on each of the lower plots indicates the total number of true coincidences between the two data sets. Ebeling *et al.* (1992) go on to extend the analysis to a spatial separation analysis, based on estimated redshifts and spectroscopic redshifts for the Abell clusters. They conclude that,

[4]These clusters were discovered by ACO on the UKST plates but were considered too poor or too distant to be included in the main catalogue.

to a flux limit of $7 \times 10^{-13}\,\mathrm{erg\,s^{-1}\,cm^{-2}}$, 18% of Abell clusters (both catalogues) and 9% of supplementary clusters are X-ray emitters. After analysing the X-ray properties of the identified Abell clusters and comparing them to the general[5] population of RASS sources, they made the following observations;

1) RASS sources identified with rich Abell clusters are more likely to be extended than the general population; 47% of selected Abell clusters feature a SASS extent of at least 30″, compared to only 8% of the sources in the general population. Figure 2.5, a reproduction of Ebeling *et al.* (1992) Figure 7, illustrates this point.

2) RASS sources identified with rich Abell clusters are likely to be spectrally harder than sources in the general population; more than 7% of the Abell cluster sample.

These findings show that it would be impossible to identify all the cluster detections in the RASS on the basis of their X-ray properties alone and that additional information must be brought to bear. For the SGP RASS Cluster Project we turned to a digitised optical catalogue, described in §2.2, to provide this additional information.

2.2 The COSMOS/UKST Object Catalogue

The identification of the 49441 sources in the RASS relies heavily on digitised object catalogues. The COSMOS/UKST Object Catalogue (CUOC) is used for southern hemisphere identifications and is the fundamental tool employed in this thesis for the selection of cluster candidates in the SGP region. The catalog contains $\sim$ 500 million objects, comprising 11% galaxies, 52% stars and 37% unclassified faint objects, Yentis *et al.* (1990). (The northern identifications are provided jointly by STScI from digitisation of POSS-II plates and by Cambridge University from APM digitised POSS-I plates.)

2.2.1 The UKST Photographic Survey

The UK Schmidt telescope (UKST) at Siding Springs in Australia was commissioned in late 1973 to carry out a systematic photographic survey of the southern hemisphere. The 1.8m UKST has an unvignetted field radius of 2.7°, which makes it ideal for the construction of such a large-area survey. The plates used subtend an area of $6.4° \times 6.4°$ on the sky with a plate scale of 67 arc seconds $\mathrm{mm^{-1}}$. To compensate for the heavy vignetting at the plate edges, the centers of the plates are separated by 5°. The survey plates were taken using a strict set of criteria to minimize systematic errors and to ensure repeatability, Cannon *et al.* (1978). The passband of the SERC J survey is defined by the response of the emulsion (Kodak IIIa-J) combined with a Schott filter. This provides an

[5] Sources that did not have a counterpart in the Abell catalogues.

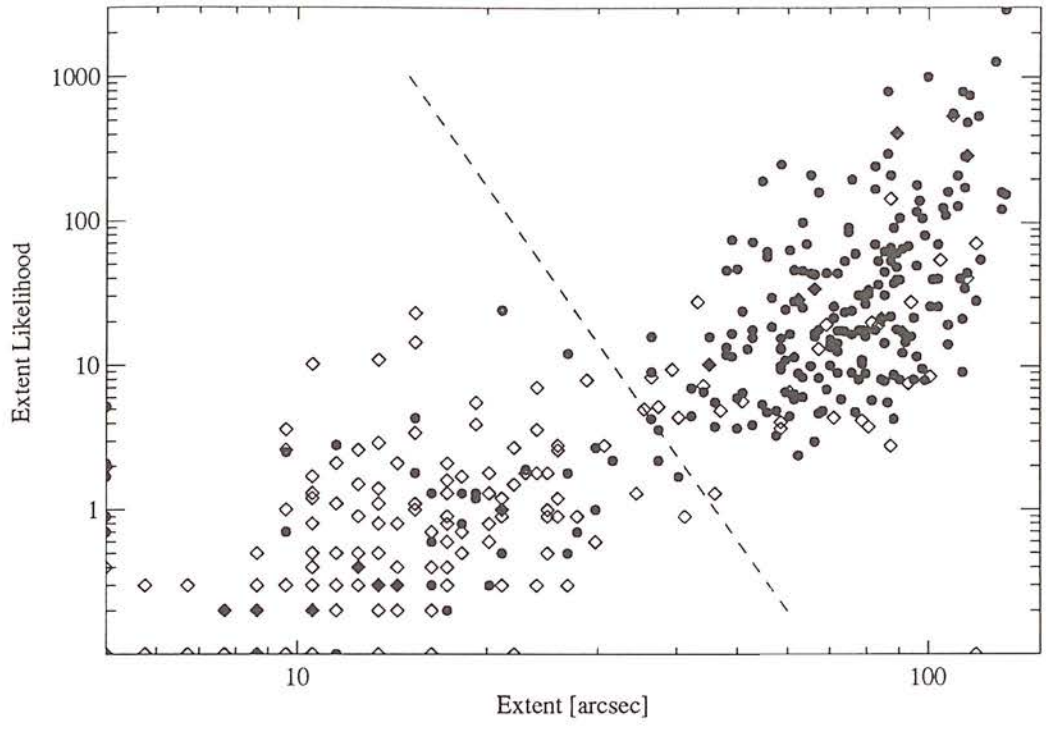

Figure 2.5: X-ray extent likelihood versus extent distribution for the Abell clusters (filled circles) and general source population (open diamonds). (Reproduction of Figure 7 in Ebeling *et al.* 1992.)

almost uniform sensitivity in the wavelength range 3500Åto 5400Å. Image magnitudes on the plates are referred to as b_j magnitudes.

2.2.2 Plate Digitisation

The CUOC has been constructed from the digitisation of 815 (IIIa-J) plates of the UKST survey by the COSMOS machine at the Royal Observatory Edinburgh. COSMOS is a high-speed flying spot microdensitometer, specifically designed and constructed for the scanning of astronomical photographic plates. A COSMOS scan covers an area of 5.4×5.4 of each UKST field. For the CUOC, the resolution of the digitisation was set to $1''$ per pixel. For each pixel, an intensity value was calculated by comparing the transmitted beam brightness with a reference signal (MacGillivray & Stobie 1984). After scanning, the pixel data were passed into the COSMOS image analyzer (Thanisch *et al.* 1984) which connects all the adjacent pixels producing a final set of objects for each plate. Each object was assigned 18 individual image parameters, such as the image magnitude, position and orientation. The magnitudes are returned as isophotal magnitudes, relative to the background magnitude of the plate.

2.2.3 Catalog Development

For the CUOC, the COSMOS scans were further analysed using the deblending software designed by Beard *et al.* (1990). This involved re-thresholding each image in intensity space to search for saddle-points. If such saddle-points were found, the separate peaks were fitted by a Gaussian and split into their daughter images. The deblending was able to distinguish faint star-star pairs, which might otherwise mimic galaxies, and to separate individual galaxies in the cores of clusters.

A typical Schmidt plate contains 2×10^5 objects, of which the majority are stars. Therefore, star-galaxy separation is a very important part of the CUOC. The star-galaxy separation in the CUOC is estimated to be successful for $> 95\%$ of the galaxies and for 99% of the stars, to magnitude limit of $b_j = 21.0$. These estimates are based on tests performed on the EDSGC (Heydon-Dumbleton *et al.* 1989, § 1.3.1). Equivalent statistics are not presently available for the CUOC itself. The COSMOS magnitudes need to be calibrated by external photometry, which is done separately for galaxies and stars. For the galaxies, CCD sequences were used. For stars, a direct calibration was obtained from the HST Guide Star Photometric catalog using extrapolation to extend the calibration to the fainter stars.

Several finding charts produced from the CUOC are shown in appendix C. These finding charts are centered on the positions of RASS sources that were flagged as potential clusters by the methods described in § 2.3.2.

2.2.4 The ROE/NRL Catalogue of "Clusters"

The possibility of large area cluster catalogues was one of the underlying scientific motivations behind the construction of the CUOC. Inspired by the scientific successes of the APM and EDCC digitised cluster catalogues, § 1.3.1, an ambitious project was undertaken jointly by ROE and NRL* to formulate a digitised cluster catalogue covering the whole southern sky from the galaxy data in the CUOC. The cluster finding algorithm for the ROE/NRL catalogue comprised of two distinct routines, 'binning' and 'percolation'. The binning technique detected galaxy density enhancements above the background (Dodd & MacGillivray 1986), while the percolation technique assembled groups of nearest neighbour galaxies. Multiple detections of a single cluster were screened using geometric and photometric criteria. For each entry an Abell-type analysis, § 1.3.1, was performed.

The resulting catalogue contains $\simeq 67,000$ entries, many of which are artifacts of the two-dimensional selection technique. (In fact most entries correspond to sparsely populated groups with $N_{gal} < 10$.) Gursky *et al.* (1992) found that 90% of the southern

*Naval Research Laboratory, Washington D.C.

Abell clusters are present in the ROE/NRL catalogue, demonstrating that the catalogue it is fairly complete for rich clusters. The ROE/NRL catalogue constitutes an invaluable tool in identification and classification of clusters in the RASS . It allows the optical properties of RASS detected clusters to be readily accessed over the whole Southern Sky, without having to resort to the Abell catalogues. In the SGP RASS Cluster Project we have used the ROE/NRL catalogue to identify clusters in the RASS , § 2.3.2.

2.3 Cluster Candidate Selection

2.3.1 The SGP Region

For the SGP RASS Cluster Project, we aimed to make comprehensive cluster identifications in an area of the RASS surrounding the South Galactic Pole. This region, referred to in future as the "SGP region", is bounded by the coordinates; $22^{hr} \lesssim \alpha \lesssim 3^{\rm hr}\,20^{m}$, $-50° \lesssim \delta \lesssim 2°$, covers some $2800\square°$ and contains a total of 4199 SASS detected sources, figure 2.6. Table 2.1 lists the Schmidt plate fields and the SASS I survey strips that fall within its boundaries. The SGP region was chosen for our study of cluster large-scale structure for several reasons, including;

1. **Low Galactic extinction**
   The extinction of extra-galactic radiations by interstellar matter in the Milky Way is at a minimum in the regions around the Galactic poles. The range in galactic latitude in our survey region is $-40 < b \leq -90$. The possible effects of galactic extinction in the SGP region are discussed in more detail in § 2.4.3

2. **Existing optical galaxy and cluster surveys**
   The availability of digitised galaxy maps in the SGP region has meant that this region has been extensively studied with regard to galaxy and cluster large-scale structure, *e.g.* Maddox *et al.* (1990) & Nichol *et al.* (1992). Thus it is possible to make direct comparisons between the clustering properties of X-ray and optical clusters. Previous redshift surveys in this region also provide a valuable resource of published cluster redshift measurements.

2.3.2 Selection of SGP RASS Cluster Candidates

The SASS I processing, § 2.1.1, has identified 4928 sources within the boundaries of the SGP region. A large fraction of these sources are actually multiple SASS "detections" of a single X-ray object, due to the fact that adjacent SASS 2° strips overlap. These multiple entries have been removed using the prescription determined by Ebeling (1994). Ebeling

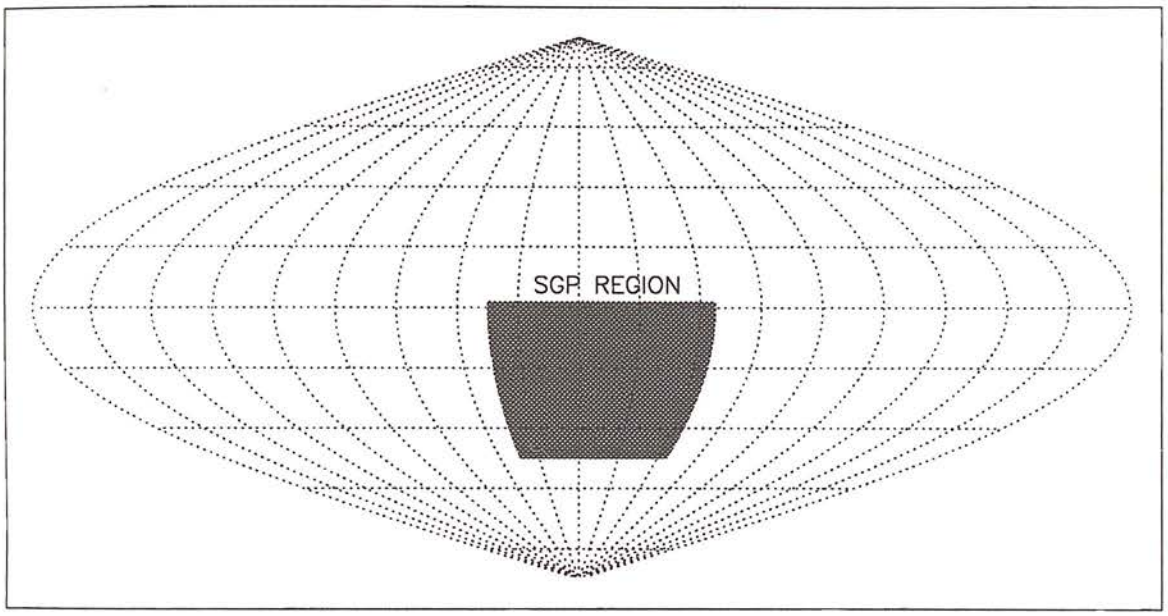

Figure 2.6: The SGP region ($22^{hr} \lesssim \alpha \lesssim 3^{\rm hr}\,20^{m}$, $-50° \lesssim \delta \lesssim 2°$) is highlighted in grey on an all sky, equal area, map.

Schmidt Plate numbers		
193-200	237-249	288-301
344-358	404-518	466-482
532-548	601-618	672-690
744-762	816-834	888-894
SASS I survey strip numbers		
1-22		68-90

Table 2.1: The SERC UK-IIIJ Schmidt plates and SASS I survey strips that overlap the SGP region.

has shown that when two SASS sources lie on different 2° strips, but are separated by $\Delta_{sep} \leq 3'$, then they are likely to represent a multiple SASS detection of a single X-ray source on the sky. There are 809 pairs of sources like this in the SGP region. In each case, the source detection with worst photon statistics was removed from the source list, thus leaving a total of 4199 sources. Only 10-15% of these 4199 sources will be X-ray clusters, § 2.1.3. The methods by which high likelihood cluster candidates were drawn from the raw source list are described below. Briefly, sources that met the last and at least one other of the following criteria were included in the candidate list;

1. A measured SASS extent.
2. A CSEARCH contamination value $< 15\%$.
3. A $> 85\%$ probability of being associated with a ROE/NRL optical cluster.
4. A hardness ratio greater than $HR + \delta(HR) = 0$

By these methods, and with no flux limit applied, the raw source list was cut down to 486 cluster candidates. (The construction of flux-limited candidate lists is described in § 2.4.2.)

1) Extended Clusters

As shown by Ebeling *et al.* (1992, § 2.1.3), Abell clusters detected in the RASS tend to show extended emission whereas the general population of RASS sources do not. Assuming that the X-ray properties of Abell clusters are representative of those for all X-ray clusters, we decided to include all 293 SGP RASS sources that showed evidence for extended emission, *i.e.* SASS extent$> 0''$, in the cluster candidate list. Identifying RASS clusters by extent criteria results in a truly "X-ray selected" candidate list. Clusters constitute the only variety of X-ray source that will be extended beyond the PSPC PSF

at recession velocities greater than $\approx 2000\,\mathrm{km\,s^{-1}}$. Therefore, an extent selected sample should be essentially free from contamination from other sources. (At redshifts less than this, X-ray emission from galaxies may be spatially resolved.)

We can make a rough estimate of the percentage of SGP RASS clusters that will be picked out by this method using the results in Cruddace *et al.* (1991) & Ebeling *et al.* (1992), § 2.1.3. Cruddace *et al.* (1991) find that only $20-40\%$ of the clusters in their simulation would be flagged as extended by the SASS detection algorithms. Ebeling *et al.* (1992) estimate that 53% of RASS sources associated with Abell clusters are not extended beyond 30″, figure 2.5. These results should be treated with some caution because; a) the Abell catalogue does not include all X-ray clusters, § 4.4.3, b) not all Abell clusters are actually physical, § 1.3.2 and c) the Cruddace *et al.* (1991) simulations did not include X-ray cluster evolution. However, despite their short comings, these results from Ebeling *et al.* (1992) & Cruddace *et al.* (199 f) do suggest that a complete set of cluster candidates cannot be derived using extent criteria alone. We cautiously conclude that one can expect to pick out between between 40% and 60% of all the clusters detected in the RASS using extent criteria alone. We hope to be able to identify the remaining clusters using two alternative methods, CSEARCH and a separation analysis with the ROE/NRL cluster catalogue, which are described below.

2) The CSEARCH algorithm

The CSEARCH [6] algorithm was designed to detect galaxy enhancements in the CUOC around ROSAT source positions. It is a simple routine that identifies RASS source positions that are embedded in regions of high projected galaxy density. To account for local fluctuations and for plate-to-plate variation, the background galaxy density is determined for each individual Schmidt plate. To this end, galaxy counts are made at 1000 random positions on each plate in five circular detect cells with radii of 1.0, 3.0, 5.0, 7.5 & 10 arc minutes. The distribution of galaxy counts in each cell can then be used to determine the probability of finding more than N_{gal} galaxies in that cell on that plate.

Galaxy counts were then made in the same 5 detect cells, this time centered on the positions of each of the 4199 RASS sources in the SGP region. (If a source position lay in an overlap region between two Schmidt plates, these counts were performed on each of the plates.) For each of the values of N_{gal} measured around SGP RASS positions, there is an associated probability that the galaxy count is due to a statistical fluctuation in the background density. If this probability was less than 15% in any of the cells surrounding a certain RASS source position, then that source was flagged as an X-ray cluster candidate.

[6] Cluster SEARCH

In total, 445 RASS sources in the SGP region were flagged as cluster candidates using this criteria. The 15% threshold was chosen empirically as a compromise between the number of bona fide clusters and the number of contaminating objects in the candidate list. This probability threshold can be interpreted as meaning that a CSEARCH selected cluster candidate list will suffer from 15% contamination by non-cluster X-ray sources. It has been shown statistically that when one sets a contamination threshold of 15%, the CSEARCH candidate list is only $\approx 45\%$ complete (Cruddace, private communications.) This completeness refers to the fraction of RASS sources statistically associated with galaxy enhancements that are included in the CSEARCH cluster candidate list.

One variety of RASS sources that might be associated with low significance projected galaxy enhancements, and hence not included among the 445 CSEARCH selected candidates, are distant clusters. The bulk of the galaxies in distant ($z \gtrsim 0.3$) clusters will have magnitudes that are fainter than the plate limit, meaning that the projected CUOC galaxy density will be only slightly heightened over the background. Therefore, we can expect that the completeness of the CSEARCH selected cluster candidate list will be a decreasing function of redshift.

The assumptions that have gone into the development of CSEARCH are as follows;

1. That X-ray clusters contain galaxies.

2. That the centres of the cluster X-ray emission and galaxy distribution coincide.

3. That the projected galaxy core radii of the clusters varies between $1'$ and $10'$.

4. That errors in the CUOC can be neglected.

A wealth of literature exists to support the first assumption, *e.g.* Henry *et al.* (1992), Kowalski *et al.* (1984), Briel & Henry (1993). Regarding the second point, this is a valid assumption only if the cluster is relaxed, *i.e.* when the gas is in thermal equilibrium and the galaxies have virialised. For example Ulmer *et al.* (1992) have found several cases of clusters undergoing merging events, where the X-ray and optical centres are discrepant ($\Delta_{sep} \lesssim 10'$). The third CSEARCH assumption is a valid approximation. However, in the case of very nearby clusters ($z \lesssim 0.03$), the CUOC galaxy distributions may be too diffuse to be picked out by CSEARCH . Referring to the point 4), the cores of clusters are characterised in the CUOC by crowded fields of galaxies. Inadequate object deblending in these fields will result in artificially low CSEARCH N_{gal} values. Among the 133 SGP RASS candidates that were observed during the spectroscopic followup a few ($\lesssim 10$) occurrences of inadequate galaxy-galaxy deblending in the CUOC were uncovered. However, we do not believe that errors in the CUOC have an adverse effect on the

CSEARCH derived candidate list. In summary, we expect CSEARCH will preferentially pick out relaxed clusters.

The major advantage of CSEARCH is that it operates at the position of every RASS source. Thus a list of CSEARCH selected cluster candidates can be described as "X-ray selected".

3) Separation analysis with the ROE/NRL cluster catalogue

An angular separation analysis of the type performed by Ebeling *et al.* (1992), see § 2.1.3 and figure 2.4, was performed between the positions of the 4199 RASS sources in the SGP region and the positions of the optical clusters in the ROE/NRL catalogue. In this analysis, a RASS source was flagged as an X-ray cluster candidate if its angular separation from one of these optical clusters was $\Delta_{sep} \lesssim 7'$. In total, 200 SGP RASS sources met this criteria. This threshold value was adopted so that the overall contamination from background coincidences was less than 15%. After setting this threshold $\approx$ 70% of the RASS sources that are statistically associated with ROE/NRL clusters will be included in the candidate list (Ebeling, private communication). The separation analysis has the following advantages over CSEARCH ;

- The SGP RASS cluster candidates selected using the separation analysis are a provided with a complete optical cluster description from the ROE/NRL catalogue.
- The effects of cluster substructure are reduced, because the assumption of exact coincidence between the galaxy and X-ray centres is relaxed.
- The effects of errors in the CUOC are reduced
- Low redshift clusters have an enhanced probability of inclusion in a candidate list.

The major disadvantage of the separation analysis is that the resulting cluster candidate list is not X-ray selected. It is, instead, an optically selected, X-ray confirmed, cluster candidate list. The ROE/NRL cluster catalogue is corrupted by many of the selection effects that afflict the Abell catalogues and which have been shown to bias measurements of the cluster large-scale structure, § 1.3.2. One might worry that a SGP RASS cluster candidate list selected using the ROE/NRL catalogue might contain relics of these selection effects. However, as has been shown by Nichol *et al.* (1994a, § 1.3.1), it is possible to remove the effects of selection biases in an optical cluster sample using RASS data.

4) Hardness Ratio Threshold

There is considerable overlap between the candidate lists derived from the three methods described above. In total 512 of the 4199 SGP RASS sources were flagged as cluster candidates. In the interests of reducing contamination in the candidate list, we excluded any sources with a negative hardness ratio 1σ upper limit, *i.e.* $HR + \delta HR \leq 0$. Twenty-six of the 512 candidates, *i.e.* 5% of the total, were excluded on the basis of this criteria. The justification for the imposition of a hardness ratio threshold was that clusters, with intracluster gas temperatures of $T \approx 10^7$K, are among the hardest known X-ray sources. Ebeling *et al.* (1992, § 2.1.3) showed that there is a clear differentiation between hardness ratios of Abell clusters detected in the RASS and those of the general RASS population. Therefore, by imposing a hardness ratio cut, it was possible to filter out some of the contaminating sources in our candidate list, without excluding any bona-fide clusters. We have checked that the HR cut does not exclude clusters by observing several of the $HR + \delta HR < 0$ candidates, finding $\simeq 30\%$ to be stars and $\simeq 70\%$ to be active galaxies.

The selection methods of the remaining 486 SGP RASS cluster candidates breaks down as follows; 281 (40) were identified by the extent method, 426 (122) by the CSEARCH method and 195 (10) by the separation analysis method. The numbers in brackets indicate the candidates that were flagged only by that particular method.

2.3.3 VTP Analysis

In section § 2.1.1 we described the SASS analysis process that has been used to identify and parameterize sources detected in the RASS . The SASS processing was designed to be used for a diversity of astronomical studies, *e.g.* of clusters, stars & AGN, and was not optimised for the detection of any particular type of X-ray source. In the case of clusters, the SASS assumption of spherically symmetric, Gaussian source profiles is a major disadvantage. (Cluster X-ray emission is more accurately modelled by a King profile, equation 2.4.) Certain groups working with RASS cluster data have chosen to ignore the SASS results and make their own analysis from the raw photon data. For example, Briel & Henry (1993) determined RASS count rates for a sample of 145 Abell clusters (see § 1.3.1), by fitting source profiles and choosing background annulii by eye. An alternative, automated, approach, the Voronoi Tessellation and Percolation (VTP) method, has been developed by Ebeling & Wiedenmann (1993). The authors claim that VTP is more suited to the detection of extended sources in the RASS and that it provides more accurate estimates of source count rates than does SASS. Unlike the SASS analysis, VTP does not make a priori judgements about source geometry. In addition, it does not sort the raw data into artificial bins, but rather works on the raw data globally, thus

being limited only by the resolution of the XRT+PSPC.

The basic method of VTP, see Ebeling & Wiedenmann (1993) for more details, is as follows;

1. A Voronoi tessellation is computed for the original raw photon data. This involves forming cells around each individual photon, so that there are neither gaps nor overlaps between adjacent cells.

2. The cumulative distribution of the cell area is compared to what would be expected for a random Poisson distribution and the background photon density is determined.

3. A spatial percolation, "friends-of-friends", algorithm is run on the individual cells, grouping photons exceeding the background density into sources. The algorithm searches for close groups of objects in the two-dimensional photon distribution.

Despite the fact that VTP was not available at MPE when the SGP RASS Cluster Project began, it was deemed prudent to incorporate VTP during the latter stages of the project. Unfortunately, it has not been possible to re-analyse the whole SGP region using VTP and make new source detections, due to the large investment of computing time required. Instead, the VTP analysis was performed[7] in $1.5^\circ \times 1.5^\circ$ regions around the positions of the 486 RASS sources flagged as potential cluster candidates by the methods described in § 2.3.2. To date, 337 of the 486 SGP RASS cluster candidates have available VTP count rate information.

Figure 2.7 shows a comparison of the count rates determined by the two algorithms for these 337 sources. It can be seen from this figure that there is not a simple relation between the VTP and SASS count rates and that the count rates can be in disagreement by up to a factor of 5. The overall trend is that the VTP count rate is larger than the SASS count rate. However, the suitability of the VTP analysis for RASS cluster detection and parameterization is still a matter of debate. Therefore, throughout this thesis we have used both methods to define cluster candidate count rates and fluxes.

2.4 Creating Flux-Limited Candidate Lists

The underlying aim of the SGP RASS Cluster Project was to provide constraints on theories of large-scale structure formation through measurements of the spatial correlation function of X-ray clusters, § 1.4. To this end, it is not possible to simply derive the spatial correlation function from a cluster sample containing *every* cluster detected in

[7] All VTP analysis was performed at MPE by Harald Ebeling.

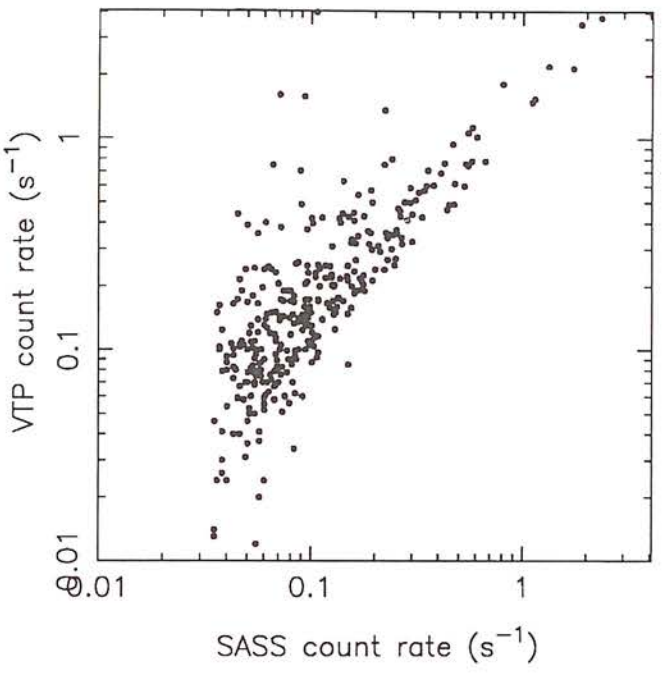

Figure 2.7: Comparison of the VTP and SASS determined count rates for the 337 SGP RASS candidates with available VTP information.

the RASS . Instead we have to define the cluster sample in such a way that its properties are easy to model. Theoretical models that predict the large-scale structure of clusters in various cosmological scenarios generally work with volume complete samples of simulated clusters. However, it has been shown by Mann *et al.* (1994, § 5.4), that it is possible to translate the theoretical predictions of the clustering properties of clusters from volume complete samples to X-ray flux-limited samples with comparative ease. From an observational point of view, it is much simpler to construct flux-limited cluster samples as opposed to volume limited samples. Therefore, for the SGP RASS Cluster Project we have decided to concentrate on the former and we describe below, how flux-limited samples were constructed from the list of 486 SGP RASS cluster candidates.

2.4.1 Calculating Source Fluxes

To be able to deduce accurate RASS source fluxes from PSPC count rates, one needs to take into account several factors that include; a) the spectrum of the source, b) the variation of telescope effective area with energy, c) the hydrogen column density along the line-of-sight and d) inaccuracies in the count rate determination. The count rate to flux conversion is, therefore, a non-trivial problem. It has been addressed thoroughly in the *UK ROSAT Announcement of Opportunity: AO2* (1991, hereafter "AO2 manual"). In §10.2 of the AO2 manual, conversion factors are presented for a wide range of X-ray spectra and line-of-sight hydrogen column densities. These conversion factors relate PSPC count rates to source flux and we have decided to use them to derive fluxes for the 486 SGP RASS cluster candidates. To do so we have to make the following assumptions; 1) That all of the 486 candidates are clusters and, therefore, have the same underlying X-ray spectrum. By assuming that all the candidates are clusters we will derive inaccurate fluxes for the contaminating sources. (The count rate-to-flux conversion factors differ between diffuse thermal, *e.g.* clusters, and power-law, *e.g.* AGN, X-ray sources.) However, as we are only trying to construct a flux-limited list of *clusters*, the true fluxes of the contaminating objects are irrelevant as these objects will be removed from the candidate list during the spectroscopic followup.

2) That the gas temperature in the clusters lies in the range 1×10^7 °K to 2×10^8 °K. The limited exposure time of the RASS means that there are insufficient source counts available with which to fit source spectra. Consequently, we are unable to measure gas temperatures for the individual cluster candidates. David *et al.* (1993) have collated temperature information from more than 100 clusters and find the range in intracluster gas temperatures to be 1–14 keV. We have, therefore, assumed that the gas temperatures of the clusters in our candidate list fall somewhere in this range.

3) The hydrogen column density in the SGP region varies between $\approx 1 \times 10^{20}\,\mathrm{cm}^{-2}$ and $1 \times 10^{21}\,\mathrm{cm}^{-2}$, see § 2.4.3.

Figure 10.3 in the AO2 manual is reproduced in figure 2.8. It shows the ROSAT PSPC energy conversion factor (ECF) for thermal line spectra[8] with temperature T for various values of the absorption column density, N_H. The hashed area demonstrates the range in N_H and T values that are expected for our SGP RASS cluster candidate list. It can be seen that ECF is independent of the gas temperature for $log_{10}(T) > 7.3$. Less than 4% of the clusters in the David *et al.* (1993) sample were cooler than this value. Therefore, the majority of the clusters in our candidate list will have ECF values in the range 0.42 to 0.74, where the exact value is dependent on the line-of-sight N_H value.

These ECF values have been calculated under the assumption that the count rate derived by the detection algorithm is an accurate description of the PSPC count rate. We have seen, § 2.3.3, that it is not clear that the SASS or VTP count rate determinations used to describe SGP RASS candidates *are* accurate. In light of the large uncertainty in the source count rates, we decided that a valid simplification was to use a single ECF irrespective of the line-of-sight N_H. (For the purposes of the SGP RASS Cluster Project, relative fluxes are more important than absolute values.) Using the average N_H column density in the region, $2 \times 10^{20}\,\mathrm{cm}^{-2}$ (§2.4.3), we assumed that the characteristic conversion factor for clusters in the SGP region is ECF=0.6.

2.4.2 Flux-Limited Candidate Lists

From § 2.4.1, flux-limited samples could be constructed by simply imposing a count rate threshold on the list of 486 SGP RASS cluster candidates. The flux limit of the sample is then, in units of $10^{-11}\,\mathrm{erg\,s^{-1}\,cm^{-2}}$, the minimum count rate divided by 0.6. As a result of the problems that have emerged concerning the SASS and VTP count rate determinations, and the active debate as to which method is more accurate, it was decided to present, in this thesis, the cluster candidates that resulted by taking both a SASS and a VTP count rate limit. The count rate limits chosen in each case were;

1. SASS determined count rate greater than $0.07\,\mathrm{s}^{-1}$
2. VTP determined count rate greater than $0.1\,\mathrm{s}^{-1}$

It was not originally intended that the SASS and VTP count rates limits should differ. When constructing lists of candidates to observe during the spectroscopic follow-

[8]The spectra were generated using Raymond-Smith (1977) codes for thermal bremsstrahlung with atomic line emission and the metallicity is set to an average value of 0.3 times the solar abundance.

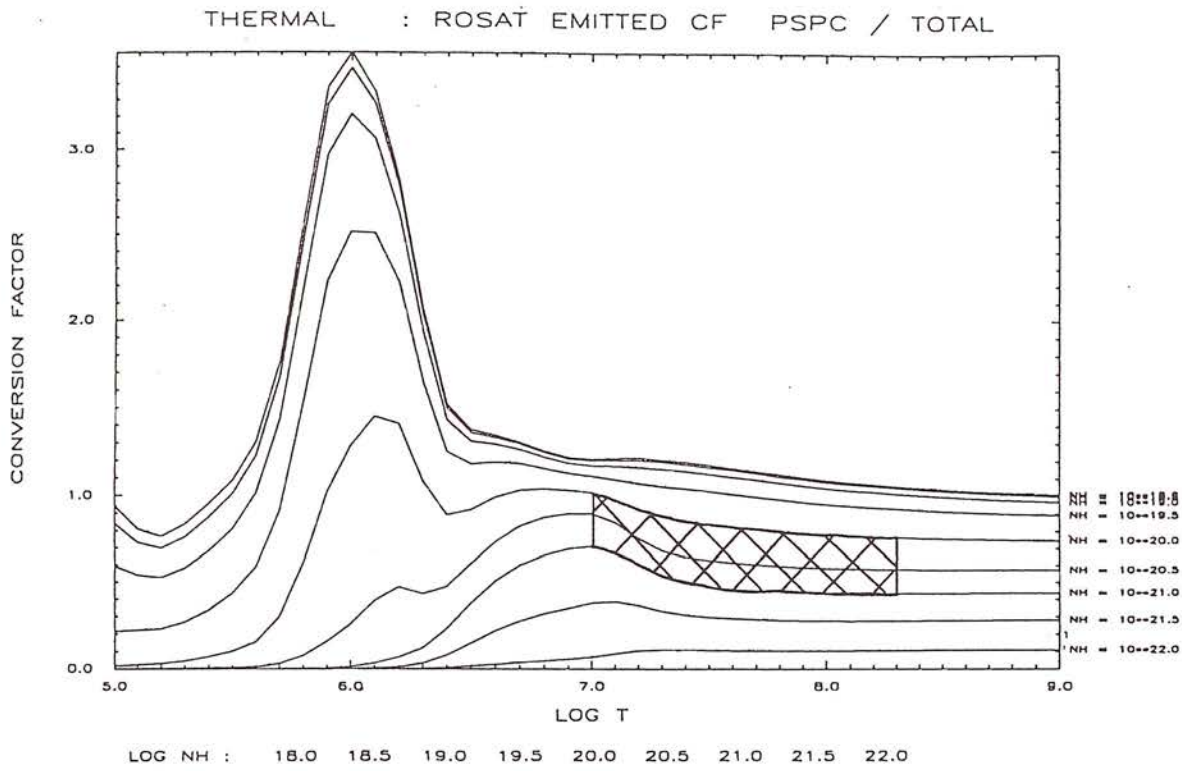

Figure 2.8: Reproduction of figure 10.3 in UK ROSAT AO2 manual: The ROSAT PSPC energy conversion factors that translate flux to PSPC count rate are presented for thermal line spectra with temperature T for various values of the absorption column density N_H in units of 10^{11} counts cm^2 erg^{-1}. The hashed area illustrates the expected range of T and N_H for clusters in the SGP region.

up (chapter 3), the following limits were set;

- For the 1991 and 1992 observing runs, a SASS count rate limit of $\geq 0.1\,s^{-1}$.
- For the 1993 observing runs, a VTP count rate limit of $\geq 0.1\,s^{-1}$.

During these observing runs, we assumed that the flux limit of our candidates lists was $\approx 1.7 \times 10^{-12}\,erg\,s^{-1}\,cm^{-2}$, *i.e.* $0.1/0.6 \times 10^{-11}\,erg\,s^{-1}\,cm^{-2}$. However, it has since transpired that the SASS fluxes available before 1993 contained a systematic error, due to incorrect vignetting correction. Figure 2.9 shows the SASS count rates before and after this vignetting correction for the 486 SGP RASS cluster candidates. It can be seen that the majority of the source count rates were over-estimated. The net effect is that several sources with true count rates between $0.07\,s^{-1}$ and $0.1\,s^{-1}$ were observed during the 1991 and 1992 campaigns. We have decided to apply an a posteriori SASS count rate on the candidate lists, so that as many clusters as possible could be included in the determination of the spatial correlation function. The flux limit for the SASS flux-limited candidate lists is, therefore, lower than that for the VTP flux-limited candidate lists, *i.e.* $\approx 1.2 \times 10^{-12}\,erg\,s^{-1}\,cm^{-2}$.

It should be noted that, before the problem with the SASS count rates was recognised, we honestly believed that $\approx 80\%$ of the SASS selected cluster candidates had redshift measurements, see § 6.4.1. This completeness value was quoted in a paper, Romer *et al.* 1994, describing the SGP RASS cluster correlation function, which was submitted for publication *before* the vignetting problem came to light. A more realistic value for the redshift completeness is $\lesssim 60\%$, § 4.6.

In total, 345 of the SGP RASS cluster candidates have SASS count rates $\geq 0.07\,s^{-1}$ and/or VTP count rates $\geq 0.1\,s^{-1}$. For each candidate the MASOL number, defined in § 2.1.1, and J2000 coordinates are listed in columns $1 \rightarrow 3$ of table A.2. The criteria by which each candidate was selected from the RASS are given in columns $4 \rightarrow 6$. A • in column 4 indicates that the candidate had a CSEARCH contamination value $< 15\%$ (299 cases). Likewise, a • in column 5 indicates that the candidate had a $> 85\%$ chance of being associated with a ROE/NRL optical cluster (147 cases). Finally, a • in column 6 indicates that the candidate featured a SASS determined extent $> 0''$ (219 cases). In columns 7&8, the type of analysis by which the candidate was included in a flux-limited sample, SASS (column 7) or VTP (column 8), are indicated by a •. If a certain candidate has a SASS count rate $> 0.07\,s^{-1}$ and no VTP count rate is available, then a ○ is placed in column 8. For example, MASOL source 0044144 was selected as a potential cluster candidate by both CSEARCH and the ROE/NRL separation analysis. VTP information is not available for this source but it has a SASS count rate in excess of $0.07\,s^{-1}$. The

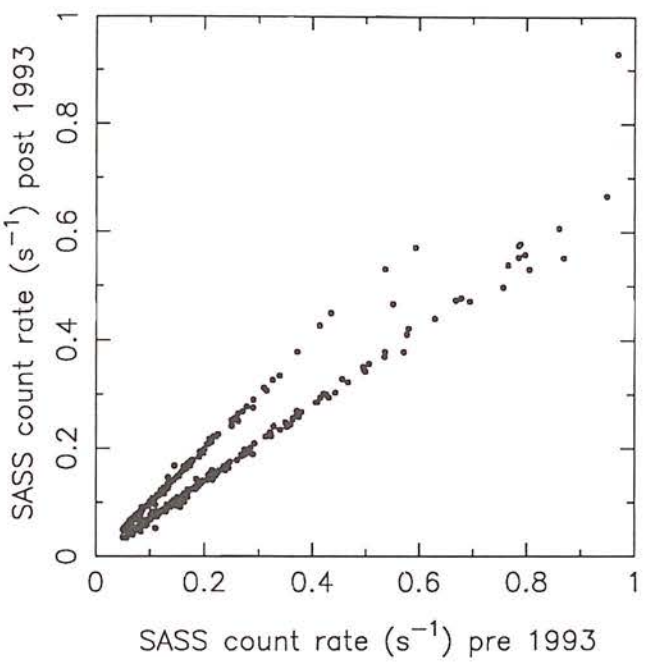

Figure 2.9: A comparison of the SASS count rates available prior to and after an extra vignetting correction was made in 1993. The count rates are plotted for all 486 SGP RASS cluster candidates.

other columns of table A.2 ($9 \rightarrow 16$) are described in chapter 4 and in the table caption.

Incompleteness in a VTP Flux-Limited Candidate List

In § 4.6, we describe various flux-limited SGP RASS cluster samples and provide an estimate the incompleteness in each sample. For VTP flux-limited samples, this estimate must take into account the that fact only 70% of the SGP RASS cluster candidates have available VTP count rates. We have attempted to predict how this fact effects the completeness of VTP flux-limited samples for 2 different VTP count rate limits, via the following stages;

1) A binned distribution, $\Delta_{ctr} = 0.05\,s^{-1}$, of the SASS count rates for the 337 candidates with available VTP count rates was constructed (distribution 1).

2) The same distribution was constructed for the other 142 candidates for which VTP information was not available (distribution 2).

3) From distribution 1; the fraction of candidates in each bin with VTP count rates greater than a) $0.1\,s^{-1}$ and b) $0.2\,s^{-1}$ were calculated.

4) From distribution 2; the number of candidates per bin that would be expected to have a VTP count rate greater than a) $0.1\,s^{-1}$ and b) $0.2\,s^{-1}$ (had they been available) were calculated by multiplying the total number of candidates per bin by the respective fractions determined from distribution 1.

The results are shown in figure 2.10. We conclude that a VTP flux-limited candidate list would have included 83 or 51 more candidates, for $0.1\,s^{-1}$ & $0.2\,s^{-1}$ count rate limits respectively, if all 486 SGP RASS cluster candidates had available VTP fluxes.

2.4.3 The Effects of Galactic Extinction

Extinction hampers the construction of a flux-limited sample of RASS clusters in two ways; (a) it reduces the X-ray flux reaching the ROSAT instruments and (b) it reduces the projected galaxy density in the CUOC. We have attempted to quantify the effect of extinction on our flux-limited candidate sample by examining the distribution of line-of-sight N_H among the candidates.

A measure of the neutral hydrogen column density, N_H, along a particular line of sight can be used to predict the extinction in that direction. (See Morrison & McCammon (1983) & Lu *et al.* (1992) for descriptions of the processes governing the absorption and/or scattering of X-ray and optical photons respectively.) The most comprehensive survey of N_H values, to date, has been performed by Stark *et al.* (1992). This survey has a resolution of 2° and covers the whole sky above a declination limit of $\delta = -40°$. A representation of this data, for the portion of the SGP region that lies above $\delta > -40°$,

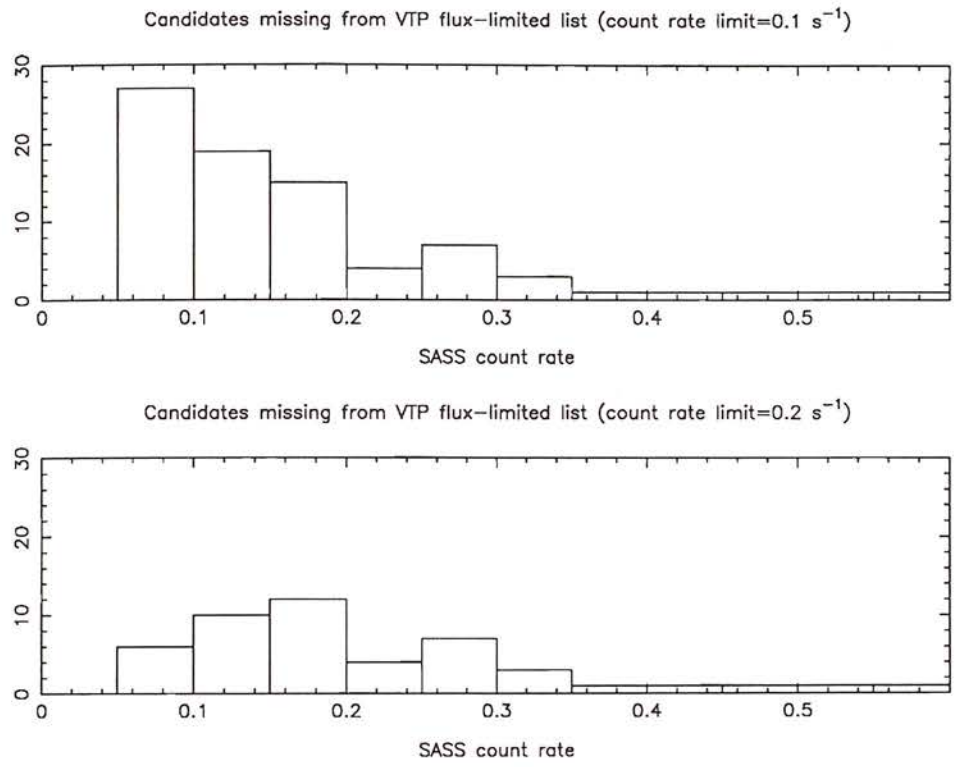

Figure 2.10: Histograms showing, as a function of SASS count rate, the expected number of candidates that are missing from VTP flux-limited lists by virtue of the fact that only 337 of the 486 SGP RASS cluster candidates have available VTP fluxes. The total number of candidates that are projected to be missing from such lists are 83 and 51 for VTP count rate limits of $0.1\,s^{-1}$ (top) and $0.2\,s^{-1}$ (bottom) respectively.

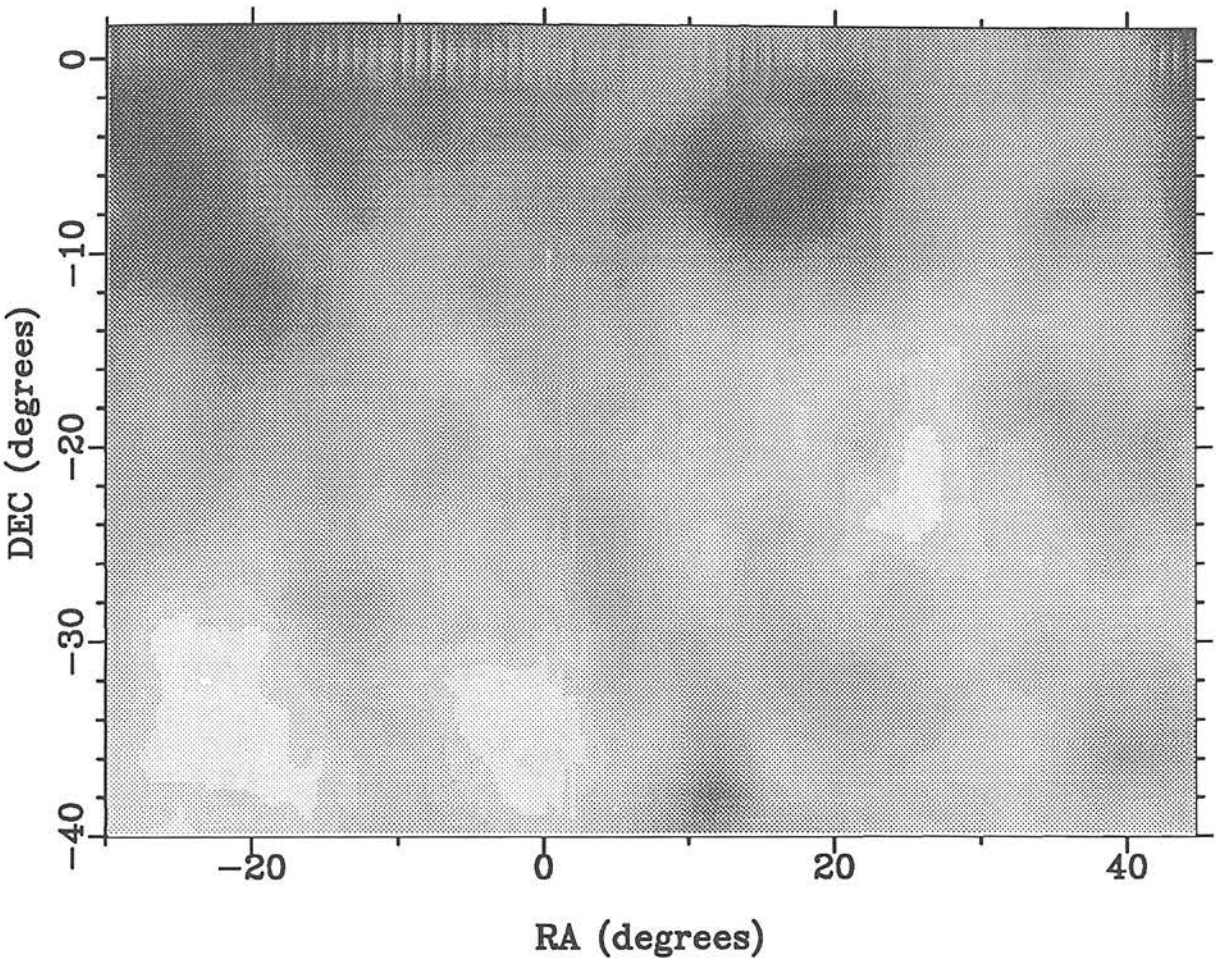

Figure 2.11: A grey-scale map of binned HI column densities (not in equal area projection) over the SGP region ($\delta > -40°$). The mean value of the HI data is $N_H = 1.96 \times 10^{20}\,\mathrm{cm}^{-2}$. The map has been scaled so that black is the maximum observed HI column density in the region ($N_H = 7.0 \times 10^{20}\,\mathrm{cm}^{-2}$) and white is the minimum ($N_H = 9.96 \times 10^{19}\,\mathrm{cm}^{-2}$).

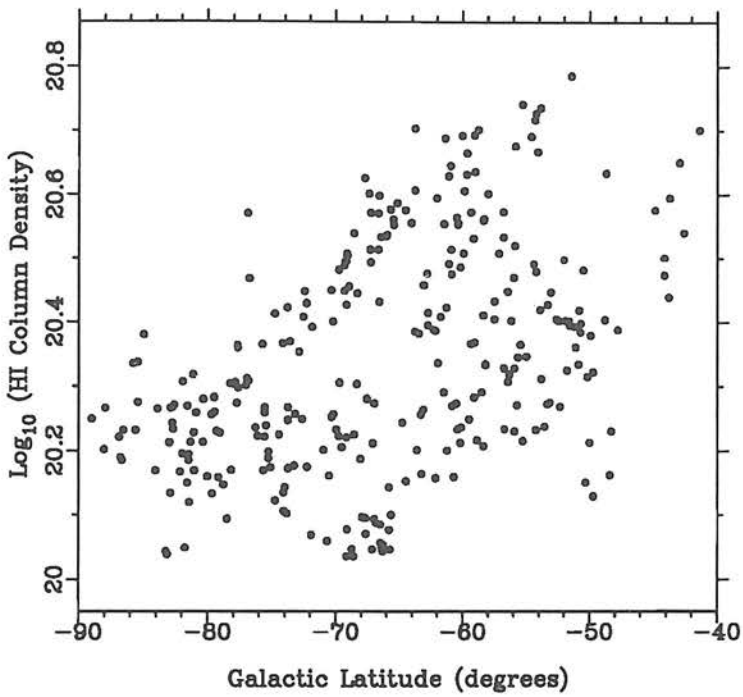

Figure 2.12: The distribution of HI column densities for the 298 $\delta > -40°$ cluster candidates in table A.2 versus their respective galactic latitudes.

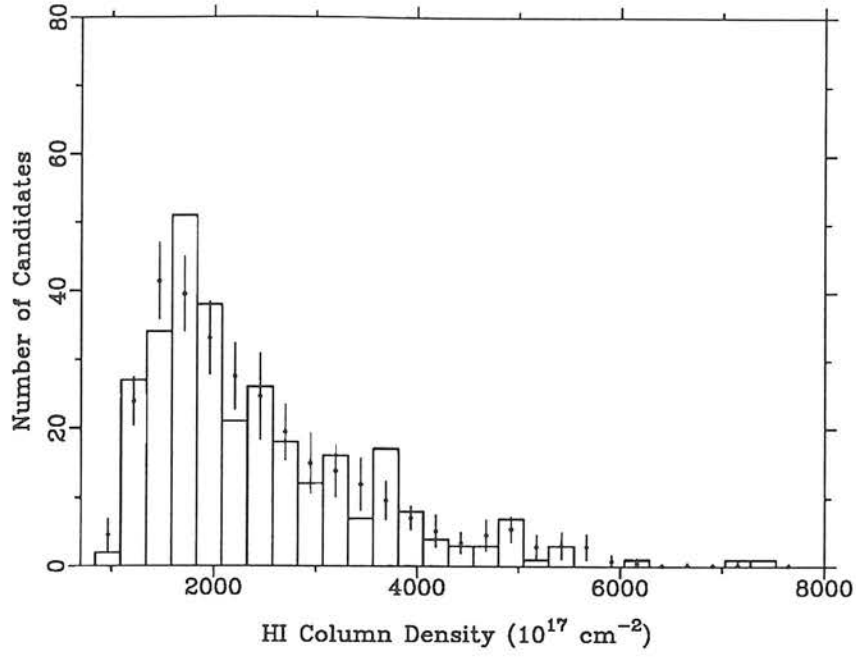

Figure 2.13: The distribution of HI column densities towards the 298 candidates in table A.2 with $\delta > -40°$. Also shown (•) is the averaged distribution from 10 samples of 298 random positions that were selected over the exact same area. (The error bars indicate the standard deviation between the 10 random samples.) The median value of the data and random distributions are $N_H = 2.95 \times 10^{20}\,\mathrm{cm}^{-2}$ and $N_H = 3.24 \times 10^{20}\,\mathrm{cm}^{-2}$ respectively.

is shown in figure 2.11. It is obvious from this figure that the N_H column density, and hence the absorption is not a smooth function of position. The N_H values in this map vary between $9.96 \times 10^{19}\,\mathrm{cm}^{-2}$ and $7.0 \times 10^{20}\,\mathrm{cm}^{-2}$, with a mean value of $1.96 \times 10^{20}\,\mathrm{cm}^{-2}$.

Figure 2.12 shows, as a function of galactic latitude, the Stark *et al.* N_H values at the position of each of the 298 $\delta \geq -40°$ cluster candidates in table A.2. These values are compared in figure 2.13 with a random distribution of N_H values, derived by averaging over 10 samples of 298 randomly chosen positions in the SGP region. The two distributions appear to be very similar, suggesting that the cluster candidates are not avoiding areas of high Galactic absorption. We conclude that the effects of Galactic extinction do not constitute a serious systematic error in our attempt to measure the large-scale clustering of X-ray clusters. We have, therefore, made the simplifying assumption, when computing correlation functions from SGP RASS cluster samples in chapter 5, of a uniform angular coverage.

2.5 Summary

A flux-limited list of 345 SGP RASS cluster candidates has been constructed using a combination of three different selection techniques. The techniques consist of; a) CSEARCH which is an automated search for galaxy enhancements around every SGP RASS source, b) a separation analysis with the ROE/NRL optical cluster catalogue and c) the selection of all extended SGP RASS sources. In addition, only those RASS sources with 1σ upper limits in their hardness ratio of $HR + \delta HR > 0$ were selected. With no flux limit applied, 486 "hard" cluster candidates were selected from the SGP region of the RASS .

The X-ray fluxes for each of the 486 candidates were calculated from the source count rates using the energy conversion factors (ECF) presented in the AO2 manual. Two methods, SASS and VTP, of source count rate determination have been described and compared. In the case of the VTP analysis, only 337 of the candidates have available VTP count rates. There remains uncertainty as to which method is the more appropriate for cluster description. We have, therefore, included in our flux-limited candidate list, those 345 candidates that fit either of the following criteria; 1) a SASS count rate greater than $0.07\,s^{-1}$ or 2) a VTP count rate greater than $0.1\,s^{-1}$. We have investigated the effects of patchy Galactic extinction among the candidates in the flux-limited sample, and conclude that the effects are not significant. The flux-limited candidate list is expected to include $45 - 70\%$ of all $\gtrsim 1 \times 10^{-12}\,erg\,s^{-1}\,cm^{-2}$ SGP RASS clusters, based on the statistical completeness of CSEARCH and the separation analysis methods. The contamination by non cluster sources in the candidate list is expected to be $\approx 15\%$.

In chapter 3 we describe the spectroscopic follow-up of these candidates and in chapter 4 we present samples of SGP RASS clusters with redshifts that were derived from the candidate list. In chapter 6 we discuss possible improvements to the selection methods described in this chapter.

Chapter 3

Spectroscopic Follow-Up of SGP RASS Cluster Candidates

In the previous chapter we introduced a flux-limited list of 345 SGP RASS cluster candidates. In this chapter we describe an intensive spectroscopic follow-up campaign that was carried out to confirm the identification of these candidates (as clusters or contaminating objects) and to find redshifts for the bona fide RASS clusters in the SGP region. The redshifts derived from these observations are used in chapter 5 to describe the spatial distribution of X-ray clusters and will be used in future for other projects, including the derivation of the X-ray luminosity function.

Four allocations of telescope time were secured for the spectroscopic follow-up; 3 runs at the 3.9m Anglo-Australian Telescope (AAT) and 1 at the South African Astronomical Observatory (SAAO) 1.9m telescope. In the course of these runs we made successful observation of 133 of the 345 cluster candidates listed in table A.2. The total number of spectra, including multiple observations, poor quality spectra and template observations, that were obtained was 712. In this chapter we present the observing procedure used to obtain these spectra (§ 3.2 & § 3.3) and the techniques employed to a) reduce the spectra (§ 3.4), b) derive redshifts (§ 3.5) and c) determine spectral type (§ 3.6). Note that in this chapter we are concerned with 311 objects observed *around* 133 SGP RASS cluster candidate positions and not with the candidates themselves. The tasks of candidate identification and cluster redshift determination are described, instead, in chapter 4.

3.1 Aims and Strategy

With telescope time at a premium, an efficient strategy had to be devised with which to follow-up the 345 SGP RASS cluster candidates. The expectation, § 2.1.3, was that $\approx 15\%$ of these candidates would turn out not to be clusters. Therefore, the spectroscopic follow-up had to weed out the rogue entries as well as provide redshifts for the genuine

cluster candidates. Unfortunately, these two aims conflict. On the one hand, one would like to take spectra of all objects in or near the X-ray error circle[1] that did not appear to be elliptical galaxies, to see if any show characteristics of X-ray emitters, *e.g.* the deep hydrogen absorbtion seen in dwarf stars or the wide emission lines seen in quasars. On the other hand, one would like to get redshifts for a few of the early-type galaxies in a wider region, in order to measure the cluster redshift. (E and S0 galaxies make up the majority of cluster members.)

The problem with all cluster redshift surveys is that there is no way to know, a priori, which galaxies in any projected distribution lie in the cluster. Nichol *et al.* (1992) found that multi-object spectroscopy is the only sure way to distinguish between real clusters and projection artifacts in *optically* selected samples. However, for the SGP RASS Cluster Project we decided instead to opt for long-slit observations at the AAT.[2] The rationale behind this decision was that, because our sample is *X-ray* selected, we can pin point the centre of the cluster potential well very accurately, § 1.3.2. If a candidate is a cluster, almost all of the galaxies within a $2'$ (*i.e.* half the length of the long slit) radius of the X-ray position should be cluster galaxies. This prediction was based on the galaxy number-magnitude count relation for the EDSGC, Heydon-Dumbleton *et al.* (1989, § 1.3.1). In the EDSGC, to a limiting magnitude of $b_j = 20$, ~ 0.2 non-cluster galaxies would be expected within a $\pi(r = 2')^2$ area.

The single slit approach allowed us to get spectral information on a much larger portion of our sample than if we had used multi-slit or multi-fibre observations. The advantages of single slit over the AAT multifibre system, AUTOFIB, include;

- No aligning of AUTOFIB fibers or punching of slit masks required.
- Improved quantum efficiency.
- Easier data reduction, especially with regard to sky subtraction.
- For AUTOFIB, the minimum separation between objects is $30''$, which places severe restrictions on the follow-up of crowded fields.

Dalton (1992) devised a maximum likelihood technique to select which galaxies to observe during the APM cluster redshift survey. This technique used the galaxy luminosity function and a magnitude-redshift relationship to predict the probability that a

[1] Where the error circle defines the 1σ error in the SASS determined position of the RASS source. The typical diameter of the error circle is $1.3'$, however, see appendix C, the diameters can range from $\simeq 0.25'$ to $\simeq 2'$.

[2] At SAAO the RPCS detector does not allow either long slit or multi-object observation. Instead single objects are observed through a $6'' \times 6''$ hole in a dekker plate.

galaxy of a certain magnitude belonged to a cluster at a certain estimated redshift. We tried, in 1991, to adopt the same technique using the galaxy magnitude information in the ROE/NRL catalogue. However, this did not turn out to be practical for three reasons; a) the magnitude calibrations and, hence, estimated redshifts in the ROE/NRL catalogue are inferior to those in the APM cluster sample, b) we had to take spectra for all objects in the error circle, regardless of magnitude, to be sure that we had identified the true X-ray source and c) only 43% of the candidates in table A.2 are associated with ROE/NRL clusters. Therefore, after the 1991 run we adopted the following, simpler, observing strategy; the spectrum of the object closest to the X-ray position and that of two or three other objects in the vicinity were measured. If, after the spectra had been reduced, the identification of the candidate or its redshift were still ambiguous, the candidate was observed again during a subsequent run. This strategy was based on the following experience which was gained during the 1991 observing run;

- In the case of clusters, the X-ray emission was often centered on a bright cD-type galaxy and the cluster redshift could be determined easily by obtaining spectra for the central galaxy and a few other galaxies close by.

- In the case of AGN that were contaminating the candidate list, the AGN was usually centered on the X-ray position. It was easy to identify AGN from optical spectra on the basis of their intense line emission, § 3.6.

Unfortunately, it has not been possible to follow-up all of the 345 SGP RASS cluster candidates. We decided to make best use of the observing time available by studying the candidates in count rate order, brightest first. As mentioned in § 2.4.2, we initially used SASS determined count rates to define this order, but switched in 1993 to VTP determined count rates. Candidates associated with optical clusters with literature redshifts, § 4.1.2, were given lower priority when it came to spectroscopic follow-up. However, if the literature redshift was determined with only 1 or 2 galaxy redshifts, then that candidate was not excluded from the observations. (As shown in § 4.1.2, literature redshifts based on so few galaxy spectra have $\approx$ 20% chance of being in error.) In addition, 8 candidates were not observed because, on inspection of the UKST plates, they appeared to be high likelihood contaminating objects. Six of these were bright stars (*e.g.* 0743009, figure C.21) and two were low redshift spiral galaxies (*e.g.* 0174101, figure C.16). (Both stars and spiral galaxies are known X-ray emitters, their X-ray properties are described in § 4.2.)

Anglo-Australian Telescope	
Location	Siding Springs
Longitude	149°3′58″ E
Latitude	31°16′37″ S
Primary Diameter	3.89m
Observing Dates	
1991	29^{th} Oct $\rightarrow$ 1^{st} Nov
1992	22^{nd}Aug $\rightarrow$ 24^{th} Aug
	30^{th}Aug $\rightarrow$ 1^{st} Sep
1993	6^{th}Sep $\rightarrow$ 11^{th} Sep
Telescope Configuration	
Spectrograph	RGO
Grating (order)	6000 V (I)
" line density	600 mm^{-1}
" blaze wavelength	5000Å
" dispersion	66 Å mm^{-1}
Detector (date)(pixels)	IPCS (1991) (2040×248)
	Tek-RGO (1992/3) (1028×1024)

Table 3.1: Details of the telescope and dates of the AAT runs, plus a summary of the observing set-up used.

3.2 Observations at the AAT

In total we have had three runs at the AAT, the relevant details of which are summarized in tables 3.1 & 3.2. All runs utilized the RGO (Royal Greenwich Observatory) spectrograph and a 600 lines mm^{-1} grating (blaze wavelength = 5000Å) and a single, 4.2′ long, slit. The grating angle ($\sim$ 18°) was set so that the central wavelength on the detector was $\simeq$ 4800Å. The slit was orientated so as to cover as many objects as possible. The corresponding slit angles were determined using the object coordinates available in the CUOC, § 2.2, database. (With careful alignment, it was possible to observe up to 5 cluster galaxies simultaneously.) After the 1991 run, we switched from the IPCS detector to the Tek-RGO CCD detector. These two detectors and their relative merits are discussed below.

3.2.1 The IPCS

The IPCS detects individual photon events in a two-dimensional image by means of a high-gain four-stage image intensifier optically coupled to a continuously scanning television camera. It then records the central positions of the photons in a digital electronic memory. An important feature of the system is the event centre detection logic

Dates	Seeing (″)	Weather (dome closed)	
Anglo-Australian Telescope			
October 29^{th} 1991	2.2	very cloudy	(78%)
October 30^{th} 1991	2.5 → 4.5	patchy cloud	(0%)
October 31^{th} 1991	1.1 → 3.0	clear → fog & cloud	(0%)
November 1^{st} 1991	2.2	clear	(0%)
August 22^{nd} 1992	0.9	clear	(0%)
August 23^{rd} 1992	1.0 →∼ 5	patchy cloud	(10%)
August 24^{th} 1992	1.1 →∼ 3	clear → very cloudy	(33%)
August 30^{th} 1992	-	very cloudy	(100%)
August 31^{st} 1992	2	patchy cloud	(0%)
September 1^{st} 1992	-	cloud & rain	(100%)
September 6^{th} 1993	-	cloud & rain	(100%)
September 7^{th} 1993	1.2 → 2.5	increasing cloud cover	(3%)
September 8^{th} 1993	-	very cloudy	(100%)
September 9^{th} 1993	-	very cloudy	(100%)
September 10^{th} 1993	1.1	clear	(0%)
September 11^{th} 1993	1.0 → 2.0	clear	(0%)

Table 3.2: Dates of, and observing conditions during, the three AAT observing runs.

which identifies the centroid of each photon event despite the degradation imposed by the electron optics, thus providing increased spatial resolution. The useable photocathode is 40 mm in diameter, but severe spatial distortions and reduced resolution are encountered beyond 30 mm.

The IPCS offers a wide variety of formats and pixel sizes. Up to 2048 columns and 514 rows are available. We selected 2040 columns & 248 rows and, with the set up described in table 3.1, this provided spatial resolution of $\approx 3''$, allowing objects very close on the sky to be observed simultaneously. The spectral resolution of the set up was 2.3Å at 5000Å assuming a focus of 2.4 channels FWHM. The spectral coverage obtained with the 600V grating at 18° was 3500 → 6000Å . The IPCS has the following advantages over available CCD detectors; larger spectral coverage, the spectra can be seen building up in real time, no readout noise and no problems with cosmic ray confusion or saturation. Disadvantages include, a maximum quantum efficiency of 20% at 4000Å and distortion in the electron optics.

3.2.2 The Tek-RGO CCD

This is a blue coated chip consisting of 1028 columns and 1024 rows. It has a physical area of 24.7 × 24.5mm. For the instrumental set-ups chosen for the AAT 1992 and AAT 1993 runs, the relevant specifications are; spectral coverage of 4000Å to 5500Å and

spectral resolution of 3.6Å. The quantum efficiency of the chip ranges from 54% to 67% in that spectral range, thus far out performing the IPCS. The only disadvantage of the Tek-RGO over the IPCS is the reduced spectral coverage. This did not prove to be a problem except for our most distinct galaxies, where certain features such as the 4300Å G band were redshifted out of the observing window. The chip was read out on slow mode, taking 120 s per readout, which introduced 3.6 electrons per ADU readout noise.

3.2.3 Observing Procedures

IPCS 1991

For the IPCS observations, optimal integration times could be judged interactively by studying the real time build up on the screen. Comparison spectra (200 s exposures) of the copper-argon arc lamp were taken before and after each observation. Spectra of a) galaxies with accurately known redshifts from 21 cm measurements and b) radial standard stars, were taken at the beginning and end of each night. A dome light flat field exposure was taken at the end of the first night. This exposure was examined for structure and bad rows or columns, none were found and no further flat field exposures were taken during the run.

Tek-RGO 1992 & 1993

Flat fielding is more important for CCD data reduction than for the IPCS, because CCD chips often suffer from "bad pixels", *i.e.* pixels with abnormal sensitivity. Therefore, multiple flat field exposures of 10 s duration were taken at the beginning of every night. Five bias frames were also taken at the beginning of each night. (The bias frames monitor the DC level on the CCD chip.) Comparison spectra (1 s exposures) of the copper-argon lamp were taken before and after each observation. Integration times for CCD exposures for the 1992 run tended to be over estimated. Often two 900 s exposures were taken when one would have sufficed. The only advantage of these extra exposures is that it allows us to check the external errors in the galaxy redshift measurements, § 3.5.5. After the experience of the 1992 run, the 1993 observations were made more efficient, by tuning integrations times to the prevalent weather conditions and galaxy magnitude. Observations of spectral templates were made each night.

3.3 Observations at SAAO

The instrumental set-up and weather conditions during the 1992 run at at the 1.9m telescope at Sutherland, South Africa are summarized in tables 3.3 & 3.4.

South African Astronomical Observatory	
Location	Sutherland
Longitude	20°48′42″ E
Latitude	32°22′42″ S
Primary Diameter	1.88m
Observing Dates	
1992	20^{th} Sep $\rightarrow$ 26^{th}
Telescope Configuration	
Spectrograph	ITS
Grating (order)	G6 (I)
" line density	210 mm^{-1}
" blaze wavelength	4600Å
" dispersion	210 Å mm^{-1}
detector (pixels)	RPCS (1872×2)

Table 3.3: Details of the telescope and a summary of the observing set-up used during the SAAO run.

Dates	Seeing (″)	Weather (dome closed)	
SAAO 1.9m Telescope			
September 20^{th} 1992	-	very cloudy	(100%)
September 21^{th} 1992	$\sim 1 \rightarrow \sim 2$	patchy cirrus	(0%)
September 22^{th} 1992	$\sim 2 \rightarrow \sim 3$	clear (high winds)	(0%)
September 23^{th} 1992	-	very cloudy	(100%)
September 24^{th} 1992	-	very cloudy	(100%)
September 25^{th} 1992	$\sim 2 \rightarrow \sim 5$	clear $\rightarrow$ fog & cloud	(60%)
September 26^{th} 1992	$\sim 2 \rightarrow \sim 4$	clear (high humidity)	(0%)

Table 3.4: The prevailing weather conditions during the SAAO run.

3.3.1 The RPCS

The Reticon Photon Counting system (RPCS), Jorden *et al.* (1982), is the primary detector for the Image Tube Spectrograph (ITS). The RPCS is a high-resolution, linear detector which is sensitive in the range 3300Å to 7500Å. It is based on two three-stage intensifiers fibre-optically coupled to a dual array of 936 photocathodes. The two 18mm arrays (channel A & B) are formed from a row of 936 30μm $\times$ 375μm diodes, with no gap between the arrays. Resolution is improved by spatially centering to half a diode accuracy. This type of detector suffers from pattern noise, which is eliminated by operating in "microscanning" mode.

A number of precautions are required when observing, because of flexure in the RPCS detector head and the flop of the electronics in the image intensifier tube. Flexure produces a large jump in wavelength to pixel relation when the telescope is slewed in declination. There follows a further slow creep in this relation as the telescope settles. Up to 5 minutes are required for the system to settle completely before integrations can commence. The amount of shift depends on the angle between the detector head and the vertical and is not readily predicted. Shift in the wavelength relation due to the flop of the electronics occurs when the axis of the intensifier passes through the horizontal. A shift of a couple of pixels is typical. The system is stable to < 0.002 pixels per hour once settled.

3.3.2 Observing Procedure

The real time readout of the RPCS on a photocathode allows integration times to be varied according to the surface brightness of the object and the observing conditions. Integrations were stopped when either the emission or absorption features were clearly visible in the spectra. Care had to be taken however, as bad pixels could be mistaken for real features, for example pixel 500 of channel A, figure 3.1. A limitation of 20 minutes for any one exposure was imposed to avoid flop in the intensifier electronics as the telescope tracked.

The spectrograph was orientated east-west across each object. A dekker plate with two 6″ $\times$ 6″ holes separated by 375μm ($\sim$ 40″) was used to observe the object and a comparison sky patch. The dekker is used to centre the object and the sky on the two diode arrays. It would have been preferable to observe the object using both arrays, to increase signal to noise. However, it was found that the decreased sensitivity of channel B, figure 3.1, made it impractical to use it for all but the brightest galaxies.

Galaxies were observed using a 300 lines mm^{-1} grating, blaze peak=4600Å. The grating angle (18°) was chosen so that the wavelength at the centre of each channel

ARC	Interactive Manual arc line identification
BCLEAN	Automatic removal of bad lines & cosmic rays from CCD data
CDIST	S-distortion correction using **SDIST** results
COSBELL	A "cosine-bell" spectral filter
EXTRACT	Adds contiguous lines of an image to produce a spectrum
ICUR	An x,y graphics cursor
IXSMOOTH	Smooth in the x-direction using a Gaussian convolution
LXSET	Set x-array of spectrum/image to specified range
OPTEXTRACT	Extracts a long slit spectrum
POLYSKY	Sky subtraction by polynomial interpolation
PROFILE	Determines the spectral profile for use in **OPTEXTRACT**
SCROSS	Simple routine to cross correlate spectra
SCRUNCH	Re-bins a spectrum into a linear or logarithmic wavelength range
SDIST	Analyse an image containing spectra for S-distortion
SFIT	Fits a polynomial to a spectrum
XCOPY	Copy x-array information (e.g. wavelengths) into a spectrum
XCORR	Cross correlation routine used in the automated redshift determination
YSTRACT	Adds contiguous columns of an image to produce a spectrum

Table 3.5: Glossary of Figaro Commands

was 3900Å. This gave a resolution of 8Å and a wavelength coverage of 3300Å. The limited spectral range of the quartz dome lamp emission meant that flat fields had to be observed using a higher resolution grating, 830 lines mm^{-1}, in order to illuminate the array evenly. Long integration flat fields were taken at the beginning and end of each night. Copper-Argon calibration arc spectra were taken before and after each observation. Radial standard stars were observed at the beginning and end of each night. The same standards were chosen each night, to build up signal to noise. The standards were observed through a neutral density filter to avoid saturating the array.

3.4 Spectral Reduction

The reduction of the spectral data was done using the STARLINK FIGARO reduction package. A glossary of the FIGARO commands used is given in table 3.5. The description of the reduction process is divided up into the main procedures that are common to all types of spectral data analysis. Within these divisions there are some operations specific to the detector used. In these cases the three detectors; IPCS, RPCS & Tek-RGO, are treated separately.

3.4.1 Treating Raw Data Frames

A median bias frame was made for each night and subtracted from every frame. The frames were then corrected for cosmic ray hits using the automatic routine BCLEAN. This identifies and removes pixels with cosmic ray hits and then interpolate s over the

neighbouring region to fill in the gaps. Small scale variations in the pixel to pixel response of the chip were removed by dividing the frames, pixel by pixel, by calibration flat fields. The preparation of the calibration flat fields was as follows;

- Co-adding the flat field frames to make a master flat field for each night.
- Compressing the co-added flat field frames in the spatial direction to a 1-D spectrum (EXTRACT) between pixels 1 and 375. The intensity of the flat field lamp was approximately constant with wavelength, so any variation in counts with wavelength in this spectrum is due to the varying response of the detector.
- The spectra are then smoothed with a 4 pixels (FWHM) filter to remove small scale variations.
- Each row of the master flat field frames was then divided by this smoothed spectra to produce a calibration frame.

The effect of the flat fielding can be seen in figure 3.2, where the chip defects around rows 53 and 238 can be clearly seen in the pre-flat fielded spectrum but are removed in the flat fielded spectrum. (The three large peaks in these plots indicate the positions of galaxies along the slit.)

RPCS

Data from RPCS observations comes not as a 2-D frame but as two 1-D spectra, one from each channel. All the RPCS spectra were flat fielded by dividing by the calibration flat field for their respective channel. In this case flat field calibration was performed by dividing the raw flat field spectra by a smoothed version. (Where the smoothing was performed using a 50 pixel FWHM filter.) When the flat field spectra were compared, it was found that, at all wavelengths, channel A was more sensitive than channel B by a factor of ≈ 1.3 (the exact value varied from night to night), figure 3.1. After flat fielding, all the spectra were clipped (LXSET) so that only data between pixel numbers 520 and 1570 were retained.

IPCS

Instruments that use image intensifiers suffer from various distortions, in particular S-distortion. The effect is to produce a spectrum that snakes across the two-dimensional image frame rather than being perfectly straight. S-distortion can be corrected by two orthogonal one dimensional corrections, but one has to first determine the exact shape

of the distortion. For IPCS spectral reduction a self-correction approach was taken. The 2-D shape of each galaxy spectra was fitted by SDIST and then the routine CDIST was used to straighten the image using the SDIST results. In the few cases where the galaxy spectra was not of high enough signal to noise for SDIST to operate, no correction was applied.

The calibrated IPCS flat field obtained on the first night of the 1991 run was found to be very smooth with minimal residual pixel to pixel variations. Therefore, to avoid the introduction of unnecessary noise, no flat fielding correction was made to the IPCS frames.

3.4.2 Extraction of Sky Subtracted Spectra

Once the images have been flat fielded and corrected for any distortions, the spectra have to be extracted from the image frame and a sky subtraction applied.

RPCS

The method of sky subtraction for RPCS data was very simple, the signal from the sky channel was subtracted from the object channel. In practice there was a shift in pixel to wavelength response between the two channels. Therefore, the spectra from the two channels were re-binned between 3000 Å and 6500Å into 1000 linear bins, using SCRUNCH. The sky data was then subtracted from the galaxy data. The difference in sensitivities of the two channels was compensated for by multiplying the data from channel B by the scale factor determined from the flat fields. The sky subtraction using this method is incomplete as shown in spectra 4 and 5 of figure3.7. The sky line at $5577\mathring{A}$ is still clearly visible in these spectra.

N.B. The integration times for the template observations were so short that the contribution from sky noise was negligible and sky-subtraction was not necessary.

IPCS and Tek-RGO

Optimal extraction was used to obtain the best possible 1-D sky subtracted spectra from the 2-D frames obtained at the AAT. This method performs a weighted spectrum extraction, where the weighting was defined by the surface brightness profile, see Horne (1986) for the details. The first stage involves removing the sky contribution in the spectrum using POLYSKY. This routine subtracts off a map of the sky contribution in the object spectrum. This map was constructed by interpolating a quadratic fit to the sky brightness in regions either side of the spectrum. The routine PROFILE was then used to fit a surface profile to the sky subtracted spectrum using a 5^{th} order

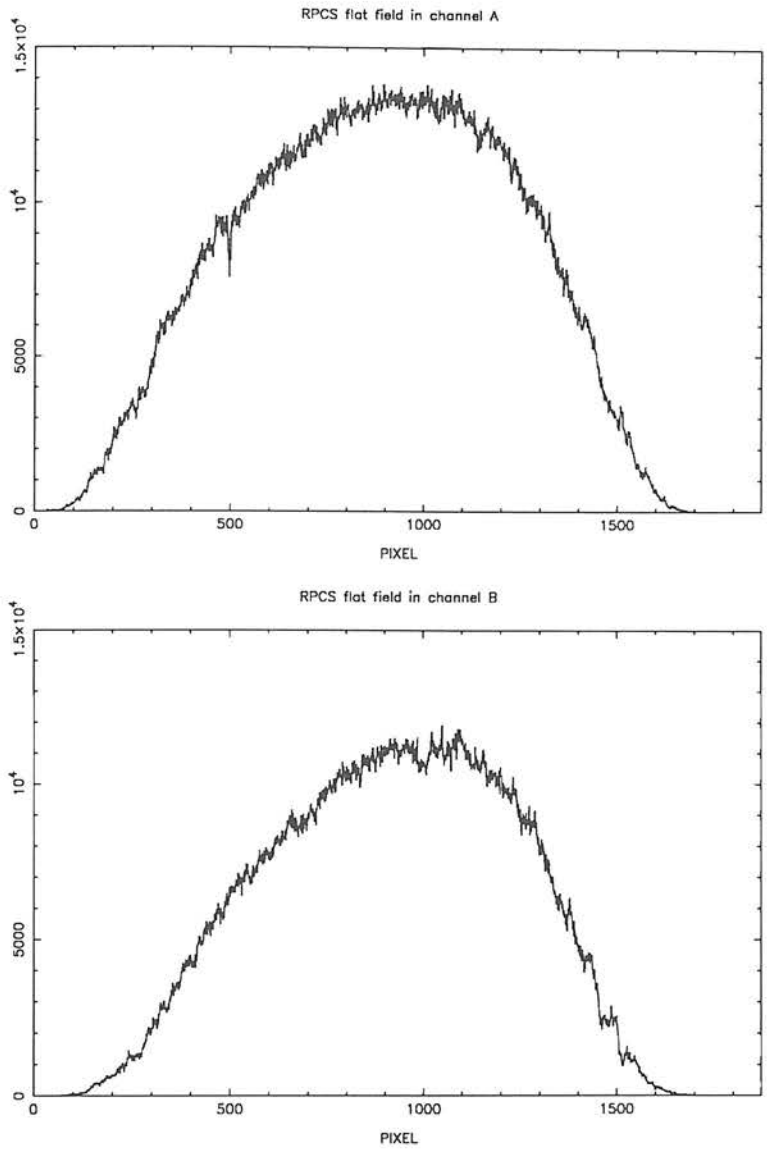

Figure 3.1: Flat field spectra taken in 10^4 s on the second night of the SAAO run. It can be seen that the signal in channel A was $\approx$ 1.3 times larger than that in channel B, reflecting the increased sensitivity in that channel. Detector defects, such as at pixel 450 in channel A, are also clearly visible.

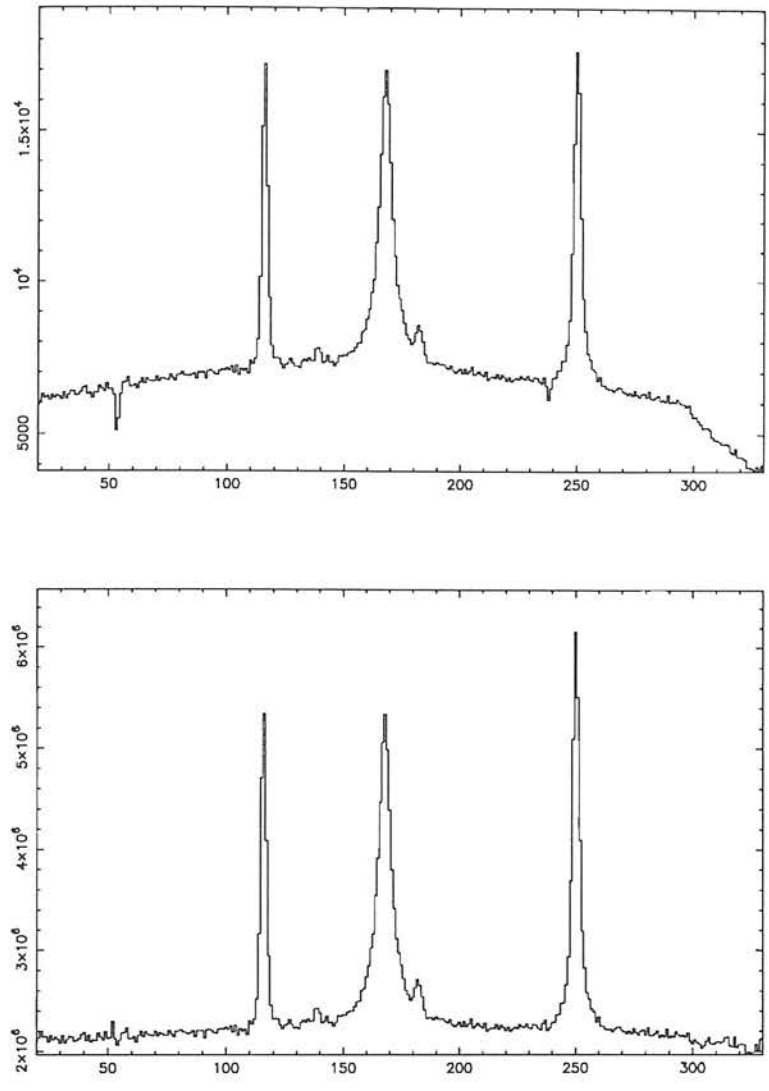

Figure 3.2: Spatial profiles (in counts versus pixel number) of the Tek-RGO CCD observation of the field surrounding RASS source 0763002 (Abell cluster 2420). The upper plot shows a cross section of the raw image frame whilst lower plot shows the same cross section after flat field correction. Bad pixels at rows 53 and 238 are compensated for in the flat fielded image. The three sharp peaks represent the intensity profiles of three cluster galaxies.

polynomial. Finally OPTEXTRACT was used to produce an optimally extracted 1-D spectrum using the output from PROFILE. The effectiveness of this method of sky subtraction is illustrated in spectra 2 and 8 in figure 3.6, where there is no evidence for any residual sky emission at 5577Å.

The optimal extraction routines require, as inputs, the outer limits, in the spatial direction, of each spectrum and their respective sky regions. These limits were determined interactively using ICUR, a calibrated cursor routine. For the IPCS data, the edges of the spectra were read off directly from the 2-D frames. The IPCS wavelength to pixel relation was not very stable in spatial direction. This meant that the sky regions needed to be as close as possible to the spectra and not very wide, if the sky subtraction was to be effective. Therefore, the sky regions were chosen to be $\approx$ 15 pixel wide and $\approx$ 5 pixels from the visible edge of the object's light profile. For the Tek-RGO frames, the positions of the sky regions were less crucial and a simpler method was employed; looking for peaks in the surface brightness profile. These profiles were created by compressing each frame in the spectral direction using YSTRACT. For example, the intensity profile for an observation of the field around RASS source 0763002, Abell cluster 2420, that yielded three galaxy spectra, see table B.1, is shown in figure 3.2.

3.4.3 Wavelength Calibration

Calibrations between detector pixel number and wavelength were achieved by taking short integrations of comparison lamps, containing low pressure gaseous elements, using the same instrumental set-up as the galaxy observations. The lamps were stored in the telescope chimney and could be switched easily into the optical path of the spectrograph. Temperature variations and telescope orientation can alter the wavelength to pixel variation from observation to observation. These variations can only be monitored accurately using arc lamp calibrations and so arc exposures needed to be taken regularly throughout the night.

The interactive line fitting programme ARC in FIGARO was used to identify lines in the observed arc spectrum using arc line wavelength maps available at each telescope. The resulting arc fits were transferred to the respective object spectra using XCOPY. ARC makes full use of interactive graphics and provides a running fit to make the manual identification process as easy as possible. It also has an automatic line identification feature that can be used to add lines to a fit. It was very important to identify arc lines at the extremities of the spectra, otherwise the polynomial fit would be poorly constrained at the edges. For example, in spectrum 9, figure 3.7, a slight error in the wavelength to pixel relation has meant that it was not possible to choose a redshift value

that would fit both the [O_{II}] line at 3727Å and the [O_{III}] lines at 5007Å. The RMS value of the discrepancy between the observed arc line centers and the line centers predicted by the polynomial fit can be used to judge the accuracy of the fit. (A rule of thumb is that the best achievable RMS value is approximately one tenth of the spectral resolution, Nichol 1992.)

IPCS

As mentioned above, the wavelength to pixel relation of the IPCS was not stable across the detector. It was found, using SCROSS, that spectra taken from the central rows of arc images were shifted by up to 1 pixel from spectra taken from rows at the edge of the images. Therefore, object spectra at different row positions on the same image frame were calibrated separately. It was found that spectra built up from 30 rows, centered on the object position, of the arc frame contained emission lines with sufficient signal-to-noise to make a good ARC fit without the lines becoming overly broadened. The wavelength to pixel relation was also temporally unstable and so the arc frames had to be individually calibrated. On average, 30 arc lines were identified manually and 30 automatically in the IPCS arc spectra and the range in RMS fit values was 0.16Å to 0.25Å, with a modal value of 0.2Å.

Tek-RGO

The wavelength to pixel relation of the Tek-RGO chip was very stable across the detector, with a typical shift of < 0.05 pixels between spectra taken from the centre to the those taken from the edge of the arc frames. As a result, no degradation in the arc fits occurred if the whole arc is compressed in the spatial direction. Therefore, only one arc fit has to be made to calibrate all the spectra on the object frames. In addition the temporal shifts were very small and often 2 or 3 arc spectra could be co-added without degrading the arc fit. These detector properties had the joint advantages of speeding up the object calibration and of increasing signal to noise in the arc spectrum. Typical values for the RMS fit values for the Tek-RGO spectra were; 0.12Å to 0.2Å for the 1992 data and 0.14Å to 0.19Å for the 1993 data. For both runs $\approx$ 30 manually identified lines were used.

RPCS

As mentioned above, the RPCS spectra were clipped after flat fielding. This was done because no arc lines could be identified, and thus the arc fit cannot be constrained,

outside the pixel range 520–1570. Variations in the wavelength to pixel relation with telescope orientation meant that the object spectra had to calibrated using only those arc spectra taken before and after the object integration. Typically $\approx$ 40 manually identified lines were used to constrain the polynomial fit, with RMS values in the range 0.7Å to 0.9Å.

3.4.4 Adding Spectra

Maximum integration times are limited by such factors as instrumental drift and the frequency of cosmic ray hits. Several objects were observed more than once to build up signal to noise in the spectrum. Most of the RPCS redshifts were derived from composite spectra. For example, spectrum 4 in figure 3.6, shows a composite spectrum of two observations of a galaxy close to the position of RASS source 0723084. The co-adding was done by adding the two wavelength calibrated, sky subtracted spectra after re-binning them into the same linear wavelength bins.

3.5 Redshift Determination

Galaxy redshifts can be determined by measuring the wavelength shift of their spectral features relative to their rest positions, § 1.2.1. The emission lines and absorption features identified during the spectroscopic follow-up are listed in table 3.6. The most commonly observed absorption features were the calcium H and K doublet, the 4000Å continuum break (caused by a discontinuity in the Balmer lines), and the G band. The most commonly observed emission line was the oxygen line $[O_{II}]$ at 3727Å, although the lines H_β, $[O_{III}]_{4959}$ and $[O_{III}]_{5007}$ also occurred frequently.

For the SGP RASS Cluster Project, the redshift determination was performed in two different ways. First, the individual spectra were displayed on a work station and the best redshift was fitted by eye using the observed spectral features. Secondly, each spectrum was cross-correlated with a library of template spectra. The first method was included in the reduction pipeline because a) it acted as a check on the automated redshift determination and b) it allowed contaminating objects, such as AGN, BL Lacertae objects and X-ray stars to be identified.

3.5.1 Manual Identifications

A comprehensive scheme to identify emission and absorption lines and to determine object redshifts was carried out using a programme, REDSHIFT , provided by Karl Glazebrook[3]. The programme, written inside the FIGARO environment, allowed the

[3]Present address; IOA, Cambridge, U.K.

Absorption Features		Emission Features	
Wavelength (Å)	Feature	Wavelength (Å)	Feature
3798.6	Hθ	3426	[Ne V]
3834.7	Hη (+ MgI & FeI)	3727	[O II]
3888.7	Hζ	3869	[Ne III]
3933.3	K (Ca II)		
3969.2	H (Ca II & Hϵ)		
4000.0	4000Å break		
4227.8	Hδ	4102	Hδ
4304.4	G (Ca II)		
4340.5	Hγ	4340	Hγ
4864.5	Hβ	4861	Hβ
5174.0	b (MgI)	4959	[O III]
5268.6	5268 (FeI + CaI)	5007	[O III]
5892.4	D (NaI)		

Table 3.6: Spectral absorption and emission features found during the spectroscopic follow-up of SGP RASS cluster candidates. The information is drawn from Corwin & Emerson (1982) and Costero & Osterbrock (1977).

user to interactively;

1. Plot and manipulate (smooth, magnify *etc.*) the spectrum.

2. Fit a redshift, by guessing the identifications of spectral features.

3. Identify features, once the redshift was known.

The results of the REDSHIFT analysis are presented in table B.1. The redshift values are listed in column 7, where only a rough redshift value was obtained, the redshift is listed with a $\sim$ sign. Often a "redshift" value is not quoted for identified stars, instead they are simply marked "star". There are several cases where "n.a." appears in column 7. In all but one case, this is occurs when strong emission lines were present in the spectrum which were not immediately recognizable using REDSHIFT . In the other case, 0843045, REDSHIFT failed to identify a redshift value, but XCORR , § 3.5.2, did. The errors on the manually determined redshifts are discussed in § 3.5.1.

The features identified in each spectrum are listed in column 8 of table B.1. To avoid confusion between hydrogen lines in absorption and in emission, the absorption features are listed as h_δ h_γ h_β *etc.* and emission lines as H_δ H_γ H_β *etc.* (Note, the calcium H line can be distinguished from hydrogen lines in emission because it has no subscript.) The identification of the other features are as given in table 3.6. The features are always listed by increasing rest wavelength. A dash, $-$, in column 8 marks the point in the sequence

where an unidentified emission line occurs. For example, none of the 7 emission lines in the third 0833006 galaxy were identified.

The superscripts in column 8 should be interpreted as follows;

- *sf* : small & fine emission lines
- *lf* : large & fine emission lines
- *sw* : small & wide emission lines
- *lw* : large & wide emission lines
- *?bl* : suspected BL Lacertae object

They refer to the observed nature of the emission lines or continuum seen in the respective spectrum. They are an attempt to make a first order classification of emission line object, see § 3.6. As the spectra have not been flux calibrated, and no equivalent width measurements made, these descriptions must be treated with caution. Briefly, "wide" indicates lines that are significantly, when judged by eye, broader than the spectral resolution, and "large" indicates that the signal to noise in the lines is $\gtrsim 5$. Unfortunately, this emission line description is not available for all the emission spectra in table B.1.

Example REDSHIFT outputs for spectra taken during each of the four runs are shown in figure 3.7. The 18 spectra, described in table 3.9, cover a range of object types and signal to noise levels. In these plots the spectra have been sky subtracted and wavelength calibrated. The continuum emission has been left in these plots to reflect the intrinsic differences between the different spectral types, *e.g.* compare spectra 1 and 13, and the different wavelength responses of the three detectors, *e.g.* compare spectra 1 and 5. Note that almost all of the absorption and emission features listed in table 3.6 can be seen in spectrum 1 and spectrum 9 respectively.

3.5.2 Cross Correlation Technique (XCORR)

In addition to the manual method described above, an automatic redshift finding routine was applied to the spectra. As is customary, the cross-correlation technique was used, see Tonry & Davis (1979) for a complete description. This technique allows redshifts and their errors to be determined objectively, by convolving the object spectrum with a template spectrum of known redshift. The resulting cross correlation function (CCF) has a peak corresponding to the redshift at which the template best matches the galaxy spectrum. The FIGARO programme XCORR , was used to perform the necessary fast fourier transforms and return the peak of the CCF.

Preparation of Spectra

Before running XCORR , the spectra (object and template) had to treated in the following way;

1) The continuum was removed by subtracting either a high order polynomial fitted to the whole spectrum (SFIT) or a heavily smoothed version of the spectrum (IXSMOOTH). For the IPCS spectra, a 4^{th} order polynomial fit was used, for the Tek-RGO spectra a 3^{rd} order polynomial fit was used and for the RPCS spectra a 50 pixel (FWHM) Gaussian smoothing was used.

2) Any remaining discontinuity between opposite ends of the spectrum was removed, using COSBELL, by multiplying with a "cosine-bell" function which is equal to unity except at the edges, where it falls smoothly to zero over the last 5% of its length. This is necessary because the discrete Fourier transform used in XCORR is made periodic by identifying the ends of the spectrum. Any discontinuity would look equivalent to a sharp break and be mistaken for a real feature, thus introducing spurious correlations.

3) The spectra are re-binned into *logarithmic* bins, *i.e.* so that the bin centers follow a geometric progression. This is vital because cross-correlation measures a shift between spectra while the effect of redshift is a multiplication by (1+z). If the binning is done as,

$$n = A \ln \lambda + B, \tag{3.1}$$

where n is the bin number, λ is the wavelength and A and B are the normalization constants, then, a shift of n_0 bins is related to the redshift by,

$$n_0 = A \ln \frac{(1+z_0)}{(1+z_t)}, \tag{3.2}$$

where z_0 is the observed, or unknown, redshift and z_t is the template redshift which is known to high accuracy.

The Method

The template and data spectrum are cross–correlated in Fourier space by multiplying the transform of the data spectrum by the complex conjugate of the transformed template spectrum. During the multiplication a filter is applied to remove residual low frequency correlations not fully removed by the continuum subtraction and very high frequency noise below the resolution of the spectra. The real part of the resulting CCF is normalized such that a perfect correlation gives a peak at zero shift of unity height. Ideally, the data and template spectra would be identical except for a shift of n_o bins. The CCF is then scanned for its highest peak. The centroid (n_0), height (H) and FWHM width (W)

of this peak are determined by fitting a parabola to the data. The observed redshift is then calculated using equation 3.2, while the error in the shift is well-approximated by

$$\delta n_o = \frac{0.375\,W}{1+R}, \tag{3.3}$$

where R is given by,

$$R = \frac{H}{\sqrt{2}\sigma_a}. \tag{3.4}$$

Here, σ_a is the rms of the antisymmetrical part of the CCF and represents the noise in the CCF since, for a perfect correlation with a symmetrical broadening function, the CCF should be symmetric about the true chosen peak. (Broadening is introduced both by instrumental effects and by the internal velocity dispersion of the galaxy.) The probability that the chosen peak is the true peak, in the form of a confidence level (C), is also returned by by XCORR . The confidence level is derived by assuming that the noise in the CCF has a Gaussian distribution of width $\sqrt{2}\sigma_a$. (See Heavens 1993 for a complete description of confidence level derivations.)

3.5.3 Spectral Templates

To be successful, the cross correlation method requires good quality template spectra, derived from objects with known radial velocities. It is preferable to use several different templates, to account for the range in spectral types in the object spectra. Table 3.7 lists the various radial standard stars and bright galaxies that were used in the cross correlation. As much as possible, cross correlations were performed with templates taken with the same instrumental set-up as the galaxy spectra and table 3.8 indicates which templates were used in the reduction of spectra from specific runs. In the case of the IPCS data, we were able to supplement the list of templates we had observed with templates provided by other observers. The additional galaxy templates were taken from Nichol (1992) and the stellar templates from Parker *et al.* (1987). The 6 different Tek-RGO templates were observed several times during the 1992 and 1993 runs, thus providing a total of 34 template spectra.

The stellar templates were selected from the listing of radial standards in §H of the Astronomical Almanac. The majority of the template galaxies were selected from de Vaucouleurs *et al.* (1991). The radial velocities of these galaxies are taken from a compilation of weighted mean 21 cm observations, Bottinelli *et al.* (1990). The exception, galaxy E348G10, represents the 10th ranked member of EDCC cluster 348 (Lumsden *et al.* 1992, Nichol 1992). This galaxy has a similar spectrum to the cluster galaxies in our programme and was thus included in the template list despite its relatively large velocity error. Two examples of template spectra are shown in figure 3.6, spectra 17 & 18.

STARS	v km s^{-1}	Type	GALAXIES	v km s^{-1}	Type
HD35410	$+20.5 \pm 0.2$	KO III	N2613	1678 ± 5	SA(s)b
HD80170	0.0 ± 0.2	K5 III-IV	N5740	1570 ± 4	SAB(rs)b
HD92588	$+42.8 \pm 0.1$	sgK1	N5921	1480 ± 4	SB(r)bc
HD145001	-9.5 ± 0.2	G8 III	N6070	2006 ± 7	SA(s)cd
HD171391	$+6.9 \pm 0.2$	G8 III	N6118	1570 ± 4	SA(s)cd
HD203638	$+21.9 \pm 0.1$	KO III	N6958	2713 ± 13	E+
			N7793	227 ± 2	SA(s)
			E348G10	8813 ± 65	-

Table 3.7: Radial velocity templates used in the cross correlation analysis. The quoted radial velocities and object types are taken from, a) the astronomical almanac, for the stars, and b) from de Vaucouleurs *et al.* 1991 for all galaxies except E348G10. The radial velocity for the latter galaxy was taken from Nichol (1992). The de Vaucouleurs redshifts are based on 21 cm observations.

Anglo-Australian Telescope IPCS observations					
HD80170	HD923588	N2613	HD35410†	HD171391†	N5740‡
N5921 ‡	N6070‡	N6118‡	N6958‡	N7793 ‡	E348G10‡
Anglo-Australian Telescope Tek-RGO observations					
HD35410	HD145001	HD203638	N5921	N6070	N6118
South African Astronomical Observatory RPCS observations					
		HD35410	HD203638		

Table 3.8: Key showing which templates were used in the XCORR redshift determination.

‡ Galaxy template provided by Nichol (1992)

† Stellar template provided by Parker *et al.* (1987)

3.5.4 Deriving Galaxy Redshifts from XCORR Results

To recap, XCORR returns; a redshift, z, and a redshift error, δz, based on the position and width of the highest peak in the CCF. In addition, XCORR returns a confidence level, C, that the highest peak in the CCF represents the true separation of the template and object spectra. We now describe how that information was interpreted to provide redshifts for the objects studied during the spectroscopic follow-up.

IPCS and Tek-RGO Data

With up to 34 cross correlations per object spectra, an automated method had to be developed with which to screen the XCORR outputs and determine the best estimate of the object redshift. The first stage was to analyse the XCORR results for each object and find the mean, $\bar{z}$, and standard deviation of the redshift values. The most deviant point was rejected and the mean re-calculated. This was repeated until either the standard deviation no longer decreased or the number of templates remaining had reached an empirically derived critical level ($n_{crit} = 15$ for the 34 Tek-RGO templates, $n_{crit} = 6$ for the 12 IPCS templates). Although certain stars and low z galaxies have genuinely negative radial velocities, it was assumed that any negative redshift was meaningless and these results were excluded from the iteration. In table B.1, if the word "bombed" appears in the 9^{th} column, then XCORR had produced a negative redshift with all the templates.

The second stage involved finding the redshift, z', with the highest confidence level, C', within one standard deviation of the last determined $\bar{z}$ value. If the following two conditions were met, then z' was assumed to be the true redshift of the object and z' & $\delta z'(\times 10^5)$ were listed in table B.1, column 9. If neither, or only one, of these conditions were met, then the object was labelled in column 9 as having an "unclear" XCORR redshift. The conditions;

1) That there was at least one other, different, *i.e.* not simply a repeat exposure, template with a redshift, z^t, within 3 sigma of z', *i.e.*

$$\left[z' - (3 \times \sqrt{(\delta z')^2 + (\delta z^t)^2})\right] < z^t < \left[z' + (3 \times \sqrt{(\delta z')^2 + (\delta z^t)^2})\right]. \qquad (3.5)$$

2) That the chance that z' had been determined from a noise peak in the CCF was less than 1% (*i.e.* $C > 0.99$) This limit was adopted based on the empirical arguments in Dalton (1992).

RPCS Data

With only two templates available from the SAAO run in 1992, each of the XCORR CCF spectra could be studied individually. If an XCORR determined redshift had a confidence level $C > 0.99$ with either stellar template, then that redshift value was adopted as the object redshift.

3.5.5 XCORR Redshift Errors

Internal Errors

The errors tabulated in column 9 of table B.1, δz, represent the internal error on the XCORR measurement ($\times 10^5$). The distribution of the 207 available XCORR error values is shown in figure 3.3. The mean of the distribution is $\delta z = 2.1 \times 10^{-4} \pm 2.8 \times 10^{-4}$ or $\delta v \approx 63\,\mathrm{km\,s^{-1}}$. This mean is weighted by a few large error values all of which have been shown to be associated with erroneous XCORR redshifts (see below). Therefore, a more representative value for the typical internal error in an XCORR determined redshift is the median value, $\delta z = 1.4 \times 10^{-4}$ or $\delta v = 42\,\mathrm{km\,s^{-1}}$.

External Errors

It is possible to determine the external error on the XCORR measurements by comparing the redshift values returned by XCORR from different observations of the same galaxy. At least two XCORR determined redshifts exist for each of 50 galaxies observed during the AAT 1992 run. The residuals between these redshift determinations are plotted in figure 3.4. The mean value and median values of these residuals are $\delta z = 7 \pm 15 \times 10^{-4}$ and $\delta z = 2 \times 10^{-4}$ ($\delta v = 60\,\mathrm{km\,s^{-1}}$) respectfully. These values are comparable to the internal errors quoted above. In addition there are five galaxies for which repeat XCORR redshift measurements exist, where the spectra were taken obtained during different runs. For these cases, the typical redshift residual was $3 \times 10^{-4} < \delta z < 8 \times 10^{-4}$.

3.5.6 Manual Redshift Errors

The primary purpose of the manual redshift finding technique was to search for possible contaminating objects in the X-ray cluster candidate list by classifying different types of object spectra. The accuracy of these manual redshift determinations was limited by the accuracy of the wavelength calibration and the ability to find the centre of any feature by eye. For object spectra which are not well matched by any of the XCORR template spectra, the manual method is the only way to discern a redshift value. Therefore, it is important to have an estimate of the errors on these manually determined redshift values.

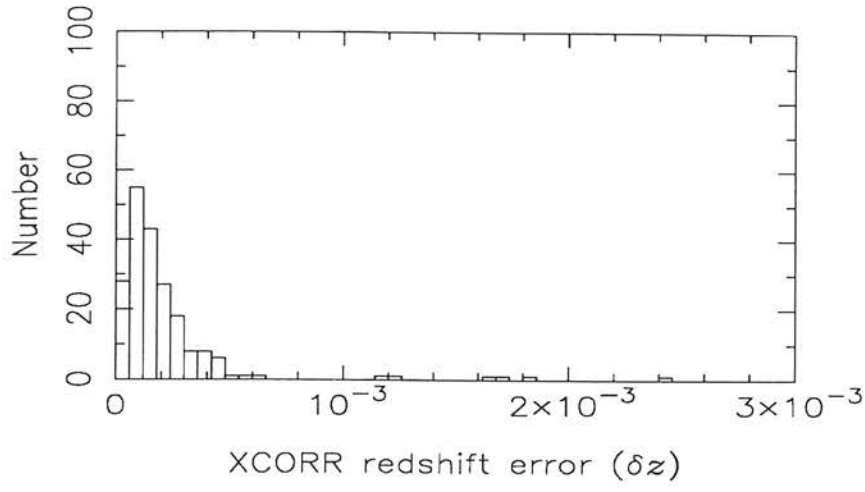

Figure 3.3: Distribution of internal errors on the XCORR determined redshifts.

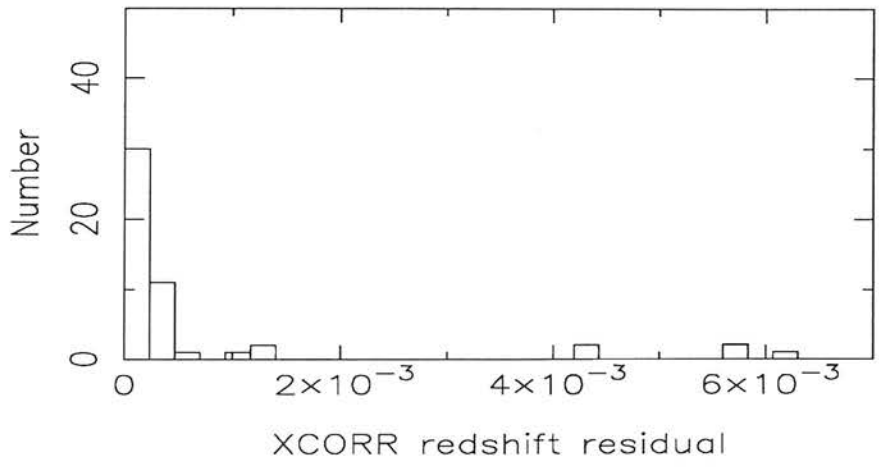

Figure 3.4: Distribution of XCORR external redshift errors, determined from 50 galaxies that were observed more than once during the AAT 1992 run.

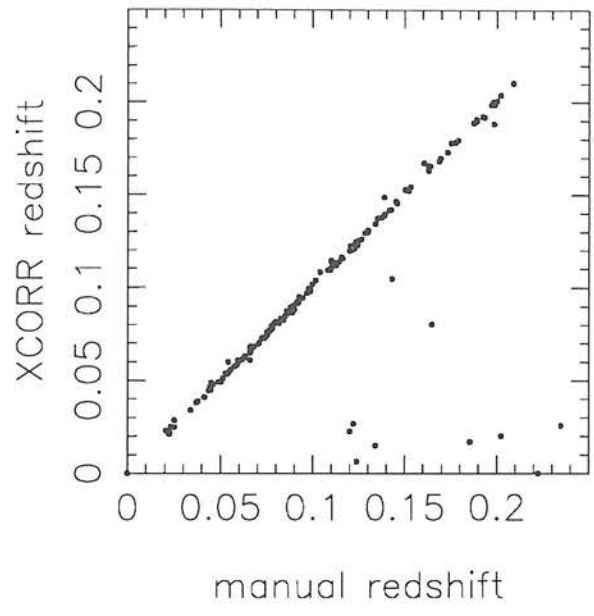

Figure 3.5: XCORR determined versus manually determined redshifts for 188 galaxies for which both measurements exist.

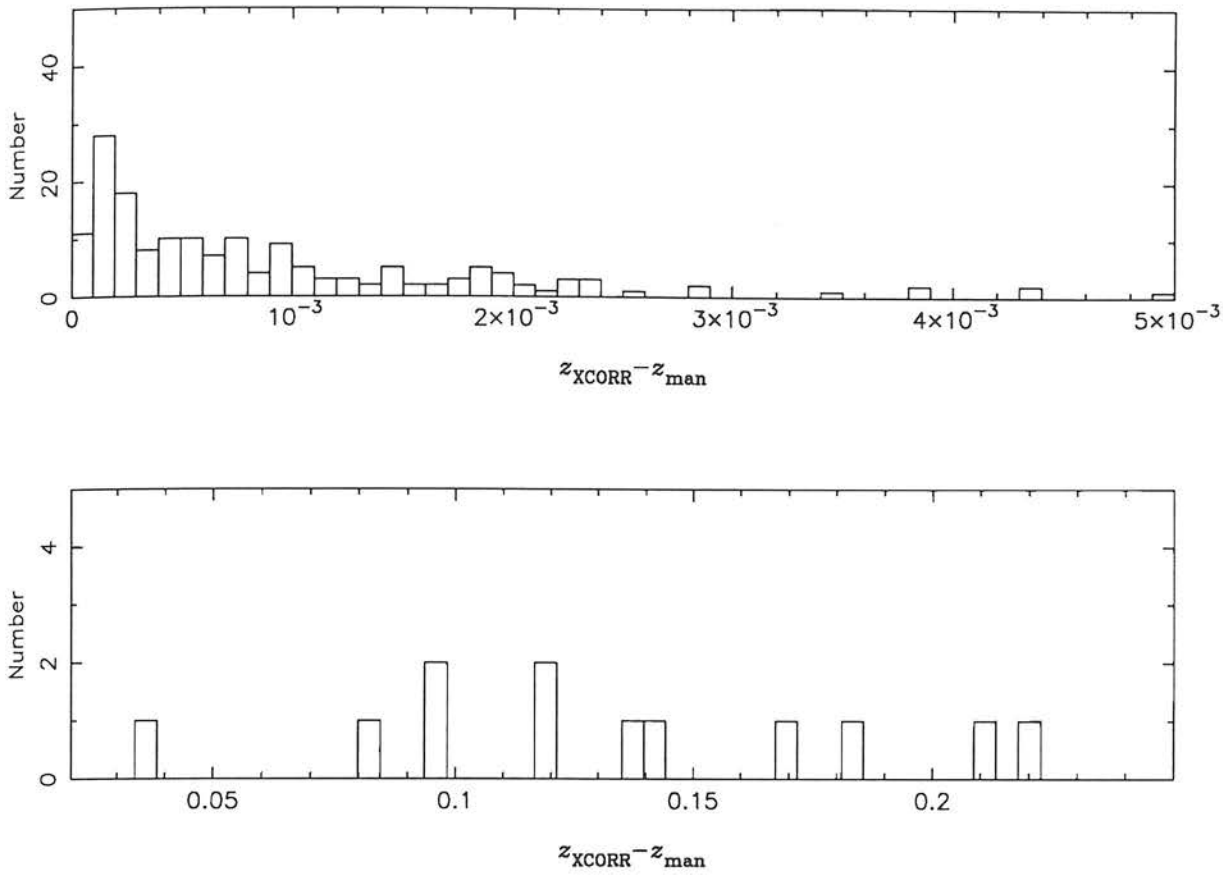

Figure 3.6: The distribution, plotted over 2 different scales, of the $z_{XCORR} - z_{man}$ residuals for 188 galaxies for which both manual (z_{man}) and XCORR (z_{XCORR}) redshift measurements exist.

Figure 3.5 shows the XCORR and manually determined redshifts for the 186 objects for which results from both techniques exist. Figure 3.6 shows the distribution of residuals between the manual and XCORR redshifts ($z_{XCORR} - z_{man}$) for these 186 cases. The median value of this residual distribution is $\delta z = 1.35 \times 10^{-4}$ ($\delta v = 41\,\mathrm{km\,s^{-1}}$), in good agreement with the external and internal errors quoted above.

There are 23 objects for which the discrepancy between z_{XCORR} and z_{man} is greater than $\delta z = 0.0033$ or $\delta v = 1000\,\mathrm{km\,s^{-1}}$, *i.e.* far in excess of what would be expected from the intrinsic errors in the two methods. These objects were examined to find the cause of the disagreement. In 15 cases the cause of the disagreement was clear, either; a) the spectrum had strong emission lines, *i.e.* it will not match any of the available XCORR templates, b) the error on the XCORR measurement was unusually large, $\delta z > 8 \times 10^{-4}$, *i.e.* more than 2σ from the mean internal error, thus suggesting

that XCORR had produced an erroneous result or c) the manual redshift value was known to be inaccurate. The adopted value for the galaxy redshift is marked in table B.1 by a †.

The cause of the discrepancy in the other 8 cases was ambiguous. If the two values differed more than the maximum error that could be introduced into a cluster redshift measurement by the velocity dispersion, *i.e.* $v < 2000\,\mathrm{km\,s^{-1}}$, neither result was assumed to be accurate or used further, *e.g.* to define cluster redshifts. Otherwise, the XCORR value was adopted as the true redshift of the galaxy. (Note that in the other 163 cases where both REDSHIFT and XCORR values are available and $z_{XCORR} - z_{man} < 0.0033$, the XCORR value was adopted as the galaxy redshift.)

In conclusion, in 87% of cases, there is good agreement between the redshift values returned by XCORR and those returned by the manual identification. Therefore, for those few objects for which reliable XCORR values were not available, but a good manual identification was, we can assume that the error on the assumed object redshift is $\delta z = 1 \rightarrow 2 \times 10^{-4}$. The errors on the object redshifts (either z_{man} or z_{XCORR}) are, therefore, insignificant in comparison to the velocity dispersion of clusters, $v \sim 700\,\mathrm{km\,s^{-1}}$ or $\delta z \sim 2 \times 10^{-3}$, Zabludoff *et al.* (1990). Note also that no correction was made to the XCORR or manual redshifts to the heliocentric coordinate system. The Earth's orbital velocity is $\simeq 30\,\mathrm{km\,s^{-1}}$ which corresponds to a redshift error of $\delta z \simeq 10^{-4}$.

3.6 Classifying Galaxies

It can be seen in table B.1 that a large fraction ($\approx 30\%$) of the objects observed during the spectroscopic survey have emission lines in their spectra. Certain objects with strong optical emission lines, those with active galactic nuclei, are strong X-ray emitters. Others, such as cD galaxies in cooling flows or starburst galaxies are relatively, when compared to intracluster gas emission, X-ray faint.[4]. It is, therefore, important to distinguish active galaxies that are contaminating our candidate list from X-ray faint emission line galaxies in clusters. The optical line excitation mechanisms in X-ray bright and X-ray faint galaxies differ; *e.g.* a) photoionization by a power-law continuum source in AGN and b) photoionization by O and B stars in starburst galaxies. Such mechanisms leave characteristic imprints on the optical spectrum. We have, therefore, attempted to classify the emission line galaxy types using the relative line strengths and widths of various emission lines.

[4] A description of the X-ray properties of various types of astronomical objects is given in § 4.2

3.6.1 Starburst and Giant Elliptical Galaxies

The term "starburst" refers to a galaxy in which there is thought to be an exceptionally high rate of star formation. Starburst galaxies are characterised in the optical by narrow emission lines similar to low-ionization HII regions. They are a commonly observed phenomena in clusters. From high resolution imaging it has been shown that these galaxies tend to be in the process of galaxy-galaxy interactions and/or to be associated with cluster sub-structure, *e.g.* Couch *et al.* (1994) & Caldwell *et al.* (1993).

A high proportion of X-ray clusters are dominated by a single bright cD galaxy. These galaxies have a nucleus of a very luminous elliptical galaxy which is embedded in an extended amorphous halo of low surface brightness. (Objects in our spectroscopic follow-up that resembled cD's are labelled as such in column 6 of table B.1.) It has been shown that a high fraction, $\approx$ 30%, of central galaxies in clusters have emission line spectra (Crawford *et al.* 1994). The emission mechanism is unclear at present, although the best received model involves energy injection into cold gas clouds by turbulent mixing, Crawford & Fabian 1992.

From the optical spectra of starburst galaxies presented in Caldwell *et al.* (1994), Fruscione & Griffiths (1991), Couch & Sharples (1987) and those of emission line cD galaxies presented in Crawford *et al.* (1994), we can deduce that the spectra of these two galaxy types will be indistinguishable in our spectroscopic survey. (This is due to the limited ($\sim 3800 - 5500$Å) wavelength range of the observations.) Both galaxy types will be characterised by;

1) Strong narrow emission lines, including $[O_{II}]_{3727}$, H_β, $[O_{III}]_{4959}$ and $[O_{III}]_{5007}$.
(Beyond a redshift of $z \sim 0.11$ only $[O_{II}]_{3727}$ will be visible.)
2) A dominance of the $[O_{II}]_{3727}$ line over the $[O_{III}]_{4959}$ and $[O_{III}]_{5007}$ lines.
3) The presence of galaxy absorbtion features among the emission lines.

3.6.2 Active Galactic Nuclei

In contrast, absorption features will occur only rarely in the spectra of active galactic nuclei. Except in the case of BL Lacertae objects, AGN spectra are dominated by emission lines that can be either narrow or broad. (BL Lacertae objects, a rare form of AGN, show bright, blue continuum and very weak, or no, emission or absorption features.) In the wavelength range of our observations, the following emission lines may be seen in AGN spectra; $[Ne_V]$, $[O_{II}]_{3727}$, $[Ne_{III}]$, H_δ, H_γ, H_β, $[O_{III}]_{4959}$ and $[O_{III}]_{5007}$. However, the most common lines will be $[O_{II}]_{3727}$, H_β, $[O_{III}]_{4959}$ and $[O_{III}]_{5007}$. Based on the results presented in Baldwin & Phillips (1981) we can expect an object spectrum

to be that of an AGN if the equivalent width of the $[O_{III}]_{5007}$ line is larger than the $[O_{II}]_{3727}$ line and the H_β line. Objects that show broad, $\gtrsim 1000\,km\,s^{-1}$, permitted emission lines and narrower forbidden lines are most probably Seyfert I objects.

3.6.3 Classification Scheme

Flux-calibration and equivalent width measurements were not included in the reduction of the spectra from our observing campaigns. It can, therefore, be misleading to make comparisons of raw line strengths if the lines were detected on very different parts of the detector. However, the following scheme was devised with which to categorize X-ray bright and X-ray faint galaxies;

1) An object with narrow emission lines and where the $[O_{II}]_{3727}$ line is larger than the $[O_{III}]_{5007}$ line was assumed to be a cD emission line nebulae or a starburst galaxy.

2) Any object with broad emission lines was classed as an AGN.

3) Any object with narrow emission line but where $[O_{III}]_{5007}$ dominates over $[O_{II}]_{3727}$ was also classed as an AGN.

4) Any object with an extremely bright continuum without strong absorption or emission features was assumed to be a BL Lac. object.

The AGN and BL Lac.'s identified this way are flagged as "AGN" in column 4 of table B.1, whereas the X-ray faint emission line galaxies are simply flagged "Galaxy" in that column. These classifications are used in § 4.1 & 4.2 to identify the underlying X-ray source behind each of our cluster candidates. In figure 3.6 several examples are shown of spectra obtained from AGN and X-ray faint emission line galaxies.

3.6.4 AGN Hidden by the Limited Wavelength Range

The limited wavelength range of the spectroscopic observations means that $[O_{II}]_{3727}$ is the only detectable emission line for $z \geq 0.11$ starburst and giant elliptical galaxies. Unfortunately, unless less common emission lines such as H_δ & H_γ are present, this is also true for AGN. Therefore, it is not possible for us to thoroughly discriminate between starburst and active galaxies at $z > 0.11$.

There are a total of 31 galaxies listed in table B.1 with $z > 0.11$ that show $[O_{II}]_{3727}$ emission. Three of these are already flagged as AGN by virtue of other identified emission lines. However, the rest show no other emission lines and have been identified as X-ray faint emission line galaxies. Of these, eight show only $[O_{II}]$ emission whilst the other 20 show $[O_{II}]$ plus absorption features. We can test the significance to which we can trust the identification of these 28 $z > 0.11$ objects as X-ray faint galaxies by making

a comparison with the 32 lower redshift galaxies that show [O II] emission. Of these 32 low z, [O II] emission line galaxies, 55% are AGN. A subset of these 32 galaxies show both [O II] emission and absorption features. Among this subset, only 30% have been classified as AGN. Therefore, we can make the following predictions; a) approximately 17 of the 31 $z > 0.11$ [O II] galaxies have hidden AGN optical emission lines and b) most of these 17 will not feature absorption lines. Three of these $\simeq$ 17 galaxies have already been identified as AGN in table B.1. Therefore, $\simeq$ 14 objects classified as "Galaxy" in column 4 of table B.1 are misidentified AGN. The effect of these misidentifications on SGP RASS cluster lists is discussed in § 4.1.1.

3.7 Summary

In this chapter we have described the observing and reduction methods employed during the spectroscopic follow-up of SGP RASS cluster candidates. These methods have resulted in typical galaxy redshift errors, $\delta z \simeq 10^{-4}$, that are negligible in comparison to cluster velocity dispersions. The spectral information gained from 311 objects that surround 133 candidates is summarized in table B.1. Every line of this table represents the spectral information from a different object. We have attempted to classify the observed emission line galaxies as AGN or X-ray faint galaxies and these classifications are listed in column 4 of table B.1. Objects that lie inside the X-ray error circle are marked by a $\bigcirc$ in column 5. (If only a single object was found in the error circle, that object is marked by a $\odot$). Objects that resembled a cD galaxy, based on their appearance on the UKST plates, are flagged as such in column 6. Note that the cD flag is only meant as a guide, and not as a thorough classification of these galaxies. In chapter 4, the information gained from the spectroscopic follow-up is combined with cluster data available in the literature to produce a redshift sample of SGP RASS clusters. Possible improvements to the object classification scheme and to the spectroscopic follow-up in general are described in chapter 6.

3.7.1 Example Spectra

We present here 18 spectra obtained during the spectroscopic follow-up that have been produced using the REDSHIFT programme, § 3.5.1. Representative spectra from each detector and spectral type are shown, as described in table 3.9. The manually determined redshift for these spectra, where available, is given in the top right corner of each plot. If solid curves are plotted above the raw data, these represent smoothing of that data by the number of pixels listed in table 3.9, column 6. Note that the objects associated with spectra $1 \rightarrow 16$ are identifiable in table B.1, via a cross reference in column 4.

Spectrum	MASOL no.	Instrument	Date	Object type & Notes	Smoothing
1	0094217	Tek-RGO	1992	Galaxy spectrum @ z=0.044†	2 pixel
2	0813010	IPCS	1991	Galaxy spectrum @ z=0.081†	3 pixel
3	0813023	Tek-RGO	1993	Galaxy spectrum @ z=0.263†	2 pixel
4	0723084	RPCS	1992	Galaxy spectrum @ z=0.122†	2 pixel
5	0184049	RPCS	1992	Low S/N galaxy spectrum†	2 pixel
6	0683081	Tek-RGO	1992	Low S/N galaxy spectrum†	2 pixel
7	0703077	Tek-RGO	1993	Starburst galaxy with emission lines†	2 pixel
8	0753011	IPCS	1991	cD galaxy with emission lines†	3 pixel
9	0104188	Tek-RGO	1993	AGN with narrow emission lines‡	-
10	0803007	Tek-RGO	1993	AGN with broad emission lines‡	-
11	0822162	Tek-RGO	1993	AGN with narrow lines, plus absorption features‡	-
12	0833006	Tek-RGO	1992	AGN with broad and narrow emission lines‡	-
13	0723053	Tek-RGO	1992	BL Lac. (strong continuum with weak features)‡	2 pixel
14	0753060	Tek-RGO	1992	BL Lac. (strong featureless continuum)‡	2 pixel
15	0124051	Tek-RGO	1992	White dwarf star‡	-
16	0683081	Tek-RGO	1992	Regular star inside X-ray error circle†	2 pixel
17	HD92588	IPCS	1991	Radial standard stellar template	3 pixel
18	NGC5921	Tek-RGO	1992	Galaxy template with known 21 cm redshift	2 pixel

† these objects have not been identified as the RASS source.
‡ these objects have been identified as the RASS source.

Table 3.9: Description of the 18 spectra presented in figure 3.6.

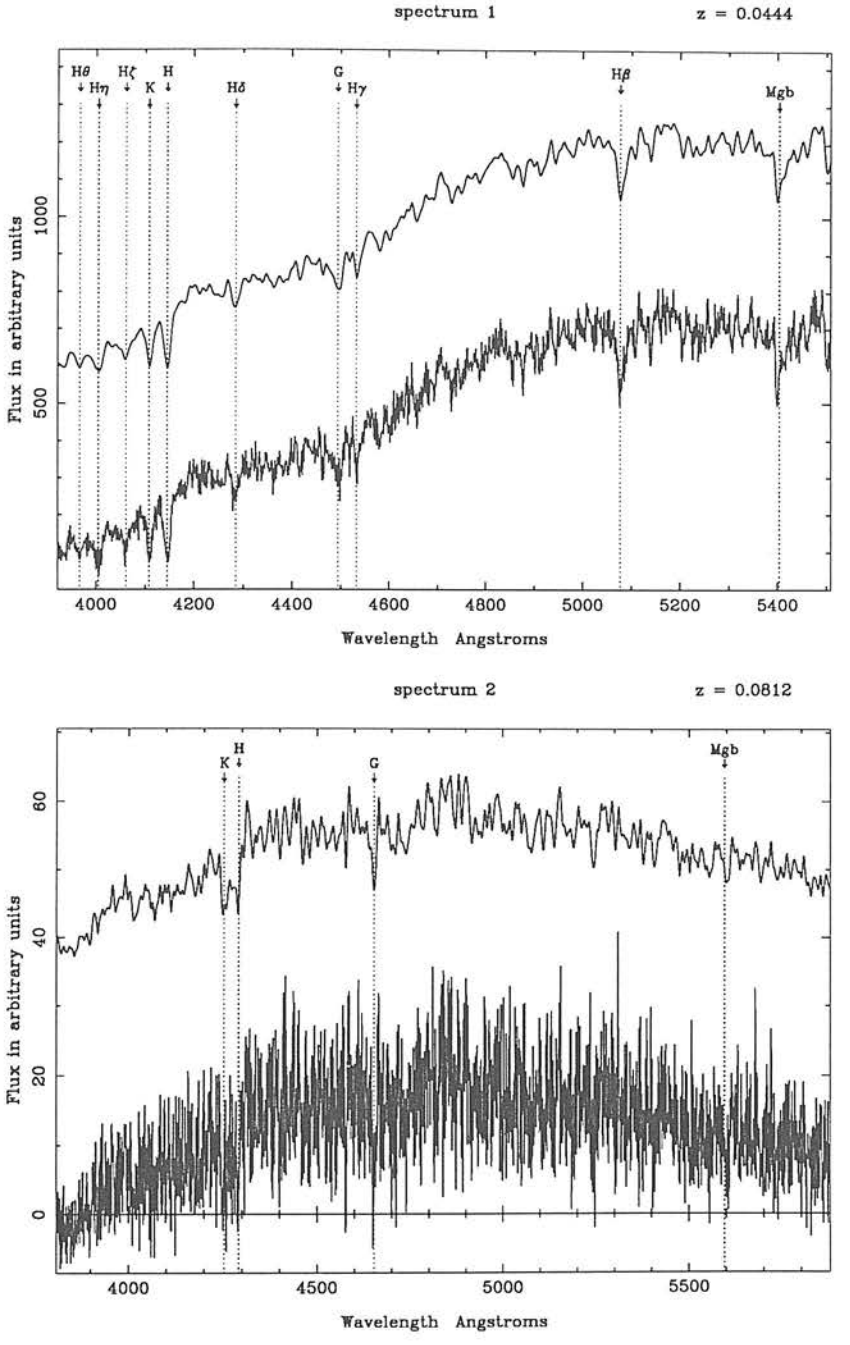

Figure 3~~7~~: Spectra 1 and 2; example galaxy spectra from the Tek-RGO (1) and the IPCS (2).

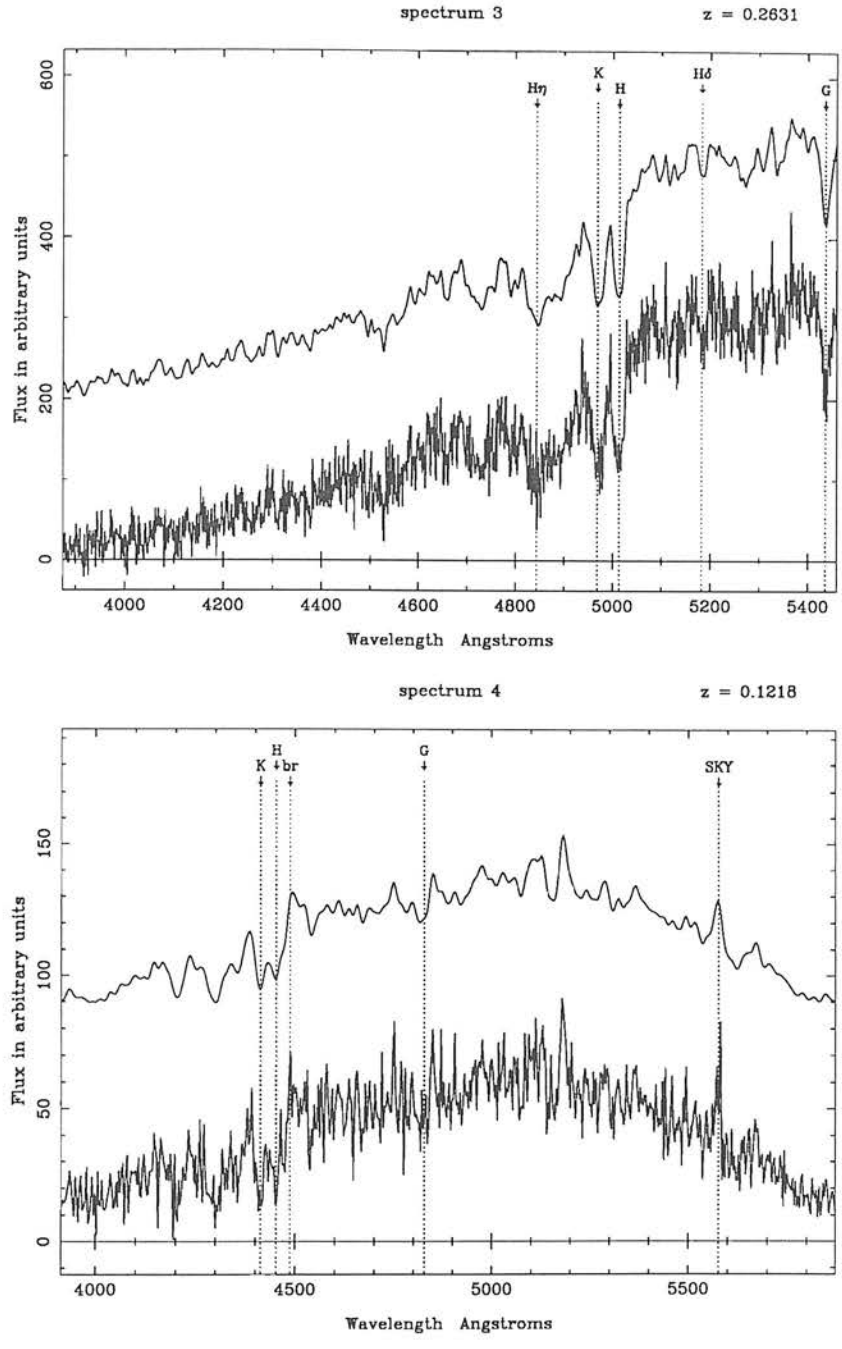

Figure 3.7: (*continued*) Spectra 3 and 4; example galaxy spectra from the Tek-RGO (3) and the RPCS (4).

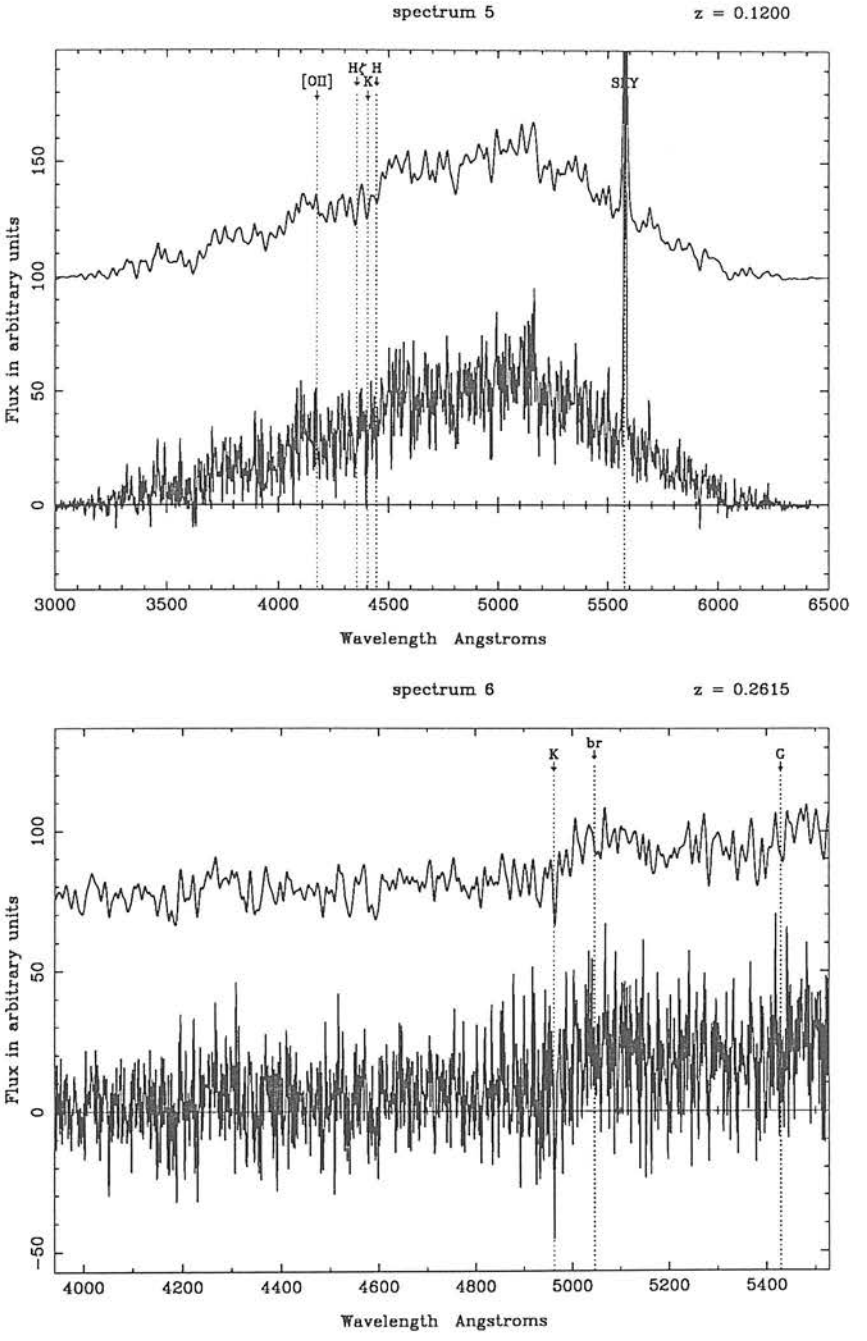

Figure 3.7: (*continued*) Spectra 5 and 6; example low signal to noise galaxy spectra from the RPCS (5) and the Tek-RGO (6).

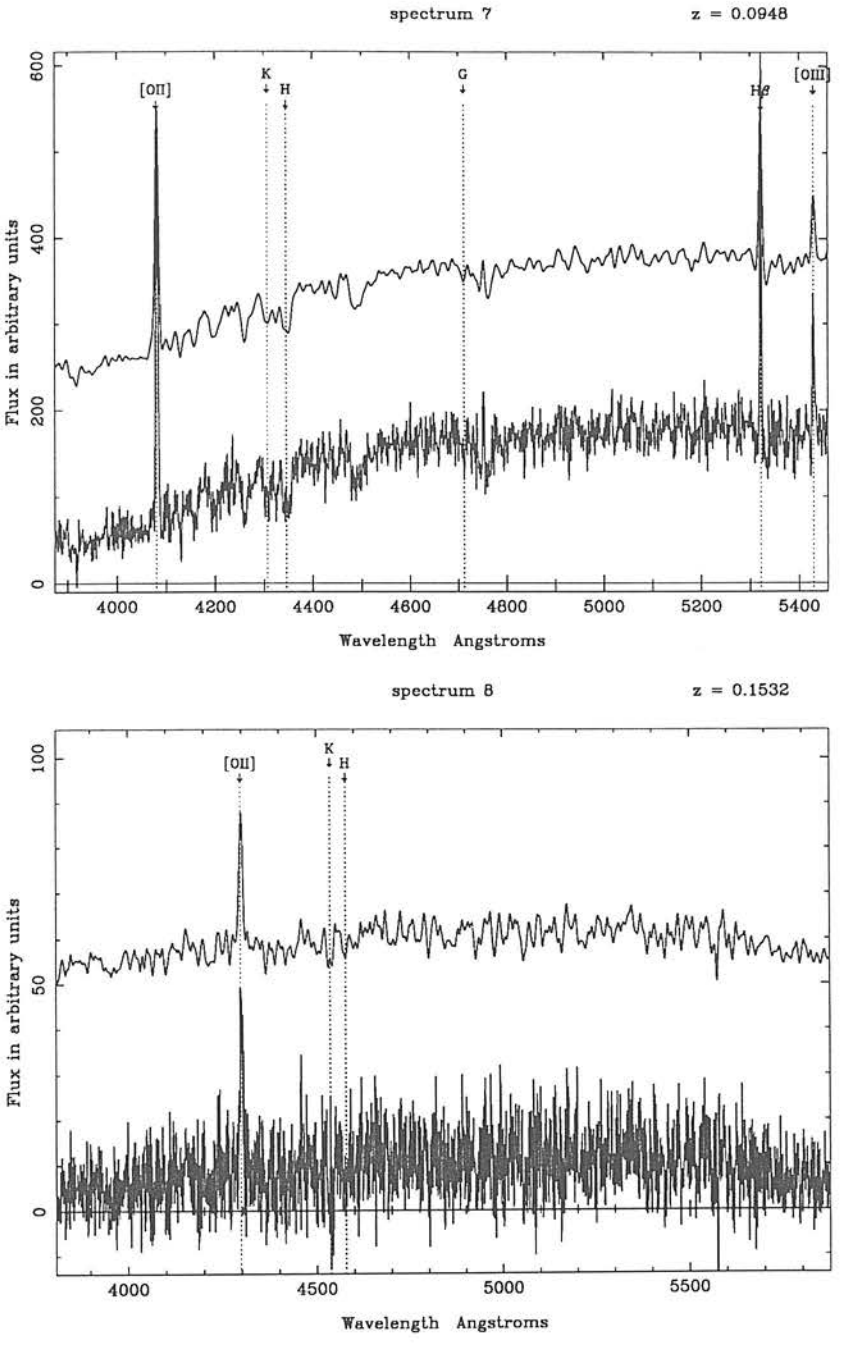

Figure 3.7 (*continued*) Spectra 7 and 8; example emission line galaxy spectra from the Tek-RGO (7) and the IPCS (8).

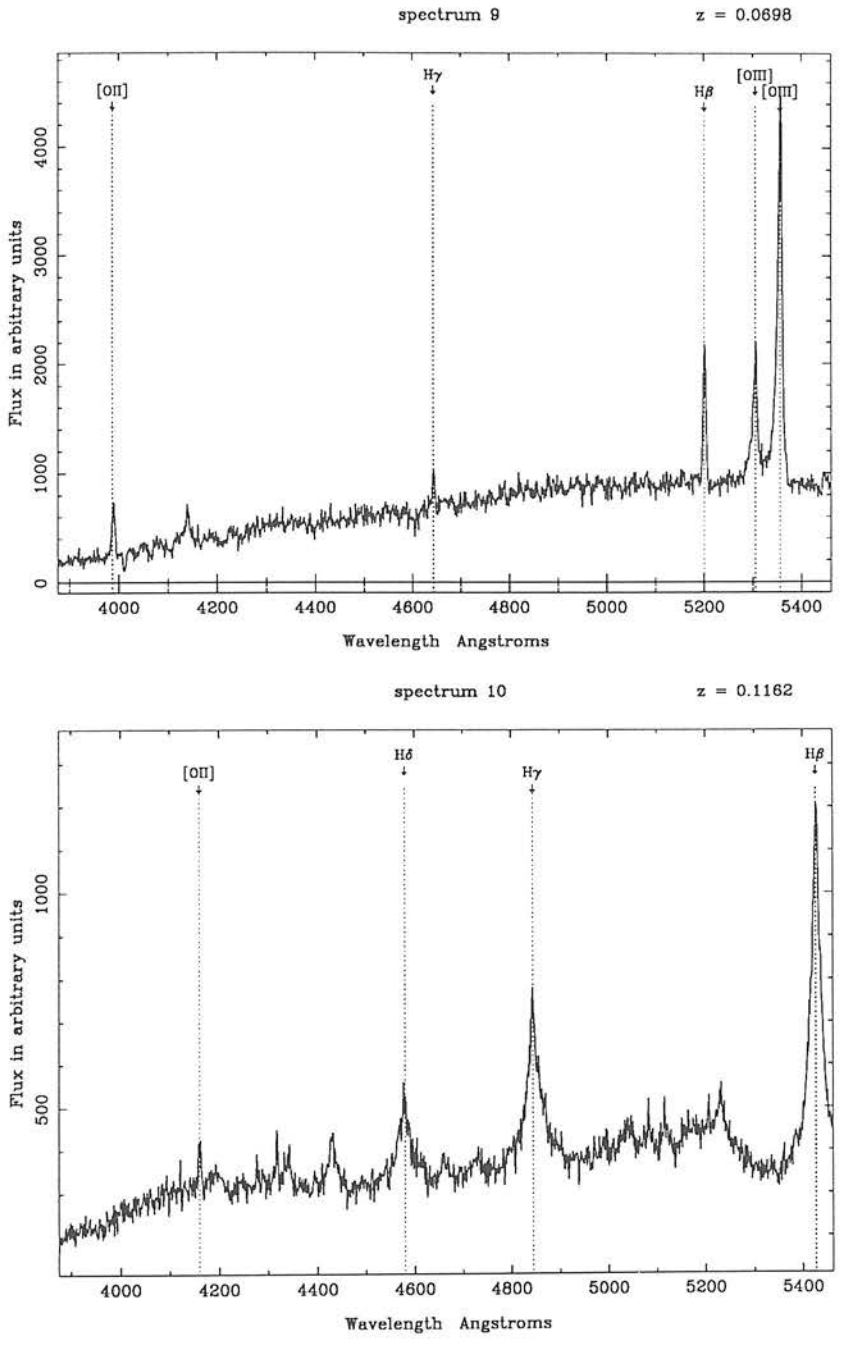

Figure 3.7: (*continued*) Spectra 9 and 10; example AGN spectra taken with the Tek-RGO.

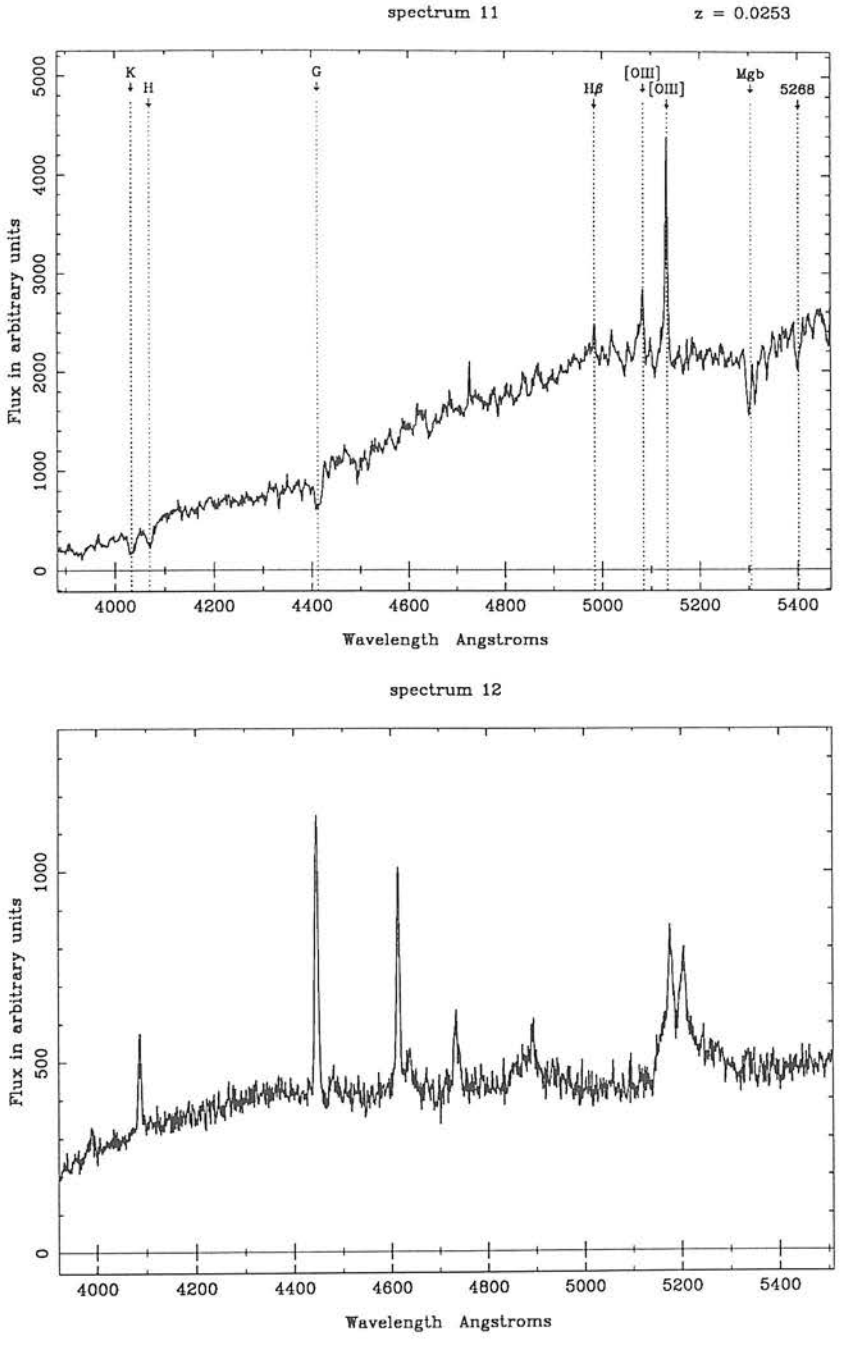

Figure 3.7: (*continued*) Spectra 11 and 12; example AGN spectra taken with the Tek-RGO.

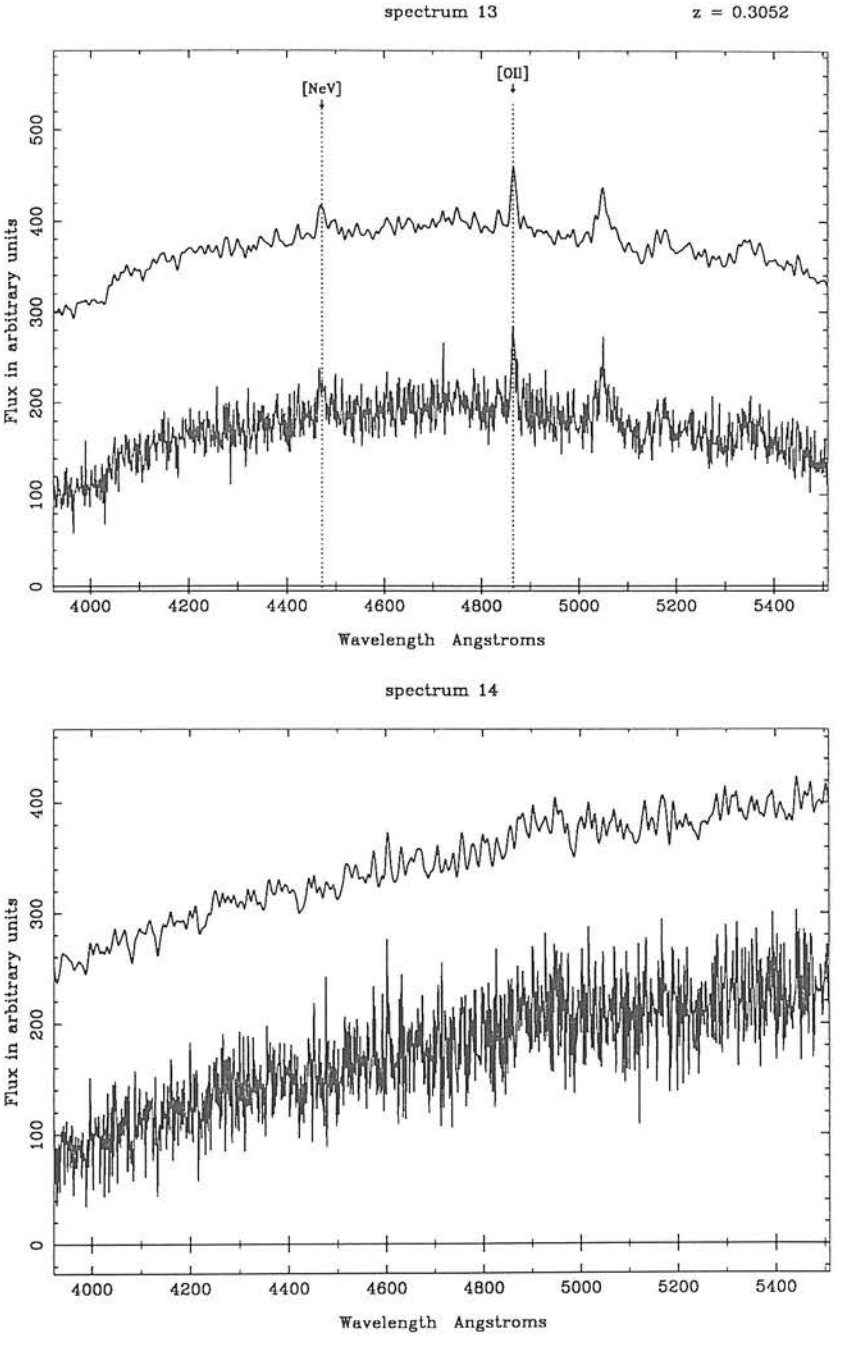

Figure 3.7: (*continued*) Spectra 13 and 14; example BL Lac. spectra taken with the Tek-RGO.

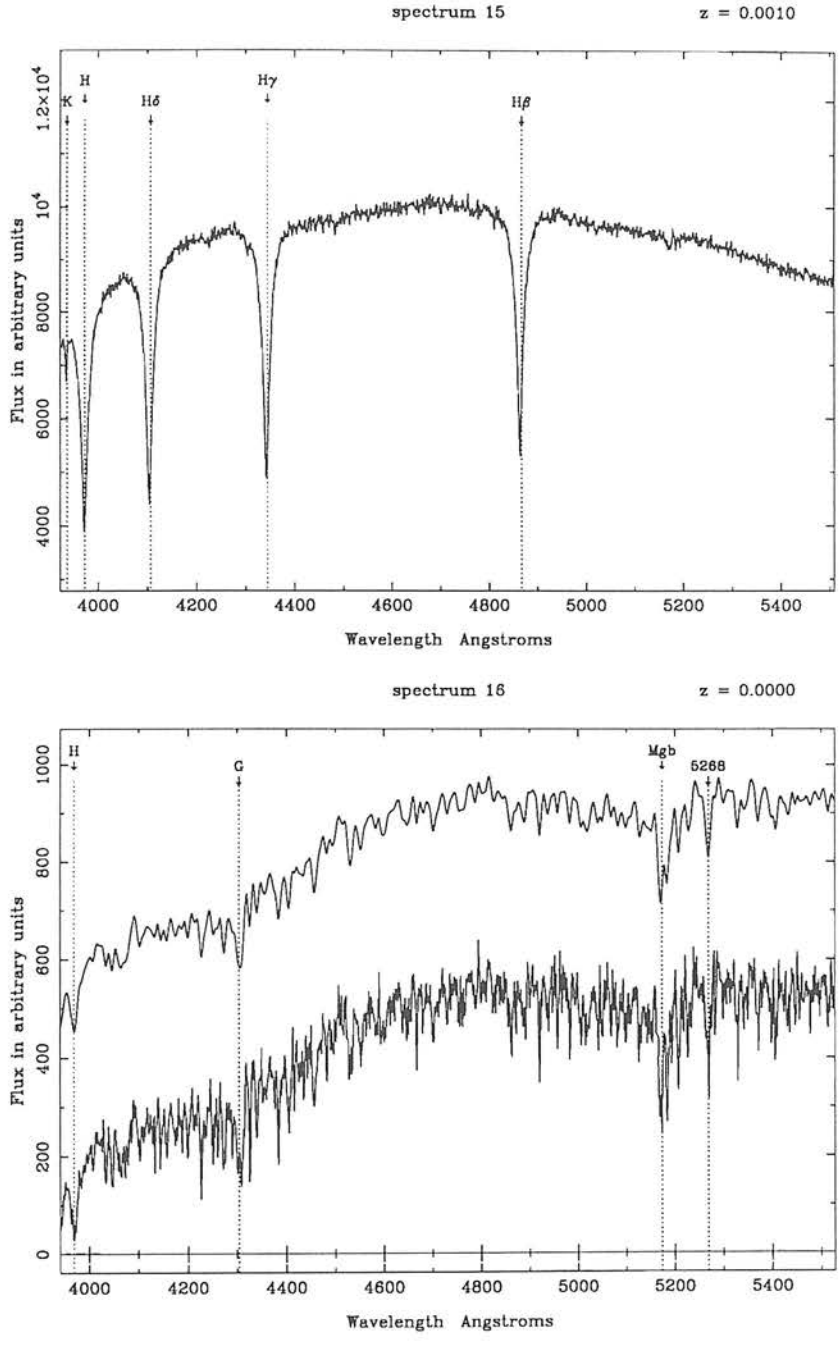

Figure 3.7: (*continued*) Spectra 15 and 16; example stellar spectra taken with the Tek-RGO.

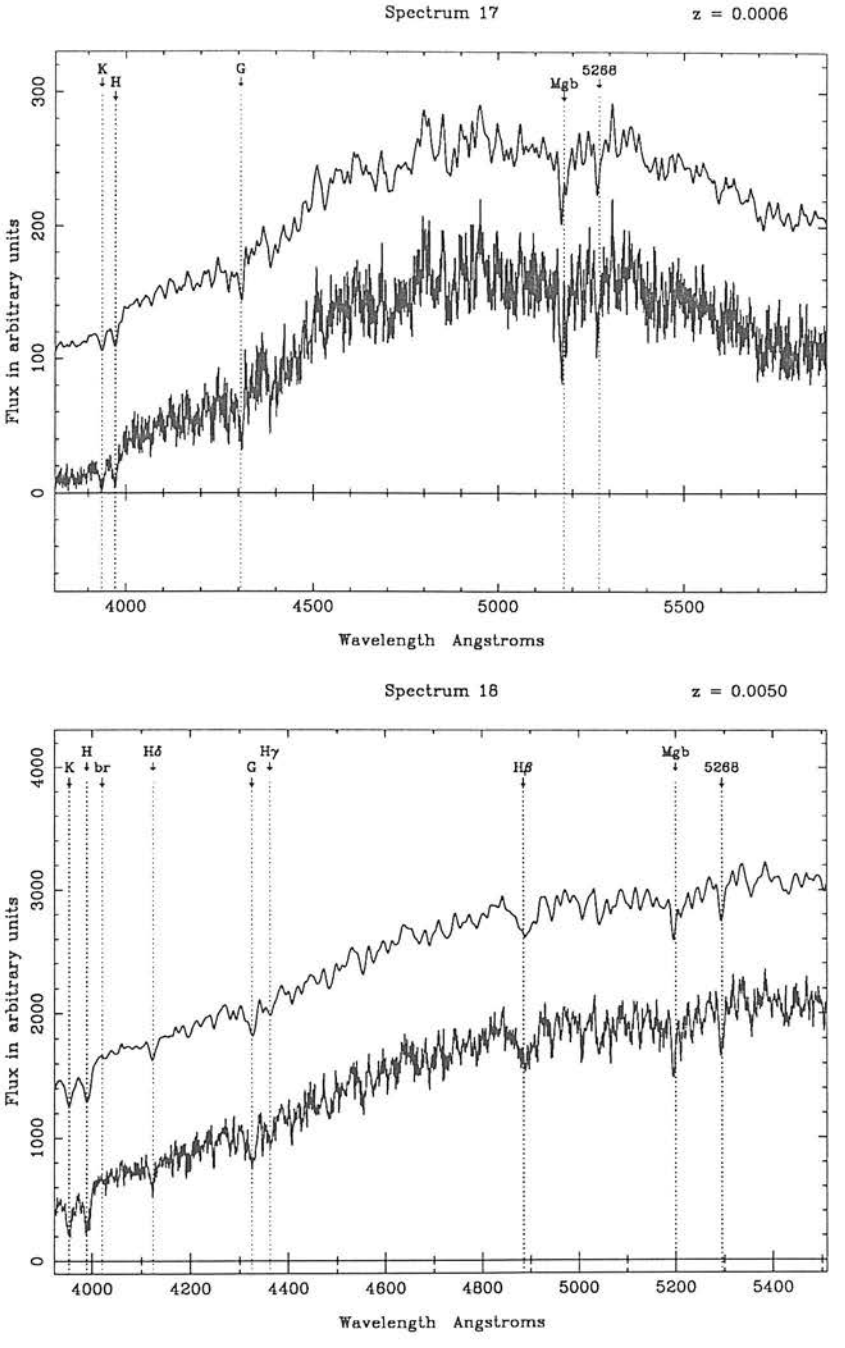

Figure 3.7: (*continued*) Spectra 17 and 18; example template spectra used in the XCORR redshift determination, taken with the IPCS (17, stellar) and the Tek-RGO (18, galaxy).

Chapter 4

The SGP RASS Cluster Sample

This chapter is concerned with the construction of the SGP RASS Cluster Sample (SRCS). The SRCS constitutes a sample of 154 SGP RASS clusters, complete with redshifts, that have been identified, to date, during the course of the SGP RASS Cluster Project. The SRCS clusters form a subset of the 345 cluster candidates presented in table A.2. The respective candidates were confirmed as clusters using a combination of the results from the spectroscopic follow-up, chapter 3, and optical cluster redshifts available in the literature. Another 36 candidates have been identified as contaminating objects, *i.e.* stars and AGN. The processes by which candidates were classified as clusters or contaminating objects are described in § 4.1 and § 4.2 respectively. Many of the candidates referred to in these sections have been illustrated, via their CUOC finding charts, in appendix C. The methods by which redshifts were assigned to the 154 SRCS clusters are also described in § 4.1. The X-ray and optical properties of the SRCS are discussed in § 4.4. Eleven subsamples of the SRCS, which represent differing selection methods and flux limits, are introduced in § 4.6. The spatial correlation function of these subsamples is presented in chapter 5.

4.1 Cluster Redshifts and Classifications

4.1.1 Cluster Redshifts from the Spectroscopic Follow-Up

By process of elimination, any candidate observed during the spectroscopic follow-up and not flagged as a contaminating object, §4.2.3, was assumed to be an X-ray cluster. In total, 98 candidates were classified as clusters in this way. Redshifts for these 98 clusters were determined by using the respective galaxy redshifts presented in table B.1. A mean of the galaxy redshifts obtained around each candidate was taken to be the cluster redshift. Observations of certain objects were not used to derive this mean and these are indicated with a $*$ in table B.1. (Such objects include foreground stars, galaxies with inaccurate redshift measurements *etc.*) Note that when XCORR and manually

MASOL no.	z_{SF}	n_{gal}^{SF}	optical id.	z_{lit}	n_{gal}^{lit}
0733023	0.0681	2	S 987	0.0693	20
0763040	0.3125	1	S1077	0.3169	42
0792131	0.0921	3	A2440	0.0912	24
0813011	0.1082	2	A2554	0.1117	29

Table 4.1: Details of 4 SRCS clusters with both SF and n_{gal}^{SF} literature redshifts, which were used to estimate the error on the SF redshifts.

determined redshifts were both available for a certain galaxy, the manually determined redshifts were not used to determine the cluster redshift, unless marked otherwise by a †, see § 3.5.6. The mean cluster redshift and the number of galaxy redshifts used to derive it, n_{gal}^{SF}, are listed in table A.2, columns 9 & 10. Hereafter we refer to cluster redshifts obtained during the spectroscopic follow-up as 'SF redshifts', to avoid confusion with cluster redshifts taken from the literature.

We have estimated the error on the SF cluster redshifts using four clusters for which accurate redshifts exist in the literature. The literature redshifts, z_{lit}, were determined using at least 20 galaxies and are compared to our redshift determinations, z_{SF}, in table 4.1. The range in redshift discrepancy ($z_{lit} - z_{SF}$) for these four clusters is $300\,\mathrm{km\,s^{-1}} \rightarrow 1300\,\mathrm{km\,s^{-1}}$. Not surprisingly, the largest discrepancy comes from a SF redshift based on only one galaxy redshift. These values are compatible with the observed range in cluster velocity dispersion; median value $\sigma_v = 744\,\mathrm{km\,s^{-1}}$ and maximum value $\sigma_v = 1330\,\mathrm{km\,s^{-1}}$ (Zabludoff *et al.* 1990). We, therefore, estimate that the typical error on the SF cluster redshifts presented in table A.2, column 9 is $\approx 1000\,\mathrm{km\,s^{-1}}$. In all but six cases, the galaxy redshifts used to find the cluster redshift were in agreement to less than this error margin. However, for the clusters corresponding to MASOL sources 0034057, 0104188 (figure C.10), 0733059, 0773037, 0863044 (figure C.33) & 0903036, the galaxy redshifts were more discrepant. The reason for the redshift spread in these cases could be the result of either; a) inaccurate galaxy redshifts, b) projection effects or c) sub-clustering. A possible example of the latter case is Abell cluster 2686, candidate 0863044, which is a known binary cluster[1], such clusters are known to have prevalent sub-clustering, *e.g.* Briel *et al.* (1991).

There are eleven candidates for which the identification as a cluster remains speculative. In these cases a $z \gtrsim 0.11$ emission line galaxy lay within the confines of the X-ray error circle. It was shown in § 3.6.4 that 55% of such galaxies may be AGN that were

[1]Binary clusters are dominated by two galaxies of roughly equal magnitude.

not readily identifiable because most of their emission lines were redshifted out of the observing window. As a result these 11 "clusters" have been assigned to cluster type 4, § 4.1.3, which indicates that the identification remains provisional. Another borderline case, 0144092, figure C.14, was assigned to cluster type 3. In this case, the source was identified with a $z = 0.2323$ cluster ($n_{gal}^{SF} = 3$), but an emission line, $z = 1.106$, galaxy was also found inside the X-ray error circle.

There are 30 candidates in table A.2 for which the cluster redshift has been derived from a single galaxy. In nine cases there is evidence from the literature and/or from the spectroscopic follow-up[2] that the galaxy does indeed lie inside a cluster, in which case the cluster redshifts derived from it will be inaccurate to $\lesssim v = 1000\,\mathrm{km\,s^{-1}}$. However, in the other 21 cases it is impossible to judge whether that galaxy lies in the cluster or not. In addition the identification of the candidate as a cluster must remain tentative if a) there are objects inside the X-ray error circle without spectra or b) the observed galaxy shows emission lines and lies at $z > 0.11$. In either case, the true candidate identification could be an AGN. The 30 $n_{gal}^{SF} = 1$ clusters were given a variety of classification flags, as described in §4.1.3.

In summary, we have identified 98 of the candidates in table A.2 as clusters based on the observations made during the spectroscopic follow-up. These clusters are referred to hereafter as "spectroscopically confirmed clusters". Redshifts have been assigned to these clusters by taking the mean of the available galaxy redshifts, unless those redshifts are inaccurate or relate to foreground or background objects. The typical error on the cluster redshifts is of the same order as measured cluster velocity dispersions, $\delta v = 1000\,\mathrm{km\,s^{-1}}$. In general, we assume that we can measure the redshift of an X-ray cluster to within that error, if 2 or more concurring galaxy redshifts are available. For candidates in which emission line $z > 0.11$ galaxies lie inside the X-ray error circle, we expect that up to 55% of the identifications (as clusters) are in error.

4.1.2 Cluster Redshifts taken from the Literature

Candidates in table A.2 for which redshift information was available in the literature were identified by performing separation analyses with three optical cluster samples described in § 1.3.1; Abell clusters (Abell 1958, ACO), EDCC clusters (Lumsden *et al.* 1992) and APM clusters (Dalton *et al.* 1992). The separation analyses were performed by Ebeling at MPE in the same manner as described in § 2.1.3. Redshifts were available in the literature for 83 of the optical clusters associated with SGP cluster candidates. The redshift information was taken mainly from the Andernach *et al.* (private

[2]From additional, inaccurate, galaxy redshifts that were not used to determine the cluster redshift.

MASOL id.	Abell id.	redshift	n_{gal}^{lit}	source	redshift	n_{gal}^{lit}	source
0014055	A 2911	0.0205	4	Z-CAT	0.0796†	8	Andernach
0034049	A 2988	0.0649	?	Z-CAT	0.1150	?	Andernach
0034122	A 284	0.0635	5	Z-CAT	0.0562†	9	Andernach
0723060	A 3854	0.1214	?	Z-CAT	0.1503†	33	Andernach
0803046	A 2764	0.0710	4	Z-CAT	0.0647†	3	Andernach
0873061	A 22	0.1432	1	Z-CAT	0.0634†	5	Andernach
0903078	A 2829	0.0510	2	APM	0.1000†	11	Andernach

Table 4.2: Details of 7 optical clusters for which redshifts estimates disagree in the literature. A ? indicates that of value of n_{gal}^{lit} is unavailable. A † indicates which redshift value was adopted in table A.2.

communication) compilation of Abell cluster redshifts. Additional information was taken from Z-CAT[3] (Huchra *et al.* , private communication), Nichol (1992), Dalton (1992) and Crawford *et al.* (1994). The cluster redshift, the number of galaxy redshift used to derive that redshift (n_{gal}^{lit}), the optical cluster identification and the separation between the optical cluster and the ROSAT position are listed in columns 11 → 14 of table A.2. Note that there are a total of 151 associations between SGP RASS cluster candidates and Abell clusters and these associated are listed in table A.2 regardless of whether that Abell cluster has a z_{lit} or not.

A key, see table A.1 to the source of the redshift information in each case is given as a superscript in column 11. If more than one redshift value was available in the literature for a certain cluster, we adopted the value with the highest, n_{gal}^{lit}. Among the clusters with more than one independent literature redshift, there were 7 cases in which the redshifts were discrepant by more than $\delta v = 1000\,\mathrm{km\,s^{-1}}$. These cases are listed in table 4.2 and a † marks the adopted redshift. Note that in the case of Abell 2988 (ROSAT source 0034049) neither redshift was used.

The value of n_{gal}^{lit} varied considerably among the 83 literature cluster redshifts, as demonstrated by table 4.3. In this table, the distribution of n_{gal}^{lit} is listed for a) 27 cases where spectroscopically confirmed clusters are associated with optical $n_{gal}^{lit} \geq 1$ clusters ["lit. + SF", column 3] and b) 56 cases where $n_{gal}^{lit} \geq 1$, but the corresponding candidate was not observed during the spectroscopic follow-up ["lit. only", column 2]. In the 27 cases where both SF and literature redshifts were available, the redshift value adopted for the purposes of correlation function studies is marked in table A.2 with the symbol $*$. For example, if the literature and SF redshifts were in agreement, *i.e.* less than a typical cluster velocity dispersion ($\delta v \lesssim 1000\,\mathrm{km\,s^{-1}}$), then it was assumed the redshift based on

[3]Z-CAT is an electronic listing of the two Abell catalogues which included all cluster redshifts obtained during the CfA surveys, *e.g.* Huchra *et al.* (1990), as well as a literature compilation.

n_{gal}^{lit}	lit. only	lit. + SF
$n \leq 2$	11	16
$2 < n \leq 5$	9	6
$5 < n \leq 10$	12	1
$10 < n \leq 20$	10	1
$n > 20$	14	3
total	56	27

Table 4.3: Distribution of the number of galaxies, n_{gal}^{lit}, used to determine redshifts for optical clusters associated with SGP RASS cluster candidates. The distribution is listed separately for the 56 clusters not observed (column 2) and for the 27 clusters which were observed (column 3) during the spectroscopic follow-up.

the highest n_{gal} value was the more accurate, (*e.g.* 0014072, figure C.1). Alternatively if the two values disagreed (*e.g.* 0074105, figure C.5), or if the $n_{gal}^{lit} = n_{gal}^{SF}$, then the SF redshift was adopted, because this redshift was obtained using galaxies known to be close to the X-ray position.

The literature and SF redshifts for these 27 clusters are shown in figure 4.1. In figure 4.2 the residuals of ($|z_{lit} - z_{SF}|$) are shown as function of separation between the optical catalogue and RASS positions. It can be seen from figures 4.1 & 4.2, that there are three cases where the literature and SF redshift measurements are in significant disagreement. For these three cases, the MASOL number, optical cluster identification, redshift discrepancy, values of n_{gal}^{lit} & n_{gal}^{SF} and the separation between the optical and X-ray positions are given in table 4.4. Notice that the value of n_{gal}^{lit} is ≤ 2 in each case and the broad range in optical to X-ray separations; $37'' < \Delta_{sep} < 161''$. Based on these results we have made the following judgements regarding the use of literature redshifts; 1) Approximately 20% of the literature clusters redshifts based on $n_{gal}^{lit} \leq 2$ are in error. 2) The separation between optical and X-ray centre cannot be used to determine the reliability of the literature redshift information.

The other 56, "lit. only", candidates were assumed to be clusters and have been assigned redshifts from the literature. From the discussion above, we assume that ≈ 2 of these 56 literature redshifts are incorrect. (Where $2 \simeq 0.2 \times 11$, and 11 is the number of $n_{gal}^{lit} \leq 2, n_{gal}^{SF} = 0$ clusters, see table 4.3.) However, in the absence of spectral information the cluster identifications remain unconfirmed. We have attempted to assess the errors associated with these identifications using; a) the data in the CUOC (§ 2.2) and b) the results from the spectroscopic follow-up.

We have compared (by eye) the CUOC finding charts, *e.g.* those featured in appendix

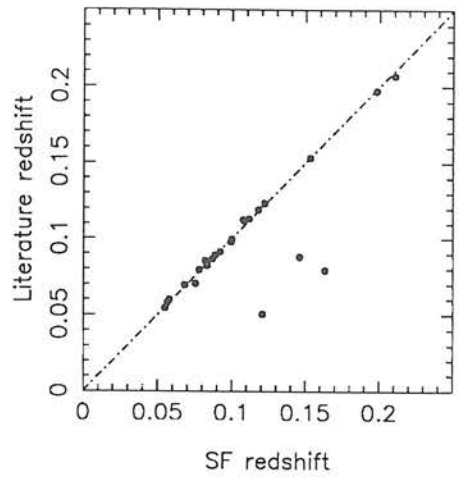

Figure 4.1: Comparison of literature and SF redshift values for 27 SRCS clusters. The line of $z_{lit} = z_{SF}$ is also shown.

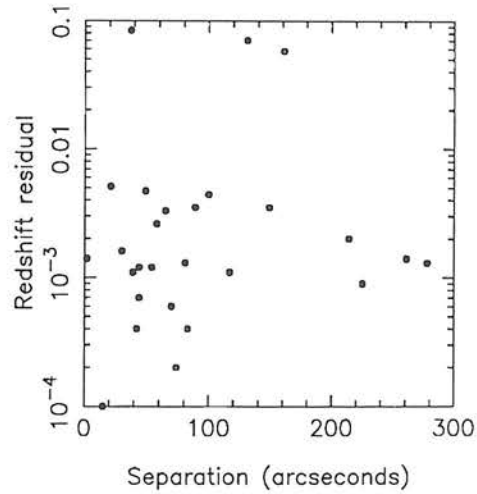

Figure 4.2: Difference between literature and SF redshifts, $|z_{lit} - z_{SF}|$, for 27 SRCS clusters as a function of separation between optical cluster and RASS source positions.

MASOL no.	Abell no.	Δz	n_{gal}^{lit}	n_{gal}^{SF}	Δ''
0074105	A 199	0.0579	0	1	161
0144162	A 286	0.0841	1	1	37
0723084	S1066	0.0701	2	3	131

Table 4.4: Details of 3 SRCS clusters for which the literature and SF redshifts disagree. The discrepancy in the redshifts is listed in column 3, the number of galaxies used to derive each redshift in columns 4 & 5 and the separation in arcseconds between the optical cluster and RASS source positions in column 6.

C, for spectroscopically confirmed clusters and contaminating objects and looked for trends that could distinguish these types of X-ray sources in the absence of spectroscopy. It was found that when the X-ray error circle around a candidate position contained only a single object in the CUOC, the chance that the candidate was a cluster decreased significantly. Of the 36 candidates that were rejected from the candidate list, 28 had a single object in the X-ray error circle, 22 of these being AGN, the rest being stars. In comparison, among the spectroscopically confirmed clusters in table A.2, only 17% had a single object (a galaxy) inside the X-ray error circle. We predict that, in the absence of spectral information, the identification of a candidate with a cluster will be in error at the $\approx$ 55% level, if that candidate's X-ray error circle contains a single galaxy . This prediction is based on the ratio of AGN to normal galaxies (22:17) among the optically identified, centrally dominant galaxies. Of the 56 "lit. only" candidates, there are 7 which feature a single, central galaxy. Although these 7 candidates have still been classified as clusters, they have been given classification flags, §4.1.3, that demonstrate that additional spectroscopic information would be required to make a definitive identification (*e.g.* 0723060 & 0903060 figures C.18 & C.38).

In the other 49 "lit. only" cases, we have estimated that $\approx$ 7% of the candidates are not clusters. This estimate is based on the fact that, of 123 candidates associated with Abell clusters that were studied during the spectroscopic follow-up, 6 were shown to be contaminating objects and 2 were not identified. As the projected margin of error in the candidate identification is so low in these cases, we have chosen to classify these clusters only according to the quality of their respective redshift information.

In summary, there are 83 SGP RASS candidates in our flux-limited sample that are associated with optical clusters for which redshifts exist in the literature. These redshifts have a $\approx$ 20% chance of being in error if only 1 or 2 galaxies were used to derive them. We have identified 56 candidates, for which spectroscopy is not available, as X-ray clusters and have assigned redshifts to them on the basis of their association with optical clusters.

Seven of these identifications remain provisional as their respective X-ray error circles contain only a single galaxy, which has been shown to indicate the presence of an AGN in 55% of cases.

4.1.3 Classification Scheme

By combining the spectroscopic data with cluster redshifts in the literature we have been able to assign cluster redshifts to a total of 154 of the cluster candidates listed in table A.2. From the discussions above, it is apparent that at least some of these candidates may not be clusters. In addition, there are cases where the assumed cluster redshift is inaccurate. As a reflection these problems, the 154 clusters have been flagged according to a) the certainty of the candidate identification and b) the accuracy of the cluster redshift. There are four categories of cluster classification, types $1 \rightarrow 4$, where type 1 indicates a solid identification with reliable redshift information and where type 4 indicates a tentative identification and/or redshift. Despite the obvious subjectivity of these classifications, they are included in table A.2 aid other groups who may wish to use the ROSAT SGP Cluster sample in future. The basic premises on which each classification class was based are described below.

Type 1 clusters: Among the 154 clusters in table A.2, 90 have been assigned to category 1, reflecting the fact that they have secure identifications and reliable redshifts *e.g.* 0823080, 0813014, 0753052, 0893097, figures C.28, C.27, C.24, C.36 respectively. In these cases there is no reason to doubt that a) the RASS source originates in a cluster and b) the dominant X-ray source in that cluster is the hot intracluster gas and not any X-ray emitting galaxies found therein. To be included in this cluster category, the candidates had to meet either of the following criteria;

- From the spectroscopic follow-up; a) $n_{gal}^{SF} \geq 2$, b) the galaxy redshifts differed by less than $\delta v = 1000\,\mathrm{km\,s^{-1}}$ and c) evidence that there are no X-ray bright point sources within the error circle.
- From the literature; $n_{gal}^{lit} \geq 3$ and an X-ray error circle containing more than one object.

Type 2 clusters: There are 12 candidates in table A.2 which would require more spectroscopic information in order to make a definitive identification as a cluster, *e.g.* 0094217 & 0723060, figures C.9 & C.18. However, if the candidates *are* clusters, then we are confident that we have measured their redshifts accurately. Candidates that meet either of the following criteria were flagged as type 2 clusters;

- From the spectroscopic follow-up, $n_{gal}^{SF} \geq 2$, but none of the observed galaxies were closer than than $1'$ from the X-ray position. N.B. A study of the Schmidt plate must have also shown that there are no objects inside the error circle.

- From the literature; $n_{gal}^{lit} \geq 3$, but there is a single, cD type, galaxy in the X-ray error circle for which a spectrum does not exist.

Type 3 clusters: There are 38 candidates in table A.2 which were assigned to cluster category 3, *e.g.* 0104188, 0144092 & 0733059, figures C.10, C.14 & C.19. One of these candidates, 0144092, was described above, §4.1.1, the others met at least one of the following criteria;

- From the spectroscopic follow-up; $n_{gal}^{SF} = 1$, excluding $z > 0.11$ emission line galaxies.

- From the spectroscopic follow-up; the galaxy redshifts used to determine the cluster redshift were discrepant by more than $\delta v = 1000\,\mathrm{km\,s^{-1}}$.

- From the literature; $n_{gal}^{lit} \leq 2$.

- From the literature; $n_{gal}^{lit} \geq 3$, but the candidate has a centrally dominant galaxy which resembles an AGN on the Schmidt plate.

Flag 4 clusters: There are 14 candidates (*e.g.* 0174111 & 0843100, figures C.17 & C.29) in table A.2 for which their identity as X-ray clusters must remain provisional for any of the following reasons;

- From the spectroscopic follow-up; a $z > 0.1$ emission line galaxy falls inside the X-ray error circle.

- From the spectroscopic follow-up; there is only 1 galaxy redshift available and this is inaccurate.

- From the spectroscopic follow-up; none of the observed galaxies were closer than $1'$ from the X-ray position and a study of the Schmidt plate has shown that there are objects inside the X-ray error circle.

4.2 Contaminating Objects

The specifications of the cluster candidate selection, § 2.3.2, were such that $\approx 15\%$ of the candidates listed in table A.2 were expected to be contaminating objects, *i.e.* X-ray bright stars and galaxies. We describe briefly below the X-ray properties of these

contaminating objects and introduce a scheme by which they can be excluded from the candidate list.

4.2.1 Galaxies

Almost all of the contamination in the cluster candidate list presented in table A.2 is from galaxies of some kind. The X-ray properties of various galaxy types are summarized below.

Spiral galaxies are extended and complex X-ray sources with total luminosities in the EINSTEIN band ($\sim 0.2 - 3.$ keV) of $\sim 10^{38} \rightarrow 10^{41}\,\mathrm{erg\,s^{-1}}$. It is thought that the collective emission from individual bright sources, such as accreting binaries and supernova remnants are responsible for spiral galaxy X-ray emission, Fabbiano (1989).

Starburst galaxies, § 3.6, have X-ray luminosities in the range $10^{39} \rightarrow 10^{42}\,\mathrm{erg\,s^{-1}}$ in the EINSTEIN band, Griffiths & Padovani (1990). The source of the X-ray emission is thought to be supernova remnants or massive young stars.

Elliptical and giant elliptical, § 3.6, galaxies are surrounded by a hot gaseous halo which emits thermal X-rays. The luminosity range for elliptical galaxies is $10^{39} \rightarrow 2 \times 10^{42}\,\mathrm{erg\,s^{-1}}$ in the EINSTEIN band (Fabbiano 1989, Ikebe *et al.* 1992).

Active galactic nuclei have X-ray luminosities in the EINSTEIN band of $5 \times 10^{42} \rightarrow 2 \times 10^{46}\,\mathrm{erg\,s^{-1}}$ (Comastri *et al.* 1992, Schwartz & Ku 1983). The nature of the AGN X-ray emission is uncertain, although it is widely believed that it might be associated with the activity induced by a central compact object, *e.g.* a massive black hole.

We have attempted to predict the effect of X-ray galaxies on the cluster candidate list by estimating ROSAT PSPC fluxes for each galaxy type as a function of redshift and intrinsic luminosity. Fluxes in the EINSTEIN energy band were calculated from the luminosities quoted above using equation 2.6. These EINSTEIN fluxes were then converted into ROSAT PSPC fluxes, using conversion factors presented in the *UK ROSAT Announcement of Opportunity* (1991). Figures 10.21 & 10.22 of that document were used to predict the fluxes of thermal and power-law sources respectively. We have calculated the maximum redshift at which a particular galaxy type will have a flux greater than our $\simeq 1 \times 10^{-12}\,\mathrm{erg\,s^{-1}}$ flux limit, and have listed these redshift values in table 4.5.

From table 4.5 it can be seen that spiral, starburst and regular elliptical galaxies have minimal effect on a flux limited cluster candidate list because they are comparatively weak X-ray sources, whose fluxes only exceed the flux-limit at low redshifts. Giant elliptical galaxies, on the other hand, may enter the candidate list at redshifts up to $z \simeq 0.06$. These $L_x \gtrsim 10^{42}\,\mathrm{erg\,s^{-1}}$ galaxies correspond to a subset of cD galaxies and are, consequently, found only in clusters, Fabbiano (1989). However, their presence in

Galaxy Type	Flux Conversion			Luminosity	Max. Redshift
	Emission	Parameter	Factor		
Spiral	Thermal	T> 3keV	2	1×10^{38} erg s^{-1}	0.0005
				1×10^{42} erg s^{-1}	0.0138
Starburst	Thermal	2 <T< 30keV	2	1×10^{39} erg s^{-1}	0.0014
				1×10^{42} erg s^{-1}	0.0460
Elliptical	Thermal	1 <T< 2 keV	2	1×10^{39} erg s^{-1}	0.0014
				2×10^{42} erg s^{-1}	0.0640
AGN	Power-law	$\alpha = 0.7$	1	5×10^{42} erg s^{-1}	0.0320
				1×10^{44} erg s^{-1}	0.3940
				2×10^{46} erg s^{-1}	-

Table 4.5: The maximum redshift (column 6) at which a galaxy of a certain type (column 1) and EINSTEIN luminosity (column 5) has a PSPC flux in excess of $\simeq 1 \times 10^{-12}$ erg s^{-1} cm^{-2}. The fluxes have been calculated using the conversion factors (column 4) presented in the *UK ROSAT Announcement of Opportunity* (1991). The conversion factors are dependent on spectral type and properties (columns 2 & 3).

a flux-limited sample of clusters still represents a contamination because they boost the flux of the cluster and make it harder to model the mass function of the sample. It would be impossible to distinguish between X-ray bright and X-ray faint cD galaxies in our clusters without detailed pointed observations. We have, therefore, assumed that the presence of X-ray bright cD galaxies will make only a second order effect on the statistical properties of a given X-ray cluster sample and have retained in our candidate list those sources associated with $z \lesssim 0.06$ cD galaxies. We recognise that this simplification may bias the cluster samples presented in §4.6 toward low luminosity systems at low redshift.

It can be seen from table 4.5 that contamination by AGN is a more serious concern. These objects can be up to $\sim 100\times$ brighter than an X-ray cluster and have PSPC fluxes that exceed $\gtrsim 1 \times 10^{-12}$ erg s^{-1} cm^{-2} even at high redshift. Therefore, it was decided to exclude from the cluster candidate list all sources that were close (within the confines of the 1σ X-ray error circle) to an optically confirmed AGN. This simple scheme may have been inappropriate for the following sources; 0084242, 0134162, 0144172 (figure C.15), 0763011, 0803007, 0873078 (figure C.34), 0893034 & 0903046 (figure C.37), where the RASS source appears to be associated with both an AGN and a cluster[4]. In principle the flux due to the intracluster gas can be calculated by subtracting the AGN contribution. However, this type of analysis is beyond the scope of the RASS data. N.B. In the case of candidate 0144172, the central galaxy was classified as an AGN by applying the criteria described in § 3.6, however, this was a borderline case and the central object may in fact

[4]The AGN may be inside the cluster or along the same line-of-sight.

be an emission line cD galaxy.

4.2.2 Stars

X-ray emission has been measured from many stellar types, the strongest X-ray emitters being dwarf stars, early type stars and accreting binaries, see Rosner *et al.* (1985) for a review. Stellar X-ray sources are typified by luminosities in the range $10^{26} \rightarrow 10^{32}$ erg s^{-1} and soft X-ray spectra. We do not expect stellar contamination to be very significant in our cluster candidate list, because of a) the hardness ratio threshold imposed on our sample (§ 2.3.2) and b) the high Galactic latitude of the SGP region. Based on the arguments in Stocke *et al.* (1991), we have excluded sources from our candidate list, for which a $b_j < 13$ star lies inside the X-ray error circle, *e.g.* 0743009, figure C.21. (Stocke *et al.* concluded that probability of finding such stars by chance inside the EINSTEIN X-ray error circles was very low, because of their rarity.) Note that the COSMOS star/galaxy separation can break down in the crowded fields of cluster cores. Therefore, the raw plate material was always inspected before a source close to a $b_j < 13$ CUOC "star" was rejected.

It has been shown (Fleming, personal communication) that optically fainter stars have been detected during the RASS , for example M dwarfs to $V = 17$. We have provisionally excluded two candidates as faint ($b_j > 13$) dwarf stars. In the case of candidate 0853043 (figure C.30) the only spectrum available is for a $b_j = 15$ magnitude star inside the error circle, which has been tentatively classified as an M dwarf. The identification, as a white dwarf, of a star close to candidate 0124051 is more solid, see figures 3.6 (spectrum 15) & figure C.12. However, we have reason to suspect that a cluster is the dominant X-ray source along that line-of-sight to this candidate; a) the star lies *outside* the X-ray error circle and b) the source has a measured SASS extent of $84''$.

4.2.3 Classification Scheme

There are 36 candidates in table A.2 which have been classified as contaminating objects because they met one of the following criteria;

1. A $b_j < 13$ star fell inside the X-ray error circle (6 cases)
2. An AGN fell inside the X-ray error circle (26 cases)
3. The X-ray position coincided with a very low redshift, $z_{est} \lesssim 0.015$, spiral galaxy (2 cases).

4. A dwarf star was found close to the X-ray position (2 cases).

These candidates have been flagged in column 15 of table A.2 by the numbers 8 & 9. The object type thought to be responsible for the RASS source is listed in column 16. In the case of the three flag 9 candidates, we have reason to doubt that identification with a contaminating object is correct. These candidates; 0124051, 0144172 & 0853043, have been discussed above.

4.3 Candidates with no Identification

There are a total of 155 SGP RASS cluster candidates in table A.2 that remain to be identified as clusters or contaminating objects. The majority $\approx 80\%$ are likely to be bona fide $f_X \gtrsim 1 \times^{-12}$ erg s^{-1} cm^{-2} X-ray clusters. Of these 155 candidates, 23 appear to be highly likelihood clusters based on their galaxy distribution in the CUOC, *e.g.* 0743011 and 0863043, figures C.22 & C.32. These candidates have been given the classification flag 5. In addition there are three entries in table A.2, which have been given the flag 7. For these candidates, information is available from the spectroscopic follow-up, but it is not not sufficient to identify the X-ray source. For example, for both candidates 0733077 & 0853062 (figures C.20& C.31) two galaxy redshifts are available, but they are too discrepant to be drawn from a common cluster, see table B.1. In the case of candidate 1044097 (figure C.39), we have failed to find a galaxy at a concurring redshift to the central cD-type galaxy. The remaining 129 unidentified candidates have been placed in category 6. The fact that almost half of the entries in the flux-limited SGP RASS cluster candidate list have neither been confirmed as being clusters nor have available redshift information, means that the redshift cluster samples presented in § 4.6 are incomplete by up to 50%. Part of the reason for this incompleteness was the alteration made to the SASS count rates in the latter stages of the spectroscopic follow-up, § 2.4.2. Future plans to extend the spectroscopic follow-up are discussed in chapter 6.

4.4 X-ray and Optical Properties of Identified Objects

With the aim of improving RASS cluster candidate selection in the future, we have investigated the optical and X-ray properties of the 154 clusters and 36 contaminating objects identified in table A.2.

4.4.1 X-ray Properties

Figures 4.3 and 4.4 show the distribution of the SASS determined extents, extent likelihoods and hardness ratios for the 154 SRCS clusters (•) and 36 identified contami-

mean hardness ratio	clusters	$HR = 0.5 \pm 0.3$
	contaminants	$HR = 0.2 \pm 0.3$
mean extent	clusters	$43'' \pm 37''$
	contaminants	$17'' \pm 20''$

Table 4.6: The mean X-ray properties of SRCS clusters and contaminating objects.

nating objects (□). The average extent and hardness ratios for the two object types are compared in table 4.6. From figure 4.4 and table 4.6 it can be seen that only one contaminating object, 0124051, has an extent more than 3σ, *i.e.* $> 77''$, from the mean value. This fact led to the suspicion, §4.2.2, that this source, identified in table A.2 as a white dwarf, may in fact be a cluster.

In chapter 2, we discussed two methods of count rate determination; SASS (§ 2.1.1) and VTP (§ 2.3.3). A comparison of these two flux determinations is made in figures 4.5 & 4.6 for the 136 clusters for which VTP count rates are available. The ratio of VTP to SASS count rate is plotted as a function of redshift in figure 4.5 and as a function of SASS extent in in figure 4.6. There are weak correlations in both plots; in figure 4.5 there seems to be a trend for the count rate discrepancy to increase with decreasing redshift and in figure 4.6 the discrepancy appears to be an increasing function of SASS extent. These results suggest that SASS systematically underestimates the count rates from nearby, extended clusters, because the emission extends beyond the SASS detect windows. However, when trying to decide which method is the more inappropriate for cluster descriptions, there are other considerations to take into account. For example SASS count rates are less contaminated by background photons than are VTP count rates, Ebeling (1994). From the information available, there do not seem to be any compelling reasons to adopt VTP over SASS as the method of count rate determination, especially when one considers that only 75% of the SGP RASS cluster candidates have available VTP count rates, § 2.3.3. Therefore, in §4.6 we have constructed flux-limited cluster subsamples using both methods.

Turning now, to possible improvements in cluster selection, we consider whether selection on the basis of extent is a more efficient method way to identify clusters in the RASS than selection on the basis of digitised plate material. Only 14% of identified contaminating sources show X-ray extents greater than $37''$, *i.e.* more than 1σ from the mean. This compares to 55% of all identified clusters. Therefore, if one selected as clusters candidates all sources with extents $> 37''$, then that candidate list would suffer from only $\simeq$ 6% contamination. (Where $6 \simeq \frac{0.14 \times 36}{0.55 \times 154} \times 100$.) In addition such

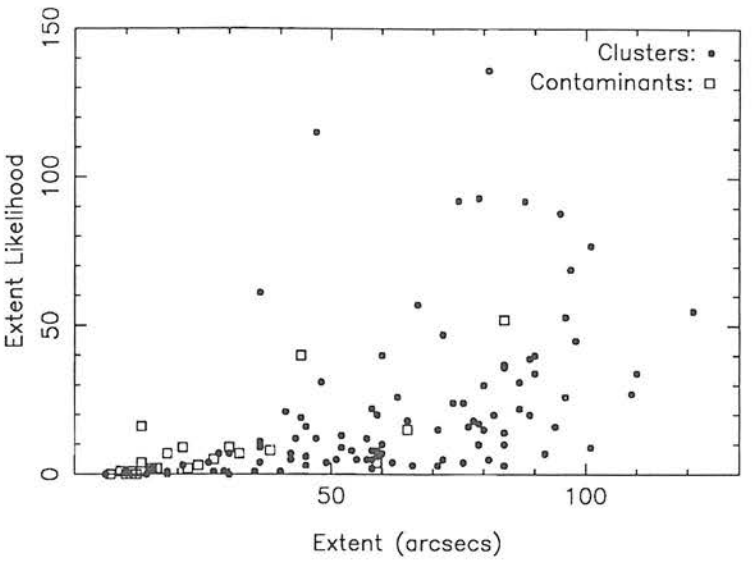

Figure 4.3: X-ray extent likelihood versus extent for SRCS clusters and contaminating objects.

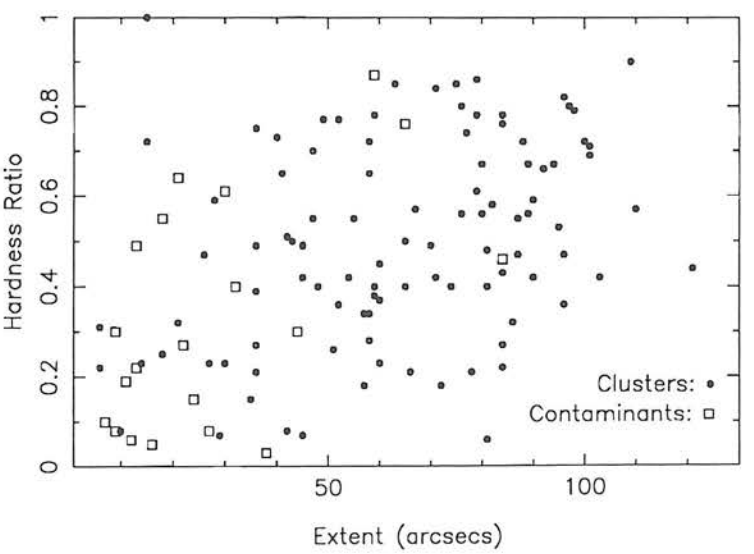

Figure 4.4: X-ray extent versus hardness ratio for SRCS clusters and contaminating objects.

a candidate list would have been selected on X-ray criteria alone. However, it would incorporate somewhat less than 55% of all $\gtrsim 1 \times 10^{-12}\,\mathrm{erg\,s^{-1}\,cm^{-2}}$ clusters, which is obviously a disadvantage.

The applicability of an extent selected candidate list to statistical studies, such as of the spatial correlation function or the luminosity function, has been investigated in figure 4.7. In this figure, we have plotted redshift histograms for the 84 extent $> 37''$ and the 70 extent $< 37'$ identified SGP RASS clusters. As expected, there is a tendency for extended clusters to lie at lower redshifts. However, the distributions look broadly equivalent and a Kolmogorov-Smirnov test reveals that there is only a 54% chance that the two cluster samples were drawn from different redshift distributions. In other words, there are no significant systematic effects that would bias the statistical properties of an extent $> 37''$ cluster sample over a complete flux-limited cluster sample. Whereas there are too few extent $> 37''$ clusters in the SRCS to be able to perform useful correlation analyses, we recommend that future RASS cluster identification programmes concentrate on X-ray properties for cluster selection and not on digitised galaxy distributions. To this end, we also point out that contamination in the cluster candidate list can be further reduced by the application of a higher hardness ratio threshold. From figure 4.4 we can see that contaminating objects rarely have hardness ratios higher than $HR > 0.5$. Of the 78 identified objects with hardness ratios greater than 0.5, 90% are clusters.

4.4.2 Optical Properties

It was stated in § 4.1.2 that majority of the identified contaminating objects in our candidate list were the sole object in the X-ray error circle. We have investigated whether this observation could have been predicted from the CSEARCH probabilities (§ 2.3.2). Various tests were made to see if the CSEARCH probability patterns in the 5 search rings differed between known clusters and known contaminating objects, with null results. Therefore, it does not appear to be possible to make a priori judgements as to the identification of an X-ray source using the distribution of CSEARCH probabilities.

4.4.3 Abell Clusters as a Possible Selection Method

We make a slight departure here to access a selection method that was not used to construct the SGP RASS cluster candidate list, but which is very common among other cluster groups working with RASS data; namely separation analyses with the Abell catalogues. Groups such as Ebeling *et al.* (1992) and Briel & Henry (1993) adopt this as the sole method of selection for their RASS cluster samples. The SRCS, having been selected entirely without the assistance of the Abell catalogue, provides an useful control sample

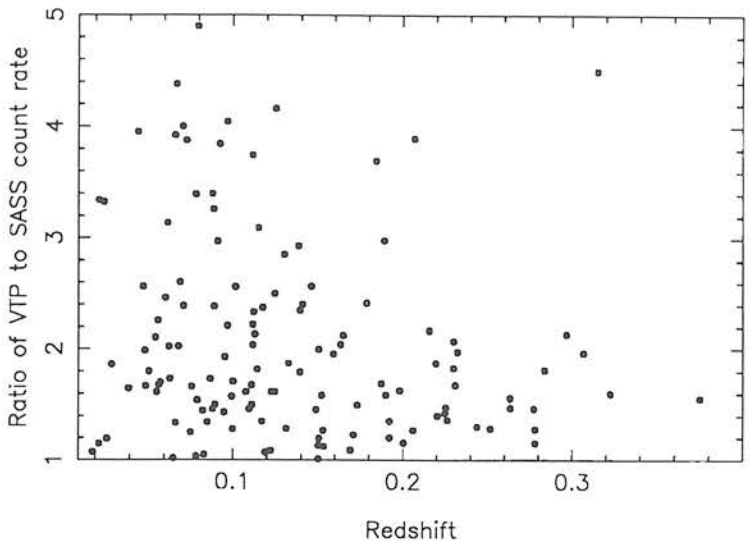

Figure 4.5: Ratio of VTP to SASS count rates for 136 SRCS clusters versus cluster redshift.

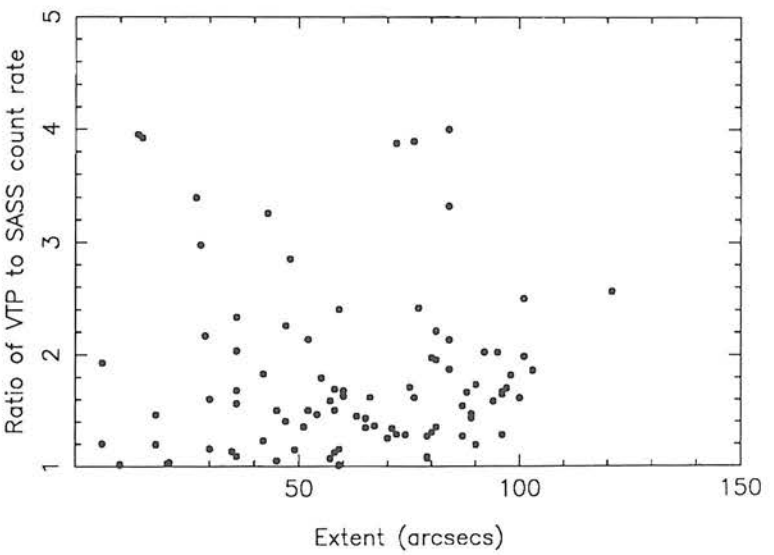

Figure 4.6: Ratio of VTP to SASS count rates for 136 SRCS clusters versus cluster extent.

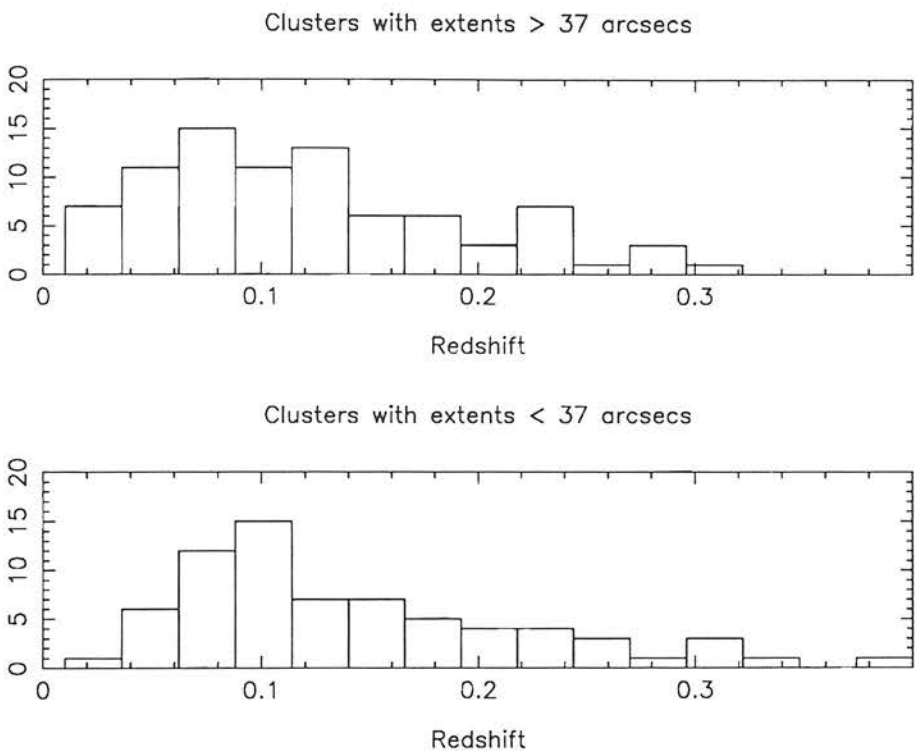

Figure 4.7: A comparison of the redshift distributions of (top) the 84 SRCS clusters that have X-ray extents greater than 37″ and (bottom) the 70 SRCS clusters with extents less than or equal to 37″

.

with which to assess the systematic errors in these other, Abell selected, RASS cluster samples.

There are three points to be addressed with regard to the use of the Abell catalogues as a selection tool;

1. How many Abell clusters are X-ray emitters?
2. Will the selection biases in the Abell catalogue, § 1.3.2, have an adverse effect on the statistical properties of X-ray cluster samples?
3. What is the incompleteness in the Abell catalogues, *i.e.* how many X-ray clusters are not listed therein?

The first point has been dealt with thoroughly by Ebeling *et al.* (1992); they find that $\simeq$ 18% of Abell clusters have PSPC fluxes greater than $7 \times 10^{-13}\,\mathrm{erg\,s^{-1}\,cm^{-2}}$. The second point has been addressed by Nichol *et al.* (1994a, § 1.3.1), who have shown that it is possible to purge Abell cluster samples of projection biases using RASS data. Therefore, the most serious concern for any cluster sample selected from the RASS using only a separation analysis with the Abell catalogue refers to the point 3. Only 25% of the 154 SRCS clusters were *not* also flagged as Abell clusters, which leads one to conclude that $\approx$ 75% of all $\gtrsim 1 \times 10^{-12}\,\mathrm{erg\,s^{-1}\,cm^{-2}}$ X-ray clusters have a corresponding entry in the Abell optical cluster catalogues. Note that our use of published optical cluster redshifts may cause this percentage to be set artificially high. In conclusion, the use of the Abell catalogues when making cluster identifications from the RASS does not adversely prejudice the cluster samples thus derived. However, the samples will have an intrinsic incompleteness of $\simeq$ 25%. In appendix C, several of the non-Abell SCRS clusters are featured, *e.g.* 0753052, 0782158, 0823080, & 0883087 (figures C.24, C.26, C.28, C.35 respectively).

4.5 Cluster Distribution and Number Density

The angular and redshift distribution of the 154 SGP RASS clusters are illustrated in figures 4.8 and 4.9. The mean redshift of the sample is $z_{mean} = 0.131$ and the maximum redshift is $z_{max} = 0.375$. The obvious gradient in cluster density with redshift in figure 4.9 is a reflection of several factors;

- The flux limit of the sample.
- Intrinsic evolution in the cluster population.
- The effect of the Schmidt plate limit.

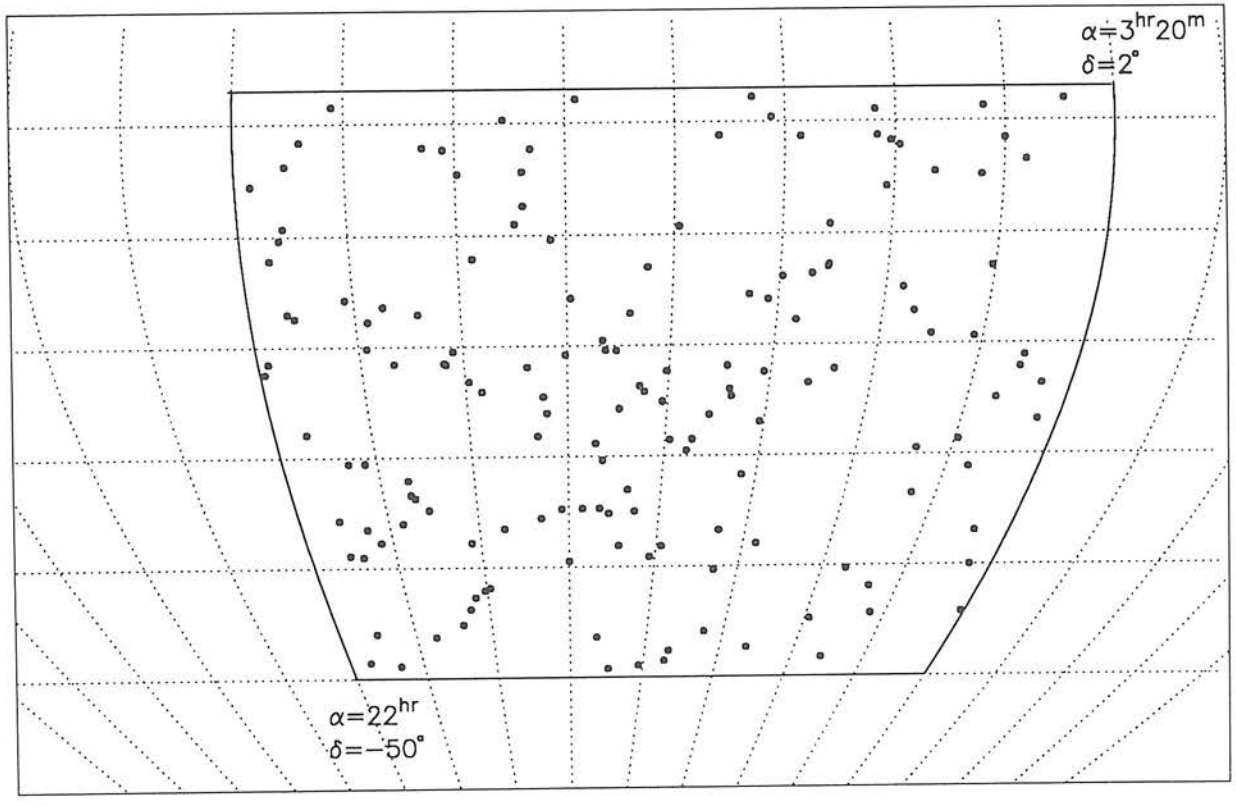

Figure 4.8: Equal area projection of the SRCS cluster distribution. The solid lines mark the boundary of the SGP survey region.

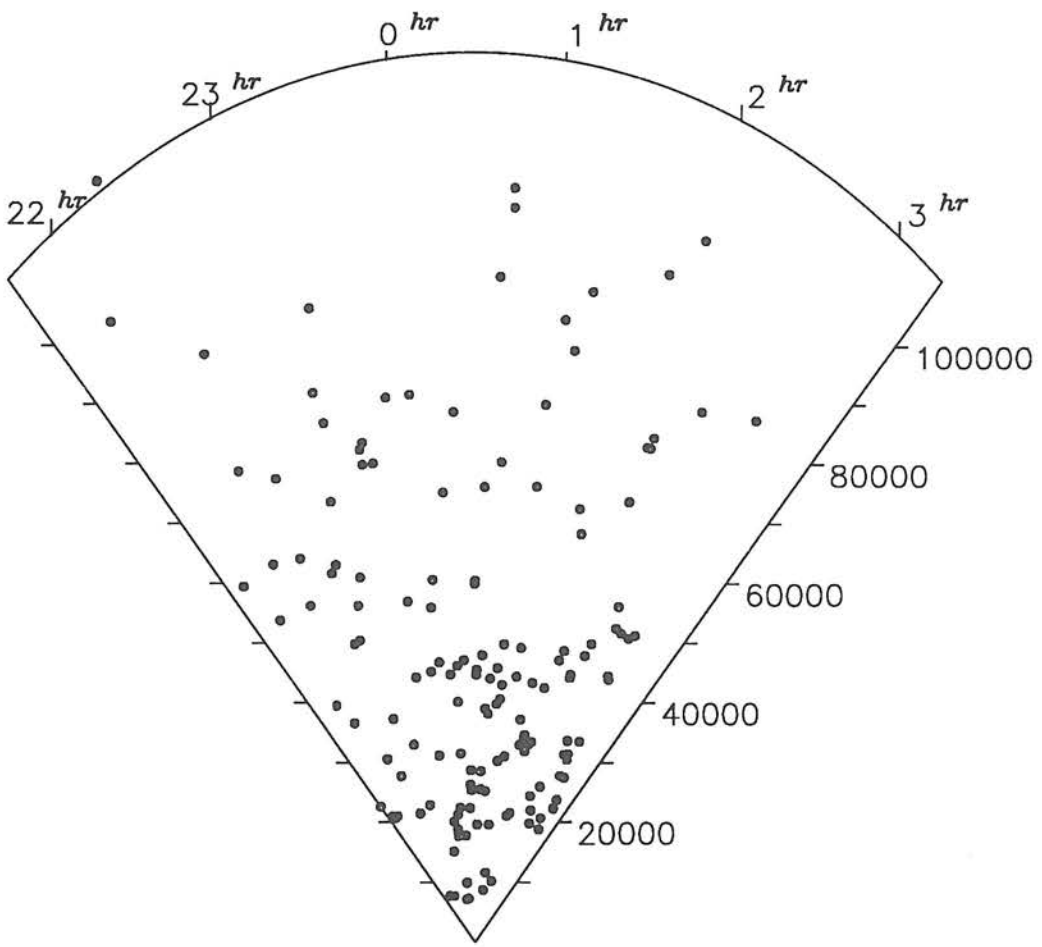

Figure 4.9: A Right Ascension cone diagram showing the redshift distribution of the 154 SRCS clusters.

- The increasing difficulty of redshift measurements.

Figure 4.10 shows the cluster redshift distribution and figure 4.11 shows the comoving number density of the SRCS as a function of redshift. The density was computed in shells at redshift intervals of $\delta z = 0.013$ to increase signal to noise and to smooth out some of the fluctuations caused by small scale clustering. The number density falls off rapidly with redshift, as would be expected from figure 4.9. The dotted line in each figure attempts to take into account the incompleteness in the sample ($\sim 45\%$, see table 4.7). In this case 126 counts were added to the raw counts in such a way so that the shape of the smoothed redshift distribution was preserved.

4.6 Eleven Samples of RASS clusters

The SGP RASS cluster candidate list presented in table A.2 is a result of a combination of the results from three different selection methods (§ 2.3.2); extent, CSEARCH & a separation analysis with the ROE/NRL cluster optical catalogue. In addition two different flux limits were applied, one related to SASS count rates and one to VTP count rates, § 2.4.2. Therefore, the 154 clusters listed in table A.2 do not constitute a statistical sample. We have attempted to create statistical subsamples of the 154 SRCS using more rigorous selection criteria. We present, in table 4.7, 11 subsamples which represent different combinations of selection method, count rate type and flux limit. For example, samples $1 \rightarrow 5$ contain collations of clusters using all three selection methods, but with differing flux limits. Alternatively, samples $5 \rightarrow 8$ contain SASS flux limited cluster samples derived from each of the three selections methods. We have chosen to present such a large array of subsamples because we do not know, a priori, if any particular selection method introduces systematic biases which might hinder the successful measurement of the cluster spatial correlation function. (A correlation analysis was performed on each sample, the results of which are presented in § 5.2.)

The selection criteria used to derive each sample are demonstrated by the entries in columns $2 \rightarrow 6$ of table 4.7. Columns 2 and 3 list the count rate limit and whether that count rate was determined by SASS or VTP analysis. Columns 4, 5 & 6 indicate which of the three selection methods, CSEARCH (C), extent (E) and separation analysis with ROE/NRL clusters (R) were used. The number of clusters (CLUS), contaminating objects (CONT) & unidentified candidates (UNID) that fitted these criteria are listed in columns $7 \rightarrow 9$. The completeness estimates in column 10 refer to the ratio of clusters to unidentified candidates. The lower bound on the completeness for each subsample was estimated by assuming that every unidentified candidate was a cluster. The upper

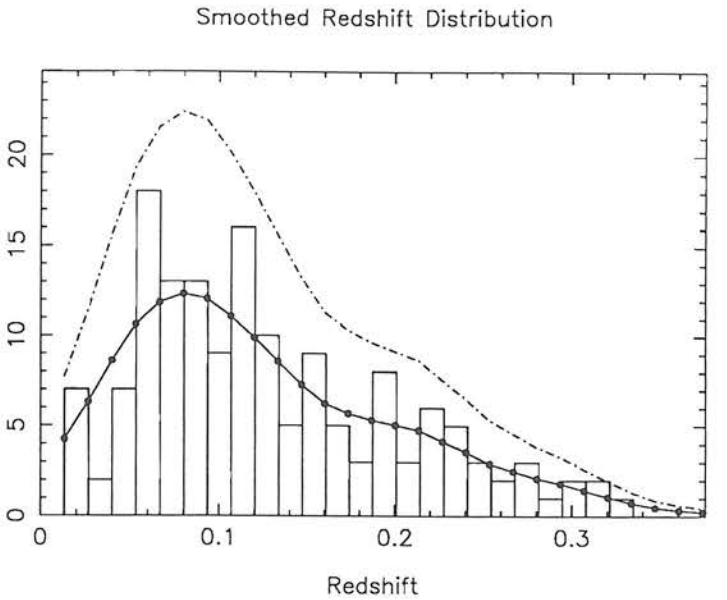

Figure 4.10: A redshift histogram generated from the 154 SRCS clusters. The smoothed distribution (solid line) was used to generate the number density function shown in figure 4.11. The dotted line represents the predicted redshift distribution for a 100% complete cluster sample, see text.

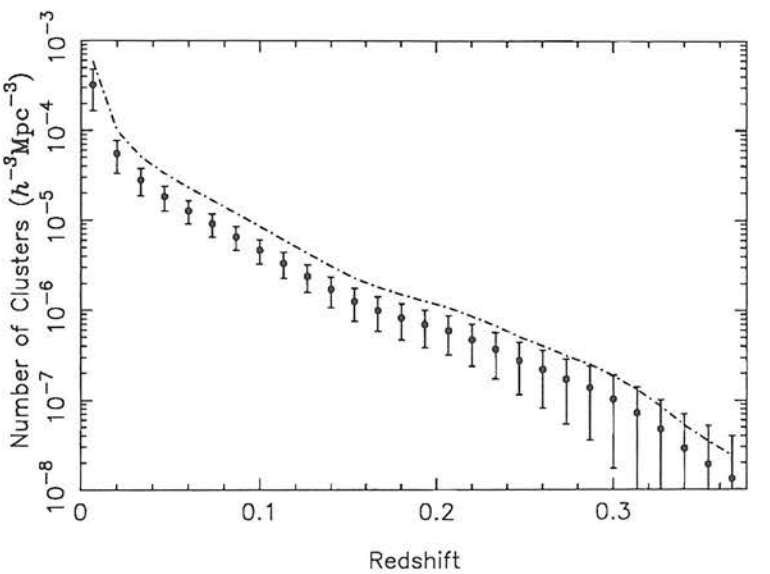

Figure 4.11: Co-moving space density of the SRCS 154 clusters (•) as a function of redshift. The number density has been calculated in volume shells $\delta z = 0.013$ wide, see text. The dotted line represents the predicted number density of a 100% complete cluster sample.

(1) hline ID.	(2) Count rate (s^{-1})	(3)	(4) (5) (6) method			(7) (8) (9) Number of;			(10) Comp.	(11) Eff.
	type	limit	C	R	E	CLUS	UNID	CONT		
1	SASS VTP	0.07 0.1	•	•	•	154	155	36	50%-55%	81%
2	SASS	0.07	•	•	•	133	125	34	51%-57%	80%
3	SASS	0.1	•	•	•	99	81	24	55%-60%	80%
4	VTP	0.1	•	•	•	136	74	28	65%-69% 46%-51%	83%
5	VTP	0.2	•	•	•	91	25	17	78%-81% 54%-59%	84%
6	SASS	0.07	•			124	98	29	56%-61%	81%
7	SASS	0.07			•	97	84	24	54%-59%	80%
8	SASS	0.07		•		85	12	16	88%-89%	84%
9	VTP	0.1	•			127	61	23	67%-71% 45%-51%	85%
10	VTP	0.1			•	90	33	18	73%-77% 44%-49%	83%
11	VTP	0.1		•		94	23	14	80%-82% 47%-50%	87%

Table 4.7: Eleven subsamples of SRCS clusters. The identification number of these samples 1 → 11 (1) will be referred to throughout chapter 5. The method used to determine the count rate (2) and count rate limit (3) set for each sample are listed with the selection methods used. These selection methods refer to CSEARCH (4), extent (6) and ROE/NRL clusters (5), see text. For each sample the number of clusters (7), contaminating objects (8) and unidentified candidates (9) that met the selection criteria are listed. The completeness of the cluster sample (10) is each case has been determined using the ratio of clusters to unidentified objects, both with and without a correction for cluster detection efficiency (11), see text.

bound on the other hand, takes into account the fact that a certain fraction of those unidentified candidates will be contaminating objects. This fraction was estimated using the efficiency of cluster detection among the identified candidates, column 11, see below. In the case of VTP flux limited samples, a second set of completeness estimates are presented. These values take into account the fact that the number of unidentified candidates in a VTP flux-limited list will be artificially low due to the fact that not every candidate has an available VTP flux, see § 2.4.2.

The cluster detection efficiency was calculated as follows,

$$\text{Efficiency} = \frac{\text{CLUS}}{\text{CLUS} + \text{CONT}}. \tag{4.1}$$

There does not seem to be any clear distinction between the different subsamples, and, hence, selection methods, with regard to this parameter. It is interesting to note, however, that most efficient way to detect clusters is to use a separation analysis with the ROE/NRL catalogue. In other words, it is possible to minimize the number of contaminating objects in a RASS cluster candidate list by choosing only those X-ray sources that are close to optical clusters. The detection efficiency for the CSEARCH selected sample 6, is lower than one would have anticipated from the initial selection condition that the contamination be less than 15%, § 2.3.2. In practice, the contamination level is $\approx 20\%$. This excess contamination may be a reflection of the fact that some of the identified contaminating objects lie along the line of sight to, or even inside, clusters, § 4.2.1. Note that the efficiencies quoted for the VTP flux-limited samples are misleadingly high as several known contaminating objects were deliberately not submitted for VTP analysis.

4.7 Summary

In this chapter we have drawn together spectroscopic information from our own observations and from the literature to develop the SGP RASS Cluster Sample (SRCS) of 154 clusters with redshifts. The identification of SGP RASS cluster candidates (as clusters or otherwise) has been shown to be a non-trivial process. In chapter 6 we develop some of the ideas discussed in § 2.1.2 to make suggestions for improved RASS cluster candidate selection and follow-up.

It is easy to be negative about SGP RASS Cluster Project, given the incompleteness of the spectroscopic follow-up and the problems associated with the RASS source count rate determinations. Therefore, we close this chapter with the positive statement that the SRCS is the **largest X-ray selected sample of clusters in existence** and that the scientific results that will ultimately be drawn from it will be profound and wide-ranging. Table 4.8 illustrates this point by summarizing some of the major scientific results that have been achieved, to date, from studies of X-ray cluster samples. Chapter 5 goes on to describe the final entry in table 4.8, *i.e.* that pertaining to the work presented in this thesis.

Postscript

As a postscript to this chapter we present two tests that were made on the SRCS. First we show that the SRCS is a fair subset of the initial candidate list and then go on to demonstrate that the internal and external errors on SRCS cluster redshifts are consistent.

As shown in table 4.7, the eleven cluster subsamples of the SRCS suffer from incompleteness at the 20% to 50% level. If this incompleteness is random it will not compromise the conclusions drawn in chapter 5 from the measured correlation functions. We have tested the randomness of the incompleteness using Kolmogorov-Smirnov tests. These tests compare the distributions of a) right ascension, b) declination and c) SASS count rates, in the cluster and candidate lists. The tests assumed a null hypothesis that the 154 clusters in the SRCS were drawn from the same underlying distribution as the 345 candidates. It was found that the distributions of cluster and candidate positions (right ascension and declination) are statistically very similar (KS probability $\approx 60\%$) but the distributions of count rates do differ. The SRCS count rate distribution has been artificially skewed towards the bright end and there is only a one in four chance that it could have been produced by random sampling of the initial candidate list. This was to be expected from our observing strategy (§ 3.1), which was to observe the candidates by X-ray brightness order irrespective of angular position and optical brightness. It is of note that the inclusion of clusters in the SRCS on the basis of literature redshifts (§ 4.1.2) has not biased the sample in a positional sense.

The implications of the bias in the count rate distribution on the cluster correlation function are difficult to assess as one has to factor in both richness dependence and errors in count rate determination. We have decided not to correct for it when deriving correlation functions, for fear of introducing further bias. However, when making comparisons with theory, § 5.4, we use predictions that were designed around the SRCS, *i.e.* using the same areal coverage, flux limit and incompleteness levels.

In § 4.1.1 we demonstrated that the z_{SF} values derived for four SRCS clusters were equivalent, to within $\simeq 1000\,\mathrm{km\,s^{-1}}$, of externally derived, accurate, z_{lit} measurements. We now discuss the internal error on the SRCS cluster redshifts and whether the method used to find cluster redshifts from multiple galaxy redshifts, *i.e.* taking a simple mean, was valid. We have taken the 69 SRCS clusters for which multiple galaxy redshifts are available in table B.1 and calculated the redshift discrepancy, Δz, between the galaxies in each cluster. (Note that of these 69 clusters, 46 have $n_{gal}^{SF} = 2$, 18 have $n_{gal}^{SF} = 3$ and 5 have $n_{gal}^{SF} = 4$.) It was found that the distribution of Δz could be well approximated by a Gaussian function. The mean and standard deviation of Δz were $600\,\mathrm{km\,s^{-1}}$ and $100\,\mathrm{km\,s^{-1}}$ respectively. These findings are in full agreement with existing studies of cluster velocity distributions and dispersions, *e.g.* Zabludoff *et al.* (1990), and with the external error quoted in § 4.1.1. We can therefore conclude that a) the method used to derive cluster redshifts from multiple galaxy redshifts is valid and b) for SRCS clusters with $n_{gal}^{SF} = 1$, the error on the derived cluster redshift will be $600 \pm 100\,\mathrm{km\,s^{-1}}$ (see § 4.1.1 for a discussion of the likelihood that the galaxy concerned is a cluster member). Note that no trend for increasing redshift discrepancy with redshift was found, suggesting that there was no significant decline in the accuracy of galaxy redshift determination with redshift.

Satellite(s)	No.	Identification method	Major results derived from the sample	Publications
UHURU ARIEL V	49	Coincidence with known clusters	Luminosity to richness relation	Jones & Forman 1978
OSO 8	20	UHURU clusters	Temperature to velocity disp. relation	Mushotzky *et al.* 1978
HEAO I	30	Coincidence with known clusters	X-ray Luminosity Function	Piccinotti *et al.* 1982
HEAO I	202	Coincidence with Abell clusters	X-ray Luminosity Function	Kowalski *et al.* 1984
EXOSAT	45	"	Temperature to luminosity relation	Edge & Stewart 1991
EXOSAT EINSTEIN HEAO I	55	Coincidence with known clusters	X-ray cluster correlation function X-ray Luminosity evolution	Lahav *et al.* 1989 Edge *et al.* 1990
EINSTEIN	53	Coincidence with Abell clusters	Origin and emission process of the gas	Abramopoulos & Ku (1983)
EINSTEIN	208	Coincidence with known clusters	Frequency of X-ray sub-clustering	Jones & Forman 1992
EINSTEIN	104	"	Temperature to luminosity relation	David *et al.* 1993
EINSTEIN	93	" plus spectroscopic followup	X-ray Luminosity evolution	Henry *et al.* 1992
ROSAT	492	Coincidence with Abell clusters	RASS Abell cluster detection statistics	Ebeling *et al.* 1992
ROSAT	66	"	Cont. levels in the Abell catalogue X-ray cluster correlation function	Briel & Henry 1993 Nichol *et al.* 1994a
ROSAT	154	Extent and galaxy enhancements	X-ray cluster correlation function	Romer 1994

Table 4.8: Review (not comprehensive) of the X-ray cluster samples presently available in the literature and the major results in cluster astronomy derived from them.

Chapter 5

The X-ray Cluster Correlation Function

In this chapter we use the spatial correlation function to analyse quantitatively the large-scale described by the 11 subsamples of the SGP RASS Cluster Sample (SRCS). presented in § 4.6 & § 1.3.1. The definition of the spatial correlation function and results from existing cluster samples were described in § 1.2.6. In this chapter we describe the methods used to compute and parameterize the correlation function (§ 5.1) and present the results from each of the X-ray cluster samples in § 5.2. The implications of these results are discussed in § 5.3 & § 5.4.

5.1 Estimating the Correlation Function

A body of literature has built up over recent years regarding the best way in which to measure the angular and spatial correlation functions of samples of galaxies and clusters, *e.g.* Peebles (1980), Hewett (1982), Landy & Szalay (1993). In the case of our 11 SRCS cluster samples, we needed to adopt a technique that could account for a) the incompleteness in the samples, § 4.6, b) for the redshift selection function, § 4.5 and c) the sharp boundaries of the survey region, § 2.3.1. It has been shown (authors as above) that the easiest way to overcome problems such as these is to compare the cluster distribution with the distribution in a sample of points which is drawn at random from the same volume as the cluster sample.

5.1.1 Creating a Random Catalogue

The random catalogue was created to have the same boundaries as the SGP region. The spatial distribution of its constituent points was defined to be Poissonian. It was created by placing a large number of points at random within the survey volume. The angular selection function, figure 4.8, was assumed to be flat across the SGP region and

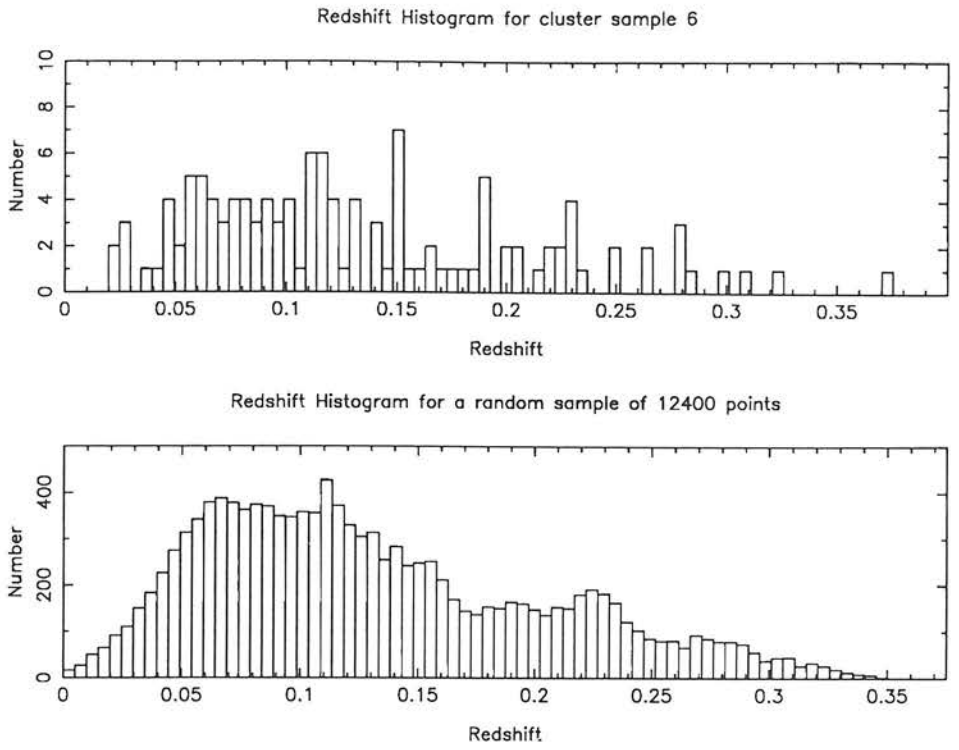

Figure 5.1: The redshift histograms for cluster sample 6 and a random sample of 12400 points. The redshift distribution for the random sample is based on that of the cluster sample with Gaussian smoothing, $\sigma_v = 3500\,\mathrm{km\,s^{-1}}$

so the angular positions of the points were simply drawn at random, with no weighting (*e.g.* to N_H column density) applied. (See § 2.4.3 for a discussion of the validity of this assumption.) In the redshift direction, there are several selection effects (§ 4.5) that contribute to the distribution of the clusters seen in figure 4.9. By imposing the same redshift distribution on the random points as was seen in the data, one can mimic the selection function without the need for complicated modelling. This was achieved by selecting redshifts at random from a smoothed version of the data redshift histogram. The Gaussian smoothing (velocity width $\sigma_v = 3500\,\mathrm{km\,s^{-1}}$) was performed to remove the effects of real redshift space clustering in the data histogram. Figure 5.1 shows the cluster and random redshift histograms derived from cluster sample 6 (see table 4.7) which consists of 124 CSEARCH (§ 2.3.2) selected SRCS clusters. Here the random catalogue comprises some 12400 points, or 100× the size of the data sample.

5.1.2 Correlation Function Estimators

In § 1.2.6 we defined the two point correlation function, $\xi(r_{12})$, to be related to the probability, δP, that an object is found in both of the volume elements δV_1 and δV_2

via $\delta P = n^2 \delta V_1 \delta V_2 [1 + \xi(r_{12})]$ (equation 1.7). It is possible to evaluate this equation, and hence measure $\xi(r_{12})$, from a set of real data positions by measuring the spatial separation of pairs of data points. If we count how many distinct data pairs there are at each separation, r, it is equivalent to integrating equation 1.7 over the range r to $r + \delta r$. In our case we are counting the number of cluster-cluster pairs as a function of separation, $Np^{CC}(r)$. This count can be related to the amplitude of the cluster-cluster two point correlation function, $\xi_{CC}(r)$, by,

$$Np^{CC}(r) = \frac{1}{2} n^2 V \langle \delta V \rangle [1 + \xi_{CC}(r)], \tag{5.1}$$

where n is the average number density and $\langle \delta V \rangle$ is the mean value of the volume defined by r to $r + \delta r$, see Peebles (1980) for a complete derivation.

If we then compare these pair counts to those derived from the random catalogue, Np^{RR}, which has a correlation amplitude at all r of $\xi_{RR}(r) = 1$, we can determine $\xi_{CC}(r)$ from,

$$1 + \xi_{CC}(r) = \frac{Np^{CC}}{Np^{RR}}, \tag{5.2}$$

where the expression has been suitably normalized to account for any differences in the sizes of the random and cluster samples.

Variations on equation 5.2 have been proposed by several authors. The most commonly used estimator utilizes cluster-random pair counts, Np^{CR}, to minimize edge effects (Davis & Peebles 1983);

$$1 + \xi_{CC}(r) = 2F \frac{Np^{CC}}{Np^{CR}} \tag{5.3}$$

where F is the ratio of random and cluster mean densities. Because the mean cluster density in the Universe is unknown, it has to be estimated from the data sample, a process that introduces errors into the correlation function, see Loveday *et al.* (1994). Recently a new estimator has been reported in the literature (Hamilton 1993),

$$1 + \xi_{CC}(r) = \frac{Np^{CC} Np^{RR}}{(Np^{CR})^2}. \tag{5.4}$$

This estimator is only affected to the second order by density fluctuations and should be much more reliable than the density-dependent traditional estimator. Landy & Szalay (1993) have also proposed that the variance on the Hamilton estimator is more accurately described by Poisson statistics than the traditional estimator.

Both estimators have been used to analyse the 11 cluster samples presented in table 4.7. The separation between each cluster-cluster, cluster-random and/or random-random pair in the 11 samples was calculated using equation 1.4 and the cosine rule. The Np^{CC}, Np^{CR}, Np^{RR} pairs were then sorted into logarithmic bins, $\Delta \log_{10}(r) =$

$0.2\,h^{-1}$ Mpc. Normalized, Np^{CC}, Np^{CR} & Np^{RR}, pair distributions in these bins are shown in figure 5.2 for cluster sample 1. It can be seen from this figure that there is a deficit of small separation cluster-cluster pairs in this sample. This deficit means that it is impossible to measure the correlation function on scales less than $\simeq 5\,h^{-1}$ Mpc using the SRCS. Note that Lahav *et al.* (1989, § 1.3.1) remarked on a similar deficit in their sample of X-ray clusters.

The error in the random-random and cluster-random pair counts was minimized by using several large random catalogues. In the case of equation 5.3, 20 different random catalogues, each 100 times larger than the cluster sample, were used. The second estimator, 5.4, takes much longer to compute. Therefore, only 10 random catalogues, each 40 times the size of the cluster samples were used in this case. This reduction in random catalogue size does not detract from the accuracy of the estimated correlation function (Szalay, private communication).

The resulting correlation amplitudes for cluster sample 6 from the two estimation techniques are shown in figure 5.3. The difference between the two methods becomes apparent at large separations, with the Hamilton estimator finding less power on large-scales than the traditional estimator. This trend is seen among all our cluster samples and is in agreement with the findings of Loveday *et al.* (1994) regarding the APM galaxy spatial correlation function. We have, therefore decided to adopt the Hamiltonian estimator during our analysis of the X-ray cluster correlation function results.

5.1.3 Errors

The correlation amplitudes derived using the estimators described above have associated errors. These errors are introduced by a) the limited size of the cluster sample, b) the uncertainty in the measured cluster number density, c) the finite binning size and d) selection biases. Two methods (Poissonian & bootstrap) have been proposed in the literature to estimate these errors and are described below.

Poissonian Errors

If the random catalogue is sufficiently large then the dominant statistical uncertainty in equation 5.4 lies in the cluster pair counts. It turns out, see Peebles (1980), that for low amplitudes of $\xi_{CC}(r)$, the error in Np^{CC} can be simplified to a counting problem in Poisson statistics, *i.e.* $\delta Np^{CC} = \sqrt{Np^{CC}}$. Therefore, the errors on the correlation amplitude derived from equation 5.4 can be estimated as follows;

$$\delta\xi_{CC}(r) = \sqrt{\frac{(Np^{CR})^2 Np^{CC} + Np^{CR}(Np^{CC})^2}{(Np^{RR})^2}}. \tag{5.5}$$

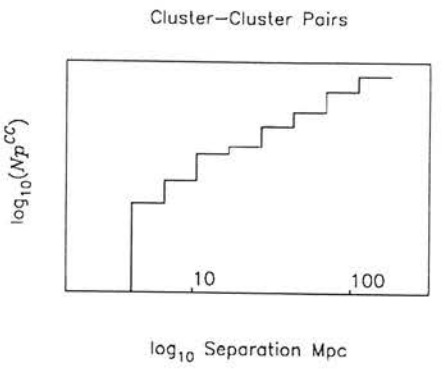

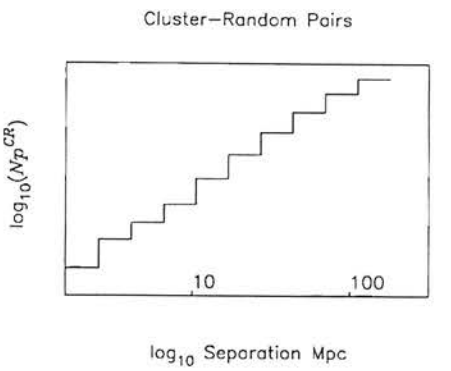

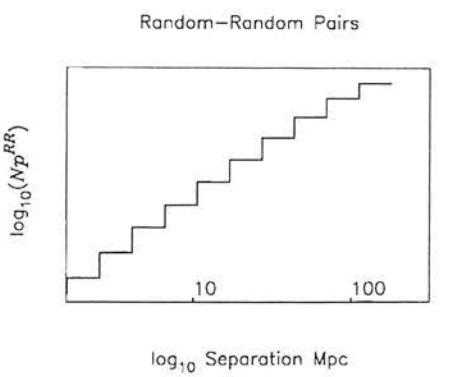

Figure 5.2: An example of normalized pair counts in $\Delta \log_{10}(r) = 0.2\,h^{-1}$ Mpc logarithmic bins for cluster-cluster pairs, cluster-random and random-random pairs. Such pair counts are used to determine the correlation function at each separation, see text.

However, if the correlation amplitude is not negligible, the errors in the pair counts $Np^{CC}(r)$ in different bins are not independent. As a consequence, the simplification of Poisson statistics is not accurate and the errors on each point will be underestimated.

Bootstrap re-sampling

An alternative method of error analysis that has become increasingly common in spatial correlation function studies is the technique of bootstrap re-sampling, Ling *et al.* (1986). This method involves the creation of a large number of pseudo data sets from the original data sample and the measurement of the correlation function for each data set. The error on the correlation function is then taken to be the standard deviation over the entire ensemble.[1] The data sets are constructed by selecting clusters at random with replacement from the original cluster sample, *i.e.* a single cluster can be included several times, or never, in the pseudo data set. The advantage of this method is that it should be applicable both in the high and in the low $\xi_{CC}(r)$ amplitude regimes. Unfortunately, full bootstrap error analysis requires a large investment of computer time. We have, therefore, decided to use the method developed by Mo *et al.* (1992) to determine bootstrap-resampling errors analytically. Mo *et al.* have shown that;
1) When $Np^{CC} \ll N_{clus}$, where N_{clus} is the number of clusters in the sample, the bootstrap error, σ_{boot}, is related to the Poissonian error, σ_{Poiss}, by $\sigma_{boot} \simeq (\sqrt{3} \times \sigma_{Poiss})$.
2) When $Np^{CC} \geq N_{clus}$, $\sigma_{boot} \simeq \sigma_{Poiss}$.
We use these expressions and equation 5.5 to determine the bootstrap errors that are plotted in figures 5.4 & 5.5 and when fitting the correlation function.

5.1.4 Fitting the Correlation Function

The cluster correlation function has been observed (§ 1.3.1) to follow a power law of the form;

$$\xi_{CC}(r) = \left(\frac{r}{r_0}\right)^{-\gamma} \tag{5.6}$$

where, r_0 is the correlation length, or separation at which the amplitude of the correlation function is unity, $\xi_{CC}(r_0) = 1$. Therefore, for each of the correlation functions presented in figure 5.4 we made a weighted, two parameter least squares fit to equation 5.6 to determine the best fit values of γ and r_0.

We perform the fit twice, first out to 36 h^{-1} Mpc and secondly out to 180 h^{-1} Mpc. The first limit represents the separation at which the correlation amplitude is almost always[2] observed to be positive and the second limit represents the full range of our

[1] N.B. Mean values calculated over the ensemble are not good estimators of the true mean.
[2] We acknowledge the presence of a negative point at $r < 35\,h^{-1}$ Mpc in sample 5.

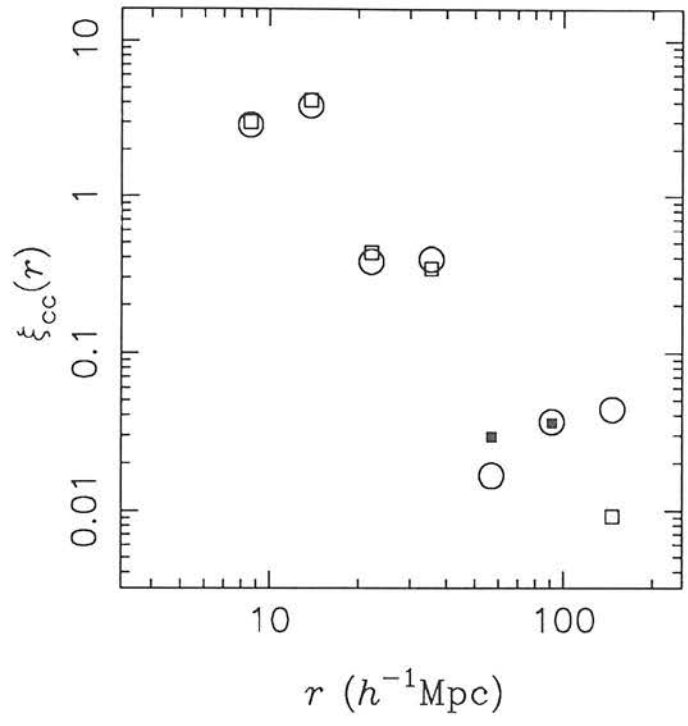

Figure 5.3: A comparison of the Hamilton (□) and traditional estimators (○) of the correlation function for SGP RASS cluster sample 6. It can be seen that at large separations $r \gtrsim 40\,h^{-1}$ Mpc that the results of the two techniques become discrepant, with the traditional estimator finding more clustering strength than the Hamilton estimator. Note that the solid points indicate separations where the correlation amplitude was negative, these points represent the *modulus* of $\xi_{CC}(r)$.

correlation analysis. The reason we made two fits in this way is because it is unclear whether points after the first zero-point crossing can be taken as significant. Some authors limit their fits to only the points before the first zero-point (*e.g.* Nichol *et al.* 1992) whereas others fit the correlation function out to large separation regardless of the appearance of negative points (*e.g.* Dalton *et al.* 1992). The point of first crossing has been taken to have critical implications to cosmological theories, Klypin & Rhee (1994). These authors also suggest that is impossible to measure the correlation function at amplitudes less than $\sim N_{clus}^{-1}$ (in our case $\xi_{CC} \lesssim 0.01$) due to the finite sample sizes and edge effects. We understand that our result may be interpreted by several groups after publication and, therefore, aiming to suit all prejudices, we present the power law fits to both separations.

Note that it is not possible, using least squares fitting, to determine whether equation 5.6 is the correct parameterization of the observed correlation functions. This is because the absolute chi-squared values cannot be interpreted in the usual way, due to the fact that the points are not independent.

Figure 5.4 displays the results of the correlation analyses performed on the 11 samples presented in table 4.7. To recap, the correlation functions have been determined using equation 5.4, logarithmic bins ($\Delta \log_{10}(r) = 0.2\, h^{-1}\,\mathrm{Mpc}$) and the 1σ bootstrap error bars shown have been derived analytically. The absolute values of any negative points are not shown on these plots. However, if the $1\sigma_{boot}$ upper limit is positive, the top portion of the error bar is shown. Some general observations that should be noted about these plots are that a) there *are* positive correlations between X-ray clusters, b) that the correlation amplitudes are decreasing roughly in a power law fashion, c) that the plots are very noisy, and d) beyond $40\, h^{-1}\,\mathrm{Mpc}$ there are very few positive points that are not consistent with zero.

Recalling from § 4.6, the 11 cluster samples represent a medley of selection techniques, flux determinations and flux limits. Every sample is internally incomplete to some degree, *i.e.* there are other clusters without redshifts that were selected by the same method. In addition every sample is externally incomplete, *i.e.* there are some RASS detected, $f_X \gtrsim 1 \times^{-12}\ \mathrm{erg\,s^{-1}\,cm^{-2}}$, clusters that were not included in the original candidate list either because; a) their count rates and/or extents were miscalculated or b) most of their galaxies are faint and are not included in the CUOC. It is not surprising, therefore, that there are discrepancies between the 11 correlation functions. Compare, for example, samples 10 and 11. Both samples contain approximately the same number of clusters and have been selected to the same (VTP) count rate limit. One (10) represents a purely X-ray selection method (extent) whereas the other (11)

sample	selection	No.	r_0^{180} (h^{-1} Mpc)	γ	r_0^{36} (h^{-1} Mpc)	γ
1	$CERS^{0.07}V^{0.1}$	154	13.12 ± 3.40	1.9 ± 0.5	15.31 ± 3.50	1.4 ± 0.5
2	$CERS^{0.07}$	133	13.97 ± 3.14	2.0 ± 0.5	15.71 ± 4.18	1.6 ± 0.7
3	$CERS^{0.1}$	99	14.03 ± 3.76	2.6 ± 1.0	16.01 ± 3.54	2.1 ± 0.7
4	$CERV^{0.1}$	136	11.23 ± 4.44	1.8 ± 0.6	12.46 ± 8.98	1.1 ± 1.0
5	$CERV^{0.2}$	91	12.51 ± 6.02	2.8 ± 1.8	13.03 ± 8.61	2.7 ± 2.4
6	$CS^{0.07}$	124	16.61 ± 2.93	2.5 ± 0.7	18.69 ± 4.13	1.9 ± 0.8
7	$ES^{0.07}$	97	14.81 ± 2.34	2.4 ± 0.7	16.28 ± 2.43	1.9 ± 0.5
8	$RS^{0.07}$	85	18.48 ± 3.41	3.2 ± 2.0	18.82 ± 4.22	2.3 ± 1.4
9	$CV^{0.1}$	127	11.58 ± 5.38	1.9 ± 1.0	13.10 ± 11.01	1.1 ± 1.3
10	$EV^{0.1}$	94	17.49 ± 1.98	5.3 ± 2.4	17.58 ± 2.41	5.2 ± 2.8
11	$RV^{0.1}$	94	14.71 ± 3.73	2.5 ± 1.0	17.45 ± 5.08	1.6 ± 0.8

Table 5.1: A listing of the best fit values of correlation length, r_0, and power law slope (γ) for each of the 11 correlation functions presented in figure 5.4. The fits were performed using a weighted least squares analysis over two ranges in separation, a) to $180\,h^{-1}$ Mpc and b) to $36\,h^{-1}$ Mpc. The number of clusters per sample are listed in column 3. The methods used to construct each of the samples are summarized in column 2, see table 4.7 for more details. The codes can be interpreted as follows;
C CSEARCH selected
E Extent selected
R ROE/NRL cluster
S SASS flux limit$^{\text{count rate limit in 1/s}}$
V VTP flux limit

has been developed using the ROE/NRL optical cluster catalogue. On a point by point comparison these plots seem quite different, but studying plots as a whole it is possible to see that the same trends are seen in the clustering properties of both samples. The same trends are seen among the other plots too, and this is reflected in the results of the two parameter power law fits table 5.1, figure 5.5.

5.2 Results from the Various SGP RASS Cluster Samples

The fits are not shown on the plots themselves because they tend to mislead the eye in cases where there are few points and the fits are poor, *e.g.* samples 9 & 10. A weighted mean of the 11 results gives $\bar{r}_0 = 16.7 \pm 1.1\,h^{-1}$ Mpc and $\bar{\gamma} = 1.7 \pm 0.2$ for $r \leq 36\,h^{-1}$ Mpc and $\bar{r}_0 = 15.32 \pm 1.0\,h^{-1}$ Mpc and $\bar{\gamma} = 2.1 \pm 0.2$ for $r \leq 180\,h^{-1}$ Mpc. (These mean values are given for illustrative purposes; the samples are not independent and so the mean values have little statistical significance.) Note the effect of changing the range of fitted points; the r_0 values are systematically higher and the slopes are systematically flatter when one fits from $5 \rightarrow 36\,h^{-1}$ Mpc than when one fits from $5 \rightarrow 180\,h^{-1}$ Mpc.

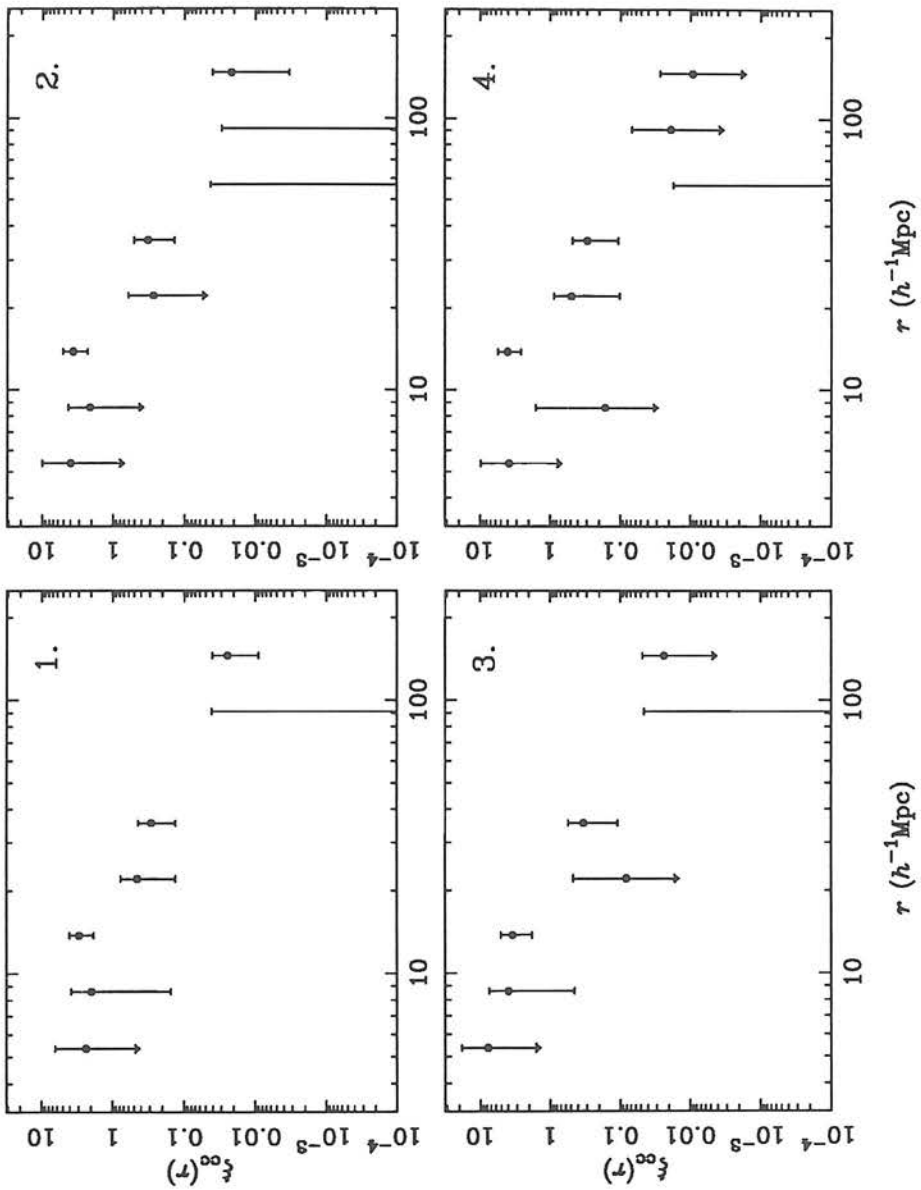

Figure 5.4: The spatial correlation function for cluster samples $1 \rightarrow 4$.

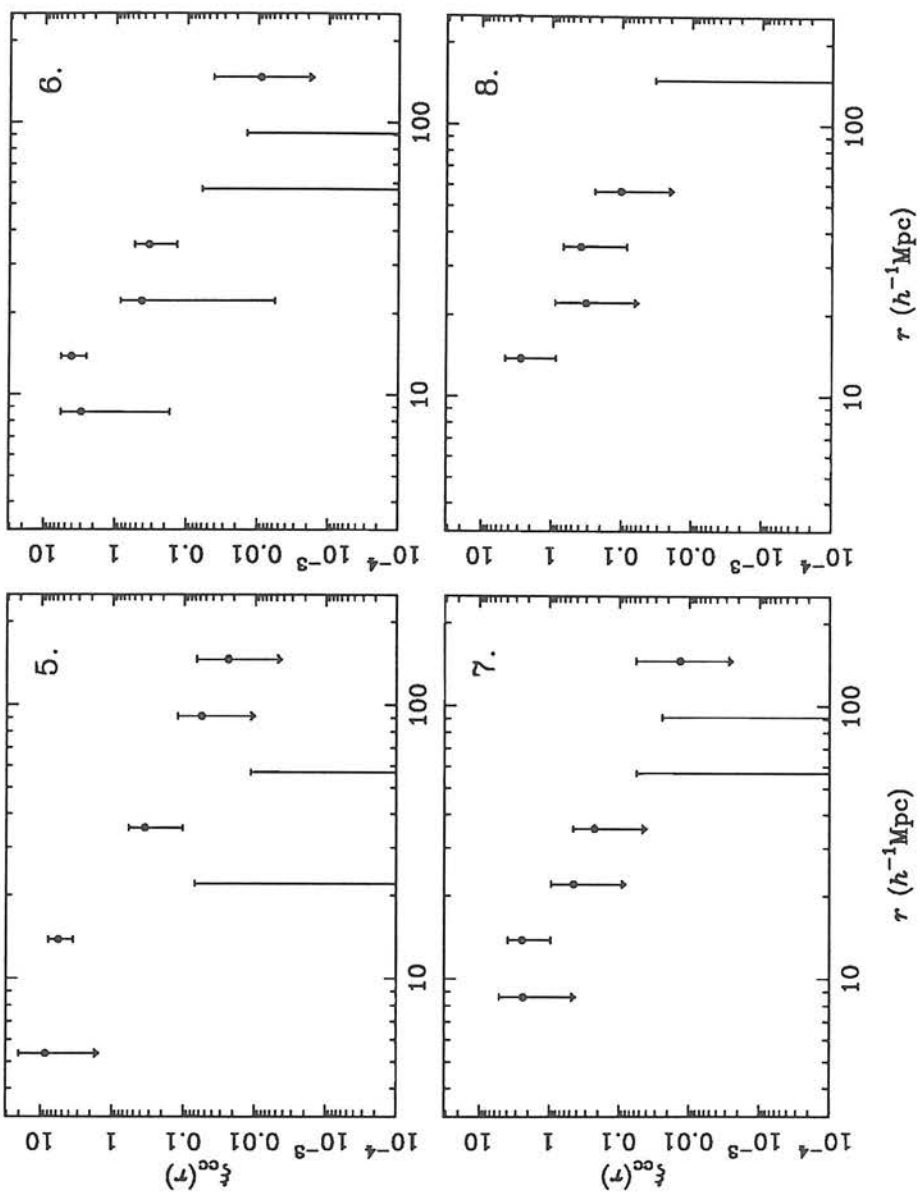

Figure 5.4: (continued) The spatial correlation function for cluster samples 5 → 8.

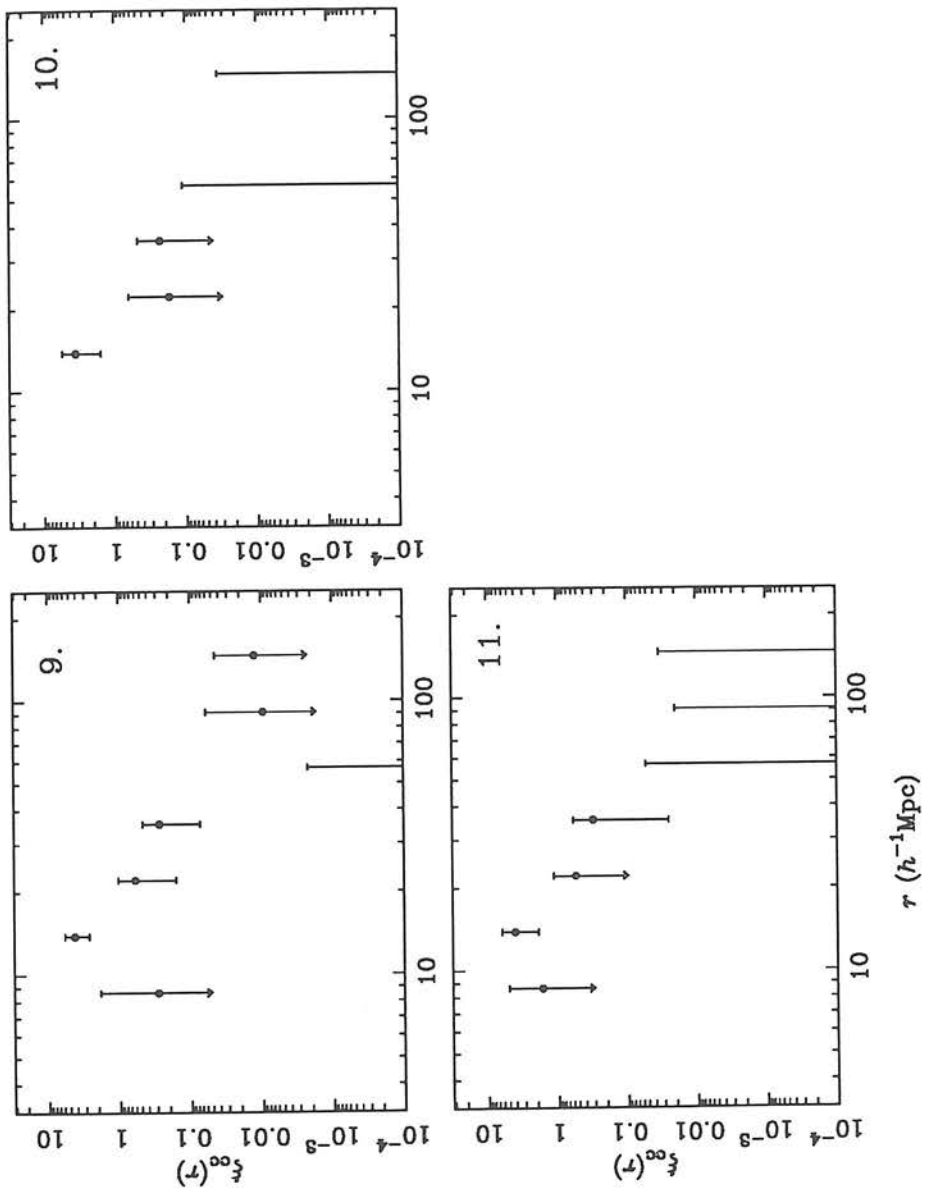

Figure 5.4: (continued) The spatial correlation function for cluster samples $9 \rightarrow 11$. See table 5.1 for the results of of a two-parameter least squares fit to $\xi_{CC}(r) = (\frac{r}{r_0})^{-\gamma}$.

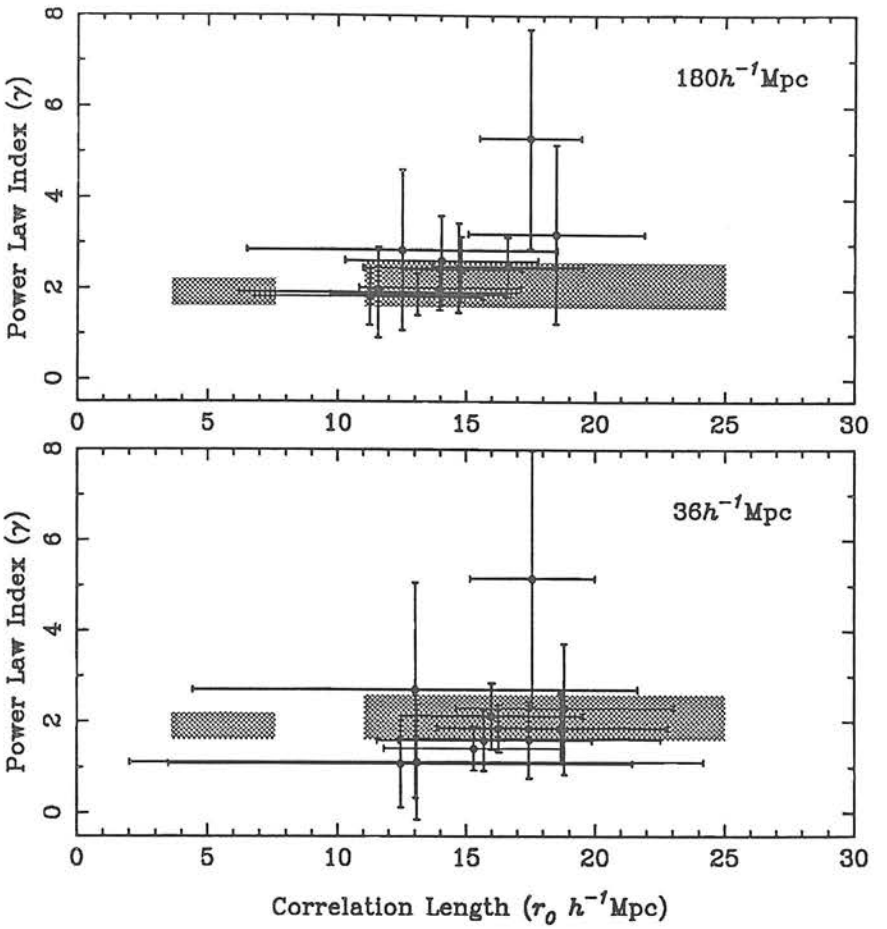

Figure 5.5: The distribution of r_0 and γ values determined from the 11 SGP RASS cluster samples, see table 5.1. The results of fitting the correlation function to 180 h^{-1} Mpc and 36 h^{-1} Mpc are shown in the upper and lower plots respectfully.

The grey boxes on figure 5.5 indicate the range in observed r_0 and γ values available in the literature, § 1.3.1, determined (in order of increasing r_0) for galaxies and optical clusters see below for a discussion.

5.2.1 The Effect on $\xi_{CC}(r)$ of Changing the Flux Limit

The samples ($1 \rightarrow 5$) that combine the results of all three selection methods (§ 2.3.2); CSEARCH , extent & ROE/NRL clusters, do not appear to have significantly different correlation functions than the samples that are derived from a single selection method ($6 \rightarrow 11$). With samples ($1 \rightarrow 5$) we have tried to investigate richness dependence in the X-ray correlation function by examining the effect of changing the flux limit on the clustering properties. A richness dependence has been reported by some authors in the optical cluster correlation function, *e.g.* Bahcall & Burgett (1986). This dependence

pertains to a (sometimes) observed strengthening of the clustering with galaxy richness, N_{gal}.

There is an observed correlation between richness and X-ray luminosity (Edge & Stewart (1991); $L_x \propto N_{gal}^3$). Therefore, it should be possible to investigate richness dependence in $\xi_{CC}(r)$ with X-ray clusters using samples with differing flux limits[3]. Comparing the results from samples 2 & 3 (SASS count rate limits of $0.07\,s^{-1}$ and $0.1\,s^{-1}$) and samples 4 & 5 (VTP count rate limits of $0.1\,s^{-1}$ and $0.2\,s^{-1}$)[4], there is no significant evidence for increasing r_0 values with flux-limit, as would be expected from Bahcall & Burgett's universal correlation function. However, one has to remember that the inherent deficiencies in the count rate determinations for our candidates, and hence in the quoted flux limits, § 2.4.2, may be blurring any physical effect that may be present. In addition, as Bahcall & Cen (1994) are at such pains to explain, "flux-limited sample[s] contain clusters of different richnesses at different distances". We will refer again to richness dependence in §5.3.3.

5.2.2 The Effect on $\xi_{CC}(r)$ of Contamination.

We have also tried to investigate the cleanness of our cluster sample by finding the correlation function for;

a.) Sample 1 plus all the identified AGN with redshifts in table A.2. (161 objects in total)

b.) Only the flag 1 and flag 2 (§ 4.1.3) clusters in sample 1. (102 objects in total)

c.) Abell clusters from sample 1 with $RC \geq 0$. (105 objects in total)

The results of these correlation functions are shown in figure 5.6 and table 5.2. Where as sample a.) is at least 5% contaminated, samples b.) and c.) should comprise of almost 100% clusters. Comparing the plots from sample a.) and sample 1 it can be seen that the introduction of low level artificial contamination in the sample has negligible effect on the measured correlation function. The effect of moving to an uncontaminated sample is unclear because the reduction in sample size introduces extra noise into the plots. Plot c.) seems to suggest that the contaminated sample has too much large-scale ($r > 40\,h^{-1}$ Mpc) power, however, plot b.) appears to have *more* large-scale power than the sample a.).

[3]Flux and luminosity are related via equation 2.6

[4]See § 2.4.1 for the relation between PSPC count rate and flux.

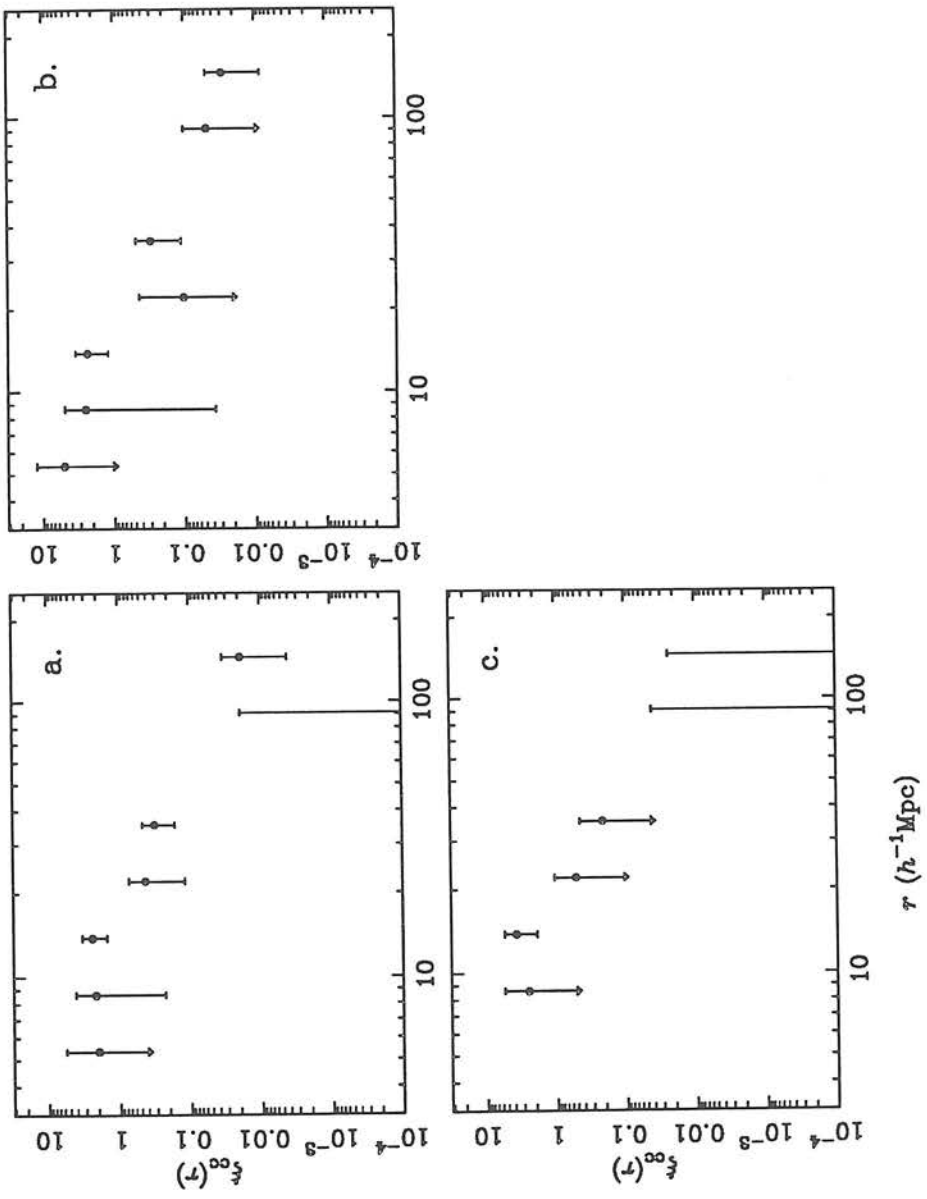

Figure 5.6 The spatial correlation function for samples a, b & c. See text for a description of the samples and table 5.2 for the results of of a two-parameter least squares fit to $\xi_{CC}(r) = (\frac{r}{r_0})^{-\gamma}$.

sample	No.	r_0^{180} (h^{-1} Mpc)	γ	r_0^{36} (h^{-1} Mpc)	γ
a (sample 1 plus AGN)	161	12.54 ± 3.30	1.9 ± 0.5	15.08 ± 3.26	1.3 ± 0.4
b (flag 1 & 2 clusters)	102	13.44 ± 3.66	2.1 ± 0.7	14.56 ± 3.17	1.8 ± 0.6
c ($RC \geq 0$ Abell clusters)	105	14.76 ± 3.37	2.8 ± 1.0	17.31 ± 3.71	1.9 ± 0.8

Table 5.2: A listing of the best fit values of the correlation length, r_0, and power law slope (γ) to the contaminated (a.) and clean (b.,c.) correlation functions presented in figure 5.5. The fits were performed using a weighted least squares analysis over two ranges in separation, a) to $180\,h^{-1}$ Mpc and b) to $36\,h^{-1}$ Mpc. The number of clusters per sample are listed in column 2.

5.2.3 Summary

The variation in the measured r_0 and γ values presented in tables 5.1 & 5.2 should represent the full range in systematic differences between the 14 different SRCS cluster subsamples. If any particular selection method or count rate determinations was fundamentally in error, then these errors should be reflected in the correlation function. However, with the data available it is impossible to make subtle assessments of the relative merits of the various samples. For example, the most discrepant point on figure 5.5 comes from sample 10, where the slope is poorly constrained due to the lack of points with which to fit to.

In conclusion, the 14 $\xi_{CC}(r)$ plots presented in figures 5.4 & 5.6 show no significant differences, in either correlation length or slope. The range over which the two parameter fit is made and the sample size have more effect on the measured correlation function than does flux limit, flux type, selection method, level of contamination or level of internal completeness. Typical values for the correlation length and power law slope are $r_0 = 15 \rightarrow 17\,h^{-1}$ Mpc and $\gamma \simeq 2$ respectively.

5.3 A Comparison with Previous Estimates of $\xi_{CC}(r)$

Until now we have presented the results from every SRCS cluster subsample with equal weight. However, for the sake of clarity, we have chosen to discuss the results from a single subsample when making comparisons between our estimate of $\xi_{CC}(r)$ and a) previous estimates of $\xi_{CC}(r)$, b) theoretical predictions (§5.4). In light of the original aim of this thesis; to measure the two-point correlation function for a large X-ray selected sample of clusters, we have chosen sample 6 to make these comparisons. Sample 6 was developed using only the CSEARCH method, § 2.3.2, it contains 124 clusters, has a SASS flux limit of 1.17×10^{-12} erg s^{-1} cm^{-2} and has $\sim 60\%$ internal completeness. The highest

Sample	No.	r_0 (h^{-1} Mpc)	γ	areal coverage	z_{max}
SRCS Sample 6 ($\rightarrow$ 180)	124	16.6 ± 2.9	2.5 ± 0.7	0.84 str.	0.375
($\rightarrow$ 36)		18.7 ± 4.1	1.9 ± 0.8		
Postman *et al.* (1992)	208	$20.6^{+4.5}_{-4.8}$	1.9 ± 0.2	6.05 str.	0.08
Nichol *et al.* (1994a)	67	16.1 ± 3.4	1.9 ± 0.3	0.17 str.	0.24
Dalton *et al.* (1994)	220	12.9 ± 1.2	2.0	1.31 str.	0.116

Table 5.3: Power law fits to the correlation functions presented in figures 5.6 & 5.7 The number of clusters in each sample is given in column 2, the areal coverage of the sample in column 5 and the maximum cluster redshift in column 6. (See §1.3.1 for more details of the literature samples.)

redshift cluster (Abell 370, RASS source 0194076) in this sample lies at $z = 0.375$.

A comparison between the correlation amplitudes derived from this sample and those derived by Postman *et al.* (1992, P92) and Dalton *et al.* (1992, D92) for optical clusters is shown in figure 5.7. In figure 5.8 a similar comparison is shown with the correlation function derived by Nichol *et al.* (1994a) from a sample of Abell clusters detected in the RASS . A full description of these other samples was given in § 1.3.1. We make a brief reiteration in table 5.3 to stress the salient differences and similarities between these samples and sample 6. Note that in figure 5.7 we have shown the results from P92's "statistical subsample" of 208 clusters not from their whole sample of 351 clusters. This subsample was limited in redshift and galactic latitude by $z \leq 0.08$, $|b| \geq 30°$, it is volume complete and is claimed to have only minimal selection biases.

5.3.1 The Correlation Length

It can be seen from table 5.3 that there are no significant discrepancies between published values of the correlation length for optical or X-ray clusters and our result from sample 6. This is also illustrated in figures 5.5, 5.7 & 5.8 In figure 5.5 the full range of previously measured r_0 and γ values are indicated as shaded regions for both galaxy ($3 < r_0 < 7\,h^{-1}$ Mpc, Loveday *et al.* 1994) and ($11 < r_0 < 25\,h^{-1}$ Mpc, D92 & P92) cluster correlation functions. (These boxes include the 1σ errors quoted in the respective publications.) The distribution of points from our SRCS samples fall, by and large, within the boundaries of the cluster shaded region. From the upper plot in figure 5.5, one might conclude that the points were more compatible with the lower range of previously measured r_0 and hence that our samples were more consistent with the D92 result than with the P92 result. However, in the lower plot, the range of measured SRCS r_0 values fills the whole shaded region and it is impossible to conclude from this whether our

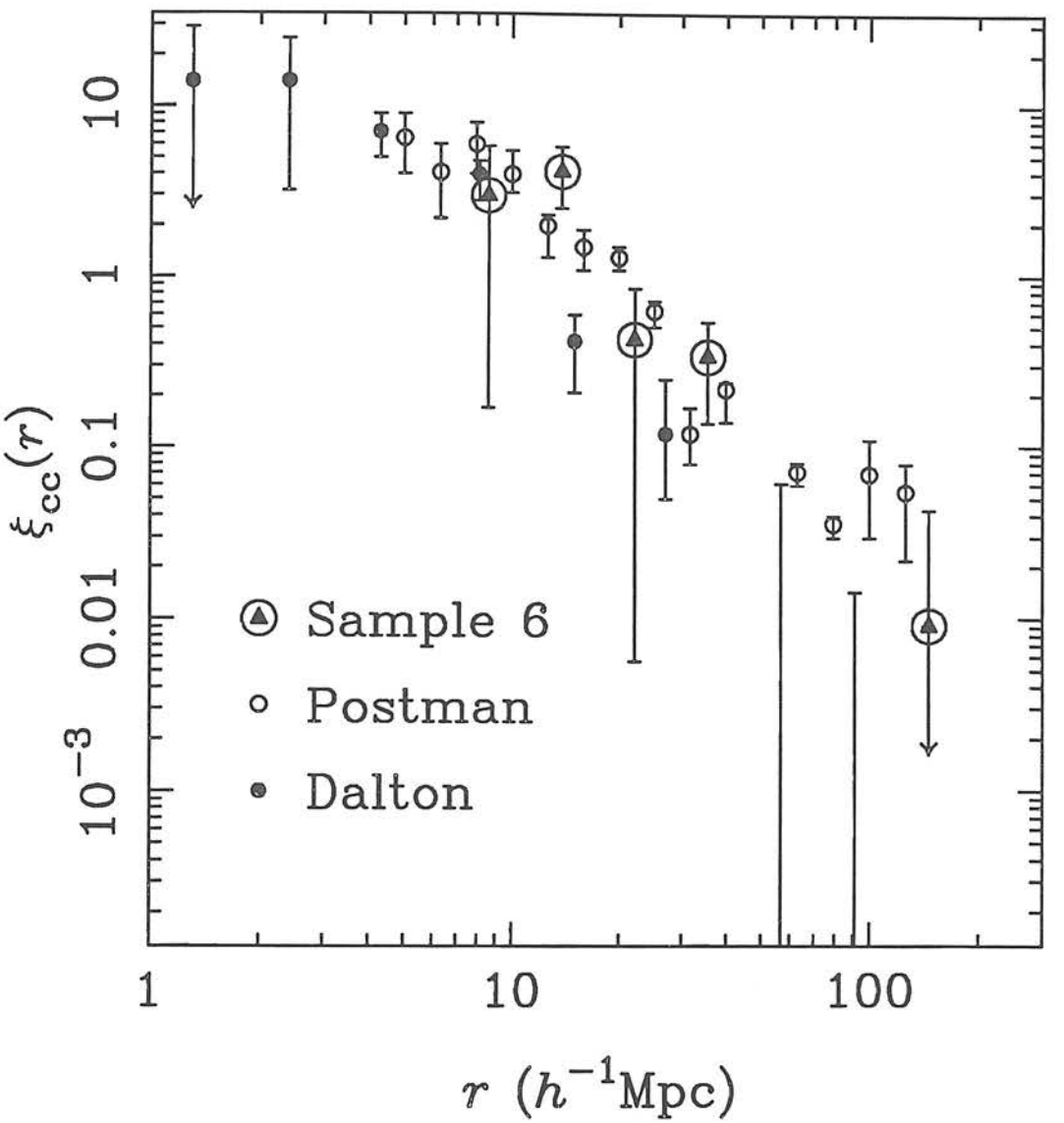

Figure 5.7: A point by point comparison of the correlation functions derived from a) SGP RASS sample 6, b) the statistical sample of Abell clusters presented in Postman *et al.* (1992) and c) the sample of digitised clusters in Dalton *et al.* (1992).

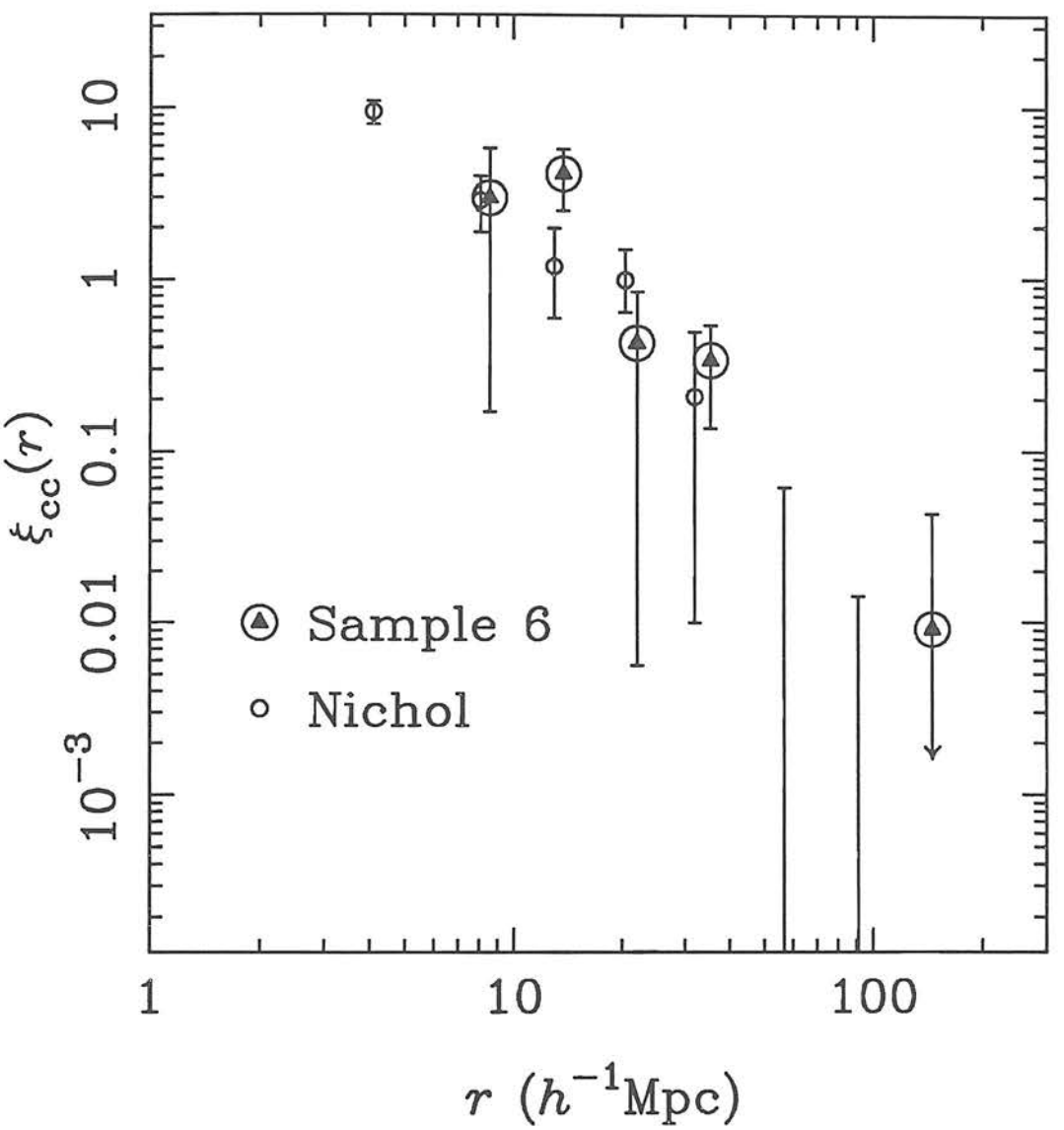

Figure 5.8: A point by point comparison of the correlation functions derived from SGP RASS sample 6 and an X-ray confirmed sample of Abell clusters presented in Nichol *et al.* (1994a).

samples are closer to digitised (D92) or Abell (P92) clusters. (Sample 6 falls at roughly the centre of the shaded region in each case.)

It seems, therefore, that the SGP RASS Cluster Project has not yet brought the debate as to the true value of the cluster correlation length (§ 1.3.1) any closer to a solution. However, studying figure 5.7 it is hard to understand where the community's obsession with r_0 stems from. In fact, if one interprets the D92 points at $r < 10\,h^{-1}$ Mpc as measuring the correlation function in a regime inaccessible to the P92 and SGP RASS samples, then the simple power law description of ξ_{CC} seems increasingly naive. In this plot it can be seen that on the scales of interest ($10 < r < 20\,h^{-1}$ Mpc) all the correlation amplitudes agree to within $\leq 3\sigma$. Whether the clusters come from X-ray selected, digitised or Abell samples, they all show roughly the same power on scales $\lesssim 40\,h^{-1}$ Mpc.

What is important to emphasize is that *none* of the samples are producing correlation lengths comparable to the galaxy correlation functions, *i.e.* $r_0 \simeq 5\,h^{-1}$ Mpc. Improvements in selection techniques, redshift follow–ups and sample sizes over the last decade have pegged the correlation length at $r_0 \leq 20\,h^{-1}$ Mpc. (Compare to $r_0 \approx 25\,h^{-1}$ Mpc for the first measured $\xi_{CC}(r)$ by Bahcall & Soneira 1983.) However, it seems unlikely that any future improvements in sample quality will shift the measurement to $r_0 \leq 10\,h^{-1}$ Mpc. In other words, there is still a discrepancy between the cluster correlation function and the galaxy correlation function that must be explained by any viable theory of large-scale structure formation.

5.3.2 Large-Scale Correlations

Let us now turn our attention to the value of $\xi_{CC}(r)$ on larger scales, $r > 40\,h^{-1}$ Mpc. It is at these scales that there seem to be real differences between the different cluster samples. D92 measure no positive power on scales greater than $r < 27\,h^{-1}$ Mpc and yet P92 are finding positive amplitudes to $r \simeq 200\,h^{-1}$ Mpc. It is crucial that the correlation function is measured accurately on these scales, because the existence of significant power in $\xi_{CC}(r)$ at $\sim 100\,h^{-1}$ Mpc puts serious constraints on theories of large-scale structure formation (*e.g.* Klypn & Rhee 1994). In a followup paper to D92, Efstathiou *et al.* (1992) interpret the differences between their result and that of P92 to be due to the Sutherland effect, § 1.3.2. As stated in § 1.3.2, an X-ray selected sample will not suffer from the Sutherland effect and so our result should provide an independent test of this hypothesis. We compare below the measured correlation amplitudes at $r \simeq 50, \&90\,h^{-1}$ Mpc for the three samples;

Sample	Distance	Amplitude	Distance	Amplitude
SRCS Sample 6 (eq. 5.4)	$57\,h^{-1}$ Mpc	-0.03 ± 0.05	$91\,h^{-1}$ Mpc	-0.04 ± 0.05
Dalton *et al.* 1992	$50\,h^{-1}$ Mpc	-0.03 ± 0.03	$90\,h^{-1}$ Mpc	-0.01 ± 0.02
Postman *et al.* 1992	$63\,h^{-1}$ Mpc	0.07 ± 0.01	$100\,h^{-1}$ Mpc	0.07 ± 0.03
SRCS Sample 6 (eq. 5.3)	$57\,h^{-1}$ Mpc	0.02 ± 0.08	$91\,h^{-1}$ Mpc	0.04 ± 0.04

Both D92 and P92 used the traditional estimator, equation 5.3, when deriving these amplitudes. Therefore, we have included in this table the results for SRCS sample 6 from both the Hamilton estimator, equation 5.4, and the traditional estimator. Whereas, the Hamilton estimator results are closer to D92, the traditional estimator results are (not surprisingly, see figure 5.3) closer to P92. It appears, therefore, that our data are not robust enough to be able to distinguish between P92 and D92 using $\xi_{CC}(r)$. To be able to do so conclusively, one needs to reduce the size of errors bars at $r > 40\,h^{-1}$ Mpc by at least a factor of two, which would require a larger, more complete sample of X-ray clusters.

However, when one examines the two dimensional correlation function, it becomes much more apparent that sample 6 is more consistent with the D92 sample of digitised clusters than they are to the P92 sample of Abell clusters. The 2-D correlation function, $\xi_{CC}(\sigma, \pi)$, was introduced in § 1.3.2 during our discussion of projection effects. To reiterate, it is calculated by de-projecting the correlation amplitude into its σ and π components, where $\pi = |cz_1 - cz_2|$ is the separation along the line of sight between two clusters at redshifts z_1 & z_2, and $\sigma = (r^2 - \pi^2)^{1/2}$ is approximately the separation perpendicular to the line of sight. Using the traditional estimator, equation 5.3, and $\Delta r = 30\,h^{-1}$ Mpc (linear) bins we have computed $\xi_{CC}(\sigma, \pi)$ for both sample 6, figure 5.9, and for the P92 statistical sample, figure 5.10 We have already shown a $\xi_{CC}(\sigma, \pi)$ plot for the P92 data, figure 1.2, however, for the purposes of fair comparison, it is necessary to plot these data again here. The sample 6 data had to be binned very coarsely to compensate for the lack of close pairs in cluster sample 6 (figure 5.2) and, when one bins the P92 data in the same way, some of the structure seen in figure 1.2 becomes washed out. However, even with this large bin size it is apparent that the P92 contour plot is extended along the redshift axis, whereas the contour plot generated from sample 6 is roughly isotropic on scales $\lesssim 60\,h^{-1}$ Mpc. We interpret these plots to mean that projection effects in the Abell catalogue are artificially boosting the correlation amplitude along the redshift axis. We infer that the excess power at scales of $40 < r < 200\,h^{-1}$ Mpc seen in the P92 data over the D92 data and sample 6, figure 5.6, is attributable to this artificial clustering.

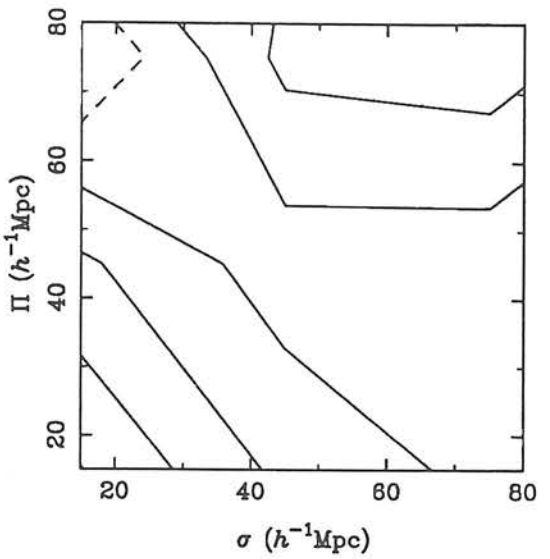

Figure 5.7: A contour plot of the 2-D correlation function derived from SGP RASS sample 6, see text. The contours are separated by $\Delta\xi_{CC}(\sigma,\pi) = 0.2$, with the highest contour level lying at $\xi_{CC}(\sigma,\pi) = 1.0$.

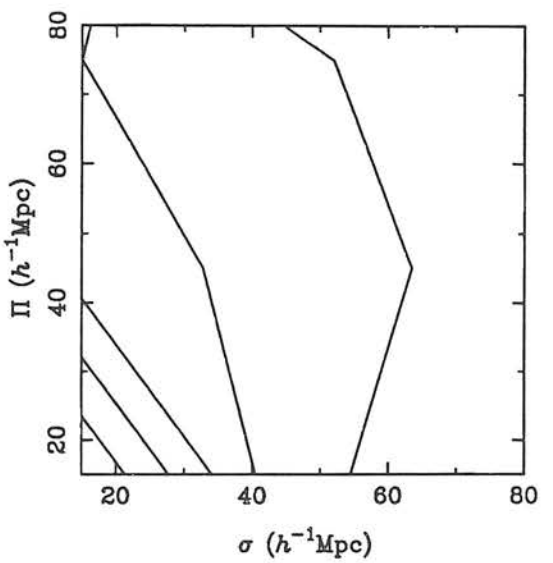

Figure 5.8: A contour plot of the 2-D correlation function derived from the Postman *et al.* (1992) statistical sample of $RC > 0$ Abell clusters, see text. The contours are separated by $\Delta\xi_{CC}(\sigma,\pi) = 0.4$, with the highest contour level lying at $\xi_{CC}(\sigma,\pi) = 2.5$. Notice the tendency for the contour lines to stretch out along the π axis.

5.3.3 A Caveat

Before completing this section it is worth pointing out that a direct comparison between our result and other determinations of $\xi_{CC}(r)$ might be misleading, due to richness dependent clustering. That there is richness dependence in the correlation function is beyond question; as shown above, single galaxies are less clustered than clusters of galaxies. However, the issue of whether there is also richness dependence in the clustering properties of clusters remains unresolved. On the theoretical side there is disagreement over whether a richness dependence can be reproduced by present models, *e.g.* Bahcall & Cen (1992, for), & Croft & Efstathiou (1994, against). On the observational side, the reliability of the measurements of large correlation amplitudes from rich clusters (Peacock & West 1992) has been called into question (Efstathiou *et al.* 1992) because these measurements rely on the Abell catalogue, which has been shown (above & § 1.3.2) to suffer from a variety of selection effects.

In light of this ongoing debate we refer the reader to a recent paper by Bahcall & Cen (1994). The authors suggest that, because of the richness dependence effect, the correlation function results from a flux-limited sample of X-ray clusters, such as ours, should not be compared directly with those from volume and richness limited optical or X-ray cluster samples, *e.g.* P92 & Nichol *et al.* (1994a). As a result, we have avoided making anything other than qualitative comparisons above. We stress here that the existence (or otherwise) of richness dependence does not compromise the ability of $\xi_{CC}(r)$ measured from flux-limited samples of X-ray clusters to put constraints on theoretical models, Mann *et al.* (1994). However, the models do need to be made specific to the sample under study, §5.4.

We present below, table 5.4, the distribution of Abell richnesses for the 115 Abell clusters in the SRCS. Notice that the modal Abell richness class in the SRCS is $RC = 1$, which is in conflict with the predictions of Bahcall & Cen (1994). We concede that it is possible that the other 39 SRCS clusters were not included in the Abell catalogues because they were too poor, *i.e.* N_{gal} was too low, and that the modal richness of our sample is, in fact, lower than $RC = 1$. However, the reader is referred to the CUOC finding charts of Abell and non-Abell SRCS clusters presented in appendix C, see table C.1 for details. The Schmidt plate material available to Abell & co-workers is reproduced, albeit in digitised form, in these finding charts. From visual inspection, the non-Abell SRCS clusters do not appear to be any different from the Abell counterparts, thus suggesting that the Abell catalogues are incomplete and *not* that the SRCS is dominated by nearby low richness systems.

Richness class	S	$RC = 0$	$RC = I$	$RC = II$	$RC = III$	$RC = IV$
No. of clusters	11	23	43	23	13	2

Table 5.4: Distribution of richness classes for 115 Abell clusters in the SRCS. (The letter S in column 2 describes supplementary clusters.)

5.4 Theoretical Implications

In chapter 1 we outlined how the study of cluster correlation functions can provide important constraints on theories of large-scale structure formation. The work presented in this thesis is primarily concerned with the development of the best possible sample of X-ray clusters with which to study large-scale structure and we will not dwell heavily on theoretical comparisons. However, for completeness we review a forthcoming paper, Mann *et al.* (1994) that is concerned with the theoretical implications of the spatial correlations presented in § 5.2.

Mann *et al.* (1994) use analytical techniques to compute the statistical and dynamical components to the clustering of a volume-limited cluster sample. To this end they employ the theory of the statistics of peaks in Gaussian random fields and the Zel'dovich Approximation to evolve the cosmological density field into the mildly non-linear regime appropriate to the present epoch cluster distribution. They then go on to make predictions, specific to the flux-limited SRCS samples, of the form of ξ_{CC} in various cosmological scenarios which takes into account richness dependence in the correlation function. (We have supplied Mann *et al.* with the details of the SRCS redshift distribution to aid their computations.)

The models that they consider all pertain to a spatially flat Universe with Gaussian, scale-invariant, initial density fluctuations. They include;

1. $\Omega_0 = 1.0$, $\lambda_0 = 0.0$, $\Gamma = 0.5$, (Model 1)
2. $\Omega_0 = 0.2$, $\lambda_0 = 0.8$, $\Gamma = 0.2$, (Model 2)
3. $\Omega_0 = 1.0$, $\lambda_0 = 0.0$, $\Gamma = 0.2$, (Model 3)
4. $\Omega_0 = 0.2$, $\lambda_0 = 0.8$, $\Gamma = 0.1$, (Model 4)

where Ω_0 represents the present mass density relative to the density required to close the Universe, equation 1.6, Γ defines the shape of the post-transition epoch (§ 1.2.4) power spectrum and $\lambda_0 = \Lambda/3H_0^2$, where Λ is the cosmological constant. Model 1 represents the standard CDM model, § 1.2.4. Model 2 is a low density CDM model

favoured by Efstathiou *et al.* (1990) for its ability to account for the strong, large angle, clustering in the APM galaxy catalogue. Model 3 is equivalent to the mixed dark matter model (30% HDM, 70% CDM), proposed by, for example, Taylor & Rowan-Robinson (1992). Model 4 was proposed by Bahcall & Cen (1992) to account for richness-dependent cluster correlation functions. All the models are normalized to the results of the CODE experiment, Smoot *et al.* (1992).

We have reproduced figure 1 of Mann *et al.* (1994) in figure 5.11. This figure shows the predictions (specific to SRCS cluster sample 6) for the cluster correlation function in models $1 \rightarrow 4$. The solid and dotted lines on these plots correspond to two different critical density contrasts; $\delta_c = 1.0$ and $\delta_c = 1.7$ respectively. (The critical density contrast refers to the enhancement that is required for a cluster sized density peak to collapse.) In these plots, the correlation amplitudes derived from SRCS sample 6 are also marked. It is apparent from these plots that the SRCS data points are not hugely inconsistent with any of the four models. This is disappointing, as it shows that the new X-ray data are not able to provide the robust constraints on theoretical models that were hoped for at the inception of the SGP RASS Cluster Project. Mann *et al.* (1994) suggest that larger, more complete samples of clusters would be required to be able to differentiate more solidly between the competing models. However, they concluded that the data seem to rule out the low density, positive cosmological constant, model 4. Despite the fact that the SRCS ξ_{CC} measurements have not provided any new theoretical constraints, they do support the constraints derived from optical cluster samples, which is itself an important result given the controversy surrounding optical cluster correlation functions, § 1.3.2.

One final point to note is that the science of theoretical modelling cluster distributions is still in its infancy. Analytical methods and n-body simulations make very naive assumptions regarding cluster formation and evolution. These assumptions may well be proved to be ill founded in light of new cluster observations, for example the baryonic mass distribution in the Coma cluster (White *et al.* 1993b) and the existence of very high redshift X-ray clusters (Castander *et al.* 1994, Nichol *et al.* 1994b). Therefore, improvements need to be made in both the X-ray cluster samples and in the theoretical predictions, before X-ray clusters can be fully exploited as cosmological diagnostics.

5.5 Summary

In this chapter we have presented the spatial correlation function results derived from 11 subsamples of SRCS clusters. From these results we have been able to conclude that the clustering properties of X-ray clusters are not strongly dependent on the selection

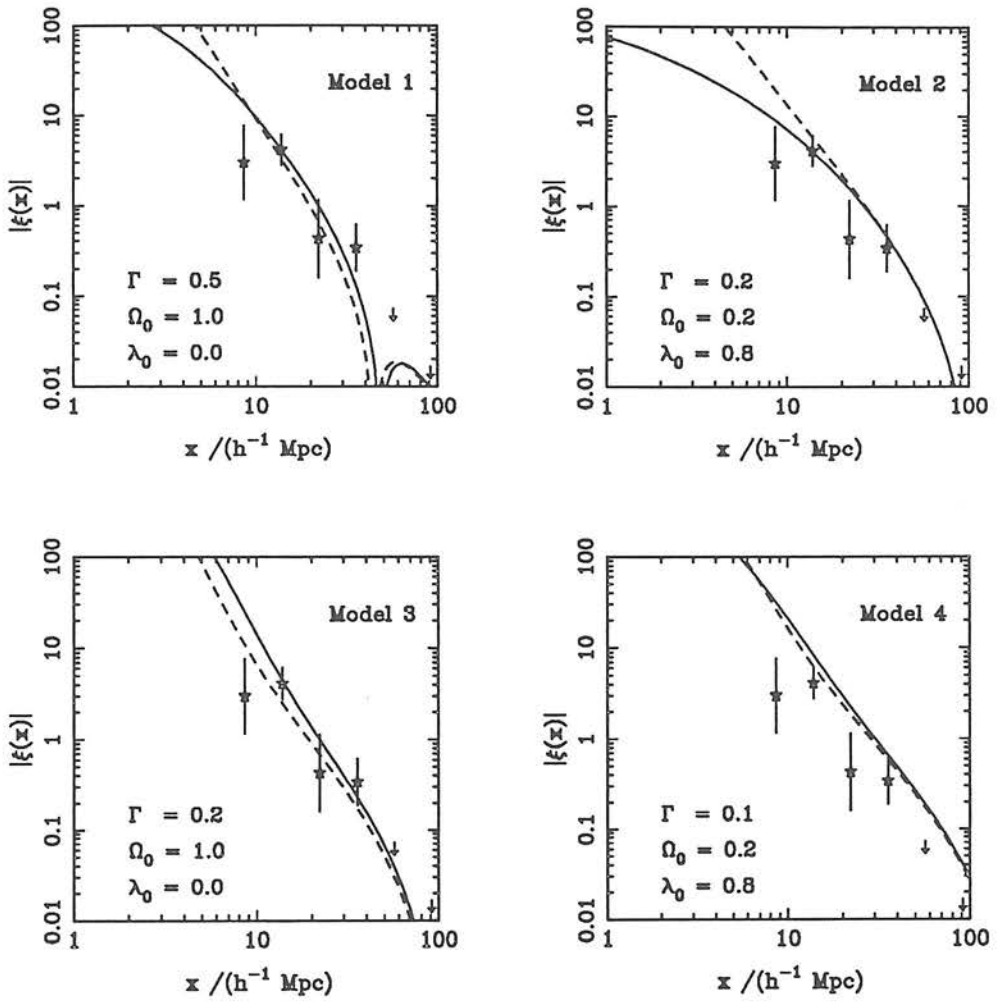

Figure 5.11 : Theoretical predictions of the X-ray cluster correlation functions in 4 different cosmological scenarios. This figure is a reproduction of figure 1 in Mann *et al.* (1994). Details of the models are given in the text. The data points refer to the correlation amplitudes derived from SRCS cluster sample 6.

method used to derive them. The size and incompleteness of the samples means that the derived correlation functions are rather noisy and, therefore, the value of the correlation length r_0 has not been clearly defined. We have found that the clustering strengths derived from any sample is strongly dependent, at large separations, on the estimation method used. We have compared the results from a single SRCS subsample, sample 6, with those from other optical and X-ray cluster samples. (Sample 6 comprises some 124 clusters is X-ray selected, via CSEARCH, and represents a SASS flux limit of $\approx 1.2 \times 10^{-12}\,\mathrm{erg\,s^{-1}\,cm^{-2}}$.) We conclude that there is evidence for artificial clustering in the Abell cluster sample of Postman *et al.* (1992). Comparisons have been made between the sample 6 ξ_{CC} results and theoretical models produced analytically by Mann *et al.* (1994). The data seem to rule out a low density, positive cosmological constant, model favoured by Bahcall & Cen (1992). However, the data provide inadequate constraints to be able to distinguish between standard CDM, mixed CDM and tilted CDM models. Larger X-ray cluster samples would be required to do so. Therefore, we plan to improve the size and completeness of the SRCS in the near future. These plans are discussed in chapter 6.

Postscript

As a postscript to this chapter we discuss the effect on ξ_{CC} of the $600 \pm 100\,\mathrm{km\,s^{-1}}$ SRCS redshift errors described in § 4.7. Such errors are equivalent to adding random peculiar velocity to the clusters. Large peculiar velocities distort redshift space and, has been shown by Bahcall *et al.* (1986), can cause line-of-sight anisotropy in the measured clustering. As no such anisotropy is seen in the SRCS correlation function, figure 5.9, we can conclude that the redshift errors are not biasing the correlation function on scales greater than $20\,h^{-1}\,\mathrm{Mpc}$. But what about smaller scales, especially the crucial regime of $10 \rightarrow 20\,h^{-1}\,\mathrm{Mpc}$ where $\xi_{CC} \simeq 1$? As $600\,\mathrm{km\,s^{-1}}$ represents $\approx 5\,h^{-1}\,\mathrm{Mpc}$ over the redshift range of the SRCS clusters, we cannot resolve two clusters in velocity space that lie $\lesssim 5\,h^{-1}\,\mathrm{Mpc}$ apart along the same line of sight. This is reflected by the fact that the closest pair of SRCS clusters lie $5.2\,h^{-1}\,\mathrm{Mpc}$ apart. However, on scales larger than $5\,h^{-1}\,\mathrm{Mpc}$, we do not expect that the redshift errors will have any significant effect on the correlation function. We have demonstrated this by predicting the number of cluster pairs that we might be "missing" at small ($r < 20\,h^{-1}\,\mathrm{Mpc}$) separations. We have constructed 100 random catalogues of 154 points in the SRCS region. The redshifts of these points were drawn from the SRCS redshift distribution after $600\,\mathrm{km\,s^{-1}}$ smoothing. It was found that the average numbers of pairs per $\Delta \log_{10}(r) = 0.2\,h^{-1}\,\mathrm{Mpc}$ bin did not vary more than 10% from those derived from the real cluster data.

We conclude that the SRCS cluster redshift errors do not have any significant effect on the measured correlation functions on scales greater than $5\,h^{-1}\,\mathrm{Mpc}$. Other projects, such as the EDCC (Nichol *et al.* 1992), have been able to probe the correlation function to smaller scales ($r \simeq 3\,h^{-1}\,\mathrm{Mpc}$) by obtaining multiple ($n \approx 10$) galaxy redshifts per cluster. Therefore, it would be advisable to obtain additional multi-object spectroscopy of SRCS clusters, especially of those with unusually large discrepancies in their galaxy redshifts.

Chapter 6

Discussion

We close this thesis with a review of the major results presented in each chapter. We make suggestions for possible improvements to the methods used in each case. We describe the planned future of the SGP RASS cluster project and its other scientific goals.

6.1 Selection of Candidates

In chapter 2 the construction of a flux-limited list of 345 SGP RASS cluster candidates was described. Three different selection techniques were used; a) CSEARCH which is an automated search for galaxy enhancements around every SGP RASS source, b) a separation analysis with the ROE/NRL optical cluster catalogue and c) the selection of all extended SGP RASS sources. In addition, only those RASS sources with hardness ratios of $HR + \delta HR > 0$ were selected. Two methods, SASS and VTP, of source count rate determination have been described and compared. In the case of the VTP analysis, only 337 of the candidates have available VTP count rates. We have investigated the effects of patchy Galactic extinction among the candidates in the flux-limited sample, and conclude that the effects are not significant. The flux-limited candidate list is expected to include $45 - 70\%$ of all $\gtrsim 1 \times 10^{-12}\,\mathrm{erg\,s^{-1}\,cm^{-2}}$ SGP RASS clusters. The contamination by non cluster sources in the candidate list is expected to be $\approx 15\%$.

From the experience gained during the SGP RASS Cluster Project, it is possible to suggest improved methods of candidate selection. Some of these suggestions will be employed to improve the SGP RASS cluster candidate list, but some will also aid other groups trying to identify cluster sources among the myriad of RASS detections.

The main stay of the candidate selection in this thesis was the CUOC. This catalogue has proved to be invaluable in the process of RASS source identifications in the southern hemisphere. It has been widely used by the various RASS working groups (cluster, quasar, stellar *etc.*) at MPE. Improvements continue to be made to this catalogue and

to the ROE/NRL cluster catalogue derived from it. If problems, such as inadequate galaxy deblending and star/galaxy separation in cluster cores, could be solved, then the efficiency of RASS cluster candidate selection must, surely improve. However, even with such improvements, the CUOC will always suffer from plate limit effects and, therefore, never be an effective tool in the process of distant cluster detection. The CSEARCH algorithm, which identified by far the most RASS clusters in the SGP region, has its strength in its simplicity. Certain sophistications have been suggested, however, and may be adopted in the near future. For example, one of the major drawbacks of the CSEARCH algorithm is its implicit assumption that the X-ray and optical cluster centres coincide. It might be possible to overcome this problem by letting the cell centre float inside the X-ray error circle so as to optimize the derived CSEARCH probability. It would also be useful if a rudimentary cluster parameterization was run at the positions of high likelihood candidates to provide background subtracted number counts, galaxy magnitude distributions *etc.*

If the scientific aims of a RASS cluster project did not require complete cluster samples, it would be possible to produce a representative, clean, sample of cluster candidates by selecting only on the basis of X-ray properties. As was shown in § 4.4, RASS sources with extents greater than $\simeq 37''$ and/or hardness ratios greater than $HR \simeq 0.5$ are highly likely to be clusters. With regard to extent selected cluster samples, they do tend to be biased in favour of low redshift clusters (figure 4.7), but not so much so that their statistical properties are significantly biased. If future RASS processing turns out to improve on SASS I in a significant way, then extent and hardness ratio selection methods may surpass the CUOC methods even with regard to number of clusters identified.

Another means by which to produce "quick and easy" cluster candidate lists is to use separation analyses with the Abell catalogues. It was shown, § 4.4.3, that candidate lists thus derived will be $\simeq 20\%$ incomplete, which is not a major concern for most purposes. In addition, Nichol *et al.* (1994a) have shown that RASS detected Abell cluster samples are purged of the Sutherland effect, § 1.3.2. There is one important point to note, however, with regard to the use of Abell selected RASS cluster samples, and that is the possibility of a new class of X-ray cluster; the X-ray bright/galaxy poor cluster. Such clusters would be massive, by virtue of their intracluster gas, but would have low Abell richnesses, if they exist in the Abell catalogue at all. Such clusters would never have been detected before RASS , because their identification requires X-ray selection, and hence good position and extent determination. One of the future goals of the SRCS is to investigate whether such clusters exist.

The RASS is by the far the best, existing, database to search for X-ray clusters,

but it is not without its problems. For example, uneven exposure. Its finite resolution also means that, even at the high Galactic latitude of the SGP region, certain X-ray sources are merged. For example source 0124051, which is thought to consist of both a white dwarf star and a cluster, § 4.4. For the SGP RASS Cluster Project the limiting sensitivity of the RASS is not a problem. In fact, it is quite helpful in reducing confusion from Galactic dwarf stars. However, if one wanted to detect a higher redshift population of clusters ($z \gtrsim 0.4$) then one would have to concentrate on the ecliptic pole regions - which have the highest RASS exposure times - or make serendipitous searches among ROSAT pointing observations. (See Bower *et al.* 1994 for a discussion of the latter technique.)

Returning again to the SGP RASS cluster candidate list described in chapter 2, its most important failing is the inaccurate flux determination. The problems with the available SASS and VTP count rate determinations make it very hard to produce a truly flux-limited sample of cluster candidates. Planned improvements in the SASS processing, will hopefully, improve on this situation.

6.2 Spectroscopic Follow-up

In chapter 3 we described the observing and reduction methods employed during the spectroscopic follow-up of SGP RASS cluster candidates. These methods are very standard and will not be discussed further. (Perhaps the only interesting fact introduced in this chapter is the proof that the cross correlation technique of redshift determination really does work!)

However, it is certainly possible to outline areas of improvement. In a very basic sense, we could have improved our observing technique by calculating appropriate exposure times for the 1992 AAT run and observed more spectral templates during the 1992 SAAO run. On a more subtle level, the observing and reduction methods were not optimized for the identification of contaminating objects in the candidate list. The fact that the identification of all $z > 0.11$ emission line galaxies (as AGN or starburst *etc.*) remains in doubt (§ 3.6.4) must be seen as a failing of the spectroscopic follow-up. In our defense, it should be stressed that we did not originally expect to find many $z > 0.1$ clusters in our sample and the chosen $3800 - 5500$Å observing window does have the advantage of being virtually free of sky lines. (For comparison, the maximum redshift of the EDCC redshift sample is $z \simeq 0.15$.) In retrospect, it would have been preferable to have sacrificed some of the spectral resolution and extended the observing window to $\gtrsim 6500\mathring{A}$. Although the accuracy of the galaxy redshifts would have been degraded, this would have minimal effect on the accuracy of the derived cluster redshifts. Because

of the limited spectral coverage of the observations, the lack of full flux-calibration in the reduction pipeline is justified - there are so few emission lines in the window that equivalent width measurements would not have aided the galaxy classification a great deal. However, flux-calibration should probably be included in the reduction of future spectroscopic measurements.

In conclusion, the spectroscopic follow-up of RASS cluster candidates did not turn out to be as trivial as we had originally hoped. The derivation of cluster redshifts was as easy as anticipated - there were usually cluster galaxies on or near the X-ray position *if* the RASS source was a cluster. However, for effective identification of contaminating objects, multi-object spectroscopy would have been a better approach. Unfortunately, multi-object spectroscopy is a costly use of limited telescope time. A compromise would be to use long-slit observations for the very likely clusters (or for that matter contaminating objects) and to opt for multi-object observations in the less obvious cases. Ways to identify high likelihood clusters and contaminating objects are discussed in the following section.

6.3 Development of the SRCS

In chapter 4 we discussed the development of the SRCS, the SGP RASS Cluster Sample, which comprises of some 154 X-ray clusters with redshifts. This is the largest X-ray selected X-ray cluster sample constructed to date and yet it only constitutes $\approx 50\%$ of the $f_X \gtrsim 1 \times^{-12}$ erg s^{-1} cm^{-2} RASS cluster candidates identified in the SGP region. Part of the reason why so few of the candidates were observed during the spectroscopic campaign, and hence identified as clusters or contaminating objects, was the late change made to the SASS determined count rates, § 2.4.2. However, another stumbling block was that we had to assume that every candidate had a high probability of being a contaminating object and, hence, laboriously follow-up faint objects in the X-ray error circle in case they turned out to be AGN, BL Lac's *etc.*

It would be possible in future to remove some of the contamination in the candidate list prior to observations by a) performing separation analyses with identified RASS AGN and stars and b) by utilizing X-ray to optical flux ratios. The latter information is now becoming available to the SGP RASS Cluster Project from the Fleming *et al.* ESO Key-Project. This key project has made comprehensive identifications of *all* RASS sources in selected regions and provides invaluable information on the statistical probability that certain optical objects within the X-ray error circle are responsible for the X-ray source. (Similar statistics were used during the construction of the EMSS, Stocke *et al.* 1991.)

One additional piece of information that could be used to aid future spectroscopic

follow-ups is the finding (§ 4.1.2) that if a CUOC object lies exactly on the X-ray position then that object will be associated with the X-ray source, whether source is a cluster, a star or an AGN.

It was shown in § 4.2.1 that certain SGP RASS cluster candidates seem to be associated with both a contamination object (white dwarf or AGN) and a cluster. Both white dwarfs and AGN can have fluxes that are below the flux-limit of our sample, in which case we would be wrong in excluding the associated cluster from the SRCS. Again the X-ray to optical flux ratios will play a vital role in helping differentiate between X-ray faint and X-ray bright point sources. In addition, it is planned to make photon maps around each SRCS cluster. These maps will be very low resolution, but may be able to differentiate between clusters dominated by central point source emission and those dominated by intracluster gas emission.

6.4 The X-ray Cluster Correlation Function

In chapter 5 we presented the spatial correlation function results derived from 11 subsamples of SRCS clusters. From these results we have been able to conclude that the clustering properties of X-ray clusters are not strongly dependent on the selection method used to derive them. The size and incompleteness of the samples means that the derived correlation functions are rather noisy and, therefore, the value of the correlation length r_0 has not been clearly defined. We conclude that there is evidence for artificial clustering in the Abell cluster sample of Postman *et al.* (1992), based on the results from the two dimension correlation function, $\xi_{CC}(\sigma, \pi)$.

Comparisons have been made between the ξ_{CC} results from SRCS subsample 6 and from theoretical models produced analytically by Mann *et al.* (1994). The data seem to rule out a low density, positive cosmological constant, model favoured by Bahcall & Cen (1992). However, the data provide inadequate constraints to be able to distinguish between standard CDM, mixed CDM and tilted CDM models. Larger X-ray cluster samples would be required to do so. Therefore, we plan to improve the size and completeness of the SRCS in the near future. Telescope time has already been secured for Fall 1994 to continue the spectroscopic follow-up of SGP RASS cluster candidates. With the improved X-ray information now becoming available, future follow-up campaigns should be more efficient than those in the past. The forthcoming observations will provide larger, more complete, redshift samples of X-ray clusters with which to constrain theories of large-scale structure formation.

With larger samples, it will be possible to look for second order effects in the X-ray cluster clustering properties, such as luminosity and redshift dependence. It may also

be possible to construct volume limited samples of clusters - which are easier to model theoretically than flux-limited samples.

6.4.1 Romer *et al.* 1994

The correlation function results presented in chapter 5 of this thesis have been written up as a letter to *Nature*, Romer *et al.* (1994). This letter is still at the (third) referee stage, but has been provisionally accepted for publication. The preprint will not be appended to this thesis, as final changes still need to be made to the manuscript. However, it is worth making some comparisons between the results presented in chapter 5 with those presented in Romer *et al.* (1994). Firstly, the sample of clusters used in Romer *et al.* (1994) does *not* constitute one of the eleven samples discussed in table 4.7. The candidate list from which the Romer *et al.* (1994) cluster sample was, instead, developed using the following criteria;

1. CSEARCH and ROE/NRL separation analysis contamination levels of $< 20\%$. (Extended clusters that were not flagged by either CSEARCH or the separation analysis were *not* included in the candidate list.)

2. A SASS determined count rate limit of $> 0.1\,s^{-1}$, where the version of the SASS processing used was that *before* the second vignetting correction was made, see § 2.4.2

From these criteria, a SGP RASS cluster candidate list was developed with 199 entries. Of these, 128 were identified as clusters with redshifts and 38 as contaminating objects. The methods used to classify clusters and contaminating objects and to assign cluster redshifts were less sophisticated than those employed in chapter 4. However, this has been shown not to make any significant difference to the derived clustering properties of the sample. The only real difference between the Romer *et al.* (1994) sample and, say sample 1 in table 4.7, is that the completeness was *over* estimated in the letter. The reason for this error, was the late notification, by MPE, of the change in the SASS fluxes described in § 2.4.2. To date, the authors of Romer *et al.* (1994) have opted to retain the 80% completeness value quoted in the original version of the letter. The conclusions of Romer *et al.* (1994) are exactly the same as those drawn in § 5.3 and § 5.4 of this thesis.

6.5 The Future of the SGP RASS Cluster Project

We have described above how improvements to the selection process, spectroscopic follow-up and candidate classification methods are expected to increase the size and

quality of the SRCS over the coming years. These improvements are summarized below in the context of the paper (Voges *et al.*) in which the final SRCS will be presented. The authors of that paper will include; Voges, Böhringer, Collins, Cruddace, Ebeling, Gursky, MacGillivray, Romer, & Yentis. This paper will draw on new information that was not available to the author of this thesis, for example;

- Photon maps of the cluster candidates.
- Accurately determined source fluxes.
- SASS II processing.
- An improved CSEARCH algorithm
- The results from the Fleming *et al.* ESO Key-Project including X-ray to optical flux measurements.
- New spectroscopic data.

Throughout this thesis I have tried to emphasize the work that was done by my collaborators (listed above) with regard to the development of the SGP RASS cluster candidate list. However, I want to re-iterate their involvement here.

- The RASS data: I am very grateful to the director of the ROSAT project, Prof. J. Trümper, and to the manager of the SASS processing team, Wolfgang Voges, for allowing me access to the ROSAT All-Sky Survey data in the SGP region.
- The CUOC: The CUOC digitised object catalogue, and the ROE/NRL cluster catalogue derived from it, provides the backbone of SGP RASS cluster candidate selection in this thesis. It is the result of many years of labour by Harvey MacGillivray & co-workers at ROE and by Darryl Yentis, John Wallin, Brad Stuart & others at NRL.
- CSEARCH: The CSEARCH algorithm was conceived by Chris Collins and designed by Darryl Yentis. All CSEARCH processing of SGP RASS sources was performed at MPE by Ray Cruddace.
- Separation Analyses: The results from separation analyses between SGP RASS source positions and several (Abell, EDCC, APM & ROE/NRL) optical cluster samples were utilized in this thesis. The analysis was performed at MPE by Harald Ebeling in each case.

- VTP Analysis: VTP processing of SGP RASS cluster candidates was performed by Harald Ebeling at MPE.

- CUOC finding charts: the finding charts presented in Appendix C form only a subset of the many used during the spectroscopic follow-up. These charts were produced at MPE, almost exclusively, by Ray Cruddace.

The final SRCS will be used for a variety of investigations, including the improved ξ_{CC} measurements described in § 6.4. We outline here some of the other investigations to which the SRCS will be applied;

1. Evolution in the X-ray Cluster Luminosity Function. With improved source count rates, it will be possible to derive accurate cluster luminosities and thus study evolution in our cluster sample. The fact that our sample is both larger and more homogeneous than those previously used to study luminosity evolution (Henry *et al.* 1992 & Edge *et al.* 1990, see table 4.8) means that we will be in a very strong position to test the reliability of this controversial observation.

2. X-ray to optical properties of clusters. To this end we will use overlaps with the APM and EDCC cluster catalogues to provide optical descriptions of the X-ray clusters in the SRCS. The best presently available X-ray to optical correlations (Edge & Stewart 1991) rely on only 37 clusters. Our sample will provide an obvious, long overdue, improvement.

3. An investigation into the Butcher Oemler Effect in X-ray selected clusters. This investigation has already begun. We have obtained multi-colour photometry for $\sim$ 20 SRCS clusters and we will use these images to correlate X-ray luminosity with blue galaxy fraction.

4. Searches for distant and/or galaxy poor, X-ray clusters. An imaging campaign is already under way to follow-up extended SGP RASS sources that were not picked out by CSEARCH as being associated with galaxy overdensities. These sources are potentially very interesting clusters, either because they are distant (*i.e.* below the plate limit) or because they are intrinsically galaxy poor.

Acknowledgements

First I am indebted to my thesis advisor Chris Collins; for involving me in such an important project, for his unique approach to supervision (guidance and trust without micro-management), for putting a roof over my head when I was homeless and for *not* telling me he was afraid of the dark whilst we were lost in the Australian Outback after nightfall! To my other collaborators, I acknowledge all their hard work (see § 6.5) on the project. A special mention has to go to Harald who has been a very loyal friend through some very hard times.

For financial support; SERC (grant 90300619), Mel Ulmer, Bob Nichol, Conrad Romer, John Romer, Lloyds Bank, Citibank & the DHSS.

I must recognise the astounding hospitality extended to me during the 18 months of my stay at Durham Physics Department by Prof Richard Ellis and Prof Carlos Frenk and the rest of Extragalactic Astronomy group (especially Jane!). To Prof Mel Ulmer I express enormous gratitude. He saved me from a life on the dole in Durham, gave me an office, a desk, a computer, a salary and a future.

For computer support; Karl Glazebrook, Alan Lotts, Jim Pendleton ("Read NEWS!"), Bob Nichol and, of course, to the original World Wide Web'er, Mr Piers O'Hanlon. Many thanks go to Bob Mann, for being my "theory guru", and to Alan Heavens who has the been landed with "binding and submission".

For sheer, soap opera entertain value, thank you to that mad bunch; the Romer family (including Mike and Jo). Three very special friends also deserve a mention on this page; Isabelle, Piers and Bob. They believed in me long after I stopped believing in myself. Without Bob, the most special of them all, I wouldn't have had clean laundry, hot meals or any fun during the last months. In addition he has patiently read my chapters over and over, always providing expert guidance without ever breaking the rules of the game. As the final, hideous[1] weekend draws to a close, I recognise that I'd have never made it without him.

[1] Not without its highlights none the less!

References

Abell, G.O., 1958, *Ap. J. Supp.*, **3**, 211.

Abell, G.O., Corwin, H.G., Olowin, R.P., 1989, *Ap. J. Supp.*, **70**, 1.

Abramopoulos, F., Ku, W.H., 1983, *Ap. J.*, **271**, 446.

Alcock, C., Akerlof, C.W., Allsman, R.A., Axlerod, T.S., Bennett, D.P., Chan, S., Cook, C.H., Freeman, K.C., Griest, K., Marshall, S.L., Park, H.S., Perlmutter, S., Peterson, B.A., Pratt, M.R., Quinn, P.J., Rodgers, A.W., Stubbs, C.W., Sutherland, W., 1993, *Nature*, **365**, 621.

Aschenbach, B., 1988, Appl. Optics, **27**, 1404.

Bahcall, N.A., Soneira, R.M., 1983, *Ap. J.*, **270**, 20.

Bahcall, N.A., Burgett, W.S., 1986, *Ap. J.*, **300**, L35.

Bahcall, N.A., Soneira, R.M., Burgett, W.S., 1986, *Ap. J.*, **311**, 15.

Bahcall, N.A., Cen, R., 1992, *Ap. J.*, **398**, L81.

Bahcall, N.A., Cen, R., 1994, *Ap. J.*, **462**, L15.

Bahcall, N.A. & Lubin, L.M., 1994, *Ap. J.*, **426**, 513.

Baldwin, J.A., Phillips, M.M., Terlevich, R., 1981, *Pub. Astr. Soc. Pac.*, **551**, 5.

Bardeen, J.M., Steinhardt, P.J. & Turner, M.S, 1983, *Phys. Rev. D.*, **28**, 679.

Beard, S.M., MacGillivrary, H.M., Thanisch, P.F., 1990, *Mon. Not. R. Ast. Soc.*, **247**, 311.

Blumenthal, G.R., Faber, S.M., Primack, J.R., Rees, M.J., 1984, *Nature*, **311**, 5.

Böhringer, H., Schwarz, R.A., Briel, U.G., Voges, W., Ebeling, H., Hartner, G., Cruddace, R.G., 1992, in *Clusters and Superclusters of Galaxies*, (Kluwer, Dordrecht), 49.

Börner, G., 1988, *The Early Universe*, (Springer-Verlag).

Bottinelli, L., Gougenheim, L., Fouqué, P., Paturel, G., 1990, *Astron. & Astrophys. Supp.*, **82**, 391.

Bower, R.G., Böhringer, H., Briel, U.G., Ellis, R.S., Castander, F.S., Couch, W.J., 1994, *Mon. Not. R. Ast. Soc.*, **268**, 345.

Briel, U.G., Pfefferman, E., 1986, *Nucl. Inst. & Methods in Phys. A*, **242**, 376.

Briel, U.G., Henry, J.P., Schwarz, R.A., Böhringer, H., Ebeling, H., Edge, A.C., Hartner, G.D., Schindler, S., Trümper, J., Voges, W., 1991, *Astron. & Astrophys.*, **246**, L10.

Briel, U.G., Henry, P., 1993, *Astron. & Astrophys.*, **278**, 379.

Broadhurst, T.J., Ellis, R.S., Koo, D.C., Szalay, A.S., 1990, *Nature*, **343**, 726.

Burns, J., Roettinger, K., Ledlow, M., Klypin, A., 1994, *Ap. J.*, **427**, L87.

Caldwell, N., Rose, J.A., Sharples, R.M., Ellis, R.S., Bower, R.G., 1993, *Ap. J.*, **106**, 473

Cannon, R.D., Hawarden, T.G., Sim, E., Tritton, S.B., 1978, *The UK 1.2m Schmidt telescope and Southern Sky Survey Survey. II*, (Royal Observatory Edinburgh).

Castander, F.J., Ellis, R.S., Frenk, C.S., Dressler, A., Gunn, J.E., 1994, *Ap. J.*, **424**, L79.

Comastri, A., Setti, G., Giovanni, Z., Elvis, M., Giommi, P., Wilkes, B.J., McDowell, J.C., 1992, *Ap. J.*, **384**, 62.

Corwin, H.G., Emerson, D., 1982, *Mon. Not. R. Ast. Soc.*, **200**, 621.

Costero, R., Osterbrock, D.E., 1977, *Ap. J.*, **211**, 675.

Couch, W.J., Sharples, R.M., 1987, *Mon. Not. R. Ast. Soc.*, **229**, 423.

Couch, W., Ellis, R.S., Sharples, R.M., Smail, I., 1994, *Ap. J.*, **430**, 121.

Crawford, C.S., Fabian, A.C., 1992, *Mon. Not. R. Ast. Soc.*, **259**, 265.

Crawford, C.S., Edge, A.C., Fabian, A.C., Allen, S.W., Böhringer, H., Ebeling, H., McMahon, R.G., Voges, W., 1994, *Mon. Not. R. Ast. Soc.*, preprint.

Croft, R.A.C., Efstathiou, G., 1994, *Mon. Not. R. Ast. Soc.*, **267**, 390.

Cruddace, R.G., Hasinger, G., Trümper , J., Schmidt, J.H.M.M., Hartner, G.D., Rosso, C., Snowden, S.L., 1991, *Exp. Astr.*, **1**, 365.

Dalton, G.B., Efstathiou, G., Maddox, S.J., Sutherland, W.J., 1992, *Ap. J.*, **390**, L1.

Dalton, G.B., 1992, *PhD thesis*, Oxford University.

David, L.P., Slyz, A., Jones, C., Forman, W., Vrtilek, S.D., Arnaud, K.A., 1993, *Ap. J.*, **412**, 479.

Davis, M., Peebles, P.J.E., 1983, *Ap. J.*, **267**, 465.

Dekel, A., 1984, *Ap. J.*, **284**, 445.

Dekel, A., Blumenthal, G.R., Primack, J.R., Olivier, S., 1989, *Ap. J.*, **338**, L5.

Dekel, A., 1994, *Ann. Rev. Astron. Astrophys.*, **32**.

de Lapparent, V., Geller, M.J., Huchra, J.P., 1986, *Ap. J.*, **302**, L1.

de Vaucouleurs, G., de Vaucouleurs, A., Corwin, H.G., Jr., Buta, R.J., Paturel, G., Fouqué, P., 1991, *Third Reference Catalogue of Bright Galaxies*, (Springer-Verlag).

Dodd, R.J. & MacGillivray, H.M., 1986, *Astron. J.*, **28**, 215.

Ebeling, H., Voges W., Böhringer, H., Edge, A.C., 1992, *Astron. & Astrophys.*, **275**, 360.

Ebeling, H., Wiedenmann, G., 1993, *Phys. Rev. E*, **47**, 704.

Ebeling, H., 1994, *PhD Thesis*, Max-Planck-Institut für Extraterrestrische Physik.

Edge, A.C., Stewart, G.C., Fabian, A.C., Arnaud, K.A., 1990, *Mon. Not. R. Ast. Soc.*, **245**, 559.

Edge, A.C., Stewart, G.C., 1991, *Mon. Not. R. Ast. Soc.*, **252**, 428.

Efstathiou, G., 1990, in *Physics of the Early Universe*, *Proc. of the* 36^{th} *Scottish Universities Summer School in Physics*, (Edinburgh University).

Efstathiou, G., Sutherland, W.J., Maddox, S.J., 1990, *Nature*, **348**, 705.

Efstathiou, G., Dalton, G.B., Sutherland, W.J., Maddox, S.J., 1992, *Mon. Not. R. Ast. Soc.*, **257**, 125.

Evrard, A.E., Henry, J.P., 1991, *Ap. J.*, **383**, 95.

Fabbiano, G., 1989, *Ann. Rev. Astron. Astrophys.*, **27**, 87.

Fich, M. & Tremaine, S., 1991, *Ann. Rev. Astron. Astrophys.*, **29**, 409.

Fisher, K.B., Davis, M., Strauss, M.A., Yahil, A., Huchra, J.P., 1993, *Ap. J.*, **405**, 42.

Frenk, C.S., White, S.D.M., Efstathiou, G., Davis, M., 1990, *Ap. J.*, **351**, 10.

Frieman, J.A., 1994, *The Standard Cosmology*, (FERMILAB-Conf-94/090-A).

Fruscione, A., Griffiths, R.E., 1991, *Ap. J.*, **380**, L13.

Gioia, I.M., Maccacaro, T., Schild, R.E., Wolter, A., Stocke, J.T., Morris, S.L., Henry, J.P., 1990, *Ap. J. Supp.*, **72**, 567.

Griffiths, R.E., Padovani, P., 1990, *Ap. J.*, **360**, 483.

Gunn, J.E., Hoessel, J., & Oke, J.B., 1986, *Ap. J.*, **306**, 60.

Gursky, H., Kellogg, E., Leong, C., Tananbaum, H., Giaconni, R., 1971, *Ap. J.*, **167**, L81.

Gursky, H., Cruddace, R.G., Stuart, B.V., Yentis, D.J., MacGillivray, H.T., Collins, C.A., 1992, in *Digitised Optical Sky Surveys*, (Kluwer, Dordrecht), 67.

Guth, A., 1981, *Phys. Rev. D*, **23**, 347.

Hamilton, A.J.S., 1993, *Ap. J.*, **417**, 19.

Heavens, A.F., 1993, *Mon. Not. R. Ast. Soc.*, **263**, 735.

Henry, J.P., Gioia, I.M., Maccacaro, T., Morris, S.L., Stocke, J.T., Wolter, A., 1992, *Ap. J.*, **386**, 408.

Henry, J.P., 1992, in *Clusters and Superclusters of Galaxies*, (Kluwer, Dordrecht), 311.

Hewett, P.C., 1982, *Mon. Not. R. Ast. Soc.*, **201**, 867.

Heydon-Dumbleton, N.H., Collins, C.A., MacGillivray, H.T., 1989, *Mon. Not. R. Ast. Soc.*, **238**, 379.

Horne, K., 1986, *Pub. Astr. Soc. Pac.*, **98**, 609.

Huchra, J.P., Henry, J.P., Postman, M., Geller, M.J., 1990, *Ap. J.*, **365**, 66.
Ikebe et.al., 1992, Ap. J., 384, L5.
Jacoby, G. H., Branch, D., Clardullo, R., Davies, R.L., Harris, W.E., Pierce, M.J., Pritchet, C.J., Tonry, J.L., Welch, D.L., 1992, *Pub. Astr. Soc. Pac.*, **104**, 559.

Jing, Y.P., Plionis, M., Valdarnini, R., 1992, *Ap. J.*, **389**, 499.

Jones, C. & Forman, W., 1978, *Ap. J.*, **224**, 1.

Jones, C. & Forman, W., 1984, *Ap. J.*, **276**, 38.

Jones, C. & Forman, W., 1992, in *Clusters and Superclusters of Galaxies*, (Kluwer, Dordrecht), 49.

Jorden, A.R., Read, P.D., van Breda, I.G., 1982, *SPIE*, **331**, 368.

Kaiser, N., 1984, *Ap. J.*, **284**, L9.

Klypin, A., Rhee, G., 1994, *Ap. J.*, preprint.

Koo, D.C. & Kron, R., 1987, in *Observational Cosmology*, (Reidel, Dordrecht), 383.

Kowalski, M.P., Ulmer, M.P., Cruddace, R.G., Wood, K.S., 1984, *Ap. J. Supp.*, **56**, 403.

Lamb, D.Q., Quashnock, J.M., 1993, *Ap. J.*, **415**, L1.

Landy, S.D., Szalay, A.S., 1993, *Ap. J.*, **412**, 64.

Lahav, O., Edge, A.C., Fabian, A.C., Putney, A., 1989, *Mon. Not. R. Ast. Soc.*, **238**, 881.

Ling, E.N., Frenk, C.S., Barrow, J.D., 1986, *Mon. Not. R. Ast. Soc.*, **223**, L21.

Loveday, J., Maddox, S.J., Efstathiou, G., Peterson, B.A., 1994, *Ap. J.*, preprint.

Lu, N.Y., Houck, J.R., Salpeter, E.E., Lewis, B.M., 1992, *Astron. J.*, **104**, L1505.

Lumsden, S.L., Nichol, R.C., Collins, C.A., Guzzo, L., 1992, *Mon. Not. R. Ast. Soc.*, **258**, 1.

Lucey, J. R., 1983, Mon. Not. R. Ast. Soc, 204, 33.

MacGillivray, H.M. & Stobie, R.S., 1984, *Vista. Astr.*, **27**, 433.

Maddox, S.J., Efstathiou, G., Sutherland, W.J., Loveday, J., 1990, *Mon. Not. R. Ast. Soc.*, **242**, L43.

Mann, R.G., Heavens, A.F., Peacock, J.A., 1993, *Mon. Not. R. Ast. Soc.*, **263**, 798.

Mann, R.G., 1994, *PhD Thesis*, Edinburgh University.

Mann, R.G., Romer, A.K., Heavens, A.F., Collins, C.A. & Peacock, J.A., 1994, *Mon. Not. R. Ast. Soc.*, preprint.

McHardy, I.M., Lawrence, A., Pye, J.P., Pounds, K.A., 1981, *Mon. Not. R. Ast. Soc.*, **197**, 893.

Mo, H.J., Jing, Y.P., Börner, G., 1992, *Ap. J.*, **392**, 452.

Morrison, R., McCammon, D., 1983, *Ap. J.*, **270**, 119.

Mould, J.R., Han, M.S., Roth, J., Staveley-Smith, L., Schrommer, R., A., Bothun, G.D., Hall, P.J., Huchra, J.P., Walsh, W., Wright, A.E., 1991, *Ap. J.*, **383**, 467.

Mushotzky, R.F., 1994, in New Horizons of X-ray Astronomy, preprint.

Mushotzky, R.F.,1992, in *Clusters and Superclusters of Galaxies*, (Kluwer, Dordrecht), 91.

Nichol, R.C., Collins, C.A., Guzzo, L., Lumsden, S.L., 1992, *Mon. Not. R. Ast. Soc.*, **255**, L21.

Nichol, R.C., 1992, *PhD Thesis*, Edinburgh University.

Nichol, R.C., Briel, U.G., Henry, J.P., 1994a, *Mon. Not. R. Ast. Soc.*, **267**, 771.

Nichol, R.C., Ulmer, M.P., Kron, R.G., Wirth, G.D., Koo, D.C., 1994b, *Ap. J.*, in press.

Parker, Q.A., Beard, S.M., MacGillivray, H.T., 1987, *Astron. & Astrophys.*, **173**, L5.

Peacock, J.A., 1991, *Mon. Not. R. Ast. Soc.*, **253**, L1.

Peacock, J.A., Nicholson, D., 1991, *Mon. Not. R. Ast. Soc.*, **253**, 307.

Peacock, J.A., West, M.J., 1992, *Mon. Not. R. Ast. Soc.*, **259**, 494.

Peebles, P.J.E., 1980, *The Large-Scale Structure of the Universe*, (Princeton University Press).

Peebles, P.J.E., 1993, *Principles of Physical Cosmology*, (Princeton University Press).

Piccinotti, G., Mushotzky, R.F., Boldt, E.D., Holt, S.S., Marshall, F.E., Serlemitsos, P.J., Shafer, R.A., 1982, *Ap. J.*, **253**, 485.

Plucinsky, P.P., Snowden, S.L., Briel, U.G., Hasinger, G., Pfefferman, E., 1993, *Ap. J.*, **418**, 519.

Postman, M., Huchra, J.P., Geller, M.J, 1992, *Ap. J.*, **91**, 1267.

Rosner, R., Golub, L., Vaiana, G.S., 1985, *Ann. Rev. Astron. Astrophys.*, **23**, 413.

Romer, A.K., Collins, C.A., Böhringer, H., Cruddace, R.G., Ebeling, H., MacGillivray, H.T., Voges, W., 1994, *Nature*, 372, 75.

Romer, A.K., 1994, *PhD Thesis*, Edinburgh University.

Sarazin, C.L., 1988, *X-ray Emissions from clusters of Galaxies*, (Cambridge University Press), 131.

Sarazin, C.L., 1992, in *Clusters and Superclusters of Galaxies*, 131, (Kluwer, Dordrecht).

Schectman, S. A., 1985, *Ap. J. Supp.*, **57**, 77.

Schramm, D., 1990, in *Astrophysical Ages and Dating Methods*, (Editions Frontieres, Gif-sur-Yvette).

Schwartz, D.A., Ku, W.H.M., 1983, *Ap. J.*, **266**, 459.

Shandarin, S.F., Doroshkevich, A.G., Zeldóvich, Ya. B., 1983, *Sov. Phys. Usp.*, **26**, 46.

Smoot, G.F., Bennet, C.L., Kogut, A., Wright, E.L., Aymon, J., Boggess, N.W., Cheng, E.S., De Amici, G., Gulkis, S., Hauser, M.G., 1992, *Ap. J.*, **396**, L1.

Snowden, S.L., Plucinsky, P.P., Briel, U., Hasinger, G., Pfeffermann, E., 1992, *Ap. J.*, **393**, 819.

Snowden, S.L. & Freyberg, M.J., 1993, *Ap. J.*, **404**, 403.

Stark, A.A., Gammie, C.F., Wilson, R.W., Bally, J., Linke, R.A., Heiles, C., Hurwitz, M., 1992, *Ap. J. Supp.*, **79**, 77.

Stocke, J.T., Morris, S.L., Gioia, I.M., Maccacaro, T., Schild, R.E., Wolter, A., Flemming, T.A., Henry, J.P., 1991, *Ap. J. Supp.*, **76**, 813.

Struble, M.F. & Rood, H.J., 1987, *Ap. J. Supp.*, **63**, 543.

Sutherland, W., 1988, *Mon. Not. R. Ast. Soc.*, **234**, 159.

Thanisch, P., McNally, B.V., Robin, A., 1984, *Image Vis. Comp.*, **2**, 191.

Tonry, J.L., Davis, M., 1979, *Astron. J.*, **84**, 1511.

Taylor, A.N., & Rowan-Robinson, M., 1992, *Nature*, **359**, 362.

Ulmer, M.P., Wirth, G.D., Kowalski, M.P., 1992, *Ap. J.*, **397**, 430.

Voges, W., 1992, in *Proceedings of Satellite Symposium 3: Space Sciences with particular emphasis on High-Energy Astrophysics, from the International Space Year Conference* (ESA), 9.

Voges, W., Gruber, R., Paul, J., Bickert, K., Bohnet, A., Bursik, J., Dennerl, K., Englhausser, J., Hartner, G., Jennert, W., Köhler, H., Rosso, C. , 1992, in *Proceedings of Satellite Symposium 3: Space Sciences with particular emphasis on High-Energy Astrophysics, from the International Space Year Conference* (ESA), 223.

Warwick, R.S., Marshall, N., Fraser, G.W., Watson, M.G., Lawrence, A., Page, C.G., Pounds, K.A., Ricketss, M.J., Sims, M.R., Smith A., 1981, *Mon. Not. R. Ast. Soc.*, **197**, 865.

Weinberg, S., 1972, *Gravitation and Cosmology*, (John Wiley & Sons, New York.)

White, S.D., Briel, U.G., Henry, J.P., 1993a, *Mon. Not. R. Ast. Soc.*, **261**, L8.

White, S.D.M., Navarro, J.F., Evrard, A.E., Frenk, C.S., 1993b, *Nature*, **366**, 429.

Yentis, D.J., Cruddace, R.G., Gursky, H., Stuart, B.V., Wallin, J.F., MacGillivray, H.T., & Collins, C.A., 1992, in *Digitised Optical Sky Surveys*, (Kluwer, Dordrecht), 67.

Zabludoff, A.I., Huchra, J.P., Geller, M.J., 1990, *Ap. J. Supp.*, **74**, 1.

Zel'dovich, Ya. B., 1970, *Astron. & Astrophys.*, **5**, 84

Zwicky, F., 1933, *Helv. Phys. Acta.*, **6**, 110

Appendix A

Flux-Limited List of SGP RASS Cluster Candidates

The flux-limited SGP RASS cluster candidate list is presented in this appendix. The methods used to construct this candidate list are described in chapter 2. The processes by which certain candidates have been identified with clusters, AGN *etc.* are described in chapter 4. Note that table A.2 does *not* constitute the final results from the SGP RASS Cluster Project. Over the coming months improvements will be made to the selection process and the RASS data processing. In addition the spectroscopic follow-up will be extended. Therefore, the data presented in this appendix should be taken as preliminary. Note that; a) when a candidate has a redshift available in both the literature and from our own spectroscopic follow-up, the value adopted for the candidate is marked in either column 9 or 11 with a * and b) the superscript in column 11 provides a key to the source of the literature redshift information, see table A.1 below.

Code	Explanation
A	Andernach Listing (Andernach *et al.*)
APM	APM cluster survey (Dalton *et al.*)
C	ROSAT Bright Cluster sample (Crawford *et al.* 1994)
E	Redshift from the EDCC cluster survey (Nichol 1992)
Ep	Redshift from the EDCC cluster literature search (Nichol 1992)
H	Z-CAT (Huchra *et al.*)

Table A.1: Key the source of the literature cluster redshifts listed in table A.2.

Explanation of the Columns in Table A.2

(1) MASOL identification number for the RASS source, see § 2.1.1.

(2) Right ascension (J2000, degrees) of the RASS source.

(3) Declination (J2000,degrees) of the RASS Source.

(4) Candidate has CSEARCH contamination value $< 15\%$ (•).

(5) Candidate has a $> 85\%$ probability of being associated with a ROE/NRL optical cluster (•).

(6) Candidate has a measured SASS extent (•).

(7) RASS source has a SASS determined count rate greater than $0.07\,s^{-1}$ (•).

(8) RASS source has either a VTP determined count rate greater than $0.1\,s^{-1}$ (•) or no VTP count rate is available (o).

(9) Redshift of source named in column 16, as determined from the spectroscopic followup, z_{SF}.

(10) The number of galaxy spectra used to determine z_{SF}.

(11) Literature redshift for an optical cluster associated with a RASS source, z_{lit}.

(12) The number of galaxies used to determine z_{lit}.

(13) The optical cluster associated with the RASS source. The prefix "A" indicates a regular Abell cluster, a "S" indicates a supplementary Abell cluster, "E" indicates an EDCC cluster and "APM" indicates an APM cluster, see § 1.3.1 for references. Note that all Abell (regular & supplementary) clusters associated with SGP RASS cluster candidates have been listed. However, for simplicity, only those APM and EDCC clusters with z_{lit} that are not also Abell clusters are listed.

(14) The separation (arc seconds) between the optical cluster and the RASS source position.

(15) An identification flag, 1 → 9, the details of which are given in § 4.1.3, 4.2.3, 4.3. The salient points are summarized below;

Flag 1: Cluster with secure identification and reliable redshift.

Flag 2: Unconfirmed cluster with reliable redshift.

Flag 3: Unconfirmed cluster with unreliable redshift.

Flag 4: Only marginal evidence to support cluster identification.

Flag 5: No spectroscopic information available, but candidate "looks" like a cluster in the CUOC.

Flag 6: Candidate with no spectroscopic information available.

Flag 7: Unidentified candidate with available spectroscopic information.

Flag 8: Confirmed contaminating object.

Flag 9: Unconfirmed contaminating object.

(16) The type of X-ray object (cluster, AGN, star) thought to be responsible for the RASS source.

(1)	(2)	(3)	(4)	(5)	(6)	(7)	(8)	(9)	(10)	(11)	(12)	(13)	(14)	(15)	(16)
MASOL	Coordinates (2000)		Criteria			Flux		z_{SF}	n_{gal}^{SF}	$z_{lit}^{(ref)}$	n_{gal}^{lit}	optical	Δ	id.	source
no.	α (°)	δ (°)	C	R	E	S	V					cluster	($''$)	no.	type
0011003	0.9583	2.0660	•	-	-	•	•	0.0994*	2	0.0978^{A}	1	A2700	30	2	cluster
0014037	29.2917	-47.3848	•	-	•	•	-							6	
0014055	21.5217	-37.9665	•	•	-	-	•			0.0797^{A}	8	A2911	39	2	cluster
0014072	14.3596	-26.3025	•	•	•	•	•	0.1117*	2	0.1130^{Ep}	2	A122	81	1	cluster
0014079	11.8808	-25.2871	-	-	•	•	○							6	
0014089	11.1846	-22.0074	•	-	•	•	○							6	
0014095	10.8529	-20.6238	•	-	•	•	•					A2813	24	6	
0014117	7.5921	-12.9181	•	-	•	•	-			0.1500^{A}	2	A46	200	3	
0014145	3.3279	-5.3754	•	-	•	•	-							5	
0014147	2.5412	-4.7073	•	-	•	•	○							6	
0024065	18.4762	-31.7599	-	-	•	•	•			0.0184^{A}	18	S141	124	1	
0024106	10.8967	-17.9861	•	-	•	•	○							6	
0024107	11.4775	-17.3899	•	•	-	•	-							6	
0024112	10.1196	-16.5173	•	-	•	•	○							6	
0024139	4.4379	-1.0488	•	-	-	•	○							6	
0034044	34.0650	-48.2748	•	•	•	•	•	0.1709	1			A2998	21	4	cluster
0034049	33.2529	-47.1361	•	•	-	-	•					A2988	65	5	
0034050	33.3729	-46.9148	•	-	-	•	•							6	
0034057	30.5771	-44.7906	-	-	•	•	○	0.0616	2					3	cluster
0034068	25.3563	-38.1351	•	-	•	•	○							6	
0034110	16.3800	-24.6316	•	•	-	•	•			0.2300^{A}	1	A141	142	3	cluster
0034113	16.1417	-23.9869	•	•	•	•	•			0.1520^{A}	12	A140	84	1	cluster
0034119	15.8429	-22.5565	•	•	-	-	•					A135	144	6	
0034121	15.5596	-22.0370	-	-	•	•	•							6	
0034122	15.6762	-21.8759	•	•	•	•	○			0.0562^{A}	9	A133	284	2	cluster
0034139	12.8238	-14.7971	•	-	-	•	•	0.0907	1					8	AGN

Table A.2: SGP RASS Cluster Candidates: Positions, Selection Methods, Redshifts & Identifications.

MASOL	Coordinates (2000)		Criteria			Flux		z_{SF}	n_{gal}^{SF}	$z_{lit}^{(ref)}$	n_{gal}^{lit}	optical	Δ	id.	source
no.	α (°)	δ (°)	C	R	E	S	V					cluster	($''$)	no.	type
0034157	10.4113	-9.4427	•	-	•	•	○							6	
0034158	10.4571	-9.3053	•	•	•	•	•			0.0556^{A}	116	A85	222	2	cluster
0034159	10.3304	-9.3234	•	-	•	•	○			0.0556^{A}	116	A85	281	6	multiple
0034160	10.4063	-9.1845	•	-	-	•	•							6	
0034165	8.4704	-7.8552	•	-	•	•	•					A56	233	5	
0034167	8.6100	-6.5031	•	-	-	•	○							6	
0044096	19.5429	-26.9692	•	•	-	•	•	0.231	1			A2895	146	3	cluster
0044117	14.9158	-18.3081	•	•	-	•	•							5	
0044144	10.1992	-7.2305	•	-	•	•	○							5	
0044160	8.7975	-0.8208	•	-	•	•	○							6	
0074030	40.5346	-46.5211	•	-	•	•	○							6	
0074035	38.0817	-44.3445	•	-	-	•	•	0.2836	2					1	cluster
0074044	36.4700	-41.9128	•	-	-	•	•	0.2195	1			A3017	16	4	cluster
0074089	23.8142	-23.4836	•	•	•	•	•	0.2157	1			A215	166	3	cluster
0074092	24.5046	-21.9212	•	-	-	•	•							6	
0074095	24.0083	-21.6291	•	•	-	-	•							6	
0074105	21.8221	-17.7669	•	•	-	•	•	0.1459*	2	0.0880^{A}	> 0	A199	161	1	cluster
0074119	20.2438	-13.8513	•	•	-	•	•	0.0511	3					1	cluster
0074124	19.1008	-12.1001	•	-	-	•	○							6	
0074142	14.1921	-1.3175	-	-	•	•	○							6	
0074143	13.9117	-1.3025	-	-	•	•	•							6	
0074144	14.0558	-1.2442	•	•	-	•	•			0.0444^{H}	23	A119	136	1	cluster
0084083	41.3079	-46.4612	•	•	•	•	•	0.0868	1			A3047	30	8	AGN
0084108	35.2354	-38.4829	-	-	•	•	-							6	
0084117	33.5492	-35.6299	•	-	•	•	•							6	
0084155	26.1750	-22.2272	•	•	•	•	•	0.2781	1			A2938	38	3	cluster
0084159	25.8092	-21.6166	•	-	•	•	○							6	

Table A.2: SGP RASS Cluster Candidates: Positions, Selection Methods, Redshifts & Identifications

MASOL	Coordinates (2000)		Criteria			Flux		z_{SF}	n_{gal}^{SF}	$z_{lit}^{(ref)}$	n_{gal}^{lit}	optical	Δ	id.	source
no.	α (°)	δ (°)	C	R	E	S	V					cluster	($''$)	no.	type
0084163	25.3750	-20.4090	•	•	-	-	•							5	
0084165	25.7542	-19.8206	•	-	•	•	•	0.0974	1			S181	148	8	AGN
0084168	24.3738	-19.9438	•	•	-	•	-					S175	7	6	
0084195	22.9671	-13.6128	•	•	•	•	•			0.2060^{A}	2	A209	151	3	cluster
0084216	18.6017	-7.9214	•	-	•	•	o							6	
0084233	17.5592	-2.3157	-	-	•	•	•							6	
0084242	16.7062	1.0574	•	-	•	•	•	0.2510	1					8	AGN
0084248	16.2571	2.0322	•	-	•	•	o							5	
0094068	44.2571	-47.6093	•	•	•	•	-					A3072	173	6	
0094069	45.2867	-47.1122	-	-	•	•	o							6	
0094171	25.4625	-14.3060	•	-	•	•	•					A242	84	6	
0094175	24.3958	-13.0035	•	•	-	-	•			0.2134^{A}	6	A222	141	1	cluster
0094176	24.4846	-12.8037	•	•	•	•	•	0.2105	1	0.2070^{A}*	4	A223	89	1	cluster
0094206	19.1508	-2.5003	•	-	•	•	-							6	
0094217	18.7600	0.3633	•	-	•	•	•	0.0477	2					2	cluster
0094225	17.0454	2.1800	•	-	•	•	-			0.0451^{A}	11	A147	48	1	cluster
0104082	38.0617	-36.4291	•	-	-	•	o							6	
0104096	34.5854	-31.6847	•	•	-	•	•							6	
0104099	34.1675	-30.9861	-	-	•	•	•							6	
0104111	32.2775	-27.5104	•	•	•	•	-							6	
0104179	24.8438	-11.3881	-	-	•	•	-					A230	120	6	
0104188	24.3100	-9.1973	•	-	•	•	•	0.0392	3					3	cluster
0104191	23.1667	-8.0687	•	-	•	•	o							6	
0104212	21.4283	-1.3567	-	-	•	-	•			0.0183^{A}	81	A194	n.a.	1	cluster
0104219	20.5112	0.3434	•	-	•	•	-					A181	190	6	
0114085	42.6987	-39.9344	•	-	-	•	o							8	star
0114103	37.3400	-33.5435	•	•	•	•	•	0.0779	2	0.0793^{E}*	6	E653	261	1	cluster

Table A.2: (continued) SGP RASS Cluster Candidates: Positions, Selection Methods, Redshifts & Identifications

MASOL	Coordinates (2000)		Criteria			Flux		z_{SF}	n_{gal}^{SF}	$z_{lit}^{(ref)}$	n_{gal}^{lit}	optical	Δ	id.	source
no.	α (°)	δ (°)	C	R	E	S	V					cluster	($''$)	no.	type
0114117	36.3008	-29.4744	•	-	-	•	•	0.0607	2					1	cluster
0114120	34.7221	-28.9633	•	-	-	•	•					A3003	31	5	
0114157	29.8337	-18.0375	•	•	•	•	•	~0.04						8	AGN
0114177	28.2454	-13.7511	-	-	•	•	o							6	
0114183	27.6188	-12.3410	•	-	-	•	o							6	
0114190	27.5858	-10.0927	-	-	•	•	-							6	
0114231	22.8946	0.5322	•	-	-	-	•					A208	32	6	
0114241	21.3762	1.7679	-	-	•	•	o							6	
0124051	48.5954	-45.4233	•	•	•	•	•	0.0002	1			A3104	51	9	w.dwarf
0124066	43.3929	-38.4386	•	-	-	•	o							6	
0124076	36.8021	-28.8548	•	•	-	•	•							5	
0124094	32.5238	-20.4182	•	-	-	•	•							6	
0124108	31.6300	-14.8923	•	-	•	•	•	0.1529	2			A305	73	1	cluster
0124117	28.2983	-11.0470	-	-	•	-	•							6	
0124129	28.1871	-7.2647	•	•	-	•	•							6	
0134039	49.4921	-44.2370	•	•	•	•	•	0.0754*	2	0.0703^{H}	?	A3112	21	1	cluster
0134078	38.8079	-29.6047	•	-	•	•	•	0.0599	1					8	AGN
0134079	39.6454	-29.0565	•	-	•	•	o							6	
0134100	34.9629	-19.1049	•	•	-	-	•			0.1393^{A}	1	A3005	9	3	cluster
0134105	32.9617	-17.0418	•	•	•	•	•	0.1731	1			A2985	36	3	cluster
0134129	31.3542	-9.7901	•	-	•	•	o							6	
0134130	30.8687	-9.8189	•	-	-	-	•							6	
0134134	29.9571	-8.8291	-	-	•	•	•							6	
0134141	28.7692	-6.2414	•	-	-	-	•							6	
0134142	29.3163	-5.8617	•	•	•	-	•			0.0881^{H}	1	A281	163	3	cluster
0134158	28.3854	-1.3163	-	-	•	•	•	0.2438	2					1	cluster
0134162	26.6892	-0.6777	•	•	•	•	•	0.0836	1					8	AGN

Table A.2: (continued) SGP RASS Cluster Candidates: Positions, Selection Methods, Redshifts & Identifications

MASOL	Coordinates (2000)		Criteria			Flux		z_{SF}	n_{gal}^{SF}	$z_{lit}^{(ref)}$	n_{gal}^{lit}	optical	Δ	id.	source
no.	α (°)	δ (°)	C	R	E	S	V					cluster	($''$)	no.	type
0144064	47.3658	-39.9904	•	•	•	•	•	0.192	1					3	cluster
0144073	46.0221	-36.9395	•	•	•	•	•		1	0.0666[A]	5	A3084	62	1	cluster
0144085	42.4008	-31.1864	•	•	•	•	o			0.0233[A]	34	S301	26	2	cluster
0144092	40.3421	-28.6560	•	•	•	•	•	0.2323	3			A3041	68	3	cluster
0144100	39.3646	-26.5062	•	-	•	•	•					A368	43	5	
0144121	35.1038	-16.2293	•	-	-	•	o							6	
0144139	32.1788	-10.0871	•	-	•	•	•							6	
0144157	30.7154	-2.3894	•	-	-	•	o							6	
0144158	30.4329	-2.1987	•	-	•	•	•	0.1981*	1	0.197 [C]	1	A291	117	4	cluster
0144161	30.4283	-1.6613	-	-	•	•	-							6	
0144162	29.6163	-1.7829	•	•	-	•	•	0.1632*	1	0.0791[A]	1	A286	37	3	cluster
0144172	28.3046	1.0461	•	•	•	•	•	0.054	1					9	AGN
0144173	28.1733	1.0088	•	-	•	•	o			0.230 [C]	1	A267	207	3	cluster
0154081	41.0112	-26.1844	•	-	-	•	•							8	spiral
0154090	39.1688	-19.3749	•	•	-	•	•			0.0891[A]	3	A367	59	1	cluster
0154102	37.0404	-13.6706	•	-	•	•	-							6	
0154121	33.6679	-4.5674	•	•	•	•	•	0.1393	2			A329	124	1	cluster
0164081	42.8588	-24.9476	•	•	•	•	•			0.1111[A]	6	A389	165	1	cluster
0164088	41.7912	-22.4909	•	-	•	•	o							6	
0164091	40.6513	-21.5309	•	-	•	•	•							6	
0164108	38.0679	-12.2748	•	-	•	•	o							6	
0164123	35.6088	-8.9505	•	-	-	•	•							6	
0164139	33.4879	-2.8971	•	-	•	•	•							6	
0174059	46.7612	-28.6657	-	•	•	•	•					A3088	39	5	
0174063	45.8213	-27.5910	•	-	•	•	•					A3082	120	5	
0174093	39.7042	-12.9835	•	•	-	•	•	0.1648	1					3	cluster
0174101	37.5196	-8.9957	•	-	•	•	o							8	spiral

Table A.2: (continued) SGP RASS Cluster Candidates: Positions, Selection Methods, Redshifts & Identifications

MASOL	Coordinates (2000)		Criteria			Flux		z_{SF}	n_{gal}^{SF}	$z_{lit}^{(ref)}$	n_{gal}^{lit}	optical	Δ	id.	source
no.	α (°)	δ (°)	C	R	E	S	V					cluster	($''$)	no.	type
0174108	37.3979	-5.8688	•	-	•	•	•							6	
0174111	37.9258	-4.8785	•	•	-	-	•	0.1843	3			A362	106	4	cluster
0184036	47.8521	-26.9043	•	•	•	•	•			0.0683^{E}	7	A3094	93	1	cluster
0184048	44.4212	-22.1562	•	-	•	•	•	0.3224	1			A402	145	3	cluster
0184049	44.5588	-21.0877	•	•	•	•	•	0.1226	1			A3073	96	3	cluster
0184079	36.8175	2.0325	-	-	•	•	•							6	
0194055	47.0683	-23.6773	•	•	•	-	•			0.0665^{H}	2	A419	227	3	cluster
0194076	39.9771	-1.5867	•	-	-	•	•			0.3750^{A}	53	A370	61	1	cluster
0194081	37.9967	1.2642	•	-	•	-	•	0.0221	2					1	cluster
0204059	42.0071	-3.5376	•	•	•	•	•	0.1899	1			A383	180	4	cluster
0204061	42.0367	-2.2828	•	-	-	•	•					A384	79	6	
0204069	40.6692	-0.0125	•	-	•	•	o							6	
0214022	48.4492	-17.0347	•	-	•	•	o							6	
0214030	43.2079	-1.2721	•	-	-	•	o							6	
0683076	332.3192	-47.1695	•	-	•	•	o							6	
0683081	332.8245	-48.5723	•	•	•	•	•	0.2633	1			A3841	102	3	cluster
0703077	334.9688	-45.9836	•	•	-	-	•	0.0925	5			A3862	136	1	cluster
0703084	336.5533	-47.7586	•	•	-	-	•					A3876	54	5	
0703085	336.8492	-48.8964	•	•	-	-	•			0.0970^{AP}	3	APM54	30	1	cluster
0713051	334.6557	-38.8954	•	•	•	•	•			0.1312^{A}	14	A3856	91	1	cluster
0723047	331.5437	-30.0856	-	-	•	•	•	$\sim$0.07	1					8	AGN
0723053	332.9537	-32.9291	-	•	-	•	•	0.3052	1					8	AGN
0723059	335.1383	-35.1651	-	•	•	•	•	0.0754	1			A3866	40	8	AGN
0723060	334.4382	-35.7243	•	•	-	•	•			0.1503^{A}	33	A3854	40	2	cluster
0723067	335.4603	-38.5648	•	-	-	-	•							5	
0723070	336.1321	-39.0345	•	-	•	•	•	0.15	1					4	cluster
0723073	337.6629	-39.7128	-	-	•	•	•							6	

Table A.2: (continued) SGP RASS Cluster Candidates: Positions, Selection Methods, Redshifts & Identifications

MASOL	Coordinates (2000)		Criteria			Flux		z_{SF}	n_{gal}^{SF}	$z_{lit}^{(ref)}$	n_{gal}^{lit}	optical	Δ	id.	source
no.	α (°)	δ (°)	C	R	E	S	V					cluster	($''$)	no.	type
0723084	342.6058	-46.2780	•	•	•	•	-	0.1207*	3	0.0506^{A}	2	S1066	131	1	cluster
0733020	330.9621	-21.5205	•	-	•	•	•	0.0732	3					4	cluster
0733023	330.4595	-22.4339	•	-	-	•	•	0.0681	2	0.0693^{A*}	20	S987	54	1	cluster
0733036	333.2753	-27.9005	-	-	•	•	○	0.0620	2					1	cluster
0733059	337.3970	-36.5382	•	•	•	•	•	0.1504	2			A3882	80	3	cluster
0733062	338.6182	-37.7314	•	-	•	•	•			0.1590^{A}	70	A3888	68	1	cluster
0733077	340.4891	-42.5995	•	•	•	•	•					A3902	35	7	
0733078	342.1841	-44.5296	•	-	•	•	•					S1063	114	5	
0743009	330.6091	-16.9640	•	-	•	•	○							8	star
0743011	331.2179	-18.2631	•	•	•	-	•							5	
0743016	332.7596	-21.2311	•	-	-	•	○							6	
0743027	336.9642	-30.5671	•	•	•	•	•			0.0570^{A}	16	A3880	46	1	cluster
0743043	346.3920	-45.1897	•	•	-	•	•	0.1253	3			A3970	187	1	cluster
0753002	330.6896	-13.0799	•	•	-	-	•	0.0390	1					8	AGN
0753011	333.6083	-17.0244	•	•	•	•	•	0.1532*	1	0.1530^{A}	1	A3847	74	4	cluster
0753013	334.2325	-17.4222	•	•	•	•	•	0.1301	2					1	cluster
0753022	335.8775	-24.7613	•	-	•	•	○							6	
0753024	336.8633	-25.4233	•	-	•	•	•	n.a.	1					8	AGN
0753028	338.7142	-30.5598	•	•	•	•	○			0.2512^{A}	19	A3889	40	1	cluster
0753035	341.5533	-36.0047	•	•	-	-	•	0.0673	2					1	cluster
0753052	347.6716	-43.7937	•	-	•	•	•	0.0882	2					1	cluster
0753060	351.3599	-48.0063	•	•	•	•	•	n.a.	1					8	AGN
0762117	330.1517	-2.7409	•	-	•	•	○							6	
0762125	331.5228	-5.3600	•	-	-	•	○							6	
0762126	331.4133	-5.5816	•	•	•	•	•	0.0577*	2	0.0597^{A}	2	A2415	214	1	cluster
0762129	333.6329	-10.3730	•	•	•	•	•	0.1001*	4	0.0995^{A}	1	A2426	70	1	cluster
0763002	332.5816	-12.1908	•	•	-	•	•	0.0831*	3	0.0838^{A}	1	A2420	44	1	cluster

Table A.2: (continued) SGP RASS Cluster Candidates: Positions, Selection Methods, Redshifts & Identifications

MASOL	Coordinates (2000)		Criteria			Flux		z_{SF}	n_{gal}^{SF}	$z_{lit}^{(ref)}$	n_{gal}^{lit}	optical	Δ	id.	source
no.	α (°)	δ (°)	C	R	E	S	V					cluster	($''$)	no.	type
0763011	334.1346	-16.0929	-	•	•	•	•	0.0895	1					8	AGN
0763023	339.6846	-24.9775	•	•	-	-	•					S1048	88	6	
0763024	338.9421	-26.0501	•	-	-	•	o							6	
0763035	342.9429	-32.1022	-	•	-	•	•	0.2254	1					3	
0763038	342.9708	-33.4093	•	-	•	•	•	0.23	2			A3926	117	1	cluster
0763039	343.3808	-33.7289	•	•	•	•	•			0.2250^{A}	6	A3934	59	1	cluster
0763040	344.6879	-34.7952	•	•	-	-	•	0.3125	1	0.3169^{A*}	42	S1077	100	1	cluster
0763049	346.6354	-38.9298	•	-	•	•	•							6	
0763051	349.7742	-42.1144	•	-	-	•	•	0.0549*	2	0.0545^{A}	3	S1111	83	1	cluster
0763052	348.4932	-42.7283	-	-	•	•	•	0.0564*	4	0.0578^{A}	3	S1101	2	1	cluster
0763059	354.0596	-48.5849	•	-	•	•	•							6	
0772150	334.0658	-9.3348	•	-	•	•	•	0.0825*	2	0.0851^{A}	1	A2428	58	1	cluster
0773010	338.6783	-19.8570	•	-	-	•	o							6	
0773023	342.1283	-25.3486	•	•	-	-	•							6	
0773025	342.4224	-27.1141	-	-	•	•	•							6	
0773031	345.8750	-34.7489	•	-	-	•	o							6	
0773037	348.9371	-37.7789	•	•	•	•	•	0.1786	3			A3984	299	3	cluster
0773041	350.4028	-41.8920	•	-	•	•	•	0.0889*	2	0.0890^{A}	3	A3998	15	1	cluster
0782148	331.6629	2.4406	•	-	-	•	o							6	
0782158	334.5629	-3.8060	•	•	-	-	•	0.0901	3					1	cluster
0783002	337.2575	-9.7580	•	-	-	-	•							6	
0783007	339.1762	-15.7621	•	-	-	•	-	0.0731	4					2	cluster
0783010	341.1496	-17.7508	•	•	•	•	•	0.1325	2			A2478	169	1	cluster
0783013	340.7645	-20.1631	•	•	-	•	•	0.1385	1			A2474	156	3	cluster
0783040	352.8583	-42.1620	•	-	•	•	o							6	
0792131	335.9525	-1.6568	•	•	-	•	•	0.0921	3	0.0912^{A*}	24	A2440	225	1	cluster
0792134	336.5578	-2.7900	•	-	-	•	o							8	star

Table A.2: (continued) SGP RASS Cluster Candidates: Positions, Selection Methods, Redshifts & Identifications

MASOL	Coordinates (2000)		Criteria			Flux		z_{SF}	n_{gal}^{SF}	$z_{lit}^{(ref)}$	n_{gal}^{lit}	optical	Δ	id.	source
no.	α (°)	δ (°)	C	R	E	S	V					cluster	($''$)	no.	type
0793011	342.1283	-16.0989	•	-	-	•	-					A2485	83	6	
0793012	342.7279	-16.3986	•	•	•	•	•	0.1221*	3	0.1233^{A}	1	A2496	44	1	cluster
0793022	343.2271	-21.5585	-	•	•	•	•	0.2004	3					1	cluster
0793035	352.8057	-36.5178	•	-	•	•	•			0.0954^{A}	8	A4010	53	1	cluster
0802175	337.2078	-0.0224	•	-	•	•	-							6	
0803004	340.8429	-9.5969	-	-	•	•	-							6	
0803007	342.5582	-11.8673	•	-	-	•	•	0.12	1					8	AGN
0803021	349.7658	-28.3860	-	-	•	•	o							6	
0803028	351.8349	-31.7712	•	•	-	•	•	0.1126	1					8	AGN
0803046	5.1779	-49.2205	•	•	•	-	•			0.0710^{A}	4	A2764	152	1	cluster
0812153	338.9216	1.4798	•	•	-	•	•			0.0621^{A}	4	A2457	60	2	cluster
0812162	342.2728	-5.4627	•	-	-	-	•					A2489	183	5	
0813006	345.9321	-17.0855	•	-	•	•	-	0.1299	1					3	cluster
0813010	349.0271	-20.4606	•	•	•	•	•	0.0834*	2	0.0821^{A}	1	A2566	278	1	cluster
0813011	348.0917	-21.5142	•	-	-	•	•	0.1082	2	0.1117^{A}*	29	A2554	149	1	cluster
0813012	348.2550	-21.6366	•	-	-	•	•	0.0869*	3	0.0865^{A}	2	A2556	42	1	cluster
0813013	349.5546	-21.3059	•	-	-	•	-							6	
0813014	350.3558	-23.2062	•	-	•	•	•	0.0897	2			A2580	196	1	
0813023	356.9583	-35.5944	•	•	-	•	•	0.2635	1			S1150	26	4	cluster
0813037	3.4842	-46.3840	•	-	-	•	-	0.1998	2			A2743	109	2	cluster
0813040	7.6042	-48.2157	-	-	•	•	o							6	
0822162	343.2929	-4.1491	•	-	•	•	•	0.0251	1					8	AGN
0823033	351.5632	-24.1022	•	•	-	-	•	0.1117	2					1	cluster
0823041	354.0083	-28.7595	•	•	•	-	•							6	
0823059	359.2475	-34.7587	•	•	•	•	•	0.0492	2					1	cluster
0823063	360.0000	-39.4854	-	•	-	•	•			0.1016^{A}	2	A4068	168	3	cluster
0823080	9.3746	-48.9446	•	•	-	-	•	0.0713	2					1	cluster

Table A.2: (continued) SGP RASS Cluster Candidates: Positions, Selection Methods, Redshifts & Identifications

MASOL	Coordinates (2000)		Criteria			Flux		z_{SF}	n_{gal}^{SF}	$z_{lit}^{(ref)}$	n_{gal}^{lit}	optical	Δ	id.	source
no.	α (°)	δ (°)	C	R	E	S	V					cluster	($''$)	no.	type
0823081	9.1512	-49.1276	•	-	•	•	○							6	
0832238	344.7182	-0.3161	•	-	•	•	○							6	
0832240	344.5075	-2.3229	•	-	-	•	•							6	
0833001	346.3996	-7.1689	•	-	•	-	•							6	
0833002	346.4671	-7.7626	•	-	-	•	○							6	
0833006	347.1871	-9.1886	•	-	•	•	•	~0.12	1					8	AGN
0833071	357.0367	-28.0317	-	-	•	•	○							6	
0833073	356.9245	-28.1399	•	•	•	•	•			0.0293^{A}	44	A4038	4	2	cluster
0833093	1.4892	-34.7265	•	•	•	•	•			0.1143^{A}	72	A2721	140	1	cluster
0833111	9.3108	-46.2365	•	-	-	•	•							6	
0842250	345.6671	0.5819	•	-	-	•	•							6	
0842258	347.0946	-2.1889	•	•	•	•	•	0.2966	2			A2537	101	1	cluster
0843019	351.3283	-12.1263	•	-	•	•	•	0.0819	1	0.0852^{A*}	3	A2597	65	1	cluster
0843045	356.1188	-21.8958	•	•	•	•	•	0.1122	3			A2655	107	4	cluster
0843053	357.5958	-24.5971	•	•	•	•	•	0.1920	3					1	cluster
0843056	357.9183	-26.0816	•	-	•	•	•	0.2264	1			A2667	289	4	cluster
0843076	3.3900	-34.7207	•	•	•	•	•	0.1096	1					3	cluster
0843081	5.6921	-38.1121	•	•	•	•	•	0.1180	2	0.1191^{A*}	4	A2767	39	1	cluster
0843099	13.2137	-47.6229	•	-	•	•	•	0.0785	1					3	cluster
0843100	12.8296	-48.5375	•	•	•	•	•	0.1873	2			A2830	166	4	cluster
0852208	347.2087	0.0179	•	-	-	•	○							6	
0852212	348.9404	-2.3800	•	-	•	•	•	0.0267	2					1	cluster
0853001	350.2159	-4.5633	•	•	•	•	-	0.1883	1			A2578	154	3	cluster
0853043	357.7496	-19.9400	-	•	-	-	•							9	star
0853046	358.2832	-22.3090	•	-	•	-	•							5	
0853055	0.1817	-26.0877	•	-	-	•	•							8	AGN
0853062	1.8513	-28.1574	•	•	-	-	•					A2726	136	7	

Table A.2: (continued) SGP RASS Cluster Candidates: Positions, Selection Methods, Redshifts & Identifications

MASOL	Coordinates (2000)		Criteria			Flux		z_{SF}	n_{gal}^{SF}	$z_{lit}^{(ref)}$	n_{gal}^{lit}	optical	Δ	id.	source
no.	α (°)	δ (°)	C	R	E	S	V					cluster	($''$)	no.	type
0853076	4.1754	-31.4502	•	-	-	•	•							6	
0853087	4.4054	-35.1848	•	•	•	•	•			0.0969^{A}	18	A2755	86	1	cluster
0853099	9.3612	-39.1152	•	•	•	•	-			0.0631^{A}	15	A2799	62	1	cluster
0862172	349.7337	0.2436	•	•	•	•	o	0.020	1					8	AGN
0863011	353.3825	-8.3362	•	-	•	•	o							6	
0863022	355.6807	-14.5421	•	-	•	•	o							6	
0863043	359.1196	-21.0355	•	•	-	-	•					A2680	12	5	
0863044	359.8288	-20.7976	•	-	-	•	•	0.1077*	3	0.1124^{A}	1	A2686	49	3	cluster
0863056	2.8471	-28.8499	•	•	•	•	•			0.0628^{H}	3	A2734	89	1	cluster
0863062	3.5917	-30.3812	•	-	-	•	•			0.3067^{A}	34	A2744	43	1	cluster
0863069	6.3779	-33.0435	•	•	•	•	•			0.0487^{A}	2	S41	75	3	cluster
0863076	7.2542	-34.9894	•	•	•	-	•			0.1110^{AP}	2	APM98	79	3	cluster
0863082	10.6050	-38.1684	•	-	•	•	•	0.2204	1			A2812	67	4	cluster
0863098	17.1446	-46.6730	•	-	•	•	•							8	star
0873004	355.0232	-4.0493	•	-	•	•	o							6	
0873006	356.0871	-7.4210	•	•	•	-	•	0.1246	1			A2654	133	3	cluster
0873010	355.3116	-9.0198	•	•	-	•	•			0.2517^{A}	5	A2645	135	1	cluster
0873020	358.3496	-12.9481	•	-	•	-	•							6	
0873029	0.3721	-15.6997	-	-	•	-	•	0.1246	3					1	cluster
0873057	4.4083	-24.2082	•	•	-	-	•							5	
0873061	5.1692	-25.7166	•	•	•	•	•			0.0634^{A}	5	A22	49	1	cluster
0873068	5.3754	-28.9797	•	-	•	•	o							6	
0873078	8.5013	-33.9067	•	-	•	•	•	n.a.	1					8	AGN
0873096	17.5683	-44.7647	•	-	-	-	•							6	
0873098	17.4708	-45.9124	•	-	•	•	•			0.0250^{A}	109	2877	57	1	cluster
0882174	353.7496	1.6066	•	-	•	•	o							6	
0882177	354.4121	0.2708	•	-	•	•	•			0.278^{C}	1	2631	82	3	cluster

Table A.2: (continued) SGP RASS Cluster Candidates: Positions, Selection Methods, Redshifts & Identifications

MASOL	Coordinates (2000)		Criteria			Flux		z_{SF}	n_{gal}^{SF}	$z_{lit}^{(ref)}$	n_{gal}^{lit}	optical	Δ	id.	source
no.	α (°)	δ (°)	C	R	E	S	V					cluster	($''$)	no.	type
0883005	356.0650	-4.3734	•	•	-	•	•	0.0786	2					1	cluster
0883007	356.1167	-4.4398	•	-	-	-	•							6	
0883019	358.5528	-10.4190	•	•	•	•	•			0.0761^A	220	2670	63	1	cluster
0883021	359.5332	-10.4761	•	•	•	•	•	0.068	1			2684	166	8	AGN
0883036	3.4008	-19.4996	•	•	•	•	•	0.0949	4			13	37	1	cluster
0883037	3.7042	-20.4049	•	•	-	-	•	0.3149	3					1	cluster
0883039	4.7708	-20.4432	•	•	•	•	•	0.2773	1			S26	59	3	cluster
0883063	12.9071	-34.6124	•	-	•	•	•							6	
0883087	23.5658	-47.3680	•	•	•	•	•	0.1141	2					1	cluster
0893004	356.8504	-2.3134	•	-	•	•	•	0.0221	2					1	cluster
0893006	357.5362	-3.6612	-	•	-	-	•					2664	142	6	
0893008	359.0842	-4.4946	-	-	•	•	-							6	
0893024	1.9813	-11.8404	•	-	-	-	•							5	
0893032	3.0321	-15.8419	•	-	•	•	o							6	
0893034	3.1429	-16.4686	•	•	-	•	•	0.1496	1			11	184	8	AGN
0893052	6.8367	-21.5534	•	-	•	-	•							5	
0893054	7.2821	-22.6021	-	-	•	•	•							6	
0893058	7.1496	-23.6465	•	•	•	•	•			0.1129^A	5	42	22	1	cluster
0893060	7.6521	-24.1754	•	•	-	•	•	0.1487	1			47	65	3	cluster
0893068	9.5238	-25.0815	•	-	•	•	o			0.0643^A	7	2800	102	1	cluster
0893077	10.5304	-28.5353	•	-	•	•	•			0.1170^A	32	2811	36	1	cluster
0893097	17.1592	-40.3406	•	•	•	•	•			0.1408^A	6	2874	48	1	cluster
0903036	6.0121	-17.0684	•	-	•	•	•	0.189	2			2768	46	3	cluster
0903046	6.5183	-18.9183	•	-	-	•	•	0.1407						8	AGN
0903053	7.0879	-20.3343	•	-	•	•	o							8	star
0903060	9.7813	-22.3330	•	•	•	•	•			0.0653^A	7	74	217	3	cluster

Table A.2: (continued) SGP RASS Cluster Candidates: Positions, Selection Methods, Redshifts & Identifications

MASOL	Coordinates (2000)		Criteria			Flux		z_{SF}	n_{gal}^{SF}	$z_{lit}^{(ref)}$	n_{gal}^{lit}	optical	Δ	id.	source
no.	α (°)	δ (°)	C	R	E	S	V					cluster	($''$)	no.	type
0903078	12.8250	-28.5116	•	•	•	•	•			0.1000^A	11	2829	64	1	cluster
0903081	12.3371	-29.5237	•	•	-	•	•			0.1150^A	20	584	21	1	cluster
0903091	16.4825	-35.9338	•	•	-	-	•					2865	162	6	
0903094	16.9583	-36.7277	•	•	-	•	•			0.1175^A	10	2871	66	2	cluster
0903126	25.8679	-46.2379	•	•	-	-	•					2937	80	6	
0903129	27.1675	-48.5138	-	•	-	•	•							6	
1044021	32.5879	-43.7184	•	-	•	•	-							6	
1044033	25.0258	-34.1728	-	-	•	•	-							6	
1044097	8.5354	-2.1574	•	•	•	•	•							7	
1054089	33.4217	-42.8270	•	-	•	•	•							6	
1054101	29.9658	-38.1270	-	-	•	•	o							6	
1054119	23.7533	-29.9111	•	•	•	•	o							8	star
1054145	19.3508	-22.4644	•	-	-	•	o	0.1145	2					4	cluster
1054171	17.2279	-15.6337	•	-	-	•	o							6	
1054172	17.2437	-15.4461	•	•	•	•	o			0.0537^A	37	151	137	1	cluster
1054182	16.0579	-13.6005	•	-	-	-	•							6	
1054191	14.0842	-9.6077	-	•	•	•	o	n.a.						8	AGN
1054218	8.9092	1.6317	•	-	-	•	•							6	
1064071	32.8483	-40.2847	•	•	•	•	o			0.1022^A	6	2984	40	1	cluster
1064093	23.8492	-27.4697	•	-	-	•	o					2928	231	5	
1064123	19.0513	-15.9041	•	-	•	-	•	0.0448	2					1	cluster
1224038	45.8458	1.9296	•	-	-	•	o					409	203	6	
1224040	45.3979	1.9184	-	-	•	•	•	0.1690	2					1	cluster

Table A.2: (continued) SGP RASS Cluster Candidates: Positions, Selection Methods, Redshifts & Identifications

Appendix B

Results from the Spectroscopic Follow-Up

Here we present the results from the spectroscopic follow-up of SGP RASS cluster candidates. Every line of table B.1 represents the the spectral information from a different object that surrounds the candidate number listed in column 1. We have attempted to classify these objects as AGN, X-ray quiet galaxies or stars (column 4) on the basis of the spectral features listed in column 8. The redshift information for the 311 objects is presented in columns 7, 9 & 10. For descriptions of the classification technique and the redshift determination, the reader is directed to sections § 3.5.1, § 3.5.2& § 3.6 of chapter 3. Note that a † in either column 7 or 9 indicates which redshift value was assumed for the object when the XCORR and manually determined redshifts disagree.

Explanation of the Columns in Table B.1

(1) SGP RASS cluster candidate MASOL number. (See table A.2 for candidate coordinates.)

(2) Place and date of observations.

(3) Total integration time.

(4) Object type identified with the spectrum. Note that a) a numeric superscript in this column indicates that the object spectrum was featured in figure 3.6 and b) a $*$ in this column indicates that the object was *not* used to determine the redshift of the underlying X-ray source.

(5) Flag indicating if the object lay inside the X-ray error circle ($\bigcirc$). If the object was the sole CUOC entry inside the error circle, it is flagged by $\odot$.

(6) Flag indicating if the object resembled a cD galaxy; either in the CUOC or on the respective Schmidt plate. (cD galaxies are bright ellipticals with an extended amorphous halo.)

(7) The redshift value determined by the manual technique, § 3.5.1. Approximate values are prefixed by a $\sim$.

(8) The features identified in the spectrum listed by increasing wavelength, refer to table 3.6 and § 3.5.1 for details. Note a) that hydrogen lines in absorption are distinguished from those in emission by the use of lower case letters for the former, *i.e.* h_δ, h_γ, h_β *etc.* , b) that if a feature is enclosed in parentheses then the feature was of low S/N in the spectrum and c) that the superscripts in this column, sf, $?bl$ *etc.* , refer to the appearance (in terms of strength and width) of the emission lines.

(9) The redshift determined by the XCORR cross correlation technique, § 3.5.2.

(10) The error ($\times 10^5$) on the XCORR redshift.

(1)	(2)	(3)	(4)	(5)	(6)	(7)	(8)	(9)	10
MASOL	place date	t(s)	object	pos.	cD	manual	spectral features	XCORR	
no.			type	flag		redshift		redshift	δz
0011003	AAT 10Sep93	300	Galaxy			0.0926	KHG	0.09493	13
	AAT 10Sep93	300	Galaxy			0.1015	KHG	0.10378	12
0014072	AAT 24Aug92	600	Galaxy		cD	0.1099	KHG	0.11067	36
	AAT 24Aug92	600	Galaxy	○		0.1126	KHGh_β	0.11280	27
0034044	AAT 01Nov91	600	Galaxy	○	cD	0.1709	$[O_{II}]^{sf}$(G)	unclear	
0034057	SAAO 21Sep92	600	Galaxy	○		0.0658	KH	0.06474	25
	AAT 22Aug92	300	Galaxy*	○	cD	0.0659	KHG	0.06095	15
	AAT 22Aug92	300	Galaxy			0.0587	$[O_{II}]^{sf}h_\theta\ h_\eta\ h_\zeta$ KHh_δ G$H_\beta{}^{lf}$	0.05846	04
0034139	AAT 11Sep93	300	AGN	⊙		0.0907	$[O_{II}]$ − −H_β $[O_{III}]^{lw}$	unclear	
0044096	AAT 24Aug92	600	Galaxy	⊙	cD	0.2310	h_η KHh_δ G	unclear	
0074035	AAT 10Sep93	1200	Galaxy		cD	0.2782	KH	bombed	
	AAT 10Sep93	1200	Galaxy	⊙		0.2889	KH	unclear	
0074044	AAT 01Nov91	300	Galaxy	○	cD	0.2195	$[O_{II}]^{lf}$	unclear	
0074089	AAT 23Aug92	900	Galaxy			0.2157	KH	unclear	
	AAT 01Nov91	1900	Star*			star			
0074105	AAT 11Sep93	600	Galaxy		cD	0.1459	KHG	0.14540	26
	AAT 11Sep93	600	Galaxy		cD	0.1453	KHG	0.14644	40
0074119	AAT 30Oct91	734	Galaxy			0.0512	KHGMgb	0.05108	11
	AAT 30Oct91	734	Galaxy	⊙	cD	0.0534	KHGMgb	0.05326	07
	AAT 07Sep93	377	Galaxy			0.0486	KHG(h_β)	0.04896	08
0084083	AAT 31Oct91	1495	Galaxy*	○		0.0943	KHG	0.09431	09
	AAT 31Oct91	1495	AGN	○		0.0868	$[O_{II}]$ H_β $[O_{II}]^{sf}[O_{III}]^{lf}$	unclear	
0084155	AAT 11Sep93	1200	Star*			star		0.00011	18
	AAT 11Sep93	1200	Galaxy	⊙	cD	0.2781†	KH(h_δ)	0.13752	163
0084165	AAT 10Sep93	400	AGN	⊙		0.0974	$[O_{II}]$ H_δ − $H_\beta{}^{sw}$	unclear	
0084242	AAT 10Sep93	1200	AGN	⊙		0.2510	$[O_{II}]^{lf}$ − −H_δ $H_\gamma{}^{sf}$	unclear	
	AAT 10Sep93	1200	Galaxy*			0.2509	KHG	unclear	

Table B.1: Results from the spectroscopic followup.

MASOL no.	place date	t(s)	object type	pos. flag	cD	manual redshift	spectral features	XCORR redshift	δz
0094176	AAT 10Sep93	1200	Galaxy*			0.1355	$[O_{II}]$ KH	bombed	
	AAT 10Sep93	1200	Galaxy	○		0.2089	KHG	0.21053	53
0094217	AAT 22Aug92	300	Galaxy[1]			0.0444	$h_\theta\, h_\eta\, h_\zeta$ KHh_δ Gh_γ h_β Mgb	0.04665	08
	AAT 22Aug92	300	Galaxy			0.0449	KHGMgb	0.04875	08
0104188	AAT 01Nov91	764	Galaxy			0.0413	KHGMgb	0.04088	41
	AAT 01Nov91	764	Galaxy	⊙	cD	0.0370	(KHGMgb)	0.03798	07
	AAT 07Sep93	600	Galaxy			0.0378	KHGMgb	0.03870	11
	AAT 07Sep93	900	AGN[9]			0.0698	$[O_{II}]$ H_γ H_β $[O_{III}]^{sf}$ $[O_{III}]^{lf}$	unclear	
0114103	AAT 22Aug92	300	Galaxy			0.0780	KHG	0.07870	15
	AAT 22Aug92	300	Galaxy	○	cD	0.0765	KHG	0.07712	23
0114117	AAT 23Aug92	300	Galaxy		cD	0.0598	KHGMgb	0.06053	31
	AAT 23Aug92	300	Galaxy	○		0.0593	KHGMgb	0.06093	16
0114157	AAT 10Sep93	900	Galaxy*			0.1639	KHG	0.16562	30
	AAT 10Sep93	900	AGN	⊙		∼0.047	$-H_\beta$ [sw]	unclear	
0124051	AAT 23Aug92	300	Galaxy*[15]	○		0.0725	KHGh_β	0.07301	16
	AAT 23Aug92	300	W.Dwarf			0.0010	KHh_δ h_γ h_β	0.00018	31
0124108	AAT 10Sep93	1200	Galaxy	○	cD	0.1532	KHG	unclear	
	AAT 10Sep93	1200	Galaxy			0.1525	($[O_{II}]$)KHG	unclear	
0134039	AAT 31Oct91	529	Galaxy	⊙	cD	0.0750	$[O_{II}]^{lf}$KHGMgb	0.07556	04
	AAT 31Oct91	529	Galaxy			0.0755	KHGMgb	0.07532	04
0134078	AAT 30Oct91	300	AGN	⊙		0.0599	$[O_{II}]^{sf}$KHG$[O_{III}]$ $[O_{III}]^{lf}$	unclear	
0134105	AAT 23Aug92	900	Galaxy*			∼0.1839	K(H)G	unclear	
	AAT 23Aug92	900	Galaxy	○	cD	0.1732	KHG	0.17310	34
0134158	AAT 11Sep93	1200	Galaxy	○		0.2436	KH	unclear	
	AAT 11Sep93	1200	Galaxy			0.244	KH	bombed	
0134162	AAT 22Aug92	600	Galaxy*			0.0839	KHGHb	0.08232	11
	AAT 22Aug92	600	AGN	⊙		0.0836	H_δ H_γ H_β $[O_{III}]$ $[O_{III}]^{lw}$	bombed	
0144064	SAAO 26Sep92	1800	Galaxy	○		0.1933	KHG	0.192	24

Table B.1: (continued) Results from the spectroscopic followup.

MASOL no.	place date	t(s)	object type	pos. flag	cD	manual redshift	spectral features	XCORR redshift	δz
0144092	AAT 10Sep93	120	Star✳	○		star		0.00009	03
	AAT 10Sep93	900	Galaxy			0.2344	KHG	unclear	
	AAT 10Sep93	900	Galaxy✳	○		0.1059	$[O_{II}]$ KHGH_β lf	unclear	
	AAT 10Sep93	900	Galaxy	○		0.2259	h_η KHG	unclear	
	AAT 10Sep93	900	Galaxy			0.2366	KHG	bombed	
0144158	SAAO 26Sep92	1054	Galaxy	○		0.1981	$[O_{II}]$ $[Ne_V]$G	unclear	
0144162	AAT 11Sep93	900	Galaxy*			∼0.1648	((KHbr))	0.08041†	08
	AAT 11Sep93	900	Galaxy	○		0.1630	KHG	0.16321	19
0144172	AAT 10Sep93	1200	Galaxy*			0.0574	KHG	unclear	
	AAT 10Sep93	1200	AGN	○	cD	0.054†	$[O_{II}]$ KHGH_β sw$[O_{III}]$ lf	0.06001	07
0154121	AAT 01Nov91	2400	Galaxy	○	cD	0.139	KHG	0.13944	42
	AAT 01Nov91	2400	Galaxy			∼0.139	(KHbrG)	0.13911	14
0174063	SAAO 26Sep92	400	Star			star		0.00015	03
0174093	SAAO 26Sep92	263	Star*			star			
	AAT 11Sep93	600	Galaxy			0.1648	($[O_{II}]$)KHh_δ G	unclear	
0174111	AAT 10Sep93	1200	Galaxy	○		0.1838	KHG	unclear	
	AAT 10Sep93	1200	Galaxy	○		0.1854†	KHG	0.0171	13
	AAT 10Sep93	1200	Galaxy	○	cD	0.1836	$[O_{II}]$ KHG	unclear	
0184048	AAT 11Sep93	1200	Galaxy	○		0.3224†	h_η h_ζ KH	0.00016	244
	AAT 11Sep93	1200	Galaxy*	○	cD	0.3170	($[Ne_V]$)KH	unclear	
0184049	SAAO 22Sep92	1600	Galaxy[5]	○		∼0.124		0.1226	27
	SAAO 22Sep92	3000	Galaxy*	○		∼0.120	$[O_{II}]$ sf(h_ζ)KH	unclear	
0194081	AAT 11Sep93	400	Galaxy		cD	0.0226	KHh_β Mgb	0.02204	10
	AAT 11Sep93	400	Galaxy			0.0223	KHh_β Mgb	0.02207	12
0204059	SAAO 26Sep92	1704	Galaxy	○	cD	0.189	$[O_{II}]$ KHG	0.1899	30
0683081	AAT 31Aug92	900	Star*[16]	○		star	HGMgb5268	0.00013	03
	AAT 31Aug92	900	Galaxy	○		0.2633	KH	unclear	
	AAT 31Aug92	900	Galaxy*[6]			∼0.26	KbrG	bombed	

Table B.1: (continued) Results from the spectroscopic followup.

MASOL no.	place date	t(s)	object type	pos. flag	cD flag	manual redshift	spectral features	XCORR redshift	XCORR δz
0703077	AAT 11Sep93	300	Galaxy			0.0915	KHG	0.09155	20
	AAT 11Sep93	300	Galaxy			0.0915	KHG	0.09136	14
	AAT 11Sep93	300	Galaxy			0.0924	KHG	0.09222	25
	AAT 11Sep93	300	Galaxy*			0.0909	(KHbr)((G))	unclear	
	AAT 11Sep93	900	Galaxy[7]	○		0.0948	$[O_{II}]$ (KHG)H_β $^{lf}[O_{III}]$ ^{sf}	unclear	
	AAT 11Sep93	900	Galaxy			0.0914	KHG	0.09231	08
0723047	AAT 11Sep93	1500	AGN	○		~0.070	$[O_{II}]$ H_δ $-$ H_β ^{sw}	unclear	
	AAT 11Sep93	1500	AGN*			~0.059	$-H_\beta$ ^{sw}	unclear	
	AAT 11Sep93	200	Galaxy*			0.1652	$[O_{II}]$ h_η h_ζ	bombed	
	AAT 11Sep93	200	Star*	○		star		0.00011	03
0723053	AAT 23Aug92	300	Star*			star		0.00010	04
	AAT 23Aug92	300	AGN[13]	⊙		0.3052	$[Ne_V][O_{II}]$ $-^{sf\ ?bl}$	unclear	
0723059	AAT 07Sep93	600	Galaxy*		cD	0.1532	$[O_{II}]$ h_ζ KH	0.15430	37
	AAT 07Sep93	600	AGN	⊙		0.0754	$[O_{II}]$ KHh_δ G$[O_{III}]$ $[O_{III}]$ ^{lf}	unclear	
	AAT 07Sep93	600	Star*			star		0.00033	03
0723070	AAT 24Aug92	600	Star*	○		star		0.00010	03
	AAT 24Aug92	600	Star*			star		0.00005	04
	SAAO 21Sep92	1200	Galaxy	○		0.15	(KHbrGMgb)	unclear	
0723084	AAT 24Aug92	600	Galaxy*	○		0.1206	(KHG)	unclear	
	AAT 24Aug92	600	Galaxy	○		0.1216	KHG	0.12226	14
	SAAO 21Sep92	400	Galaxy			0.1192	KHGMgb	unclear	
	SAAO 21Sep92	1200	Galaxy[4]			0.1218	KHbrG	0.12050	3
0733020	AAT 31Aug92	600	Galaxy			0.0709	h_η h_ζ KHh_δ Gh_γ h_β	0.07034	18
	AAT 31Aug92	600	Galaxy			0.0750	KHG	0.07607	06
	AAT 31Aug92	600	Galaxy			0.074	KHG	0.07312	17
0733023	AAT 23Aug92	600	Galaxy		cD	0.0660	KHGhb	0.0681	21
	AAT 23Aug92	600	Galaxy			0.0681	KHG	0.0682	09
0733036	AAT 22Aug92	600	Galaxy			0.0631	KHGh_β Mgb	0.06311	16
	AAT 22Aug92	600	Galaxy	⊙	cD	0.0612	$[O_{II}]$ KHGMgb	0.06095	14

Table B.1: (continued) Results from the spectroscopic followup.

MASOL no.	place date	t(s)	object type	pos. flag	cD flag	manual redshift	spectral features	XCORR redshift	XCORR δz
0733059	AAT 10Sep93	400	Galaxy			0.1503	$h_\theta\, h_\eta\, h_\zeta$ KHh_δ Gh_γ	0.15281	15
	AAT 10Sep93	400	Galaxy			0.1480	[O II] K(H)h_δ (G)	unclear	
	AAT 10Sep93	900	Galaxy*			0.202	[O II] KHhdG	0.20397	27
0733077	AAT 24Aug92	700	Galaxy	◯		0.0339	KHGhcMgb	0.03408	05
	AAT 24Aug92	700	Galaxy	◯		0.2023†	KHG	0.02038	27
0743043	AAT 23Aug92	900	Galaxy			0.1245	KHG	0.12523	23
	AAT 23Aug92	900	Galaxy			0.1232	KHG	0.12461	12
	AAT 23Aug92	600	Galaxy		cD	0.1263	K(H)G	0.12596	20
	AAT 23Aug92	600	Galaxy*			∼0.1245	G	unclear	
0753002	AAT 30Oct91	400	AGN	⊙		0.0390	H_β ^{sw}[O III] [O III] ^{lf}	unclear	
0753011	AAT 31Oct91	1200	Galaxy[8]	◯	cD	0.1532	[O II] ^{lf}KH	unclear	
0753013	AAT 30Oct91	1200	Galaxy	◯		∼0.135	brG	0.13719	10
	AAT 30Oct91	1200	Galaxy	◯	cD	∼0.134	KHG	0.1329	44
0753024	AAT 10Sep93	600	AGN	⊙		n.a.	?bl	0.01515	119
	AAT 10Sep93	600	Galaxy*			0.0457	KHG	0.04758	06
0753035	AAT 29Oct91	636	Galaxy			∼0.0674		0.0677	14
	AAT 29Oct91	636	Galaxy	◯	cD	0.0658	KHG	0.0669	10
0753052	AAT 22Aug92	600	Galaxy	◯		0.0876	KHGhb	0.08812	09
	AAT 22Aug92	600	Galaxy	◯	cD	0.0883	$h_\theta\, h_\eta$ KHh_δ Gh_γ h_β	0.08833	17
0753060	AAT 24Aug92	300	AGN[14]	⊙		n.a.	?bl	unclear	
0762126	AAT 11Sep93	600	Galaxy	⊙	cD	0.0577	[O II] KHG	0.05758	12
	AAT 11Sep93	600	Galaxy			0.0577	KHG	0.05794	04
0762129	AAT 22Aug92	600	Galaxy			0.1038	KHG	0.10811	09
	AAT 22Aug92	600	Galaxy	◯		0.0987	KHGbrh_β	0.09891	17
	AAT 22Aug92	600	Galaxy	◯		0.0987	KHbrGh_β	0.09850	25
	AAT 22Aug92	600	Galaxy	◯		0.0986	KHbrGh_β	0.09813	12
0763002	AAT 07Sep93	900	Galaxy			0.0828	KHG	0.08348	12
	AAT 07Sep93	900	Galaxy		cD	0.0828	KHG	0.08305	07
	AAT 07Sep93	900	Galaxy			0.0828	KHG	0.08262	07

Table B.1: (continued) Results from the spectroscopic followup.

MASOL no.	place date	t(s)	object type	pos. flag	cD	manual redshift	spectral features	XCORR redshift	δz
0763011	AAT 22Aug92	900	Galaxy*			0.0868	$[O_{II}]^{sf} h_\beta\ h_\eta$ KHG	0.08665	10
	AAT 22Aug92	900	AGN	⊙		0.0895	$[O_{II}]^{sf} h_\eta\ h_\zeta$ KHGH_β $[O_{III}]^{lw}$	unclear	
	AAT 07Sep93	300	Star*			star		0.00006	03
0763035	AAT 24Aug92	300	Star*			star		0.00004	08
	AAT 10Sep93	900	Star*			star		0.00009	03
	AAT 10Sep93	900	Star*			∼0.2224	($h_\zeta\ h_\epsilon$)G	0.00007†	08
	AAT 10Sep93	900	Galaxy			0.2254	$[O_{II}]$ KHh_δ G	unclear	
0763038	AAT 01Nov91	2500	Galaxy	◯		0.232	KHG	unclear	
	AAT 01Nov91	2500	Galaxy	◯		0.23	KHG	unclear	
	AAT 01Nov91	2500	Galaxy*			∼0.23	br	unclear	
0763040	AAT 10Sep93	1200	Galaxy			0.3056	$[O_{II}]$ KH	unclear	
	AAT 10Sep93	1200	Star*			∼0.3161	(KH)	0.00016†	05
	AAT 10Sep93	1200	Galaxy*			∼0.3158	(KH)	unclear	
0763051	AAT 23Aug92	300	Galaxy		cD	0.0545	KHGh_β Mgb	0.05450	15
	AAT 23Aug92	300	Galaxy			0.0550	KHGh_β Mgb	0.05536	16
0763052	AAT 22Aug92	300	Galaxy			0.0537	KHGMgb	0.05346	05
	AAT 22Aug92	300	Galaxy			0.0527	KHGMgb	0.05395	19
	AAT 22Aug92	300	Galaxy	⊙		0.0556	$[O_{II}]$ KHGMgb	0.05609	11
	AAT 22Aug92	300	Galaxy			0.0629	KHGh_β Mgb	0.06222	07
0772150	AAT 30Oct91	930	Galaxy	◯	cD	0.0816	KHG	0.08084	11
	AAT 30Oct91	930	Galaxy	◯		0.0844	KHG	0.08411	42
	AAT 30Oct91	930	Star*			star			
0773037	AAT 22Aug92	900	Galaxy*			0.1799	G	unclear	
	AAT 22Aug92	900	Galaxy			0.1775	KHG	0.17826	20
	AAT 22Aug92	900	Galaxy*			0.1818	KHGh_α	unclear	
	AAT 22Aug92	900	Galaxy*			0.1845	KHh_γ	unclear	
	AAT 22Aug92	600	Galaxy			0.1752		0.17809	57
	AAT 22Aug92	600	Galaxy			0.1790		0.17944	32

Table B.1: (continued) Results from the spectroscopic followup.

MASOL no.	place date	t(s)	object type	pos. flag	cD	manual redshift	spectral features	XCORR redshift	δz
0773041	AAT 23Aug92	600	Galaxy*			~0.228	KHh$_\beta$	unclear	
	AAT 23Aug92	600	Galaxy			0.0895	KHG	0.09034	23
	AAT 23Aug92	600	Galaxy	○	cD	0.0859	([O$_{II}$])KHG	0.08748	22
0782158	AAT 07Sep93	1200	Galaxy			0.0943	KHG	0.09442	23
	AAT 07Sep93	1200	Galaxy			0.0879	KHG	0.08787	13
	AAT 07Sep93	600	Galaxy			0.0877	KHG	0.08807	18
0783007	SAAO 22Sep92	1200	Galaxy			0.0723	KHbrG	0.07244	34
	SAAO 22Sep92	900	Galaxy			0.0736	KHbrG	0.07263	22
	SAAO 22Sep92	1500	Galaxy			0.0749	KHbr	0.07423	29
	AAT 23Aug92	600	Galaxy			0.0743	KHGh$_\beta$	0.07372	18
	AAT 23Aug92	600	Galaxy*			~0.0744	(KHG)	bombed	
0783010	AAT 29Oct91	1442	Galaxy	○		0.1340	KHbrG	0.1342	42
	AAT 29Oct91	1442	Galaxy	○	cD	0.1300	KHG	0.1308	09
0783013	AAT 11Sep93	600	Galaxy			0.1384	KHG	0.13850	15
	AAT 11Sep93	600	Galaxy*			~0.1413	((KHG))	unclear	
	AAT 11Sep93	600	Galaxy*			~0.1435	((KHG))	unclear	
0792131	AAT 22Aug92	600	Galaxy			0.0960	KHG	unclear	
	AAT 22Aug92	600	Galaxy	○		0.0922	(KH)G	unclear	
	AAT 22Aug92	600	Galaxy	○	cD	0.0901	KHGh$_\gamma$	0.08816	19
	AAT 22Aug92	600	Galaxy			~0.0933	(KHG)	unclear	
0793012	AAT 10Sep93	600	Galaxy			0.1220†	KH(h$_\delta$)G	0.02680	123
	AAT 10Sep93	600	Galaxy*			0.1259	(KH)G	unclear	
	AAT 10Sep93	600	Galaxy	○		0.1206	KHG	0.12196	12
	AAT 10Sep93	600	Galaxy	○		0.1203	KHG	0.12226	17
	AAT 10Sep93	600	Galaxy*			0.1286	(KH)	unclear	
0793022	AAT 10Sep93	900	Galaxy			0.2019	KHG	unclear	
	AAT 10Sep93	900	Galaxy			0.1970	KHG	0.19882	31
	AAT 10Sep93	900	Galaxy			0.1982	KHG	0.20048	41

Table B.1: (continued) Results from the spectroscopic followup.

MASOL no.	place date	t(s)	object type	pos. flag	cD flag	manual redshift	spectral features	XCORR redshift	XCORR δz
0803007	AAT 10Sep93	600	AGN[10]	⊙		~0.116	$[O_{II}] - -^{sf}H_\delta\, H_\gamma\, H_\beta{}^{lw}$	0.02285	184
	AAT 10Sep93	600	Galaxy*			0.1160	$[O_{II}]\, KHh_\delta\, Gh_\gamma$	0.11565	14
0803028	SAAO 25Sep92	3609	AGN	⊙		0.1126	$[O_{II}]\, H_\beta\, [O_{III}]$	unclear	
	SAAO 25Sep92	393	Star			star		-0.00007	07
0813006	AAT 24Aug92	600	Galaxy	○		0.1299	KHG	0.12990	27
0813010	AAT 30Oct91	1200	Galaxy[2]	○		0.0812	KHGMgb	unclear	
	AAT 30Oct91	1200	Galaxy	○	cD	0.0826	KHG	0.08355	41
0813011	AAT 23Aug92	600	Galaxy	○		0.1071	$KHGh_\beta$	unclear	
	AAT 23Aug92	600	Galaxy	○	cD	0.1082	KHG	0.10922	20
0813012	AAT 11Sep93	900	Galaxy*			0.1499	KHG	unclear	
	AAT 11Sep93	900	Galaxy	○		0.0849	$KHGh_\beta$	0.08498	09
	AAT 11Sep93	900	Galaxy	○	cD	0.0888	$KHGh_\beta$	0.08839	13
	AAT 11Sep93	900	Galaxy			0.0880	$KHGh_\beta$	0.08719	05
0813014	AAT 22Aug92	600	Galaxy	○	cD	0.0879	$[O_{II}]\, KHGh_\beta$	0.08791	13
	AAT 22Aug92	600	Galaxy	○		0.0910	$KHGh_\beta$	0.09154	10
0813023	AAT 11Sep93	1200	Galaxy*	○	cD	~0.2633	$([O_{II}])$	bombed	
	AAT 11Sep93	1200	Galaxy[3]			0.2631	$(h_\eta)KHh_\delta\, G$	unclear	
0813037	AAT 22Aug92	450	Galaxy			0.1999	KHG	0.20083	27
	AAT 22Aug92	450	Galaxy			0.1987	KHG	0.19883	05
0822162	AAT 10Sep93	900	AGN[11]	⊙		0.0253	$rm[O_{II}]\, KHGH_\beta\, [O_{III}]^{sf}[O_{III}]^{lf}Mgb$	0.02510	06
	AAT 10Sep93	900	Galaxy*			0.1629	$KHh_\delta\, G$	0.16573	13
0823033	AAT 11Sep93	600	Galaxy			0.1127	KHG	0.11170	45
	AAT 11Sep93	600	Galaxy	⊙	cD	0.1117	KHG	0.11161	24
0823059	AAT 22Aug92	400	Galaxy*			~0.0405	HGH_γ	unclear	
	SAAO 21Sep92	450	Galaxy	⊙	cD	0.0500	KHbrGMgb	0.04921	13
	SAAO 21Sep92	400	Galaxy			0.05	KHbrG(Mgb)	0.04926	24
0823080	AAT 11Sep93	600	Galaxy	⊙	cD	0.0736	KHG	0.07306	17
	AAT 11Sep93	600	Galaxy			0.0703	$KH(h_\delta\, h_\gamma)$	0.06951	07

Table B.1: (continued) Results from the spectroscopic followup.

MASOL no.	place date	t(s)	object type	pos. flag	cD	manual redshift	spectral features	XCORR redshift	δz
0833006	AAT 22Aug92	600	Star*			star	KHMgb	0.00007	02
	AAT 22Aug92	600	Galaxy*[12]			0.1897	$[O_{II}]^{lf}$KHbrh$_\delta$ h$_\gamma$	unclear	
	AAT 22Aug92	600	AGN	⊙		n.a.	$-\,-\,-\,-\,-\,-\,-^{lw}$	unclear	
0842258	AAT 10Sep93	1200	Galaxy*			0.298	(KH)	unclear	
	AAT 10Sep93	1200	Galaxy	○		0.2906	KH	bombed	
	AAT 10Sep93	1200	Galaxy			0.3026	KH	unclear	
0843019	AAT 01Nov91	200	Galaxy	⊙	cD	0.0819	$[O_{II}]$		
0843045	AAT 31Oct91	900	Galaxy*	○	cD	0.0971	$[O_{II}]^{lf}$	unclear	
	AAT 31Oct91	900	Galaxy			n.a.		0.10926	11
	AAT 07Sep93	900	Galaxy	○		0.1146	$[O_{II}]$ (KH)	unclear	
	AAT 07Sep93	900	Galaxy*			0.2316	h$_\theta$ h$_\eta$ h$_\zeta$ (KH)h$_\gamma$		
	AAT 07Sep93	900	Galaxy			0.1121	KHGh$_\beta$	0.11264	19
0843053	AAT 22Aug92	600	Galaxy	⊙	cD	0.1924	KHG	0.19227	45
	AAT 22Aug92	600	Galaxy			0.1919	KHG	unclear	
	AAT 22Aug92	600	Galaxy			0.1919	h$_\beta$ h$_\eta$ KHG	unclear	
0843056	AAT 31Oct91	1264	Galaxy			0.2264	$[O_{II}]^{sf}$KH		
	AAT 31Oct91	1264	Galaxy*			0.2346	$[O_{II}]^{lf}$	0.02577	08
0843076	AAT 31Oct91	900	Galaxy	○	cD	0.1094	KHbrG	0.10963	15
0843081	AAT 31Oct91	1219	Galaxy*			0.1237	KHbr	0.00637	09
	AAT 31Oct91	1219	Galaxy			0.1156		0.11622	08
	AAT 31Oct91	1219	Galaxy	○	cD	0.1200	KHbrGMgb	0.11971	10
0843099	AAT 24Aug92	640	Galaxy	⊙	cD	0.0782	KHGhb	0.07846	11
	SAAO 22Sep92	245	Star			star			
0843100	AAT 23Aug92	300	Star*	○		star	KHGMgb	0.05338	04
	AAT 23Aug92	600	Galaxy		cD	0.1875	K(H)G	0.18900	62
	AAT 23Aug92	600	Galaxy			0.1856	KH	unclear	
	AAT 23Aug92	600	Galaxy*			∼0.1857	($[O_{II}]$)	unclear	
	AAT 23Aug92	600	Galaxy*			∼0.1869	($[O_{II}]$HG)	unclear	

Table B.1: (continued) Results from the spectroscopic followup.

MASOL no.	place date	t(s)	object type	pos. flag	cD	manual redshift	spectral features	XCORR redshift	δz
0852212	AAT 22Aug92	300	Galaxy	○	cD	0.0251		0.02490	12
	AAT 22Aug92	300	Galaxy			0.0251		0.02854	06
0853001	AAT 31Oct91	1305	Galaxy	○		0.1983	(KH)	0.18831†	11
0853043	AAT 11Sep93	90	MStar?	○		star			
0853055	AAT 23Aug92	900	AGN	○		0.0593	$[O_{II}]\, h_\zeta\, KHG - h_\beta\, [O_{III}]^{sf}$	0.05913	06
	AAT 23Aug92	900	Galaxy✳			0.1372	$[O_{II}]^{sf} KHG$	0.13769	24
	SAAO 25Sep92	2400	Galaxy✳	○		0.0866	KHbrG	0.0864	17
	SAAO 25Sep92	900	Galaxy✳			0.0889	KHbrG	0.0866	21
0853062	AAT 11Sep93	1200	Galaxy			0.0617	$KHGh_\beta$	0.06151	03
	AAT 11Sep93	1200	Galaxy			0.0770	$KHGh_\beta$	0.07689	04
0862172	AAT 01Nov91	298	AGN	⊙		0.020	$H_\beta\, [O_{III}]\, [O_{III}]^{lw\ ?bl}$		
0863044	AAT 11Sep93	900	Galaxy			0.1127	$KHGh_\delta$	0.11236	14
	AAT 11Sep93	900	Galaxy*	⊙		0.0966	KHG	0.09691	14
	AAT 11Sep93	900	Galaxy			0.1142	KHG	0.1138	09
0863082	AAT 01Nov91	615	Galaxy	○		0.2204	$[O_{II}]^{lf} KH$	unclear	
0873006	SAAO 26Sep92	3000	Galaxy	○		0.1244	KHbr	0.12455	26
0873029	AAT 24Aug92	600	Galaxy			0.1233	KHG	unclear	
	AAT 24Aug92	600	Galaxy			0.1284	KHG	0.12930	12
	AAT 24Aug92	600	Galaxy			~0.1225	G	0.12108	11
0873078	AAT 11Sep93	900	Galaxy*	○		0.0661	$[O_{II}]\, KH$	0.06521	05
	AAT 11Sep93	900	Galaxy*			0.1095	$[O_{II}]\, KHh_\delta\, Gh_\gamma\, h_\beta$	0.10927	11
	AAT 11Sep93	200	AGN	○		n.a.	?bl		
0883005	AAT 11Sep93	1200	Galaxy		cD	0.0775	$KHGh_\beta$	0.07935	20
	AAT 11Sep93	1200	Galaxy			0.0779	$KHGh_\beta$	0.07783	04
	AAT 11Sep93	1200	Galaxy*			0.0863	KHh_β	0.08613	06
0883021	AAT 22Aug92	600	AGN	⊙		~0.068	$[O_{II}]\, H_\delta\, {}^{sf}H_\gamma\ ------^{sw}$	unclear	
	AAT 22Aug92	600	Galaxy*			0.1605	$h_\theta\, h_\eta\, KHGh_\gamma$	0.16713	32

Table B.1: (continued) Results from the spectroscopic followup.

MASOL no.	place date	t(s)	object type	pos. flag	cD	manual redshift	spectral features	XCORR redshift	δz
0883036	AAT 10Sep93	250	Galaxy	◯		0.0976	KHG	0.09947	10
	AAT 10Sep93	250	Galaxy	◯		0.0879	$h_\theta\, h_\eta\, h_\zeta$ KHh_δ G	0.08921	09
	AAT 10Sep93	250	Galaxy	◯		0.0996	K(H)$h_\delta\, h_\gamma\, h_\beta$	0.10161	11
	AAT 10Sep93	250	Galaxy	◯		0.0878	$h_\theta\, h_\eta\, h_\zeta$ KHh_δ G	0.08929	06
0883037	AAT 10Sep93	900	Galaxy	◯		0.3162†	$h_\eta\, h_\zeta$ KH	0.00391	42
	AAT 10Sep93	900	Galaxy	◯		0.3125†	KH	0.17551	168
	AAT 10Sep93	900	Galaxy			0.3160	KH	unclear	
0883039	AAT 22Aug92	600	Galaxy	◯		0.2773	$h_\theta\, h_\eta$ KHh_δ G	unclear	
0883087	AAT 01Nov91	716	Galaxy	◯		∼0.11	(KH)	0.11437†	05
	AAT 01Nov91	716	Galaxy	◯	cD	∼0.11	KH	0.11381†	21
0893004	AAT 23Aug92	300	Galaxy			0.0207	KHGMgb	0.02307	07
	AAT 23Aug92	300	Galaxy			0.0224	KHGh_β Mgb	0.02121	18
0893034	AAT 11Sep93	1200	Galaxy*			0.1521	KHG	0.15230	12
	AAT 11Sep93	1200	AGN	⊙		0.1496	$[O_{II}]$ $--H_\gamma$ ^{lw}	bombed	
0893060	AAT 01Nov91	2400	Galaxy	◯		∼0.1388	KHbr(G)	0.14871†	33
	AAT 01Nov91	2400	Galaxy*		cD	∼0.1430	KHbr	0.10479	21
0903036	AAT 10Sep93	1200	Galaxy			0.1874	$[O_{II}]\, h_\zeta$ KHh_δ (G)	unclear	
	AAT 10Sep93	1200	Galaxy			0.1889	KHG	0.19077	39
0903046	AAT 24Aug92	600	Galaxy*	◯		0.1425	KHG	0.14192	16
	AAT 24Aug92	600	Galaxy*	◯	cD	0.1415	$[O_{II}]$ ^{sf}KHG	0.14161	20
	AAT 24Aug92	200	AGN	◯		0.1407	$[O_{II}]\,[O_{III}]\,[O_{III}]$ $^{sw\ ?bl}$	unclear	
1044097	AAT 31Aug92	600	Galaxy	◯		0.0579	KHGMgb	0.05774	09
	AAT 10Sep93	600	Galaxy			0.0799	KHG	0.08164	05
	AAT 10Sep93	600	Galaxy			0.0789	KHG	0.08066	05
1054145	AAT 24Aug92	900	Galaxy	⊙	cD	0.1158	$[O_{II}]$ KHG	0.11565	21
	AAT 24Aug92	900	Galaxy			0.1126	KHG	0.11339	13
1054191	AAT 31Aug92	600	AGN	⊙		n.a.	$^{?bl}$	unclear	

Table B.1: (continued) Results from the spectroscopic followup.

MASOL no.	place date	t(s)	object type	pos. flag	cD flag	manual redshift	spectral features	XCORR redshift	XCORR δz
1064123	AAT 07Sep93	577	Star*			star		unclear	
	AAT 07Sep93	577	Galaxy	○		0.0447	H(G)Mgb	0.04489	10
	AAT 07Sep93	577	Galaxy	○	cD	0.0437	HGMgb	0.04468	09
1224040	AAT 11Sep93	1200	Galaxy			0.1694	[O_{II}] KHG	0.16978	39
	AAT 11Sep93	1200	Galaxy			0.1687	HG	0.16827	20

Table B.1: (continued) Results from the spectroscopic followup.

Appendix C

CUOC Finding Charts

This appendix presents, in numerical order, COSMOS/UKST Object Catalogue (CUOC) finding charts for 40 of the SGP RASS cluster candidates listed in table A.2. The plots include magnitude and positional information for all objects within a 90″ radius of the X-ray centre. The X-ray centre is marked with an $\times$ and the X-ray error circle is shown via a solid black line. The dotted line marks a circle of radius 200″. In these plots, the object ellipses determined by COSMOS are shown. Stars and galaxies are distinguished via light and dark shading respectively. These plots were produced by Ray Cruddace using software developed by Jacob Englhauser at MPE. Any noteworthy points concerning the individual finding charts are listed in table C.1 below. In this table "SF" refers to "spectroscopic follow-up", "lit." refers to "literature" and "X-ray ◯" refers to "X-ray error circle". Many of the candidates featured have been highlighted, in chapter 4, as examples of the 9 classification flags used in table A.2. In addition several Abell and non-Abell clusters are featured, to show their similarity.

MASOL no.	id. no.	Notes.
0014072	1	(Abell) cluster with agreeing z_{lit} and z_{SF}
0034044	4	A $z > 0.11$ cluster with an emission line galaxy inside the X-ray ◯
0034158	2	Candidate identified with Abell 85.
0034159	6	Candidate associated with, but not identified as, Abell 85.
0074105	1	(Abell) Cluster whose z_{lit} and z_{SF} disagree
0084165	8	AGN identified during the SF
0094175	1	Abell 222, forms closest cluster pair in sample with 0094175
0094176	1	Abell 223, forms closest cluster pair in sample with 0094175
0094217	2	None of the available redshifts are inside the X-ray ◯
0104188	3	Possible high velocity dispersion cluster
0104212	1	(Abell) cluster whose count rate was severely underestimated by SASS
0124051	9	Candidate provisionally identified with a white dwarf star
0134078	8	AGN identified during the SF
0144092	3	(Abell) Cluster with a foreground starburst (or possibly active) galaxy
0144172	9	"AGN" on X-ray centre may be emission line cD galaxy
0174101	8	Candidate identified with nearby spiral galaxy on X-ray centre
0174111	4	A $z > 0.11$ cluster with an emission line galaxy inside the X-ray ◯
0723060	2	Abell cluster, with z_{lit}, dominated by a single cD-type galaxy
0733059	3	Galaxy redshifts obtained outside the X-ray ◯
0733077	7	Candidate from the SF that has not been identified
0743009	8	Candidate identified with bright star on X-ray centre
0743011	5	Candidate with no identification that "looks" like a cluster
0753011	4	A $z > 0.11$ (Abell) cluster with an emission line galaxy inside the X-ray ◯
0753052	1	Type 1, non-Abell cluster
0753060	8	BL Lac. object on X-ray centre was misid.'d as a star in the CUOC
0782158	1	Type 1, non-Abell cluster
0813014	1	Type 1, Abell cluster, observed during the SF
0823080	1	Type 1, non-Abell cluster
0843100	4	There are galaxies inside the X-ray ◯ with no spectra
0853043	9	Candidate provisionally identified with an M-dwarf star
0853062	7	Candidate from the SF that has not been identified
0863043	5	Candidate with no identification that "looks" like a cluster
0863044	3	Possible high velocity dispersion cluster
0873078	8	AGN identified with X-ray source lies inside a cluster
0883087	6	Type 1, non-Abell cluster
0893097	1	Type 1, Abell cluster that was not observed during the SF
0903046	8	AGN identified with X-ray source lies inside a cluster
0903060	3	Abell cluster, with z_{lit}, dominated by a single, AGN-type, galaxy
1044097	7	Candidate from the SF that has not been identified
1064123	1	Type 1, non-Abell cluster

Table C.1: Listing of the CUOC finding charts presented in figures C.1 to C.40.

ROSAT Identification | **ROSAT / MPE / RSDC | 28-JUN-94 08:59:42 | RGC** | Page: 1

UKST IIIaJ (blue) | **ROE/NRL COSMOS Finding Chart** | MASOS file: roe_disk:[roedat.masos]001_N1_SI04_N1_P2.mos

Field No. 475 | MASOL Nr.: 000072

Plate Epoch: 1982.6360 | RASS Info: | ROSAT Source Name: RX J00574-2618

Equinox: J2000.0 | Error radii: 1 sigma = 20.5" ; plotted: 90% conf. = 1.645 sigma = 33.8" | ROSAT Position (2000.0): 00 57 26.3 -26 18 09

(1950.0): 00 55 00.7 -26 34 21

Galactic II (l,b): 181.63059 -88.42580

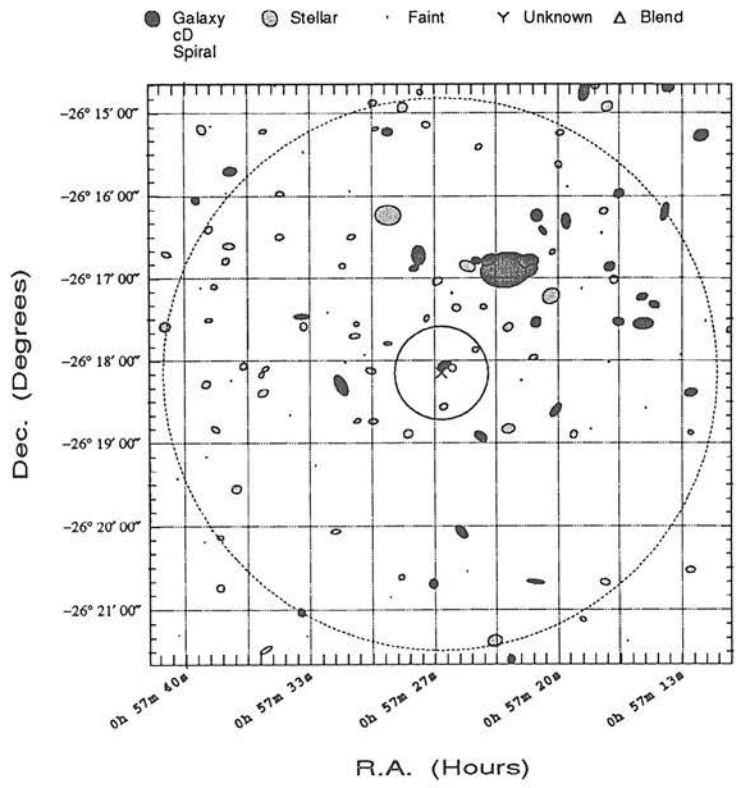

#	CLASS	B	R.A.	Dec.	DIST.
01	Galaxy	19.04	00 57 26.2	-26 18 03	6.2
02	Stellar	21.31	00 57 25.7	-26 18 05	8.9
03	Stellar	21.42	00 57 26.2	-26 18 33	24.5
04	Stellar	22.02	00 57 24.5	-26 17 52	30.0
05	Stellar	22.26	00 57 27.1	-26 17 29	41.0
06	Stellar	22.57	00 57 29.2	-26 17 47	44.2
07	Stellar	20.81	00 57 25.5	-26 17 22	48.7
08	Stellar	20.58	00 57 28.1	-26 18 53	50.4
09	Stellar	20.61	00 57 30.1	-26 18 07	51.0
10	Galaxy	19.45	00 57 24.2	-26 18 55	54.0
11	Stellar	22.30	00 57 24.0	-26 17 21	57.0
12	Faint	25.06	00 57 30.4	-26 17 56	57.0
13	Faint	23.70	00 57 22.0	-26 18 15	58.4
14	Faint	23.64	00 57 25.7	-26 17 11	58.6
15	Stellar	20.39	00 57 22.7	-26 17 36	58.8
16	Stellar	21.00	00 57 30.0	-26 18 44	60.6
17	Stellar	18.64	00 57 22.7	-26 18 50	63.2
18	Stellar	20.19	00 57 26.5	-26 17 02	66.8
19	Stellar	21.84	00 57 21.3	-26 17 58	67.7
20	Stellar	21.29	00 57 30.9	-26 17 42	68.0
21	Stellar	22.36	00 57 30.8	-26 18 44	69.8
22	Faint	24.42	00 57 31.5	-26 18 01	69.9
23	Stellar	22.73	00 57 30.8	-26 17 33	70.8
24	Galaxy	18.33	00 57 31.7	-26 18 18	72.9
25	Galaxy	19.32	00 57 21.2	-26 17 32	77.7
26	Galaxy	21.91	00 57 27.8	-26 16 53	78.9
27	Stellar	20.82	00 57 24.9	-26 16 51	79.9
28	Galaxy	21.81	00 57 24.4	-26 16 47	85.9
29	Galaxy	19.50	00 57 20.1	-26 18 36	87.2
30	Galaxy	17.30	00 57 27.5	-26 16 43	87.4

Selection criterion: distance
Galaxy Density = 430 per sq. deg.
Sample Radius = 200.0 arc sec

Stars	=	53
Total galaxies	=	28 (cDs = 0, spirals = 0)
Blend objects	=	0
Faint objects	=	24
Unknown objects	=	0
Sum	=	105

Figure C.1: CUOC Finding chart of candidate 0014072

ROSAT Identification	ROSAT / MPE / RSDC | 28-JUN-94 08:59:57 | RGC	Page: 2
UKST IIIaJ (blue)	ROE/NRL COSMOS Finding Chart	MASOS file: roe_disk:[roedat.masos]003_N1_SI04_N1_P1.mos
Field No. 198	....	MASOL Nr.: 000044
Plate Epoch: 1977.7750	RASS Info:	ROSAT Source Name: RX J02162-4816
Equinox: J2000.0	Error radii: 1 sigma = 15.2" ; plotted: 90% conf. = 1.645 sigma = 24.9"	ROSAT Position (2000.0): 02 16 15.6 -48 16 29

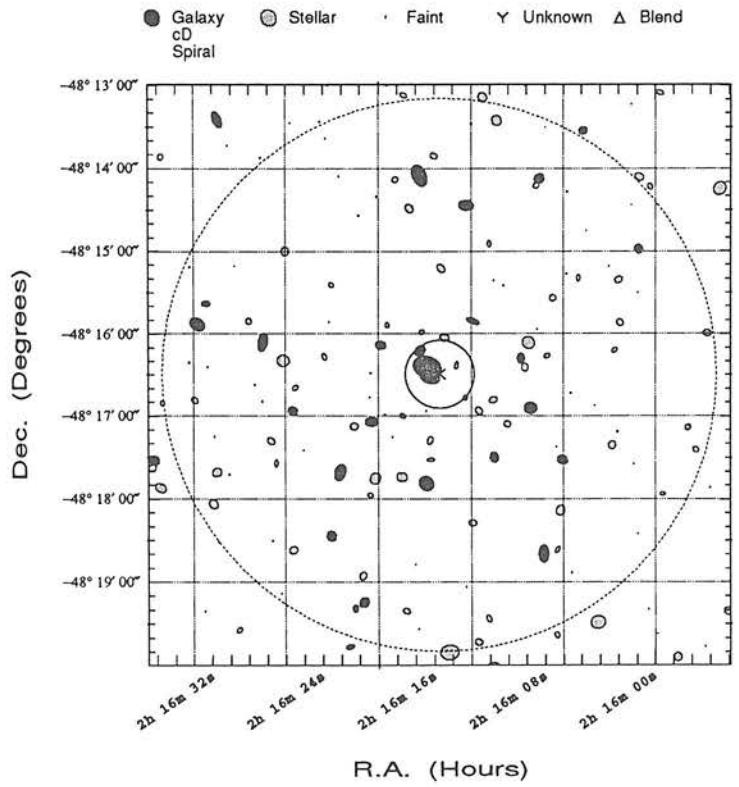

(1950.0): 02 14 23.8 -48 30 22
Galactic II (l,b): 270.66471 -63.19570

#	CLASS	B	R.A.	Dec.	DIST.
01	Galaxy	16.92	02 16 16.3	-48 16 32	7.6
02	Galaxy	15.05	02 16 16.5	-48 16 24	10.5
03	Stellar	21.81	02 16 14.4	-48 16 23	13.8
04	Galaxy	19.65	02 16 17.0	-48 16 12	22.3
05	Stellar	22.21	02 16 13.8	-48 16 47	25.2
06	Stellar	18.86	02 16 15.3	-48 16 03	26.9
07	Faint	24.98	02 16 16.6	-48 16 56	28.7
08	Stellar	22.01	02 16 16.9	-48 15 59	33.4
09	Stellar	20.53	02 16 12.8	-48 16 56	38.5
10	Stellar	21.53	02 16 18.3	-48 17 00	40.3
11	Stellar	20.18	02 16 11.7	-48 16 48	42.8
12	Galaxy	19.74	02 16 13.2	-48 15 51	45.3
13	Galaxy	18.69	02 16 19.9	-48 16 08	47.4
14	Stellar	20.25	02 16 16.3	-48 17 18	48.6
15	Faint	23.20	02 16 19.5	-48 16 59	49.0
16	Faint	24.83	02 16 20.6	-48 16 29	49.5
17	Stellar	22.25	02 16 19.4	-48 15 54	52.1
18	Faint	23.20	02 16 20.7	-48 16 46	53.3
19	Faint	25.09	02 16 19.0	-48 17 15	57.1
20	Galaxy	19.50	02 16 09.7	-48 16 18	59.7
21	Galaxy	17.89	02 16 20.5	-48 17 04	59.9
22	Stellar	20.62	02 16 10.7	-48 17 05	60.6
23	Stellar	20.03	02 16 09.4	-48 16 24	61.7
24	Stellar	21.59	02 16 16.3	-48 17 32	62.6
25	Stellar	16.68	02 16 09.2	-48 16 06	68.0
26	Galaxy	17.48	02 16 09.0	-48 16 54	70.0
27	Galaxy	19.23	02 16 11.7	-48 17 30	71.7
28	Stellar	19.63	02 16 21.7	-48 17 07	72.2
29	Stellar	19.83	02 16 15.5	-48 15 12	77.0
30	Faint	23.91	02 16 08.6	-48 15 57	77.5

Selection criterion: distance
Galaxy Density = 1227 per sq. deg.
Sample Radius = 200.0 arc sec
Stars = 54
Total galaxies = 24 (cDs = 0, spirals = 0)
Blend objects = 0
Faint objects = 42
Unknown objects = 0
Sum = 120

Figure C.2: CUOC Finding chart of candidate 0034044

ROSAT Identification | **ROSAT / MPE / RSDC | 28-JUN-94 09:00:09 | RGC** | Page: 1

UKST IIIaJ (blue) | **ROE/NRL COSMOS Finding Chart** | MASOS file: roe_disk:[roedat.masos]003_N1_SI04_N1_P1.mos

Field No. 681 | .... | MASOL Nr.: 000158

Plate Epoch: 1982.8710 | RASS Info: | ROSAT Source Name: RX J00418-0918

Equinox: J2000.0 | Error radii: 1 sigma = 6.0" ; plotted: 90% conf. = 1.645 sigma = 9.9" | ROSAT Position (2000.0): 00 41 49.7 -09 18 19

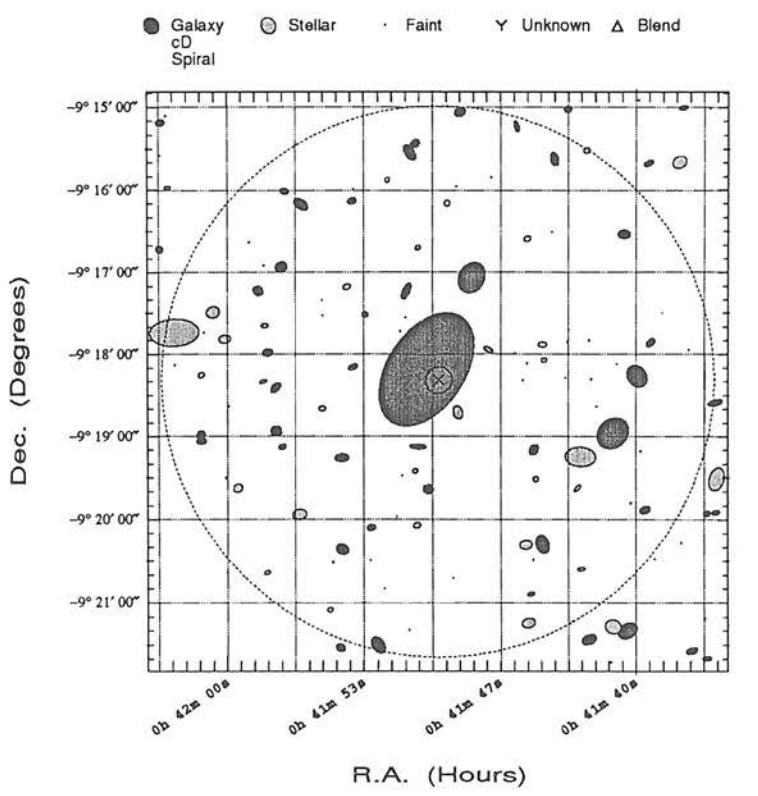

(1950.0): 00 39 18.0 -09 34 45

Galactic II (l,b): 115.22622 -72.03303

#	CLASS	B	R.A.	Dec.	DIST.
01	Spiral	8.75	00 41 50.3	-09 18 11	11.7
02	Stellar	19.64	00 41 48.8	-09 18 43	27.5
03	Stellar	21.00	00 41 47.3	-09 17 57	42.4
04	Faint	21.58	00 41 51.6	-09 17 43	45.4
05	Galaxy	19.92	00 41 50.7	-09 19 07	50.8
06	Faint	23.08	00 41 51.3	-09 17 33	51.6
07	Faint	21.34	00 41 46.0	-09 17 59	58.8
08	Faint	23.08	00 41 45.6	-09 18 19	61.0
09	Galaxy	19.60	00 41 53.9	-09 18 09	62.6
10	Faint	22.45	00 41 45.4	-09 18 07	65.2
11	Stellar	21.31	00 41 50.8	-09 19 25	68.1
12	Galaxy	18.26	00 41 51.3	-09 17 14	69.1
13	Galaxy	20.36	00 41 53.3	-09 17 31	71.3
14	Faint	22.71	00 41 51.5	-09 19 28	74.0
15	Stellar	21.07	00 41 44.5	-09 18 04	77.8
16	Galaxy	13.15	00 41 48.1	-09 17 04	78.7
17	Stellar	18.74	00 41 44.6	-09 17 53	79.5
18	Galaxy	17.28	00 41 50.2	-09 19 38	79.7
19	Galaxy	17.87	00 41 45.0	-09 19 09	85.5
20	Stellar	20.06	00 41 55.4	-09 18 40	86.5
21	Galaxy	17.26	00 41 54.4	-09 19 15	89.8
22	Faint	23.31	00 41 43.5	-09 18 17	92.0
23	Stellar	19.39	00 41 54.2	-09 17 10	95.1
24	Faint	22.13	00 41 55.3	-09 17 32	96.1
25	Faint	21.46	00 41 43.4	-09 17 51	97.6
26	Stellar	20.95	00 41 50.7	-09 16 42	97.8
27	Stellar	21.31	00 41 44.9	-09 19 31	100.6
28	Faint	23.89	00 41 43.3	-09 17 42	101.2
29	Faint	23.41	00 41 55.4	-09 17 20	102.4
30	Faint	23.77	00 41 51.7	-09 19 58	103.3

Selection criterion: distance
Galaxy Density = 733 per sq. deg.
Sample Radius = 200.0 arc sec
Stars = 29
Total galaxies = 35 (cDs = 0, spirals = 1)
Blend objects = 0
Faint objects = 37
Unknown objects = 0
Sum = 101

Figure C.3: CUOC Finding chart of candidate 0034158

ROSAT Identification | **ROSAT / MPE / RSDC | 28-JUN-94 09:00:28 | RGC** | Page: 1

UKST IIIaJ (blue) | **ROE/NRL COSMOS Finding Chart** | MASOS file: roe_disk:[roedat.masos]003_N1_SI04_N1_P1.mos

Field No. 681 | .... | MASOL Nr.: 000159

Plate Epoch: 1982.8710 | RASS Info: | ROSAT Source Name: RX J00413-0919

Equinox: J2000.0 | Error radii: 1 sigma = 28.6" ; plotted: 90% conf. = 1.645 sigma = 47.1" | ROSAT Position (2000.0): 00 41 19.3 -09 19 24

(1950.0): 00 38 47.5 -09 35 51

Galactic II (l,b): 114.81682 -72.03549

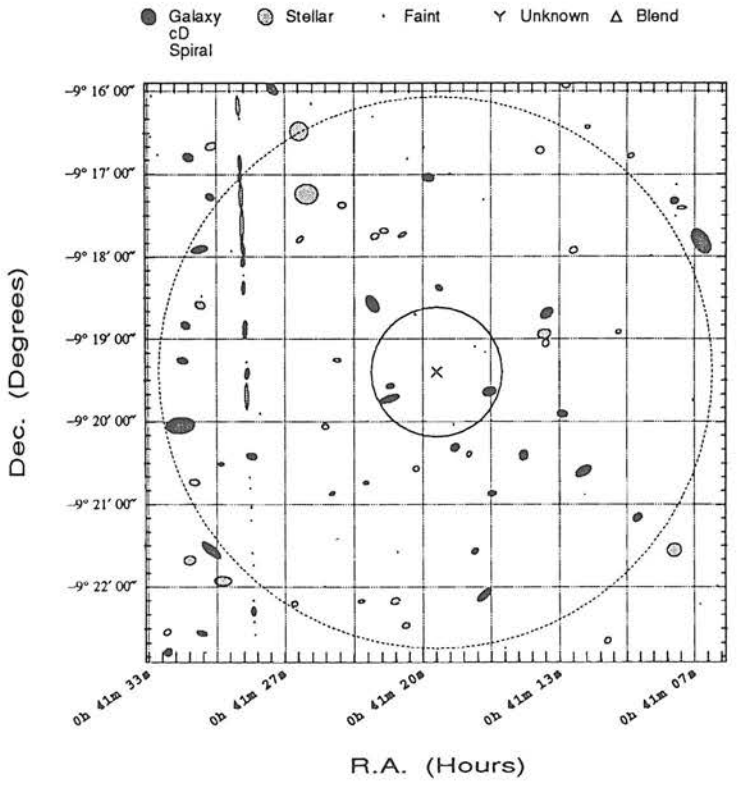

#	CLASS	B	R.A.	Dec.	DIST.
01	Faint	21.53	00 41 17.5	-09 19 06	32.9
02	Galaxy	19.79	00 41 21.6	-09 19 34	34.9
03	Faint	22.76	00 41 16.9	-09 19 09	37.9
04	Galaxy	16.28	00 41 21.6	-09 19 44	39.3
05	Faint	22.74	00 41 18.5	-09 20 02	39.9
06	Galaxy	17.29	00 41 16.7	-09 19 38	40.7
07	Faint	21.93	00 41 20.4	-09 18 42	44.7
08	Faint	22.17	00 41 16.7	-09 19 59	52.5
09	Galaxy	18.36	00 41 18.4	-09 20 19	56.4
10	Galaxy	20.21	00 41 19.2	-09 18 23	61.4
11	Stellar	20.80	00 41 17.7	-09 20 24	63.9
12	Galaxy	16.38	00 41 22.4	-09 18 34	68.0
13	Stellar	20.04	00 41 20.3	-09 20 34	71.8
14	Stellar	20.99	00 41 24.1	-09 19 15	72.3
15	Stellar	18.56	00 41 14.0	-09 19 03	81.4
16	Stellar	16.05	00 41 14.1	-09 18 57	82.2
17	Galaxy	18.98	00 41 15.1	-09 20 24	86.7
18	Stellar	20.14	00 41 24.7	-09 20 03	89.1
19	Galaxy	17.67	00 41 14.0	-09 18 41	90.0
20	Stellar	21.17	00 41 22.7	-09 20 44	95.1
21	Galaxy	18.00	00 41 13.2	-09 19 55	95.5
22	Galaxy	20.28	00 41 16.6	-09 20 52	96.7
23	Stellar	20.70	00 41 21.0	-09 17 44	103.0
24	Stellar	18.53	00 41 22.3	-09 17 45	108.6
25	Stellar	18.88	00 41 21.9	-09 17 41	109.6
26	Stellar	21.17	00 41 24.4	-09 20 52	115.9
27	Galaxy	16.60	00 41 12.1	-09 20 36	128.0
28	Faint	22.25	00 41 17.0	-09 17 18	130.1
29	Faint	21.90	00 41 27.9	-09 19 54	130.9
30	Stellar	18.56	00 41 12.7	-09 17 55	132.5

Selection criterion: distance
Galaxy Density = 765 per sq. deg.
Sample Radius = 200.0 arc sec

Stars	=	27
Total galaxies	=	25 (cDs = 0, spirals = 0)
Blend objects	=	0
Faint objects	=	26
Unknown objects	=	0
Sum	=	78

Figure C.4: CUOC Finding chart of candidate 0034159

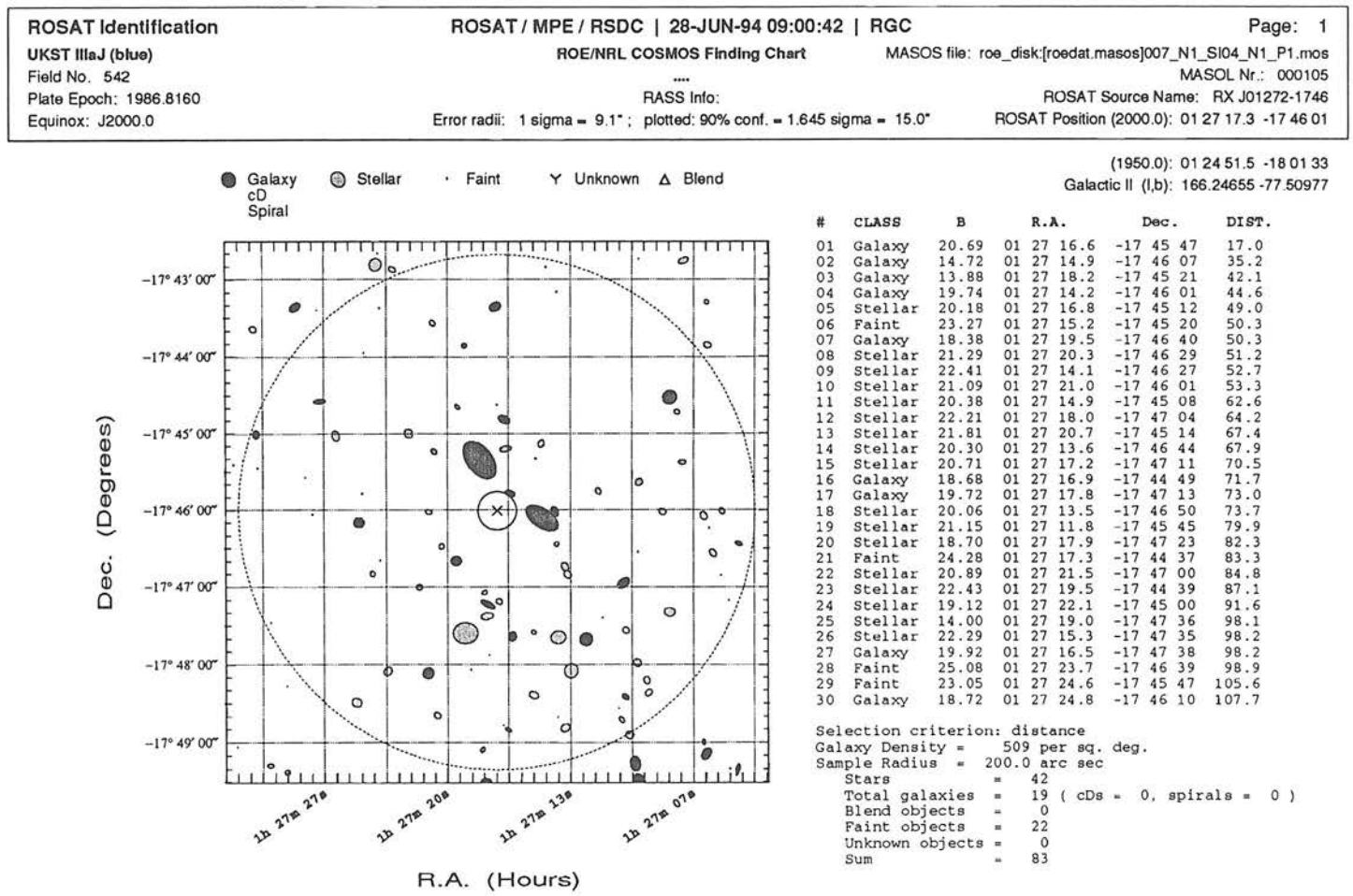

Figure C.5: CUOC Finding chart of candidate 0074105

ROSAT Identification | **ROSAT / MPE / RSDC | 28-JUN-94 09:00:53 | RGC** | Page: 1

UKST IIIaJ (blue) | **ROE/NRL COSMOS Finding Chart** | MASOS file: roe_disk:[roedat.masos]008_N1_SI04_N1_P1.mos

Field No. 543 | .... | MASOL Nr.: 000165

Plate Epoch: 1978.6899 | RASS Info: | ROSAT Source Name: RX J01430-1949

Equinox: J2000.0 | Error radii: 1 sigma = 4.8" ; plotted: 90% conf. = 1.645 sigma = 7.9" | ROSAT Position (2000.0): 01 43 01.0 -19 49 14

(1950.0): 01 40 37.7 -20 04 19

Galactic II (l,b): 183.93074 -76.11091

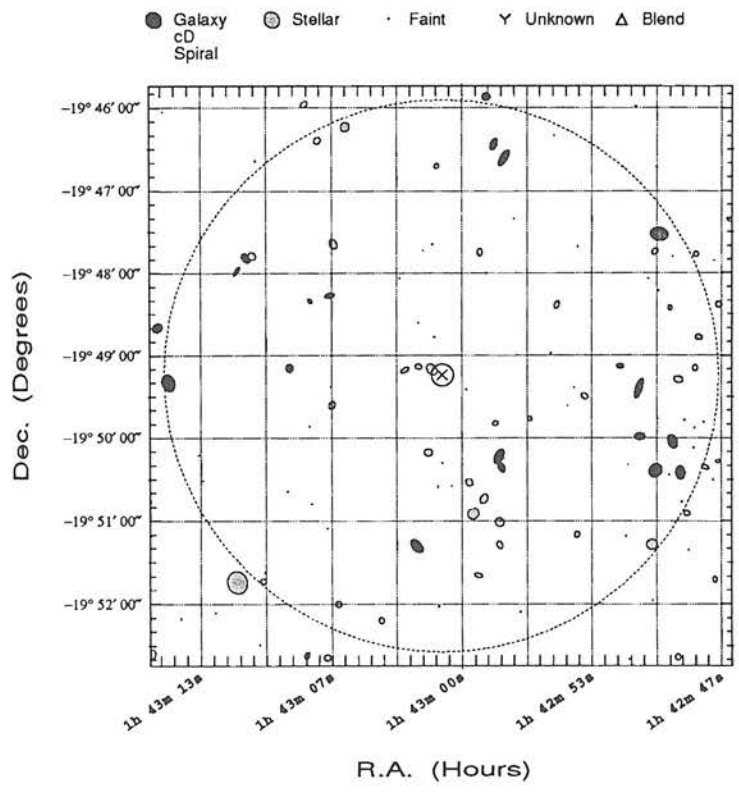

#	CLASS	B	R.A.	Dec.	DIST.
01	Stellar	17.72	01 43 01.5	-19 49 10	8.6
02	Stellar	20.95	01 43 02.2	-19 49 08	18.4
03	Faint	24.07	01 42 59.8	-19 49 25	19.9
04	Stellar	21.78	01 43 02.9	-19 49 11	27.1
05	Faint	24.33	01 43 01.4	-19 48 46	28.8
06	Faint	25.54	01 43 02.2	-19 48 36	42.1
07	Stellar	22.16	01 42 58.3	-19 49 49	52.0
08	Stellar	19.11	01 43 01.7	-19 50 11	57.2
09	Faint	24.91	01 43 01.0	-19 50 18	63.5
10	Stellar	22.56	01 42 56.5	-19 49 46	70.6
11	Galaxy	18.10	01 42 58.1	-19 50 13	71.8
12	Faint	24.71	01 43 03.2	-19 48 03	77.2
13	Galaxy	20.49	01 42 58.0	-19 50 21	79.7
14	Faint	24.65	01 42 55.5	-19 48 58	79.9
15	Stellar	20.61	01 42 59.6	-19 50 32	80.1
16	Faint	24.49	01 43 00.5	-19 50 34	80.4
17	Faint	23.61	01 43 01.2	-19 50 35	80.8
18	Faint	23.75	01 42 58.8	-19 48 00	81.0
19	Faint	25.54	01 43 06.7	-19 49 22	81.4
20	Stellar	19.93	01 43 06.7	-19 49 36	83.0
21	Faint	25.17	01 43 02.0	-19 47 43	92.2
22	Faint	23.14	01 42 54.6	-19 49 36	93.1
23	Stellar	21.18	01 42 59.1	-19 47 45	93.5
24	Stellar	18.16	01 42 58.9	-19 50 44	94.6
25	Faint	24.43	01 42 54.3	-19 49 23	95.6
26	Faint	22.96	01 43 01.5	-19 47 38	96.0
27	Stellar	21.66	01 42 55.1	-19 48 23	97.2
28	Galaxy	20.83	01 43 06.8	-19 48 16	99.8
29	Stellar	17.24	01 42 59.4	-19 50 55	103.0
30	Faint	25.62	01 43 07.8	-19 49 52	103.1

Selection criterion: distance
Galaxy Density = 557 per sq. deg.
Sample Radius = 200.0 arc sec
Stars = 32
Total galaxies = 17 (cDs = 0, spirals = 0)
Blend objects = 0
Faint objects = 37
Unknown objects = 0
Sum = 86

Figure C.6: CUOC Finding chart of candidate 0084165

ROSAT Identification | **ROSAT / MPE / RSDC | 28-JUN-94 09:01:03 | RGC** | Page: 1

UKST IIIaJ (blue) | **ROE/NRL COSMOS Finding Chart** | MASOS file: roe_disk:[roedat.masos]009_N1_SI04_N1_P1.mos

Field No. 612 | .... | MASOL Nr.: 000175

Plate Epoch: 1982.7321 | RASS Info: | ROSAT Source Name: RX J01375-1300

Equinox: J2000.0 | Error radii: 1 sigma = 11.1" ; plotted: 90% conf. = 1.645 sigma = 18.3" | ROSAT Position (2000.0): 01 37 35.0 -13 00 13

(1950.0): 01 35 07.7 -13 15 27

Galactic II (l,b): 162.59095 -72.22207

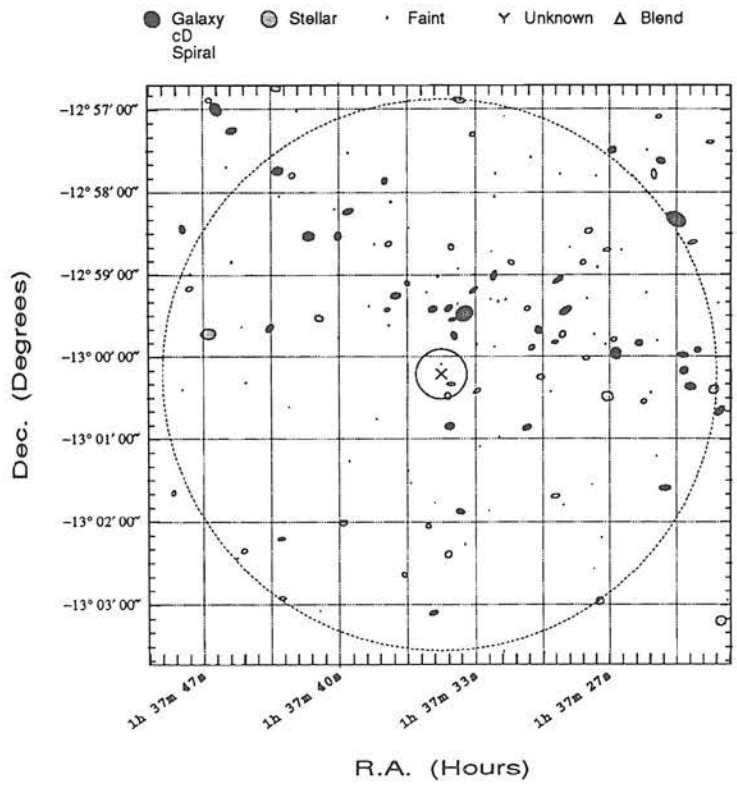

#	CLASS	B	R.A.	Dec.	DIST.
01	Faint	23.33	01 37 35.0	-13 00 05	7.3
02	Stellar	19.56	01 37 34.5	-13 00 20	10.1
03	Stellar	18.70	01 37 34.7	-13 00 29	16.6
04	Faint	21.82	01 37 35.7	-13 00 28	18.2
05	Faint	22.21	01 37 33.8	-13 00 16	18.3
06	Stellar	20.00	01 37 33.2	-13 00 25	28.4
07	Galaxy	19.33	01 37 34.4	-12 59 45	29.5
08	Faint	21.65	01 37 33.3	-12 59 51	33.3
09	Galaxy	18.18	01 37 34.6	-13 00 51	38.6
10	Galaxy	20.52	01 37 34.5	-12 59 33	40.7
11	Faint	21.63	01 37 32.4	-12 59 53	42.8
12	Galaxy	16.04	01 37 33.9	-12 59 29	46.9
13	Galaxy	18.29	01 37 35.4	-12 59 25	47.8
14	Galaxy	19.49	01 37 34.7	-12 59 24	48.4
15	Faint	21.49	01 37 37.6	-12 59 37	51.9
16	Faint	23.12	01 37 34.2	-12 59 21	52.7
17	Faint	22.97	01 37 38.2	-13 00 45	57.2
18	Faint	22.78	01 37 33.1	-13 01 05	59.4
19	Faint	21.97	01 37 35.7	-12 59 13	60.8
20	Stellar	20.46	01 37 37.7	-12 59 25	61.1
21	Faint	21.05	01 37 32.2	-13 00 58	61.9
22	Faint	22.37	01 37 32.6	-12 59 18	65.1
23	Galaxy	19.93	01 37 33.4	-12 59 11	65.6
24	Galaxy	17.95	01 37 37.2	-12 59 15	65.9
25	Faint	23.29	01 37 32.2	-12 59 20	66.8
26	Stellar	20.39	01 37 30.5	-12 59 53	68.1
27	Stellar	19.60	01 37 36.7	-12 59 06	70.7
28	Faint	21.17	01 37 35.2	-12 59 01	71.3
29	Stellar	18.59	01 37 30.1	-13 00 15	71.5
30	Faint	22.97	01 37 31.8	-12 59 18	71.5

Selection criterion: distance
Galaxy Density = 700 per sq. deg.
Sample Radius = 200.0 arc sec
Stars = 34
Total galaxies = 29 (cDs = 0, spirals = 0)
Blend objects = 0
Faint objects = 61
Unknown objects = 0
Sum = 124

Figure C.7: CUOC Finding chart of candidate 0094175

ROSAT Identification | **ROSAT / MPE / RSDC | 28-JUN-94 09:01:13 | RGC** | Page: 1

UKST IIIaJ (blue) | **ROE/NRL COSMOS Finding Chart** | MASOS file: roe_disk:[roedat.masos]009_N1_SI04_N1_P1.mos

Field No. 612 | .... | MASOL Nr.: 000176

Plate Epoch: 1982.7321 | RASS Info: | ROSAT Source Name: RX J01379-1248

Equinox: J2000.0 | Error radii: 1 sigma = 24.6" ; plotted: 90% conf. = 1.645 sigma = 40.4" | ROSAT Position (2000.0): 01 37 56.3 -12 48 13

(1950.0): 01 35 28.9 -13 03 27

Galactic II (l,b): 162.44153 -72.00924

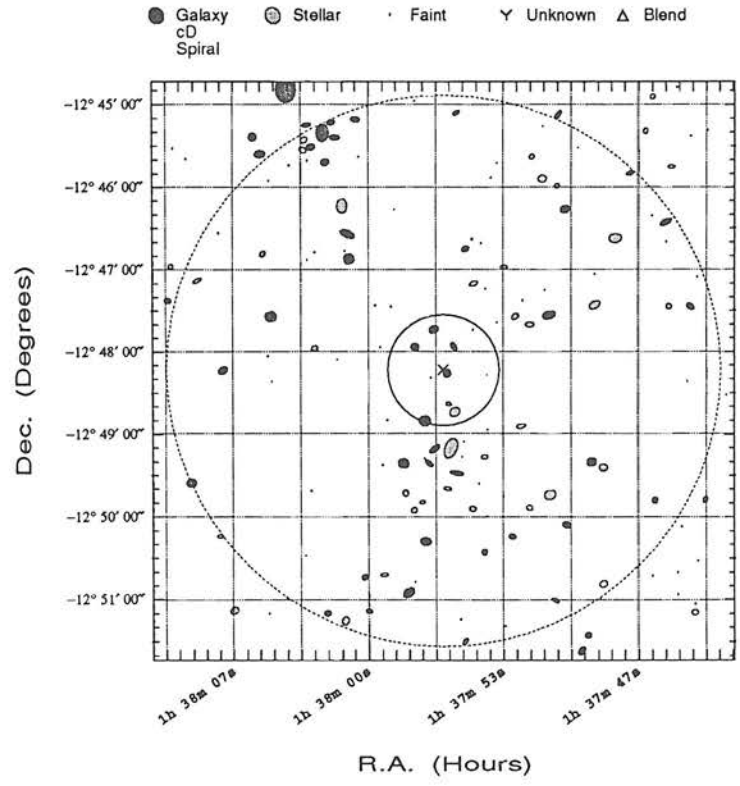

#	CLASS	B	R.A.	Dec.	DIST.
01	Galaxy	18.24	01 37 56.1	-12 48 16	3.9
02	Faint	21.75	01 37 56.9	-12 48 19	10.8
03	Galaxy	20.23	01 37 55.8	-12 47 56	18.7
04	Stellar	20.64	01 37 56.0	-12 48 38	25.1
05	Galaxy	18.09	01 37 57.7	-12 47 57	26.4
06	Galaxy	18.31	01 37 56.8	-12 47 44	30.4
07	Faint	22.53	01 37 54.2	-12 48 17	31.7
08	Stellar	16.59	01 37 55.7	-12 48 44	31.8
09	Faint	23.24	01 37 54.8	-12 47 44	36.6
10	Galaxy	16.68	01 37 57.2	-12 48 51	39.4
11	Faint	20.89	01 37 59.4	-12 47 57	48.5
12	Faint	21.63	01 37 53.7	-12 47 39	52.0
13	Faint	21.44	01 37 54.1	-12 48 57	53.9
14	Faint	23.40	01 37 55.3	-12 49 05	54.3
15	Faint	22.13	01 37 59.1	-12 48 50	54.8
16	Stellar	16.73	01 37 55.9	-12 49 10	57.2
17	Galaxy	18.85	01 37 56.7	-12 49 11	57.7
18	Faint	22.83	01 37 58.9	-12 47 27	60.0
19	Faint	20.98	01 37 55.4	-12 49 16	64.5
20	Stellar	18.93	01 37 52.8	-12 47 34	64.9
21	Faint	21.56	01 37 57.2	-12 49 18	65.9
22	Stellar	19.88	01 37 54.8	-12 47 10	66.8
23	Faint	22.20	01 37 54.2	-12 47 14	66.8
24	Faint	21.97	01 37 59.7	-12 47 26	68.3
25	Galaxy	19.92	01 37 57.0	-12 49 21	68.6
26	Stellar	18.75	01 37 52.5	-12 48 54	69.4
27	Stellar	20.30	01 37 54.3	-12 49 16	69.6
28	Stellar	19.16	01 37 52.0	-12 47 40	70.7
29	Galaxy	17.37	01 37 58.3	-12 49 21	73.7
30	Galaxy	18.50	01 37 55.6	-12 49 28	75.5

Selection criterion: distance
Galaxy Density = 700 per sq. deg.
Sample Radius = 200.0 arc sec

Stars	=	34
Total galaxies	=	37 (cDs = 0, spirals = 0)
Blend objects	=	0
Faint objects	=	48
Unknown objects	=	0
Sum	=	119

Figure C.8: CUOC Finding chart of candidate 0094176

ROSAT Identification | **ROSAT / MPE / RSDC | 28-JUN-94 09:01:21 | RGC** | Page: 1

UKST IIIaJ (blue) | **ROE/NRL COSMOS Finding Chart** | MASOS file: roe_disk:[roedat.masos]009_N1_SI04_N1_P1.mos

Field No. 827 | .... | MASOL Nr.: 000217

Plate Epoch: 1983.8440 | RASS Info: | ROSAT Source Name: RX J01150+0021

Equinox: J2000.0 | Error radii: 1 sigma = 25.2" ; plotted: 90% conf. = 1.645 sigma = 41.5" | ROSAT Position (2000.0): 01 15 02.4 +00 21 48

(1950.0): 01 12 28.6 +00 05 57

Galactic II (l,b): 135.55100 -61.92873

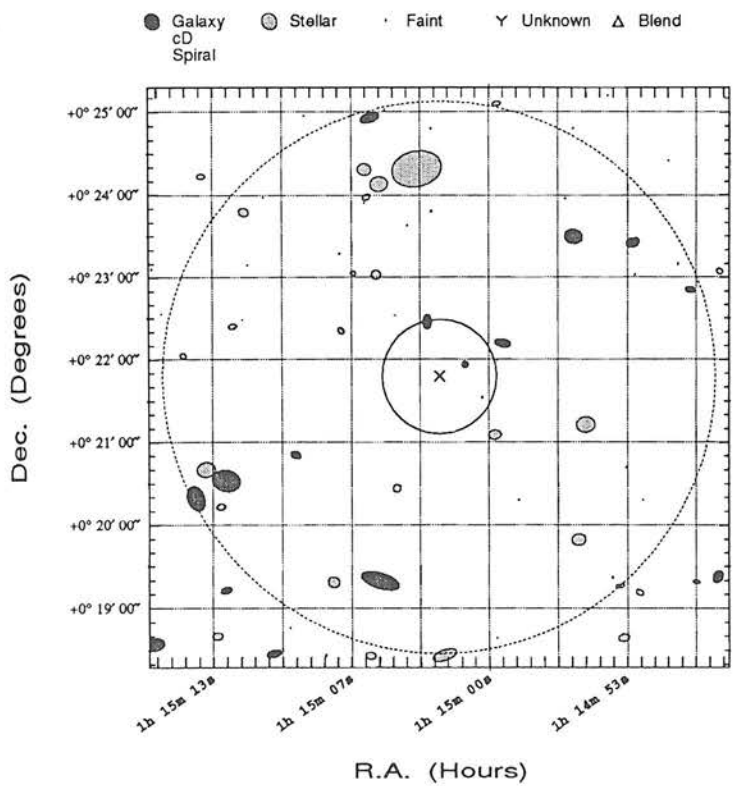

#	CLASS	B	R.A.	Dec.	DIST.
01	Galaxy	21.36	01 15 01.2	+00 21 56	20.6
02	Faint	23.75	01 15 00.3	+00 21 33	34.4
03	Galaxy	18.61	01 15 03.0	+00 22 28	40.6
04	Faint	25.03	01 14 59.6	+00 22 00	43.5
05	Galaxy	18.32	01 14 59.3	+00 22 12	51.9
06	Stellar	17.54	01 14 59.7	+00 21 06	58.3
07	Stellar	21.67	01 15 07.2	+00 22 21	79.0
08	Stellar	20.03	01 15 04.5	+00 20 27	86.9
09	Stellar	18.82	01 15 05.5	+00 23 02	87.3
10	Stellar	22.30	01 15 06.6	+00 23 03	97.9
11	Faint	23.54	01 14 58.6	+00 20 18	106.2
12	Stellar	14.75	01 14 55.3	+00 21 13	111.6
13	Faint	23.25	01 15 04.0	+00 23 38	112.9
14	Faint	23.90	01 15 07.2	+00 23 18	115.7
15	Galaxy	19.80	01 15 09.4	+00 20 51	118.9
16	Faint	24.23	01 15 02.8	+00 23 49	121.0
17	Faint	22.64	01 15 06.1	+00 23 54	138.1
18	Galaxy	15.82	01 14 55.9	+00 23 30	140.8
19	Stellar	21.23	01 15 05.9	+00 23 59	141.1
20	Stellar	15.11	01 15 05.3	+00 24 08	147.1
21	Faint	22.93	01 15 11.9	+00 22 30	149.1
22	Faint	24.75	01 14 53.4	+00 20 42	149.6
23	Stellar	12.06	01 15 03.5	+00 24 19	151.9
24	Galaxy	13.83	01 15 05.3	+00 19 20	154.1
25	Stellar	21.36	01 15 12.4	+00 22 24	154.3
26	Stellar	16.38	01 14 55.7	+00 19 49	155.5
27	Faint	23.47	01 14 56.3	+00 23 58	158.9
28	Faint	24.55	01 14 53.0	+00 23 02	159.8
29	Stellar	16.64	01 15 06.0	+00 24 19	160.3
30	Faint	23.48	01 15 11.7	+00 23 09	161.5

Selection criterion: distance
Galaxy Density = 430 per sq. deg.
Sample Radius = 200.0 arc sec
Stars = 17
Total galaxies = 11 (cDs = 0, spirals = 0)
Blend objects = 0
Faint objects = 19
Unknown objects = 0
Sum = 47

Figure C.9: CUOC Finding chart of candidate 0094217

ROSAT Identification
UKST IIIaJ (blue)
Field No. 684
Plate Epoch: 1984.5980
Equinox: J2000.0

ROSAT / MPE / RSDC | 28-JUN-94 09:01:30 | RGC
ROE/NRL COSMOS Finding Chart
....
RASS Info:
Error radii: 1 sigma = 16.5" ; plotted: 90% conf. = 1.645 sigma = 27.1"

Page: 1
MASOS file: roe_disk:[roedat.masos]010_N1_SI04_N1_P1.mos
MASOL Nr.: 000188
ROSAT Source Name: RX J01372-0911
ROSAT Position (2000.0): 01 37 14.4 -09 11 50

(1950.0): 01 34 45.2 -09 27 06
Galactic II (l,b): 156.18177 -69.05771

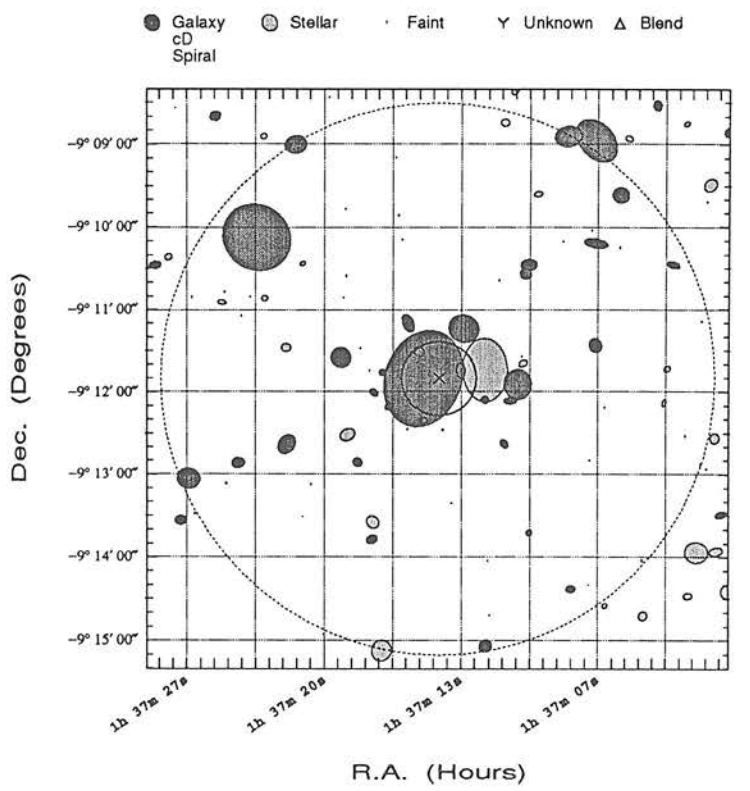

#	CLASS	B	R.A.	Dec.	DIST.
01	Galaxy	10.31	01 37 15.2	-09 11 50	11.3
02	Galaxy	20.02	01 37 13.3	-09 11 44	16.9
03	Galaxy	19.85	01 37 15.4	-09 11 30	24.4
04	Galaxy	21.90	01 37 15.1	-09 12 21	32.7
05	Stellar	12.00	01 37 12.2	-09 11 44	33.7
06	Galaxy	21.71	01 37 12.2	-09 12 06	36.7
07	Faint	25.53	01 37 14.2	-09 12 28	37.5
08	Galaxy	15.71	01 37 13.2	-09 11 14	40.8
09	Galaxy	22.04	01 37 17.2	-09 11 46	41.3
10	Galaxy	22.12	01 37 16.8	-09 12 11	41.4
11	Faint	23.39	01 37 15.9	-09 12 27	43.3
12	Galaxy	18.68	01 37 15.9	-09 11 10	46.1
13	Galaxy	21.70	01 37 17.6	-09 12 01	48.3
14	Faint	24.11	01 37 17.8	-09 11 44	51.0
15	Galaxy	21.31	01 37 10.9	-09 12 07	53.9
16	Galaxy	14.19	01 37 10.5	-09 11 55	57.3
17	Faint	23.03	01 37 18.3	-09 11 28	61.3
18	Stellar	21.79	01 37 10.3	-09 11 39	61.7
19	Faint	25.06	01 37 10.4	-09 11 34	61.9
20	Galaxy	21.28	01 37 11.2	-09 12 38	67.0
21	Galaxy	15.87	01 37 19.2	-09 11 35	72.6
22	Stellar	17.08	01 37 18.9	-09 12 31	77.5
23	Faint	23.21	01 37 11.5	-09 10 38	83.9
24	Galaxy	19.89	01 37 18.4	-09 12 51	84.8
25	Faint	24.64	01 37 13.8	-09 13 21	90.9
26	Faint	25.47	01 37 19.1	-09 10 51	91.0
27	Galaxy	19.25	01 37 10.2	-09 10 34	98.9
28	Faint	24.07	01 37 18.9	-09 10 35	100.9
29	Faint	23.70	01 37 16.2	-09 10 09	104.9
30	Galaxy	17.64	01 37 10.0	-09 10 27	105.2

Selection criterion: distance
Galaxy Density = 621 per sq. deg.
Sample Radius = 200.0 arc sec
Stars = 12
Total galaxies = 31 (cDs = 0, spirals = 1)
Blend objects = 0
Faint objects = 32
Unknown objects = 0
Sum = 75

Figure C.10: CUOC Finding chart of candidate 0104188

ROSAT Identification | ROSAT / MPE / RSDC | 28-JUN-94 09:01:39 | RGC | Page: 1

UKST IIIaJ (blue) | ROE/NRL COSMOS Finding Chart | MASOS file: roe_disk:[roedat.masos]010_N1_SI04_N1_P1.mos

Field No. 827 | MASOL Nr.: 000212

Plate Epoch: 1983.8440 | RASS Info: | ROSAT Source Name: RX J01257-0121

Equinox: J2000.0 | Error radii: 1 sigma = 49.0" ; plotted: 90% conf. = 1.645 sigma = 80.6" | ROSAT Position (2000.0): 01 25 42.8 -01 21 24

(1950.0): 01 23 09.7 -01 36 59

Galactic II (l,b): 142.05163 -62.94901

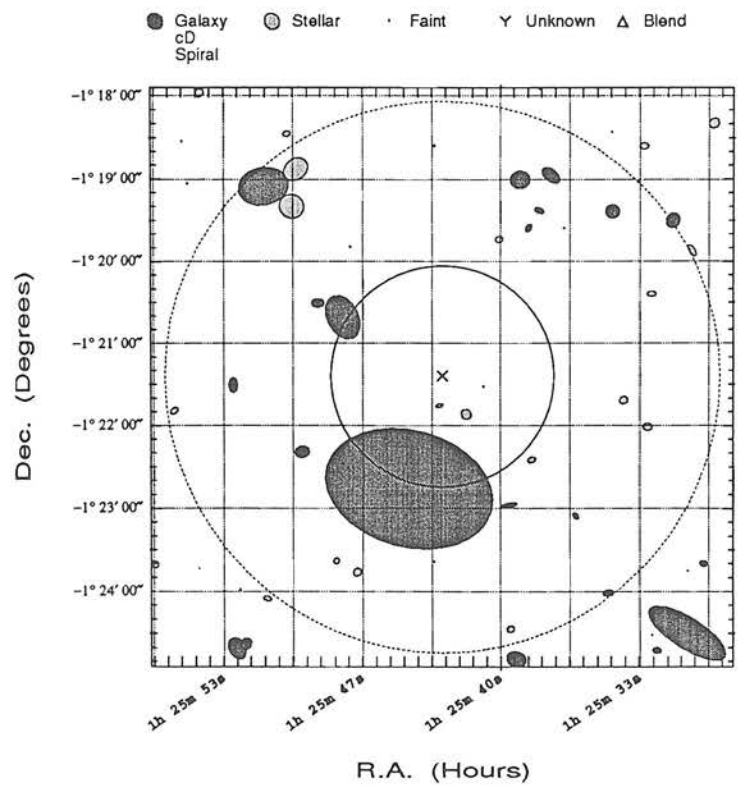

#	CLASS	B	R.A.	Dec.	DIST.
01	Stellar	22.30	01 25 42.9	-01 21 46	21.8
02	Faint	24.31	01 25 40.8	-01 21 32	30.6
03	Stellar	18.32	01 25 41.7	-01 21 52	32.5
04	Galaxy	12.19	01 25 47.6	-01 20 41	83.9
05	Spiral	7.37	01 25 44.4	-01 22 46	85.2
06	Stellar	21.00	01 25 38.5	-01 22 25	88.8
07	Galaxy	18.59	01 25 48.8	-01 20 30	104.8
08	Galaxy	21.06	01 25 39.6	-01 22 58	105.5
09	Stellar	20.96	01 25 40.1	-01 19 44	108.1
10	Galaxy	17.22	01 25 49.6	-01 22 19	115.2
11	Faint	22.68	01 25 47.2	-01 19 49	115.7
12	Galaxy	21.78	01 25 38.6	-01 19 36	125.0
13	Stellar	19.43	01 25 34.1	-01 21 42	131.8
14	Faint	23.14	01 25 43.2	-01 23 39	134.9
15	Faint	22.99	01 25 36.9	-01 19 36	139.6
16	Galaxy	22.30	01 25 36.4	-01 23 06	139.9
17	Galaxy	21.99	01 25 38.1	-01 19 23	140.0
18	Galaxy	19.62	01 25 52.9	-01 21 31	150.9
19	Stellar	19.36	01 25 33.0	-01 22 01	152.0
20	Galaxy	16.09	01 25 39.0	-01 19 01	154.3
21	Stellar	21.71	01 25 47.9	-01 23 38	154.6
22	Stellar	20.22	01 25 46.9	-01 23 46	154.9
23	Stellar	20.56	01 25 32.8	-01 20 24	162.2
24	Stellar	13.85	01 25 50.0	-01 19 20	164.8
25	Galaxy	18.02	01 25 37.6	-01 18 57	166.6
26	Faint	23.58	01 25 43.2	-01 18 36	168.0
27	Galaxy	17.87	01 25 34.6	-01 19 24	171.8
28	Stellar	14.20	01 25 49.8	-01 18 53	184.4
29	Galaxy	11.83	01 25 51.4	-01 19 05	189.3
30	Stellar	21.32	01 25 39.5	-01 24 27	189.6

Selection criterion: distance
Galaxy Density = 318 per sq. deg.
Sample Radius = 200.0 arc sec

Stars	=	13
Total galaxies	=	14 (cDs = 0, spirals = 1)
Blend objects	=	0
Faint objects	=	5
Unknown objects	=	0
Sum	=	32

Figure C.11: CUOC Finding chart of candidate 0104212

ROSAT Identification
UKST IIIaJ (blue)
Field No. 248
Plate Epoch: 1977.7841
Equinox: J2000.0

ROSAT / MPE / RSDC | 7-JUN-94 13:17:18 | RGC
ROE/NRL COSMOS Finding Chart
....
RASS Info: 0.450 263 122 84 52 0.46 0.11 0.38 0.493 346
Error radii: 1 sigma = 16.4" ; plotted: 90% conf. = 1.645 sigma = 27.1"

Page: 1
MASOS file: roe_disk:[roedat.masos]012_N2_SI04_N1_P1.mos
MASOL Nr.: 000051
ROSAT Source Name: RX J03143-4525
ROSAT Position (2000.0): 03 14 22.9 -45 25 24

(1950.0): 03 12 40.1 -45 36 30
Galactic II (l,b): 255.32084 -56.28824

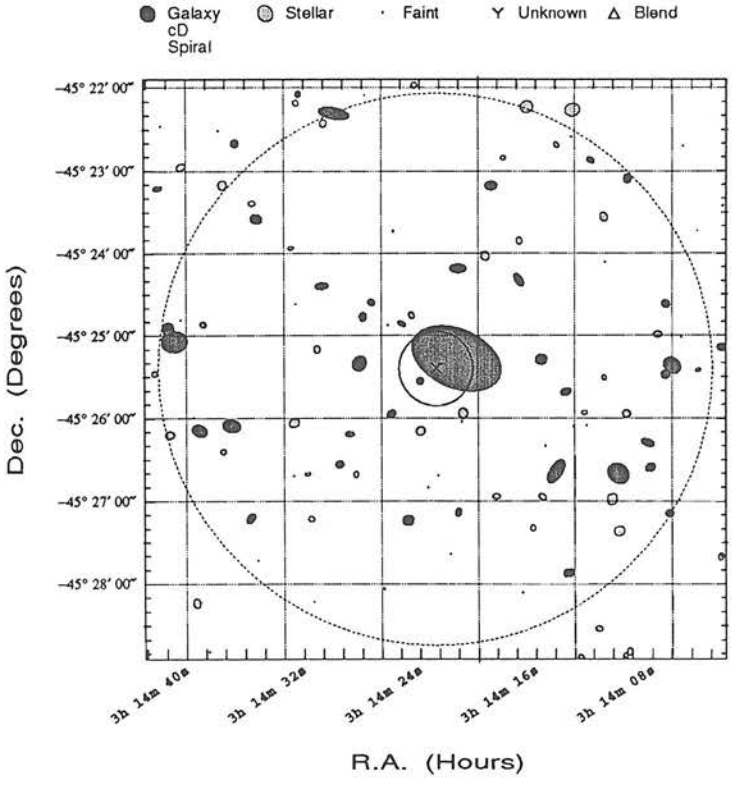

#	CLASS	B	R.A.	Dec.	DIST.
01	Galaxy	21.59	03 14 24.0	-45 25 33	15.0
02	Spiral	10.20	03 14 21.5	-45 25 17	16.8
03	Stellar	18.27	03 14 21.0	-45 25 56	38.0
04	Galaxy	22.14	03 14 25.3	-45 24 52	40.9
05	Stellar	20.82	03 14 24.6	-45 24 45	42.7
06	Faint	23.45	03 14 21.1	-45 26 02	42.8
07	Galaxy	20.33	03 14 26.0	-45 25 57	46.1
08	Stellar	18.48	03 14 24.0	-45 26 09	46.7
09	Faint	23.04	03 14 26.2	-45 24 52	47.2
10	Galaxy	16.70	03 14 28.2	-45 25 20	56.0
11	Galaxy	20.25	03 14 27.9	-45 24 46	65.1
12	Galaxy	21.21	03 14 27.4	-45 24 36	67.2
13	Galaxy	17.05	03 14 21.4	-45 24 11	75.0
14	Galaxy	18.05	03 14 15.6	-45 25 18	76.9
15	Faint	24.20	03 14 22.8	-45 26 41	77.3
16	Galaxy	21.27	03 14 28.9	-45 26 12	78.7
17	Faint	25.36	03 14 23.5	-45 26 50	86.1
18	Stellar	20.53	03 14 31.1	-45 25 10	87.2
19	Galaxy	18.45	03 14 17.2	-45 24 19	88.4
20	Stellar	18.96	03 14 19.5	-45 24 02	89.7
21	Galaxy	19.45	03 14 13.9	-45 25 41	96.1
22	Stellar	21.94	03 14 28.4	-45 26 41	96.5
23	Faint	25.02	03 14 15.3	-45 26 20	97.2
24	Galaxy	20.21	03 14 29.6	-45 26 33	98.6
25	Stellar	20.76	03 14 18.7	-45 26 56	102.2
26	Galaxy	18.64	03 14 30.8	-45 24 24	102.6
27	Faint	24.77	03 14 25.9	-45 23 44	105.0
28	Galaxy	21.00	03 14 21.4	-45 27 08	105.4
29	Faint	24.08	03 14 13.4	-45 26 06	108.4
30	Stellar	18.62	03 14 32.7	-45 26 03	109.9

Selection criterion: distance
Galaxy Density = 1036 per sq. deg.
Sample Radius = 200.0 arc sec
Stars = 29
Total galaxies = 35 (cDs = 0, spirals = 1)
Blend objects = 0
Faint objects = 21
Unknown objects = 0
Sum = 85

Figure C.12: CUOC Finding chart of candidate 0124051

ROSAT Identification | **ROSAT / MPE / RSDC | 28-JUN-94 09:01:48 | RGC** | Page: 1

UKST IIIaJ (blue) | **ROE/NRL COSMOS Finding Chart** | MASOS file: roe_disk:[roedat.masos]013_N2_SI04_N1_P3.mos

Field No. 416 | .... | MASOL Nr.: 000078

Plate Epoch: 1978.8160 | RASS Info: | ROSAT Source Name: RX J02352-2936

Equinox: J2000.0 | Error radii: 1 sigma = 6.0" ; plotted: 90% conf. = 1.645 sigma = 9.9" | ROSAT Position (2000.0): 02 35 13.9 -29 36 17

(1950.0): 02 33 04.0 -29 49 21

Galactic II (l,b): 225.26447 -67.08093

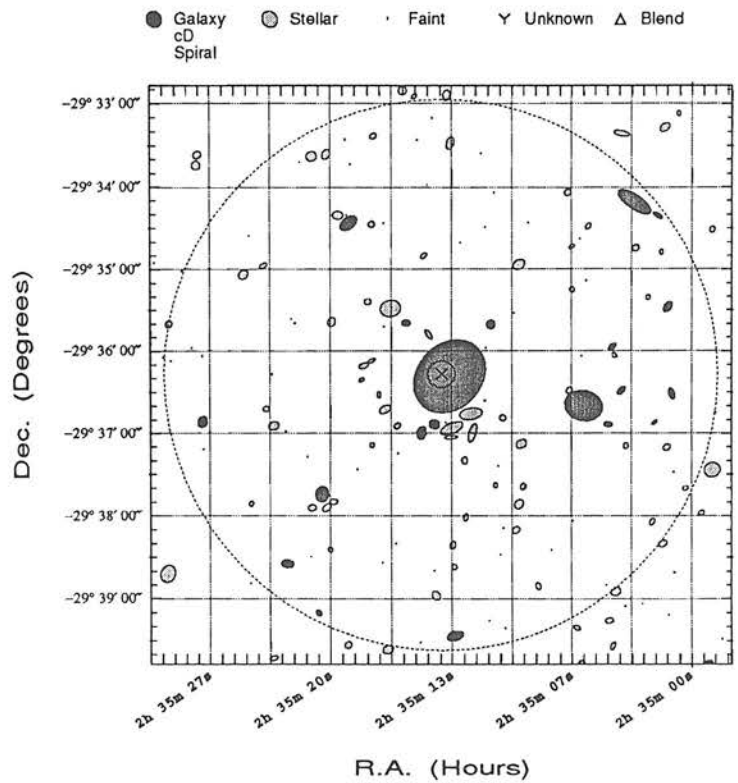

#	CLASS	B	R.A.	Dec.	DIST.
01	Spiral	9.96	02 35 13.4	-29 36 18	6.1
02	Stellar	22.56	02 35 14.6	-29 35 48	30.6
03	Faint	24.85	02 35 13.7	-29 36 52	35.0
04	Stellar	19.14	02 35 12.3	-29 36 46	35.8
05	Faint	23.65	02 35 11.5	-29 36 36	36.4
06	Galaxy	20.36	02 35 14.3	-29 36 54	36.9
07	Faint	24.15	02 35 11.4	-29 35 57	37.5
08	Stellar	19.83	02 35 13.3	-29 36 56	40.1
09	Galaxy	17.96	02 35 15.0	-29 37 00	45.1
10	Galaxy	20.90	02 35 15.8	-29 35 39	45.3
11	Stellar	22.54	02 35 13.4	-29 37 03	46.6
12	Stellar	22.64	02 35 17.4	-29 36 32	47.5
13	Stellar	18.67	02 35 17.0	-29 36 43	48.0
14	Stellar	19.50	02 35 12.2	-29 37 00	48.2
15	Stellar	19.74	02 35 16.3	-29 36 55	49.2
16	Galaxy	19.16	02 35 11.2	-29 35 40	50.9
17	Stellar	21.75	02 35 17.8	-29 36 07	51.2
18	Faint	24.69	02 35 17.1	-29 35 42	54.2
19	Stellar	20.78	02 35 10.5	-29 36 49	54.3
20	Stellar	19.89	02 35 18.2	-29 36 11	56.1
21	Stellar	22.45	02 35 18.3	-29 36 21	57.6
22	Stellar	15.26	02 35 16.7	-29 35 29	60.6
23	Stellar	20.40	02 35 12.6	-29 37 20	65.1
24	Faint	23.12	02 35 16.3	-29 37 14	65.3
25	Faint	24.79	02 35 09.9	-29 35 32	69.1
26	Stellar	21.98	02 35 17.7	-29 37 09	71.8
27	Stellar	20.90	02 35 18.0	-29 35 24	75.3
28	Stellar	17.55	02 35 09.5	-29 37 08	76.7
29	Faint	24.33	02 35 10.8	-29 37 24	78.2
30	Stellar	18.32	02 35 19.9	-29 35 39	87.2

Selection criterion: distance
Galaxy Density = 877 per sq. deg.
Sample Radius = 200.0 arc sec
Stars = 59
Total galaxies = 19 (cDs = 0, spirals = 1)
Blend objects = 0
Faint objects = 47
Unknown objects = 0
Sum = 125

Figure C.13: CUOC Finding chart of candidate 0134078

ROSAT Identification | **ROSAT / MPE / RSDC | 28-JUN-94 09:01:58 | RGC** | Page: 1

UKST IIIaJ (blue) | **ROE/NRL COSMOS Finding Chart** | MASOS file: roe_disk:[roedat.masos]014_N2_S104_N1_P1.mos

Field No. 416 | .... | MASOL Nr.: 000092

Plate Epoch: 1978.8160 | RASS Info: | ROSAT Source Name: RX J02413-2839

Equinox: J2000.0 | Error radii: 1 sigma = 26.6" ; plotted: 90% conf. = 1.645 sigma = 43.8" | ROSAT Position (2000.0): 02 41 22.1 -28 39 21

(1950.0): 02 39 12.0 -28 52 08

Galactic II (l,b): 222.98817 -65.71490

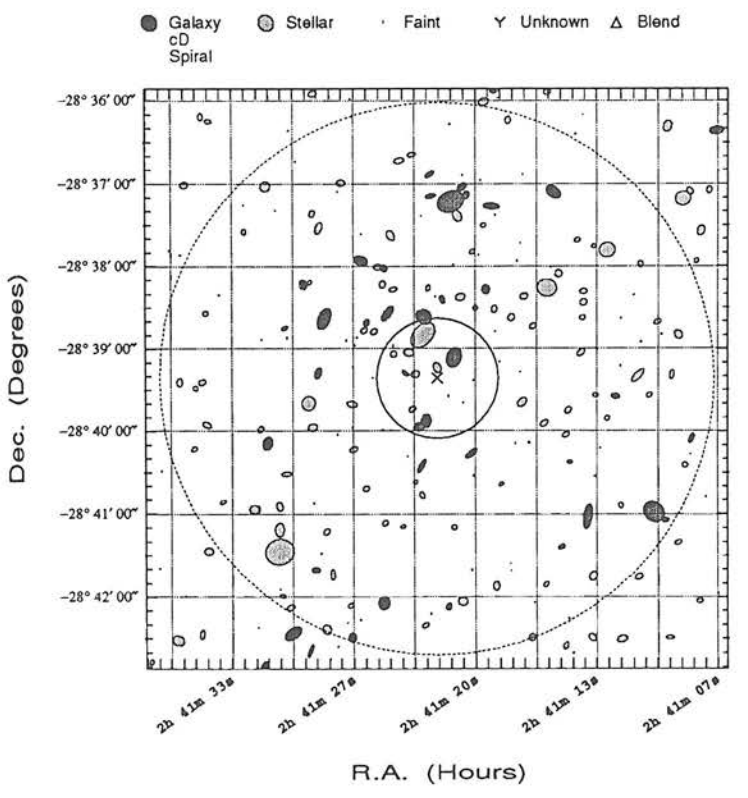

#	CLASS	B	R.A.	Dec.	DIST.
01	Stellar	19.29	02 41 22.1	-28 39 14	7.6
02	Faint	25.29	02 41 21.5	-28 39 35	15.3
03	Stellar	19.56	02 41 23.3	-28 39 19	15.8
04	Galaxy	16.68	02 41 21.2	-28 39 07	19.3
05	Galaxy	22.20	02 41 23.8	-28 39 18	23.1
06	Faint	23.14	02 41 20.2	-28 39 23	25.4
07	Faint	24.83	02 41 20.7	-28 39 39	25.5
08	Stellar	21.32	02 41 23.6	-28 39 03	27.5
09	Stellar	20.84	02 41 23.5	-28 39 44	28.7
10	Galaxy	17.98	02 41 22.7	-28 39 52	32.0
11	Stellar	15.21	02 41 22.9	-28 38 50	32.9
12	Stellar	20.51	02 41 24.5	-28 39 04	35.9
13	Galaxy	18.79	02 41 23.1	-28 39 57	37.8
14	Faint	24.87	02 41 24.5	-28 38 58	40.0
15	Galaxy	16.33	02 41 22.8	-28 38 37	45.9
16	Faint	24.42	02 41 18.7	-28 39 09	46.2
17	Faint	22.85	02 41 25.7	-28 39 21	46.9
18	Faint	24.94	02 41 24.6	-28 39 59	50.3
19	Faint	23.40	02 41 18.9	-28 38 47	54.0
20	Faint	23.24	02 41 25.1	-28 39 59	54.8
21	Stellar	21.73	02 41 25.6	-28 38 48	57.0
22	Galaxy	21.48	02 41 21.8	-28 38 24	57.6
23	Stellar	21.87	02 41 20.0	-28 38 30	58.0
24	Galaxy	18.83	02 41 24.8	-28 38 34	59.4
25	Faint	24.38	02 41 17.6	-28 39 17	59.4
26	Faint	23.86	02 41 22.2	-28 38 22	59.5
27	Galaxy	18.96	02 41 20.2	-28 40 16	59.9
28	Faint	23.24	02 41 23.7	-28 40 19	60.9
29	Faint	23.94	02 41 26.7	-28 39 13	61.3
30	Stellar	19.58	02 41 20.8	-28 38 22	61.4

Selection criterion: distance
Galaxy Density = 718 per sq. deg.
Sample Radius = 200.0 arc sec
Stars = 92
Total galaxies = 34 (cDs = 0, spirals = 0)
Blend objects = 0
Faint objects = 60
Unknown objects = 0
Sum = 186

Figure C.14: CUOC Finding chart of candidate 0144092

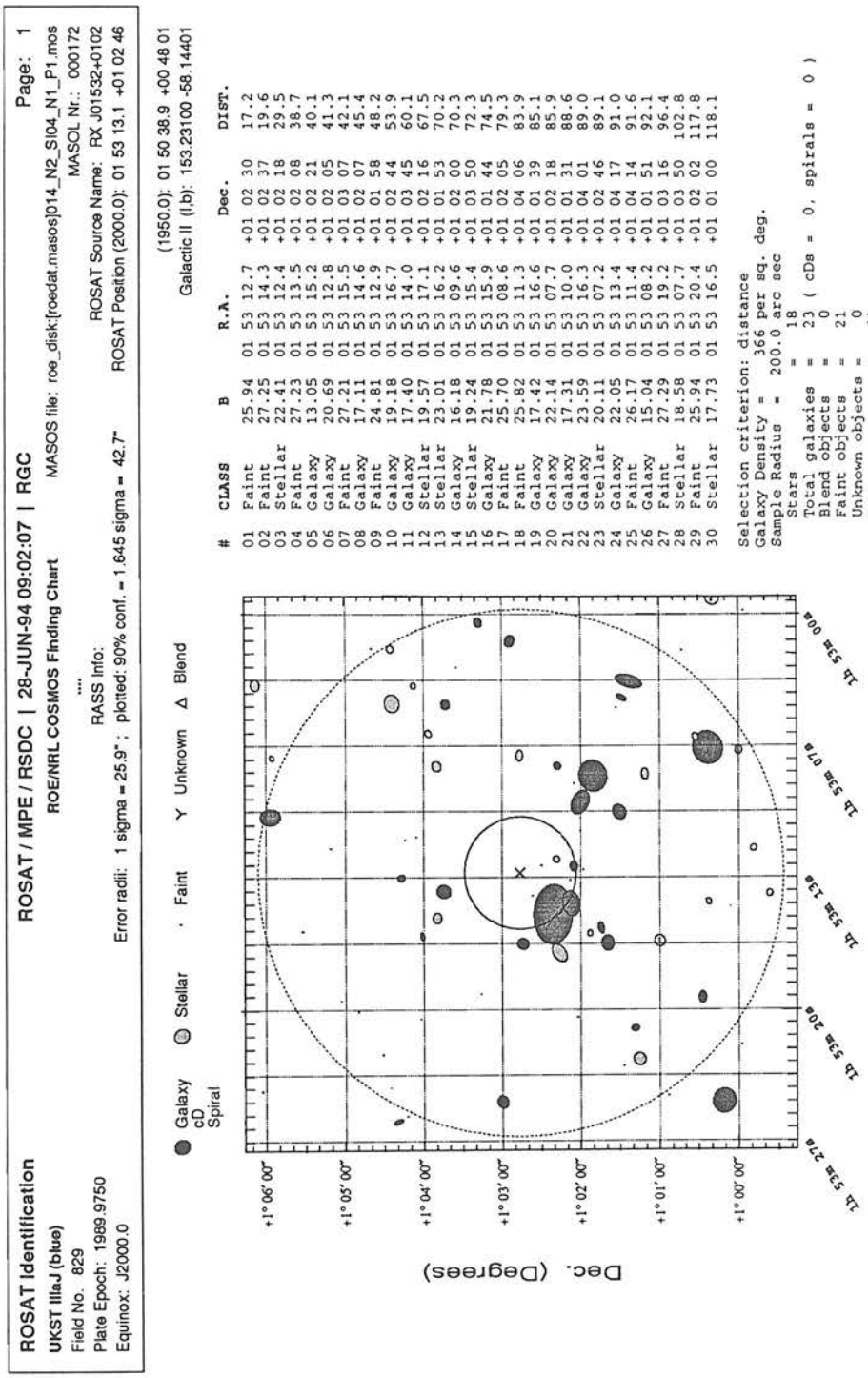

#	CLASS	B	R.A.	Dec.	DIST.
01	Faint	25.94	01 53 12.7	+01 02 30	17.2
02	Faint	27.25	01 53 14.3	+01 02 37	19.6
03	Stellar	22.41	01 53 12.4	+01 02 18	29.5
04	Faint	27.23	01 53 13.5	+01 02 08	38.7
05	Galaxy	13.05	01 53 15.2	+01 02 21	40.1
06	Galaxy	20.69	01 53 12.8	+01 02 05	41.3
07	Faint	27.21	01 53 15.5	+01 03 07	42.1
08	Galaxy	17.11	01 53 14.6	+01 02 07	45.4
09	Faint	24.81	01 53 12.9	+01 01 58	48.2
10	Galaxy	19.18	01 53 16.7	+01 02 44	53.9
11	Galaxy	17.40	01 53 14.0	+01 03 45	60.1
12	Stellar	19.57	01 53 17.1	+01 02 16	67.5
13	Stellar	23.01	01 53 16.2	+01 01 53	70.2
14	Galaxy	16.18	01 53 09.6	+01 02 00	70.3
15	Stellar	19.24	01 53 15.4	+01 03 50	72.3
16	Galaxy	21.78	01 53 15.9	+01 01 44	74.5
17	Faint	25.70	01 53 08.6	+01 02 05	79.3
18	Faint	25.82	01 53 11.3	+01 04 06	83.9
19	Galaxy	17.42	01 53 16.6	+01 01 39	85.1
20	Galaxy	22.14	01 53 07.7	+01 02 18	85.9
21	Galaxy	17.31	01 53 10.0	+01 01 31	88.6
22	Galaxy	23.59	01 53 16.3	+01 04 01	89.0
23	Stellar	20.11	01 53 07.2	+01 02 46	89.1
24	Galaxy	22.05	01 53 13.4	+01 04 17	91.0
25	Faint	26.17	01 53 11.4	+01 04 14	91.6
26	Galaxy	15.04	01 53 08.2	+01 01 51	92.1
27	Faint	27.29	01 53 19.2	+01 03 16	96.4
28	Stellar	18.58	01 53 07.7	+01 03 50	102.8
29	Faint	25.94	01 53 20.4	+01 02 02	117.8
30	Stellar	17.73	01 53 16.5	+01 01 00	118.1

Selection criterion: distance
Galaxy Density = 366 per sq. deg.
Sample Radius = 200.0 arc sec
Stars = 18
Total galaxies = 23 (cDs = 0, spirals = 0)
Blend objects = 0
Faint objects = 21
Unknown objects = 0
Sum = 62

Figure C.15: CUOC Finding chart of candidate 0144172

ROSAT Identification
UKST IIIaJ (blue)
Field No. 686
Plate Epoch: 1982.8521
Equinox: J2000.0

ROSAT / MPE / RSDC | 28-JUN-94 09:02:15 | RGC
ROE/NRL COSMOS Finding Chart
RASS Info:
Error radii: 1 sigma = 7.3" ; plotted: 90% conf. = 1.645 sigma = 12.1"

Page: 1
MASOS file: roe_disk:[roedat.masos]017_N1_SI04_N1_P2.mos
MASOL Nr.: 000101
ROSAT Source Name: RX J02300-0859
ROSAT Position (2000.0): 02 30 04.7 -08 59 44

(1950.0): 02 27 37.5 -09 13 02
Galactic II (l,b): 179.68650 -60.47808

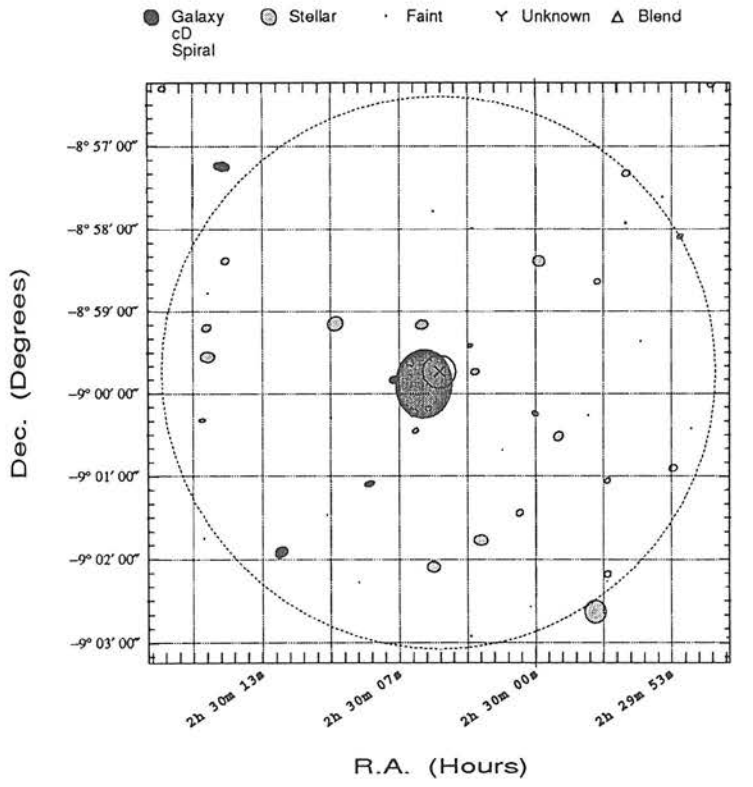

#	CLASS	B	R.A.	Dec.	DIST.
01	Faint	19.85	02 30 05.1	-08 59 36	10.4
02	Galaxy	10.71	02 30 05.5	-08 59 53	14.5
03	Galaxy	18.71	02 30 06.2	-08 59 37	22.8
04	Stellar	17.82	02 30 03.0	-08 59 44	25.8
05	Galaxy	19.63	02 30 05.3	-09 00 11	27.5
06	Stellar	19.65	02 30 03.2	-08 59 25	29.2
07	Galaxy	18.35	02 30 07.0	-08 59 50	33.9
08	Galaxy	18.37	02 30 06.0	-09 00 14	35.2
09	Stellar	15.98	02 30 05.6	-08 59 10	36.6
10	Stellar	19.73	02 30 05.9	-09 00 27	46.3
11	Faint	20.21	02 30 01.6	-09 00 41	72.6
12	Stellar	19.40	02 30 00.0	-09 00 15	75.6
13	Stellar	14.73	02 30 09.8	-08 59 09	83.0
14	Faint	21.01	02 30 10.0	-09 00 18	85.5
15	Galaxy	18.01	02 30 08.1	-09 01 05	95.7
16	Stellar	16.43	02 29 58.9	-09 00 31	98.4
17	Faint	20.90	02 30 03.1	-08 58 00	107.4
18	Stellar	15.72	02 29 59.8	-08 58 24	108.3
19	Faint	20.81	02 29 57.4	-09 00 16	112.4
20	Faint	19.93	02 30 05.0	-08 57 47	117.3
21	Stellar	17.89	02 30 00.8	-09 01 27	117.6
22	Stellar	15.59	02 30 02.7	-09 01 46	125.7
23	Faint	21.96	02 30 10.2	-09 01 28	131.7
24	Stellar	19.10	02 29 56.9	-08 58 39	132.5
25	Stellar	15.58	02 30 05.0	-09 02 06	141.2
26	Stellar	19.57	02 29 56.4	-09 01 03	145.4
27	Faint	20.34	02 29 54.9	-08 59 22	147.6
28	Faint	20.88	02 30 08.6	-09 02 17	163.0
29	Stellar	15.36	02 30 16.0	-08 59 33	167.7
30	Stellar	17.45	02 30 16.0	-08 59 12	171.1

Selection criterion: distance
Galaxy Density = 557 per sq. deg.
Sample Radius = 200.0 arc sec
Stars = 20
Total galaxies = 7 (cDs = 0, spirals = 0)
Blend objects = 0
Faint objects = 15
Unknown objects = 0
Sum = 42

Figure C.16: CUOC Finding chart of candidate 0174101

ROSAT Identification | **ROSAT / MPE / RSDC | 28-JUN-94 09:02:29 | RGC** | Page: 1

UKST IIIaJ (blue) | **ROE/NRL COSMOS Finding Chart** | MASOS file: roe_disk:[roedat.masos]017_N1_SI04_N1_P2.mos

Field No. 758 | .... | MASOL Nr.: 000111

Plate Epoch: 1982.6410 | RASS Info: | ROSAT Source Name: RX J02317-0452

Equinox: J2000.0 | Error radii: 1 sigma = 13.2" ; plotted: 90% conf. = 1.645 sigma = 21.7" | ROSAT Position (2000.0): 02 31 42.2 -04 52 43

(1950.0): 02 29 12.1 -05 05 56

Galactic II (l,b): 174.42595 -57.35429

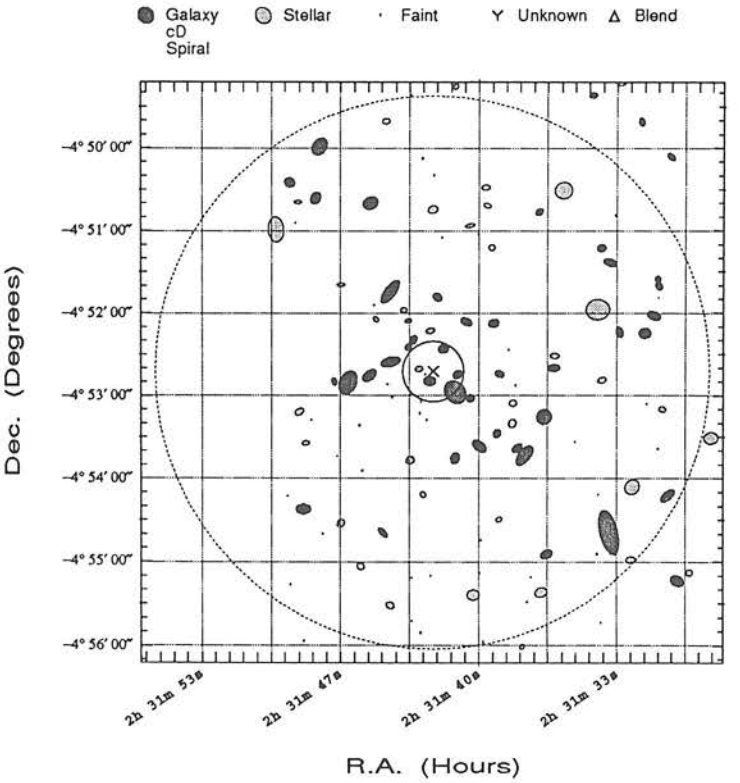

#	CLASS	B	R.A.	Dec.	DIST.
01	Faint	24.83	02 31 42.1	-04 52 40	2.9
02	Faint	24.46	02 31 42.6	-04 52 44	5.9
03	Galaxy	18.57	02 31 42.4	-04 52 50	7.4
04	Stellar	21.61	02 31 42.9	-04 52 41	10.3
05	Galaxy	20.10	02 31 41.0	-04 52 45	17.7
06	Galaxy	19.30	02 31 41.7	-04 52 26	18.1
07	Galaxy	16.52	02 31 41.1	-04 52 57	21.7
08	Faint	24.38	02 31 42.8	-04 53 04	23.4
09	Galaxy	21.74	02 31 43.4	-04 52 25	25.4
10	Galaxy	21.14	02 31 43.2	-04 52 19	27.1
11	Stellar	20.92	02 31 42.3	-04 52 13	29.5
12	Galaxy	18.40	02 31 44.2	-04 52 36	31.3
13	Faint	22.60	02 31 42.9	-04 53 13	31.6
14	Galaxy	20.73	02 31 40.4	-04 53 02	32.9
15	Faint	23.13	02 31 44.4	-04 52 51	34.1
16	Faint	22.47	02 31 44.2	-04 53 01	34.9
17	Faint	24.48	02 31 42.5	-04 53 17	35.0
18	Galaxy	22.37	02 31 43.4	-04 52 06	41.1
19	Galaxy	19.36	02 31 40.6	-04 52 06	43.3
20	Galaxy	18.30	02 31 45.3	-04 52 45	46.1
21	Galaxy	20.08	02 31 39.0	-04 52 44	47.9
22	Stellar	21.70	02 31 43.6	-04 51 58	49.3
23	Galaxy	20.28	02 31 42.0	-04 51 49	54.0
24	Galaxy	19.51	02 31 39.3	-04 52 08	55.9
25	Stellar	22.23	02 31 45.0	-04 52 04	56.1
26	Faint	24.48	02 31 38.6	-04 52 27	56.4
27	Faint	22.66	02 31 38.2	-04 52 52	60.2
28	Stellar	20.78	02 31 38.4	-04 53 05	61.9
29	Galaxy	17.24	02 31 46.3	-04 52 50	62.0
30	Galaxy	18.38	02 31 40.0	-04 53 37	63.6

Selection criterion: distance
Galaxy Density = 525 per sq. deg.
Sample Radius = 200.0 arc sec

Stars	=	32
Total galaxies	=	41 (cDs = 0, spirals = 0)
Blend objects	=	0
Faint objects	=	38
Unknown objects	=	0
Sum	=	111

Figure C.17: CUOC Finding chart of candidate 0174111

ROSAT Identification | **ROSAT / MPE / RSDC | 28-JUN-94 09:02:47 | RGC** | Page: 1

UKST IIIaJ (blue) | **ROE/NRL COSMOS Finding Chart** | MASOS file: roe_disk:[roedat.masos]072_N2_SI03_N1_P1.mos

Field No. 405 | .... | MASOL Nr.: 000060

Plate Epoch: 1980.6071 | RASS Info: | ROSAT Source Name: RX J22177-3543

Equinox: J2000.0 | Error radii: 1 sigma = 8.0"; plotted: 90% conf. = 1.645 sigma = 13.1" | ROSAT Position (2000.0): 22 17 45.2 -35 43 27

(1950.0): 22 14 50.4 -35 58 29

Galactic II (l,b): 8.45943 -56.33748

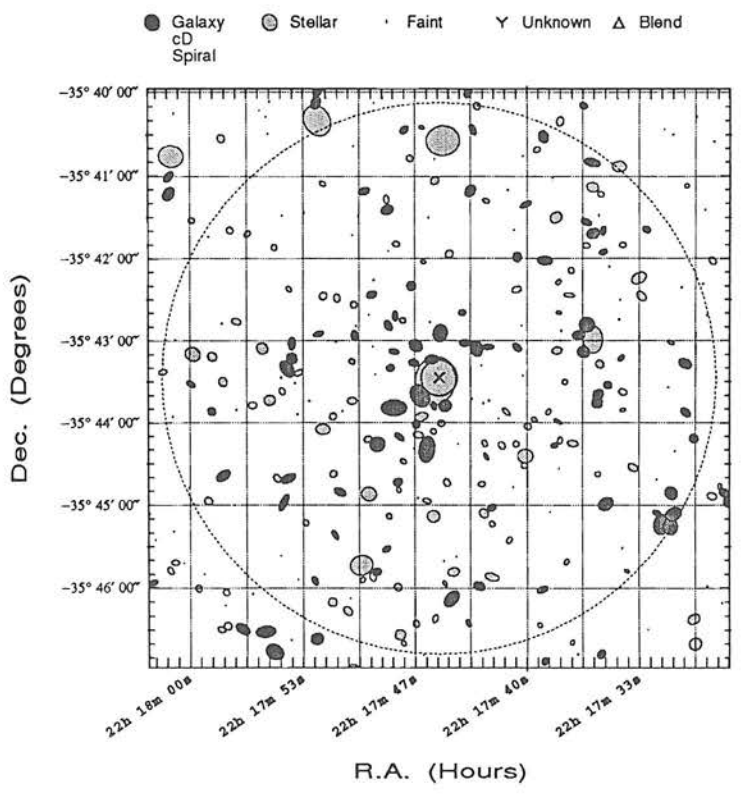

#	CLASS	B	R.A.	Dec.	DIST.
01	Stellar	12.88	22 17 45.5	-35 43 29	3.7
02	Galaxy	18.41	22 17 45.7	-35 43 14	14.4
03	Galaxy	15.47	22 17 46.4	-35 43 41	19.3
04	Galaxy	20.98	22 17 45.5	-35 43 48	20.9
05	Galaxy	18.01	22 17 44.8	-35 43 48	21.0
06	Galaxy	19.07	22 17 46.7	-35 43 16	21.7
07	Faint	24.16	22 17 43.3	-35 43 42	28.0
08	Galaxy	16.95	22 17 46.6	-35 43 04	29.3
09	Stellar	19.28	22 17 46.3	-35 43 56	31.3
10	Faint	22.96	22 17 42.7	-35 43 18	31.5
11	Galaxy	18.65	22 17 43.7	-35 43 02	31.8
12	Galaxy	16.64	22 17 45.2	-35 42 54	33.1
13	Stellar	19.56	22 17 45.1	-35 44 01	33.3
14	Galaxy	16.90	22 17 43.0	-35 43 06	34.5
15	Galaxy	19.89	22 17 48.1	-35 43 20	36.4
16	Faint	24.20	22 17 42.6	-35 43 46	36.5
17	Galaxy	20.23	22 17 46.6	-35 44 01	38.0
18	Galaxy	20.15	22 17 47.9	-35 43 08	38.5
19	Stellar	20.53	22 17 45.6	-35 44 06	39.2
20	Galaxy	15.84	22 17 47.9	-35 43 49	39.8
21	Faint	21.92	22 17 42.2	-35 43 44	39.8
22	Faint	22.21	22 17 45.8	-35 42 46	41.7
23	Galaxy	19.62	22 17 42.3	-35 43 05	41.8
24	Stellar	19.49	22 17 46.5	-35 44 09	44.4
25	Faint	22.89	22 17 49.0	-35 43 25	46.9
26	Stellar	20.74	22 17 47.4	-35 42 45	49.7
27	Faint	22.30	22 17 44.1	-35 44 15	49.9
28	Galaxy	20.49	22 17 43.8	-35 42 39	50.8
29	Galaxy	19.80	22 17 47.6	-35 44 10	52.0
30	Faint	23.40	22 17 41.7	-35 43 57	52.1

Selection criterion: distance
Galaxy Density = 972 per sq. deg.
Sample Radius = 200.0 arc sec
Stars = 103
Total galaxies = 78 (cDs = 0, spirals = 0)
Blend objects = 0
Faint objects = 62
Unknown objects = 0
Sum = 243

Figure C.18: CUOC Finding chart of candidate 0723060

ROSAT Identification
UKST IIIaJ (blue)
Field No. 405
Plate Epoch: 1980.6071
Equinox: J2000.0

ROSAT / MPE / RSDC | 28-JUN-94 09:03:08 | RGC
ROE/NRL COSMOS Finding Chart
RASS Info:
Error radii: 1 sigma = 17.9" ; plotted: 90% conf. = 1.645 sigma = 29.4"

Page: 1
MASOS file: roe_disk:[roedat.masos]073_N2_SI03_N1_P1.mos
MASOL Nr.: 000059
ROSAT Source Name: RX J22295-3632
ROSAT Position (2000.0): 22 29 35.3 -36 32 18

(1950.0): 22 26 42.2 -36 47 40
Galactic II (l,b): 6.52558 -58.63822

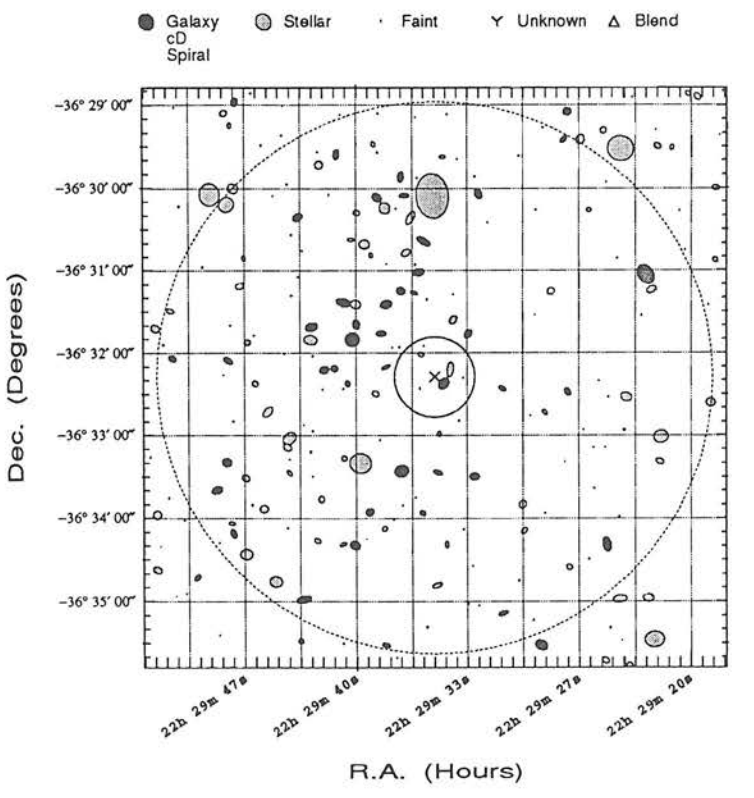

#	CLASS	B	R.A.	Dec.	DIST.
01	Galaxy	18.98	22 29 34.8	-36 32 22	8.2
02	Stellar	20.56	22 29 34.4	-36 32 12	12.5
03	Faint	24.21	22 29 36.2	-36 32 26	13.3
04	Stellar	21.02	22 29 36.1	-36 32 01	19.2
05	Faint	23.08	22 29 33.6	-36 32 18	20.5
06	Faint	21.87	22 29 36.0	-36 31 55	24.3
07	Faint	23.07	22 29 37.4	-36 31 56	33.6
08	Faint	23.85	22 29 33.8	-36 32 49	36.0
09	Galaxy	20.82	22 29 38.2	-36 32 10	36.2
10	Faint	22.11	22 29 37.8	-36 31 56	37.4
11	Galaxy	19.36	22 29 33.3	-36 31 46	39.8
12	Stellar	21.40	22 29 35.0	-36 32 59	41.5
13	Stellar	19.49	22 29 34.2	-36 31 36	43.6
14	Stellar	20.75	22 29 38.8	-36 32 30	44.2
15	Galaxy	21.28	22 29 31.2	-36 32 26	49.8
16	Galaxy	20.41	22 29 38.5	-36 31 46	50.0
17	Faint	22.79	22 29 35.7	-36 31 21	56.8
18	Faint	23.50	22 29 38.6	-36 33 03	60.7
19	Faint	22.54	22 29 34.2	-36 31 17	61.9
20	Galaxy	21.28	22 29 40.5	-36 32 22	62.8
21	Galaxy	21.57	22 29 36.6	-36 31 16	63.2
22	Galaxy	18.98	22 29 38.2	-36 31 25	63.4
23	Galaxy	17.54	22 29 40.2	-36 31 50	65.5
24	Faint	21.69	22 29 40.8	-36 32 26	66.4
25	Galaxy	19.38	22 29 37.3	-36 31 15	67.4
26	Galaxy	20.39	22 29 40.0	-36 31 39	68.4
27	Galaxy	20.75	22 29 35.1	-36 33 27	69.3
28	Galaxy	16.72	22 29 37.3	-36 33 26	72.4
29	Galaxy	20.60	22 29 41.3	-36 32 11	72.5
30	Faint	23.10	22 29 29.6	-36 32 46	74.6

Selection criterion: distance
Galaxy Density = 1131 per sq. deg.
Sample Radius = 200.0 arc sec
Stars = 53
Total galaxies = 41 (cDs = 0, spirals = 0)
Blend objects = 0
Faint objects = 79
Unknown objects = 0
Sum = 173

Figure C.19: CUOC Finding chart of candidate 0733059

ROSAT Identification | **ROSAT / MPE / RSDC | 28-JUN-94 09:03:22 | RGC** | Page: 2

UKST IIIaJ (blue) | **ROE/NRL COSMOS Finding Chart** | MASOS file: roe_disk:[roedat.masos]073_N2_SI03_N1_P1.mos

Field No. 290 | .... | MASOL Nr.: 000077

Plate Epoch: 1976.7410 | RASS Info: | ROSAT Source Name: RX J22419-4235

Equinox: J2000.0 | Error radii: 1 sigma = 37.7" ; plotted: 90% conf. = 1.645 sigma = 62.1" | ROSAT Position (2000.0): 22 41 57.4 -42 35 58

(1950.0): 22 39 02.7 -42 51 41

Galactic II (l,b): 353.95152 -59.53782

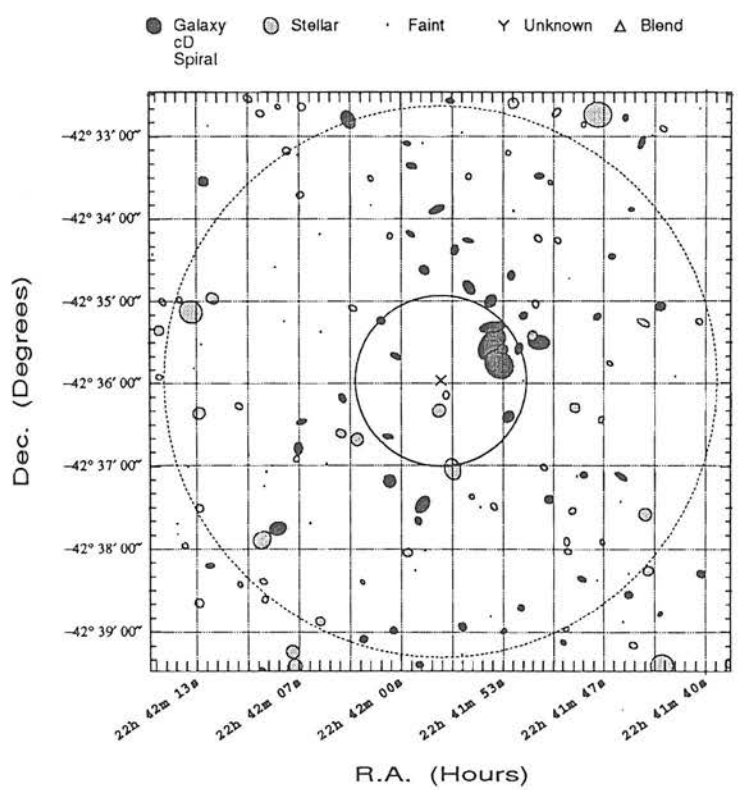

#	CLASS	B	R.A.	Dec.	DIST.
01	Stellar	21.35	22 41 57.1	-42 36 09	11.2
02	Stellar	17.38	22 41 57.5	-42 36 20	21.8
03	Galaxy	22.07	22 42 00.3	-42 35 40	37.0
04	Galaxy	15.47	22 41 53.6	-42 35 47	43.8
05	Galaxy	14.64	22 41 54.1	-42 35 32	45.3
06	Galaxy	19.85	22 41 53.3	-42 35 35	50.6
07	Galaxy	18.80	22 41 54.0	-42 35 19	53.9
08	Galaxy	21.54	22 42 00.9	-42 36 39	55.6
09	Galaxy	19.81	22 41 53.0	-42 36 25	55.7
10	Faint	25.61	22 41 52.0	-42 35 59	59.7
11	Galaxy	20.53	22 41 52.3	-42 35 35	61.3
12	Galaxy	20.80	22 42 01.3	-42 35 14	61.8
13	Faint	26.52	22 41 55.0	-42 36 54	62.3
14	Stellar	15.71	22 41 56.7	-42 37 03	65.0
15	Galaxy	19.30	22 41 54.1	-42 35 00	68.3
16	Galaxy	18.99	22 41 55.6	-42 34 50	71.1
17	Galaxy	21.29	22 42 03.9	-42 36 11	72.3
18	Stellar	17.77	22 42 02.9	-42 36 41	74.1
19	Stellar	18.82	22 41 51.4	-42 35 25	74.2
20	Galaxy	21.70	22 41 52.0	-42 35 11	76.5
21	Galaxy	16.76	22 41 51.0	-42 35 30	76.5
22	Galaxy	18.55	22 42 00.8	-42 37 11	81.5
23	Galaxy	19.46	22 41 58.5	-42 34 37	81.6
24	Stellar	18.99	22 42 03.9	-42 36 37	81.8
25	Stellar	21.17	22 42 03.2	-42 35 05	82.8
26	Stellar	23.29	22 41 55.4	-42 37 22	87.0
27	Stellar	21.50	22 41 51.1	-42 35 02	89.0
28	Galaxy	17.92	22 41 58.6	-42 37 28	90.8
29	Galaxy	20.61	22 41 52.8	-42 34 42	92.1
30	Faint	24.50	22 42 05.3	-42 35 23	93.8

Selection criterion: distance
Galaxy Density = 1036 per sq. deg.
Sample Radius = 200.0 arc sec

Stars	=	43
Total galaxies	=	40 (cDs = 0, spirals = 0)
Blend objects	=	0
Faint objects	=	31
Unknown objects	=	0
Sum	=	114

Figure C.20: CUOC Finding chart of candidate 0733077

ROSAT Identification
UKST IIIaJ (blue)
Field No. 673
Plate Epoch: 1983.7700
Equinox: J2000.0

ROSAT / MPE / RSDC | 7-JUN-94 13:17:26 | RGC
ROE/NRL COSMOS Finding Chart
....
RASS Info: 0.099 317 52 11 0 0.19 0.49 0.28 0.150 321
Error radii: 1 sigma = 11.2" ; plotted: 90% conf. = 1.645 sigma = 18.4"

Page: 1
MASOS file: roe_disk:[roedat.masos]074_N1_SI03_N1_P1.mos
MASOL Nr.: 000009
ROSAT Source Name: RX J22024-1657
ROSAT Position (2000.0): 22 02 26.2 -16 57 51
(1950.0): 21 59 42.3 -17 12 21
Galactic II (l,b): 38.54174 -49.74384

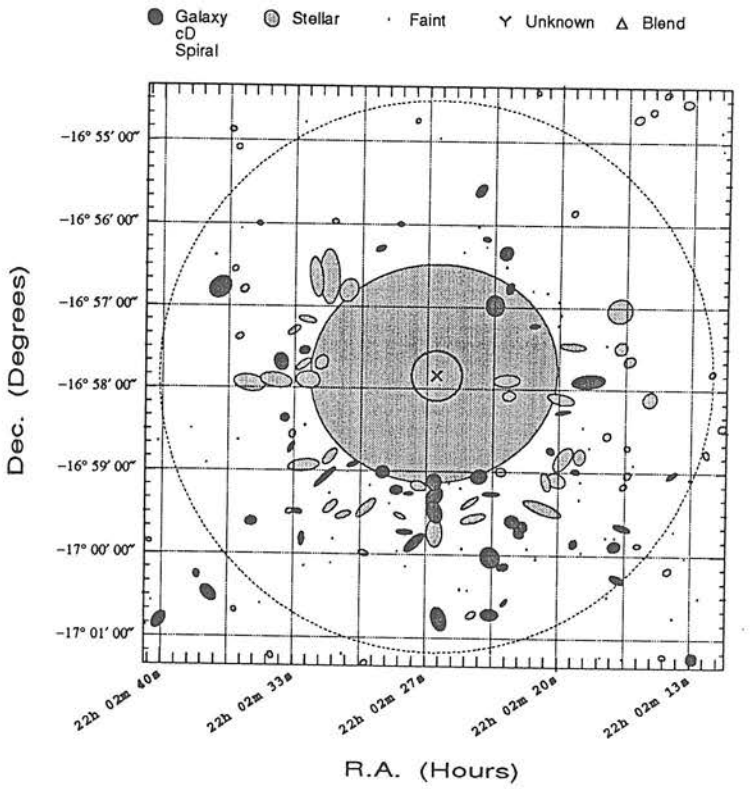

#	CLASS	B	R.A.	Dec.	DIST.
01	Stellar	4.82	22 02 26.3	-16 57 48	2.7
02	Stellar	14.75	22 02 22.7	-16 57 54	50.9
03	Stellar	16.27	22 02 22.5	-16 58 05	54.5
04	Galaxy	16.98	22 02 23.3	-16 56 59	66.3
05	Galaxy	16.70	22 02 26.3	-16 59 08	77.0
06	Faint	21.78	22 02 25.5	-16 59 09	78.9
07	Galaxy	15.62	22 02 24.0	-16 59 04	79.7
08	Galaxy	16.75	22 02 28.9	-16 59 00	79.9
09	Galaxy	21.46	22 02 21.3	-16 57 14	79.9
10	Stellar	19.93	22 02 27.1	-16 59 10	80.8
11	Galaxy	20.40	22 02 22.5	-16 56 46	83.1
12	Faint	22.48	22 02 25.0	-16 59 12	83.2
13	Stellar	19.59	22 02 32.0	-16 57 42	83.2
14	Stellar	20.47	22 02 22.9	-16 59 00	83.9
15	Galaxy	17.39	22 02 28.2	-16 59 13	87.5
16	Galaxy	16.28	22 02 26.3	-16 59 18	87.5
17	Galaxy	21.26	22 02 27.6	-16 59 16	87.7
18	Galaxy	21.29	22 02 30.4	-16 58 55	88.2
19	Stellar	15.93	22 02 30.7	-16 56 48	89.2
20	Stellar	19.47	22 02 19.9	-16 58 07	91.5
21	Faint	22.67	22 02 24.9	-16 56 20	92.3
22	Faint	22.24	22 02 29.5	-16 59 10	92.4
23	Stellar	15.75	22 02 32.7	-16 57 54	92.7
24	Faint	22.99	22 02 21.4	-16 56 48	93.1
25	Faint	22.46	22 02 22.7	-16 56 31	94.1
26	Faint	22.44	22 02 30.6	-16 59 00	94.3
27	Galaxy	19.92	22 02 23.4	-16 59 16	94.4
28	Stellar	19.77	22 02 24.5	-16 59 23	95.3
29	Galaxy	21.08	22 02 19.8	-16 58 16	95.3
30	Faint	21.81	22 02 20.1	-16 57 13	95.4

Selection criterion: distance
Galaxy Density = 940 per sq. deg.
Sample Radius = 200.0 arc sec
Stars = 52
Total galaxies = 45 (cDs = 0, spirals = 0)
Blend objects = 0
Faint objects = 42
Unknown objects = 0
Sum = 139

Figure C.21: CUOC Finding chart of candidate 0743009

ROSAT Identification | **ROSAT / MPE / RSDC | 28-JUN-94 09:03:32 | RGC** | Page: 1

UKST IIIaJ (blue) | **ROE/NRL COSMOS Finding Chart** | MASOS file: roe_disk:[roedat.masos]074_N1_SI03_N1_P1.mos

Field No. 601 | .... | MASOL Nr.: 000011

Plate Epoch: 1977.5430 | RASS Info: | ROSAT Source Name: RX J22048-1815

Equinox: J2000.0 | Error radii: 1 sigma = 16.5" ; plotted: 90% conf. = 1.645 sigma = 27.2" | ROSAT Position (2000.0): 22 04 52.3 -18 15 47

(1950.0): 22 02 07.8 -18 30 22

Galactic II (l,b): 36.98369 -50.75964

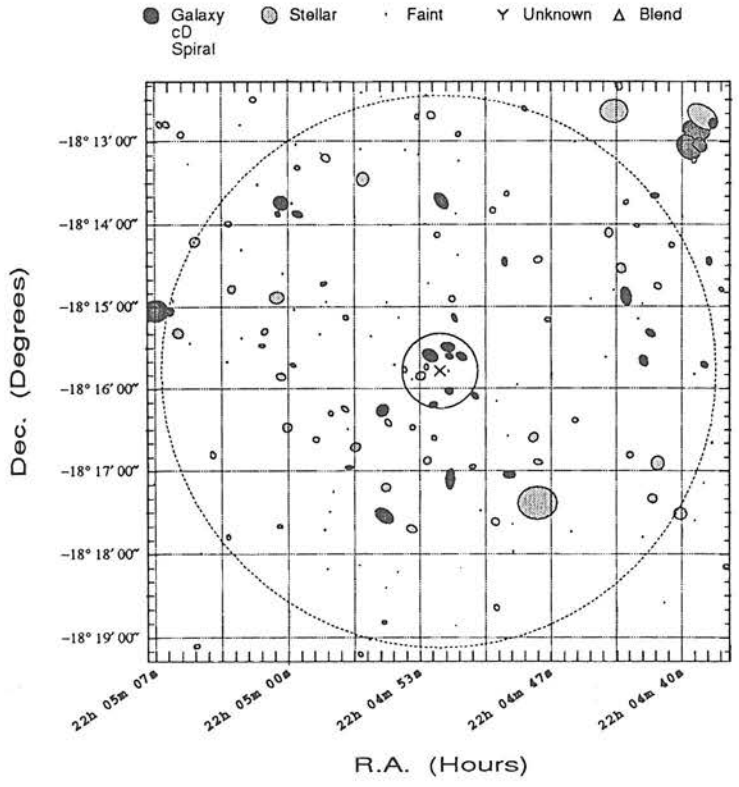

#	CLASS	B	R.A.	Dec.	DIST.
01	Faint	24.52	22 04 51.9	-18 15 47	6.2
02	Stellar	21.76	22 04 53.0	-18 15 44	10.2
03	Galaxy	20.67	22 04 51.8	-18 15 36	12.8
04	Galaxy	17.63	22 04 52.8	-18 15 36	13.0
05	Stellar	18.02	22 04 53.3	-18 15 51	14.5
06	Galaxy	19.95	22 04 51.8	-18 16 02	16.1
07	Galaxy	18.96	22 04 51.9	-18 15 30	18.4
08	Galaxy	18.59	22 04 51.2	-18 15 36	19.0
09	Faint	24.77	22 04 53.7	-18 15 53	21.0
10	Galaxy	20.36	22 04 52.6	-18 16 12	25.3
11	Stellar	21.39	22 04 54.1	-18 15 46	25.7
12	Galaxy	21.15	22 04 50.5	-18 16 05	31.2
13	Faint	24.98	22 04 54.6	-18 15 42	33.1
14	Galaxy	21.55	22 04 51.6	-18 15 09	40.0
15	Stellar	21.94	22 04 53.7	-18 16 28	45.6
16	Faint	23.74	22 04 49.5	-18 16 09	46.0
17	Stellar	22.01	22 04 52.6	-18 16 36	49.0
18	Faint	24.99	22 04 54.4	-18 15 08	49.3
19	Galaxy	17.23	22 04 55.2	-18 16 16	50.7
20	Stellar	21.09	22 04 51.7	-18 14 55	53.2
21	Stellar	20.10	22 04 54.9	-18 16 25	53.4
22	Faint	24.42	22 04 48.4	-18 15 57	56.2
23	Faint	22.92	22 04 55.8	-18 15 22	56.2
24	Faint	23.71	22 04 55.0	-18 14 57	63.3
25	Faint	23.01	22 04 52.9	-18 14 43	64.8
26	Stellar	19.11	22 04 53.0	-18 16 53	66.2
27	Faint	24.02	22 04 48.9	-18 16 35	68.0
28	Stellar	21.48	22 04 50.7	-18 16 57	73.7
29	Stellar	20.98	22 04 57.1	-18 16 15	74.2
30	Stellar	21.83	22 04 57.1	-18 15 08	78.4

Selection criterion: distance
Galaxy Density = 1259 per sq. deg.
Sample Radius = 200.0 arc sec
Stars = 56
Total galaxies = 24 (cDs = 0, spirals = 0)
Blend objects = 0
Faint objects = 54
Unknown objects = 0
Sum = 134

Figure C.22: CUOC Finding chart of candidate 0743011

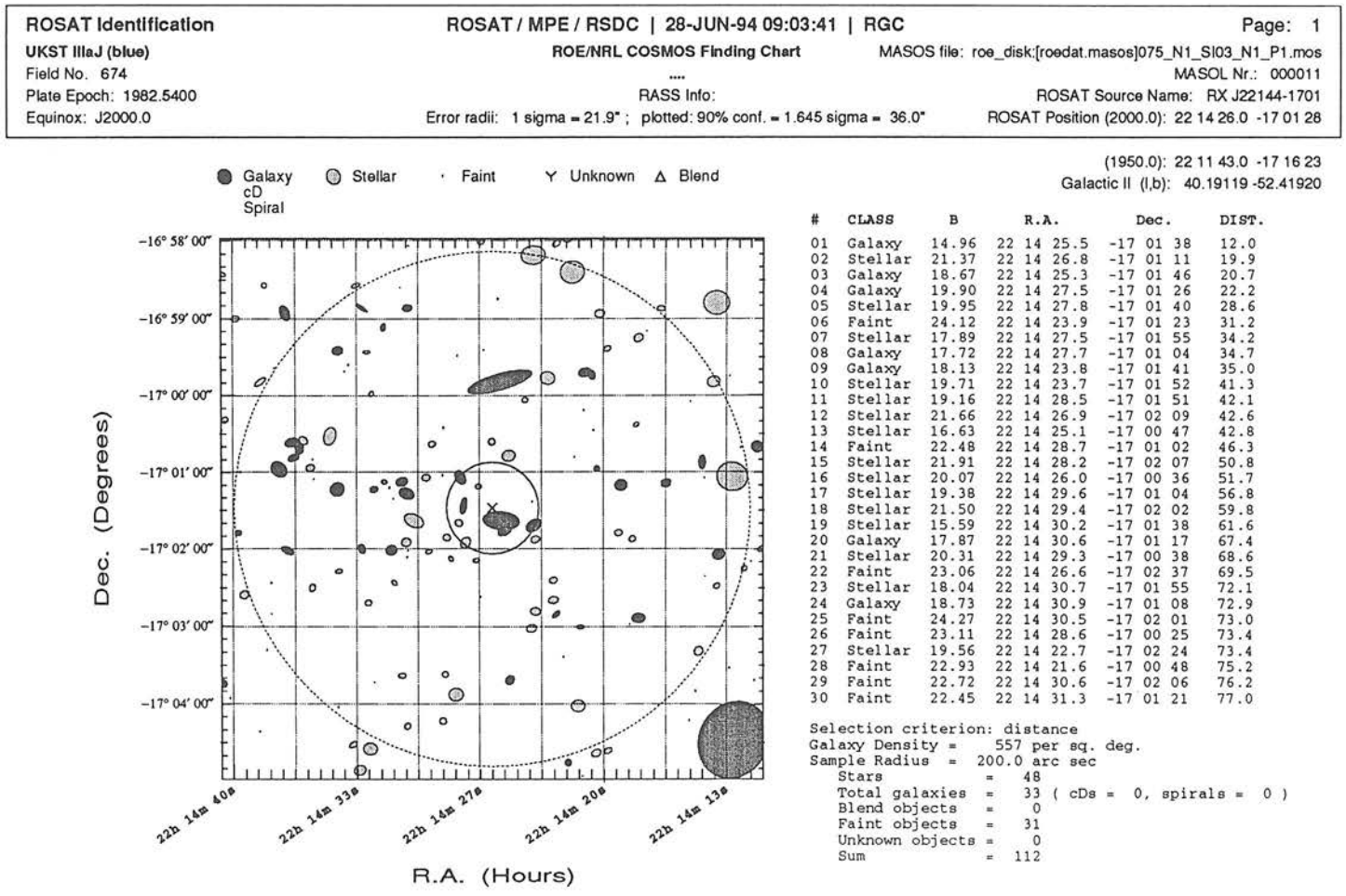

Figure C.23: CUOC Finding chart of candidate 0753011

ROSAT Identification | **ROSAT / MPE / RSDC | 28-JUN-94 09:03:51 | RGC** | Page: 1

UKST IIIaJ (blue) | **ROE/NRL COSMOS Finding Chart** | MASOS file: roe_disk:[roedat.masos]075_N1_SI03_N1_P1.mos

Field No. 291 | .... | MASOL Nr.: 000052

Plate Epoch: 1976.6370 | RASS Info: | ROSAT Source Name: RX J23106-4347

Equinox: J2000.0 | Error radii: 1 sigma = 9.8"; plotted: 90% conf. = 1.645 sigma = 16.2" | ROSAT Position (2000.0): 23 10 41.2 -43 47 37

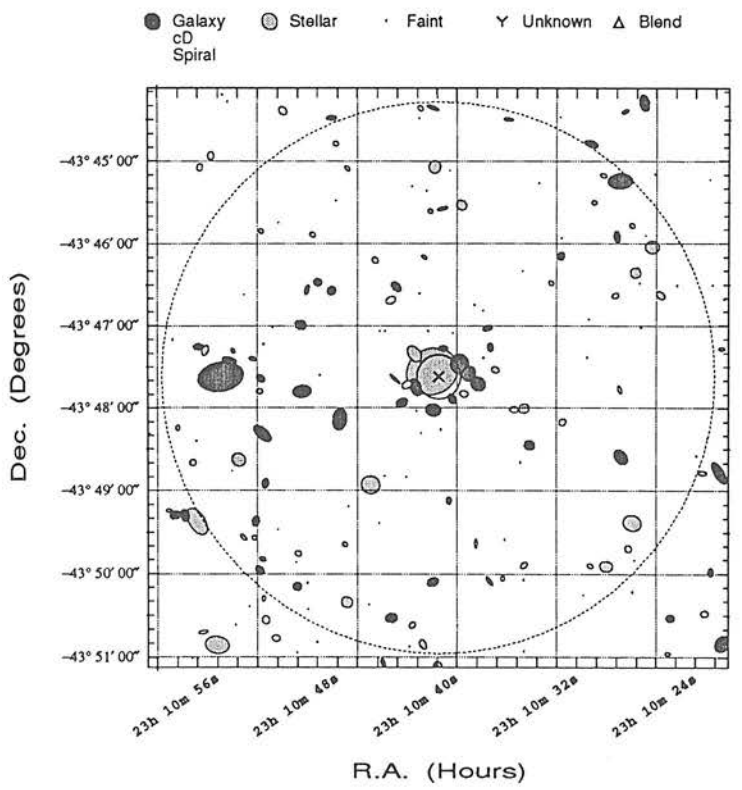

(1950.0): 23 07 53.4 -44 03 55

Galactic II (l,b): 346.93543 -63.75536

#	CLASS	B	R.A.	Dec.	DIST.
01	Stellar	12.36	23 10 41.6	-43 47 33	6.2
02	Galaxy	15.61	23 10 39.8	-43 47 28	17.8
03	Galaxy	18.90	23 10 42.7	-43 47 45	18.4
04	Galaxy	18.78	23 10 40.3	-43 47 53	19.1
05	Galaxy	20.63	23 10 40.9	-43 47 16	21.2
06	Galaxy	17.03	23 10 39.2	-43 47 35	21.9
07	Stellar	18.71	23 10 39.5	-43 47 50	22.0
08	Stellar	20.56	23 10 43.4	-43 47 43	24.2
09	Galaxy	15.96	23 10 41.6	-43 48 01	24.3
10	Stellar	19.02	23 10 42.9	-43 47 20	24.6
11	Galaxy	16.96	23 10 38.6	-43 47 42	28.9
12	Faint	22.21	23 10 42.7	-43 48 02	29.8
13	Galaxy	21.77	23 10 44.2	-43 47 39	32.3
14	Galaxy	17.76	23 10 43.7	-43 47 56	33.1
15	Faint	24.32	23 10 40.2	-43 47 06	33.4
16	Faint	23.76	23 10 41.9	-43 47 04	34.2
17	Faint	23.36	23 10 38.2	-43 47 24	35.3
18	Faint	22.31	23 10 41.0	-43 48 16	38.7
19	Stellar	18.62	23 10 37.4	-43 47 32	41.4
20	Galaxy	20.70	23 10 37.8	-43 47 16	43.0
21	Faint	23.68	23 10 42.4	-43 48 18	43.1
22	Galaxy	20.63	23 10 37.9	-43 47 02	50.0
23	Faint	23.57	23 10 44.8	-43 47 04	51.2
24	Faint	23.75	23 10 45.2	-43 47 04	54.5
25	Faint	23.54	23 10 38.2	-43 46 49	58.1
26	Faint	23.87	23 10 38.8	-43 46 45	58.6
27	Stellar	19.34	23 10 36.2	-43 48 01	59.3
28	Faint	23.52	23 10 42.5	-43 46 37	62.3
29	Stellar	18.67	23 10 44.4	-43 46 41	65.9
30	Stellar	17.26	23 10 35.5	-43 48 00	65.9

Selection criterion: distance
Galaxy Density = 1515 per sq. deg.
Sample Radius = 200.0 arc sec
Stars = 50
Total galaxies = 40 (cDs = 0, spirals = 0)
Blend objects = 0
Faint objects = 51
Unknown objects = 0
Sum = 141

Figure C.24: CUOC Finding chart of candidate 0753052

ROSAT Identification | **ROSAT / MPE / RSDC | 28-JUN-94 09:04:01 | RGC** | Page: 1

UKST IIIaJ (blue) | **ROE/NRL COSMOS Finding Chart** | MASOS file: roe_disk:[roedat.masos]075_N1_SI03_N1_P1.mos

Field No. 240 | MASOL Nr.: 000060

Plate Epoch: 1975.5400 | RASS Info: | ROSAT Source Name: RX J23254-4800

Equinox: J2000.0 | Error radii: 1 sigma = 8.5"; plotted: 90% conf. = 1.645 sigma = 14.0" | ROSAT Position (2000.0): 23 25 26.4 -48 00 23

(1950.0): 23 22 41.1 -48 16 52

Galactic II (l,b): 335.92965 -63.24149

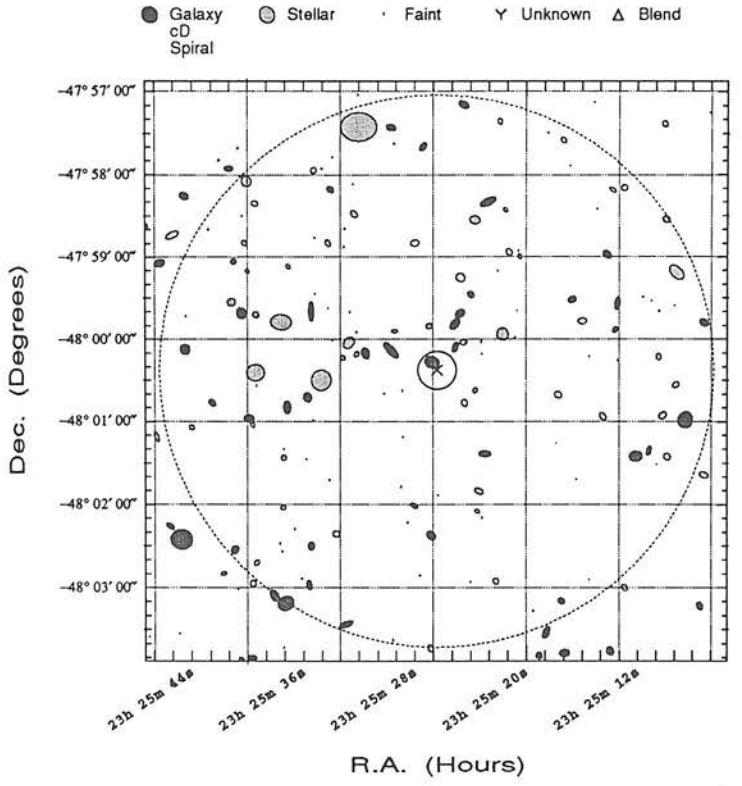

#	CLASS	B	R.A.	Dec.	DIST.
01	Galaxy	15.35	23 25 26.8	-48 00 17	6.9
02	Galaxy	18.04	23 25 25.1	-48 00 06	21.3
03	Stellar	18.66	23 25 24.5	-48 00 02	28.0
04	Faint	20.41	23 25 28.9	-48 00 38	29.4
05	Stellar	17.65	23 25 24.4	-48 00 46	30.8
06	Stellar	19.21	23 25 23.7	-48 00 37	30.9
07	Stellar	18.34	23 25 27.0	-47 59 51	32.5
08	Faint	19.53	23 25 23.2	-48 00 11	34.3
09	Galaxy	17.11	23 25 25.1	-47 59 49	35.9
10	Galaxy	15.95	23 25 29.7	-48 00 08	36.2
11	Faint	20.52	23 25 23.2	-48 00 02	37.8
12	Stellar	19.42	23 25 29.5	-47 59 54	41.9
13	Faint	20.75	23 25 30.2	-48 00 40	41.9
14	Galaxy	17.66	23 25 24.8	-47 59 41	44.6
15	Galaxy	16.79	23 25 31.5	-48 00 10	53.0
16	Stellar	15.31	23 25 21.7	-47 59 56	53.9
17	Faint	20.64	23 25 28.9	-48 01 11	54.8
18	Stellar	18.64	23 25 32.2	-48 00 11	59.3
19	Galaxy	18.45	23 25 24.0	-47 59 27	60.1
20	Faint	20.16	23 25 20.9	-47 59 59	60.6
21	Faint	20.16	23 25 32.2	-47 59 55	64.6
22	Stellar	15.73	23 25 32.7	-48 00 03	66.6
23	Stellar	19.05	23 25 33.2	-48 00 14	68.4
24	Galaxy	17.47	23 25 23.0	-48 01 23	69.5
25	Stellar	16.47	23 25 24.7	-47 59 15	69.6
26	Faint	20.33	23 25 20.7	-47 59 39	71.7
27	Faint	20.68	23 25 32.7	-47 59 41	76.0
28	Faint	19.68	23 25 33.9	-48 00 01	78.6
29	Stellar	14.01	23 25 34.8	-48 00 30	84.1
30	Faint	20.58	23 25 22.1	-47 59 10	84.5

Selection criterion: distance
Galaxy Density = 1355 per sq. deg.
Sample Radius = 200.0 arc sec
Stars = 51
Total galaxies = 36 (cDs = 0, spirals = 0)
Blend objects = 0
Faint objects = 54
Unknown objects = 0
Sum = 141

Figure C.25: CUOC Finding chart of candidate 0753060

ROSAT Identification | **ROSAT / MPE / RSDC | 28-JUN-94 09:04:10 | RGC** | Page: 1

UKST IIIaJ (blue) | **ROE/NRL COSMOS Finding Chart** | MASOS file: roe_disk:[roedat.masos]078_N1_SI02_N1_P1.mos

Field No. 818 | .... | MASOL Nr.: 000158

Plate Epoch: 1989.7590 | RASS Info: | ROSAT Source Name: RX J22182-0348

Equinox: J2000.0 | Error radii: 1 sigma = 32.1" ; plotted: 90% conf. = 1.645 sigma = 52.8" | ROSAT Position (2000.0): 22 18 15.1 -03 48 22

(1950.0): 22 15 39.4 -04 03 24

Galactic II (l,b): 58.66215 -46.65254

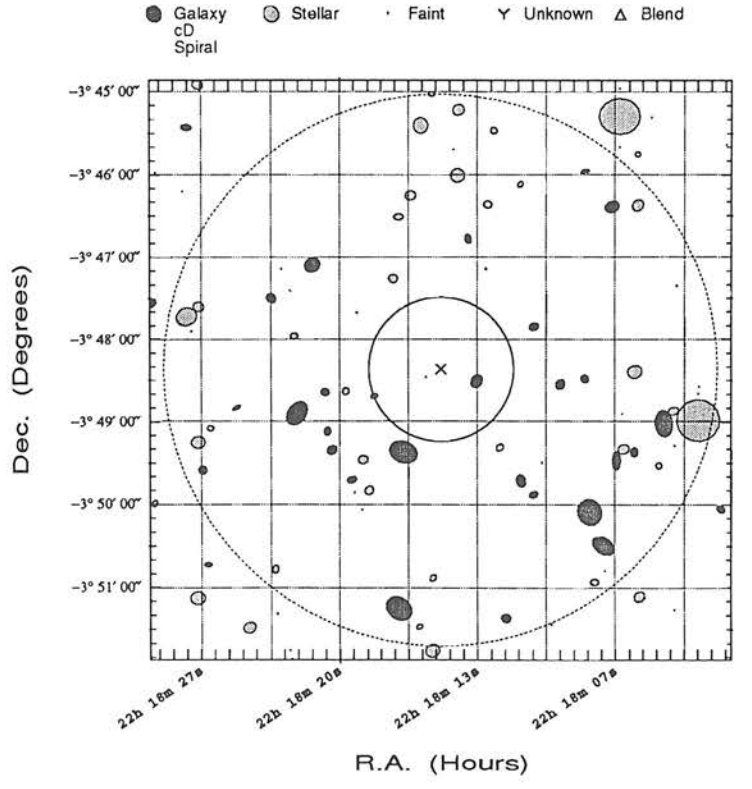

#	CLASS	B	R.A.	Dec.	DIST.
01	Faint	23.35	22 18 15.8	-03 48 27	12.1
02	Galaxy	18.59	22 18 13.4	-03 48 30	27.4
03	Stellar	21.80	22 18 18.3	-03 48 41	52.4
04	Galaxy	15.78	22 18 16.9	-03 49 22	66.4
05	Stellar	20.71	22 18 19.7	-03 48 38	70.9
06	Stellar	21.10	22 18 12.3	-03 49 19	71.2
07	Faint	25.78	22 18 19.2	-03 47 40	73.9
08	Galaxy	20.52	22 18 10.6	-03 47 51	74.6
09	Stellar	19.37	22 18 17.4	-03 47 15	74.7
10	Faint	26.17	22 18 12.9	-03 47 08	80.2
11	Galaxy	20.93	22 18 20.7	-03 48 39	85.8
12	Stellar	18.94	22 18 18.9	-03 49 27	86.6
13	Galaxy	19.53	22 18 09.3	-03 48 33	87.4
14	Faint	23.68	22 18 20.0	-03 49 15	91.0
15	Galaxy	21.10	22 18 20.6	-03 49 07	93.9
16	Galaxy	21.28	22 18 13.8	-03 46 47	97.0
17	Galaxy	19.59	22 18 20.4	-03 49 21	98.3
18	Galaxy	18.63	22 18 11.2	-03 49 43	99.8
19	Faint	24.77	22 18 10.2	-03 49 29	99.9
20	Stellar	18.87	22 18 18.6	-03 49 50	102.5
21	Galaxy	20.79	22 18 19.4	-03 49 42	103.0
22	Galaxy	21.39	22 18 08.1	-03 48 29	104.5
23	Stellar	21.55	22 18 22.2	-03 47 58	109.1
24	Galaxy	15.76	22 18 22.1	-03 48 54	109.1
25	Faint	25.45	22 18 19.3	-03 49 51	109.1
26	Galaxy	21.51	22 18 10.6	-03 49 53	113.1
27	Stellar	20.07	22 18 17.2	-03 46 31	115.1
28	Faint	26.44	22 18 18.9	-03 50 04	117.1
29	Galaxy	17.60	22 18 21.3	-03 47 06	120.2
30	Faint	24.56	22 18 22.4	-03 47 24	123.6

Selection criterion: distance
Galaxy Density = 430 per sq. deg.
Sample Radius = 200.0 arc sec

Stars	=	29
Total galaxies	=	26 (cDs = 0, spirals = 0)
Blend objects	=	0
Faint objects	=	18
Unknown objects	=	0
Sum	=	73

Figure C.26: CUOC Finding chart of candidate 0782158

ROSAT Identification | **ROSAT / MPE / RSDC | 28-JUN-94 09:04:19 | RGC** | Page: 1

UKST IIIaJ (blue) | **ROE/NRL COSMOS Finding Chart** | MASOS file: roe_disk:[roedat.masos]081_N1_SI03_N1_P1.mos

Field No. 536 | .... | MASOL Nr.: 000014

Plate Epoch: 1977.5540 | RASS Info: | ROSAT Source Name: RX J23214-2312

Equinox: J2000.0 | Error radii: 1 sigma = 32.7" ; plotted: 90% conf. = 1.645 sigma = 53.8" | ROSAT Position (2000.0): 23 21 25.4 -23 12 22

(1950.0): 23 18 46.7 -23 28 49

Galactic II (l,b): 38.85409 -69.28874

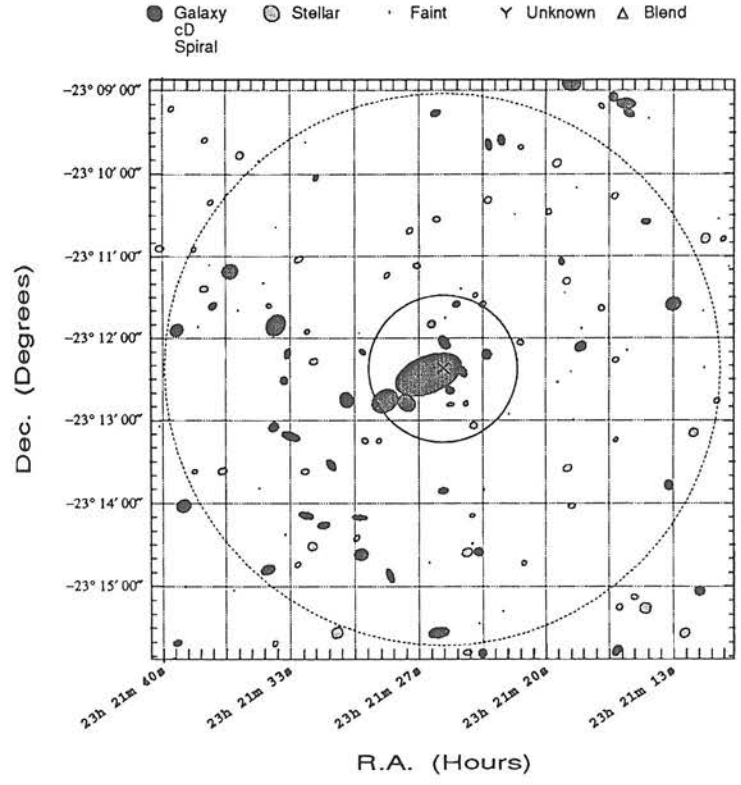

#	CLASS	B	R.A.	Dec.	DIST.
01	Galaxy	11.41	23 21 26.2	-23 12 27	11.6
02	Galaxy	20.44	23 21 24.4	-23 12 25	14.6
03	Galaxy	19.98	23 21 25.1	-23 12 38	16.6
04	Galaxy	18.30	23 21 25.3	-23 12 03	19.1
05	Stellar	21.38	23 21 25.0	-23 12 49	26.9
06	Stellar	22.09	23 21 24.2	-23 12 48	30.4
07	Galaxy	18.59	23 21 23.1	-23 12 12	33.0
08	Stellar	18.93	23 21 26.0	-23 11 50	33.7
09	Galaxy	16.81	23 21 27.3	-23 12 47	36.3
10	Faint	22.20	23 21 25.3	-23 11 45	37.3
11	Stellar	19.88	23 21 23.8	-23 13 04	47.3
12	Galaxy	19.75	23 21 24.7	-23 11 35	48.0
13	Galaxy	14.71	23 21 28.5	-23 12 46	48.3
14	Stellar	20.51	23 21 23.3	-23 11 35	55.3
15	Faint	23.44	23 21 22.0	-23 12 55	57.8
16	Stellar	21.73	23 21 23.7	-23 11 29	58.4
17	Stellar	21.14	23 21 21.4	-23 12 03	59.0
18	Galaxy	21.60	23 21 29.6	-23 12 10	59.3
19	Faint	22.37	23 21 24.5	-23 11 24	59.9
20	Faint	23.05	23 21 29.8	-23 11 56	65.8
21	Stellar	21.73	23 21 28.8	-23 13 15	70.1
22	Galaxy	16.16	23 21 30.4	-23 12 45	73.1
23	Stellar	21.01	23 21 29.5	-23 13 15	77.0
24	Stellar	20.71	23 21 26.8	-23 11 07	77.6
25	Stellar	21.25	23 21 28.3	-23 11 14	79.4
26	Faint	23.03	23 21 19.4	-23 12 32	83.7
27	Galaxy	19.31	23 21 25.4	-23 13 51	88.8
28	Faint	22.17	23 21 23.3	-23 13 50	92.7
29	Faint	23.07	23 21 18.7	-23 12 25	92.7
30	Stellar	19.48	23 21 32.1	-23 12 17	92.8

Selection criterion: distance
Galaxy Density = 893 per sq. deg.
Sample Radius = 200.0 arc sec

Stars	=	41
Total galaxies	=	37 (cDs = 0, spirals = 0)
Blend objects	=	0
Faint objects	=	27
Unknown objects	=	0
Sum	=	105

Figure C.27: CUOC Finding chart of candidate 0813014

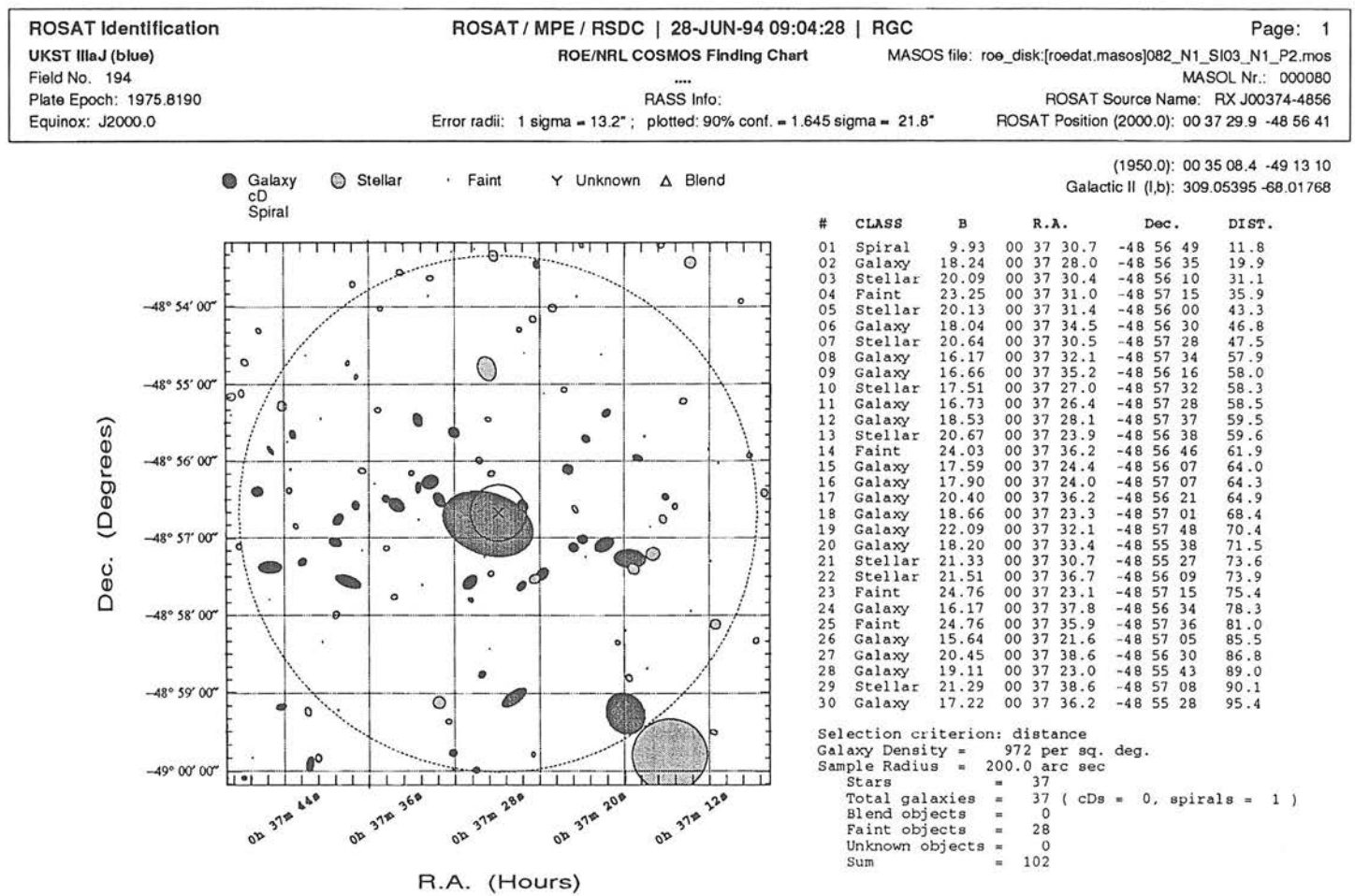

Figure C.28: CUOC Finding chart of candidate 0823080

ROSAT Identification
UKST IIIaJ (blue)
Field No. 195
Plate Epoch: 1975.6899
Equinox: J2000.0

ROSAT / MPE / RSDC | 28-JUN-94 09:04:37 | RGC
ROE/NRL COSMOS Finding Chart
....
RASS Info:
Error radii: 1 sigma = 34.1" ; plotted: 90% conf. = 1.645 sigma = 56.0"

Page: 1
MASOS file: roe_disk:[roedat.masos]084_N1_SI03_N1_P1.mos
MASOL Nr.: 000100
ROSAT Source Name: RX J00513-4832
ROSAT Position (2000.0): 00 51 19.1 -48 32 15

(1950.0): 00 49 01.9 -48 48 33
Galactic II (l,b): 302.98564 -68.59079

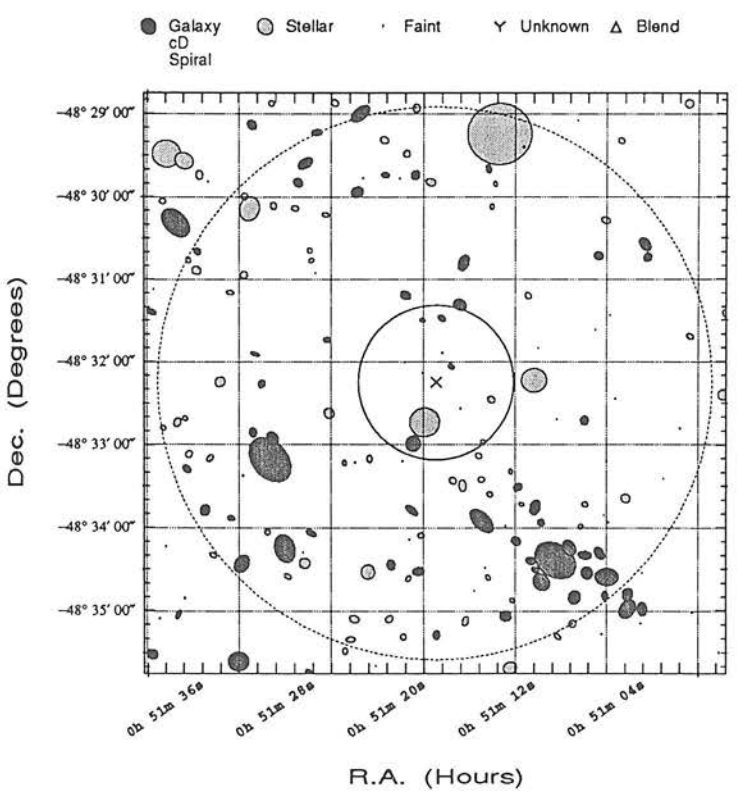

#	CLASS	B	R.A.	Dec.	DIST.
01	Faint	23.89	00 51 20.1	-48 32 08	11.8
02	Galaxy	23.16	00 51 18.0	-48 32 04	15.8
03	Faint	23.85	00 51 18.7	-48 31 54	21.6
04	Faint	24.70	00 51 17.3	-48 32 34	25.6
05	Faint	23.75	00 51 21.4	-48 32 01	26.8
06	Stellar	13.43	00 51 20.0	-48 32 44	30.2
07	Stellar	20.18	00 51 15.1	-48 32 27	41.8
08	Stellar	23.39	00 51 20.1	-48 31 30	45.9
09	Galaxy	22.23	00 51 18.7	-48 31 28	46.7
10	Galaxy	17.04	00 51 20.7	-48 32 59	47.2
11	Stellar	23.08	00 51 15.7	-48 32 58	54.7
12	Galaxy	18.31	00 51 17.4	-48 31 19	58.9
13	Stellar	22.60	00 51 16.0	-48 33 08	61.3
14	Faint	24.60	00 51 21.5	-48 33 12	61.9
15	Galaxy	20.20	00 51 21.3	-48 31 12	67.0
16	Stellar	14.32	00 51 12.0	-48 32 13	70.7
17	Stellar	21.15	00 51 17.9	-48 33 26	71.8
18	Stellar	21.98	00 51 23.9	-48 33 10	72.9
19	Stellar	19.97	00 51 17.2	-48 33 29	76.7
20	Stellar	22.21	00 51 15.8	-48 33 25	77.4
21	Faint	26.05	00 51 11.7	-48 31 50	77.7
22	Stellar	18.97	00 51 26.8	-48 32 37	79.8
23	Faint	24.47	00 51 24.9	-48 33 13	82.0
24	Stellar	23.39	00 51 13.7	-48 33 19	83.7
25	Galaxy	22.73	00 51 27.0	-48 31 44	84.0
26	Stellar	23.27	00 51 25.7	-48 33 13	87.8
27	Galaxy	18.85	00 51 17.1	-48 30 48	89.0
28	Stellar	21.73	00 51 15.2	-48 33 36	89.7
29	Faint	23.62	00 51 10.3	-48 32 42	91.3
30	Stellar	21.98	00 51 12.4	-48 31 12	91.6

Selection criterion: distance
Galaxy Density = 972 per sq. deg.
Sample Radius = 200.0 arc sec
Stars = 58
Total galaxies = 50 (cDs = 0, spirals = 0)
Blend objects = 0
Faint objects = 26
Unknown objects = 0
Sum = 134

Figure C.29: CUOC Finding chart of candidate 0843100

ROSAT Identification | ROSAT / MPE / RSDC | 28-JUN-94 09:05:07 | RGC | Page: 1

UKST IIIaJ (blue) — **ROE/NRL COSMOS Finding Chart** — MASOS file: roe_disk:[roedat.masos]086_N1_SI03_N1_P1.mos

Field No. 606 — MASOL Nr.: 000043

Plate Epoch: 1976.8770 — RASS Info: — ROSAT Source Name: RX J23564-2102

Equinox: J2000.0 — Error radii: 1 sigma = 17.9" ; plotted: 90% conf. = 1.645 sigma = 29.4" — ROSAT Position (2000.0): 23 56 28.7 -21 02 08

(1950.0): 23 53 54.5 -21 18 50

Galactic II (l,b): 55.90175 -76.06788

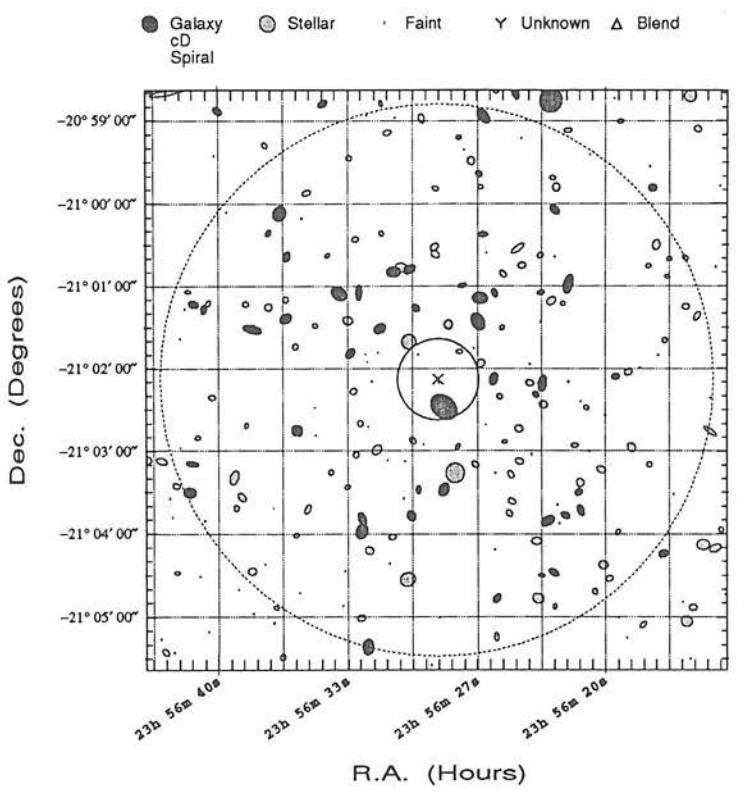

#	CLASS	B	R.A.	Dec.	DIST.
01	Faint	24.89	23 56 28.7	-21 02 10	2.6
02	Galaxy	15.52	23 56 28.4	-21 02 28	20.5
03	Faint	24.55	23 56 29.8	-21 01 50	23.3
04	Stellar	21.64	23 56 27.6	-21 01 48	25.1
05	Stellar	19.78	23 56 26.5	-21 01 56	33.1
06	Faint	25.05	23 56 26.9	-21 01 45	33.9
07	Stellar	16.28	23 56 30.2	-21 01 40	34.8
08	Galaxy	19.51	23 56 25.8	-21 02 08	40.1
09	Stellar	19.40	23 56 28.2	-21 01 28	40.4
10	Stellar	20.83	23 56 25.5	-21 02 20	46.3
11	Faint	24.35	23 56 31.8	-21 01 49	47.7
12	Faint	25.05	23 56 26.2	-21 02 41	47.9
13	Faint	23.70	23 56 32.1	-21 02 10	48.0
14	Stellar	21.41	23 56 30.0	-21 02 53	48.1
15	Faint	23.15	23 56 29.5	-21 02 55	48.5
16	Stellar	22.50	23 56 27.7	-21 02 57	50.8
17	Galaxy	16.38	23 56 26.6	-21 01 26	51.1
18	Faint	22.65	23 56 32.3	-21 01 55	52.5
19	Galaxy	20.83	23 56 29.9	-21 01 16	54.5
20	Faint	24.19	23 56 32.4	-21 01 50	55.5
21	Galaxy	19.24	23 56 31.7	-21 01 31	55.9
22	Stellar	22.05	23 56 25.4	-21 01 30	59.7
23	Faint	23.15	23 56 32.3	-21 02 42	61.2
24	Stellar	20.47	23 56 33.1	-21 02 17	61.8
25	Stellar	21.16	23 56 32.7	-21 02 40	64.4
26	Faint	23.13	23 56 30.4	-21 03 08	64.4
27	Stellar	22.29	23 56 25.3	-21 02 53	66.1
28	Galaxy	19.40	23 56 33.2	-21 01 49	66.2
29	Galaxy	17.82	23 56 26.5	-21 01 09	66.3
30	Stellar	19.79	23 56 24.0	-21 02 10	66.4

Selection criterion: distance
Galaxy Density = 1052 per sq. deg.
Sample Radius = 200.0 arc sec
Stars = 88
Total galaxies = 45 (cDs = 0, spirals = 0)
Blend objects = 0
Faint objects = 50
Unknown objects = 0
Sum = 183

Figure C.30: CUOC Finding chart of candidate 0853043

ROSAT Identification | **ROSAT / MPE / RSDC | 28-JUN-94 09:04:56 | RGC** | Page: 1

UKST IIIaJ (blue) | **ROE/NRL COSMOS Finding Chart** | MASOS file: roe_disk:[roedat.masos]085_N1_SI03_N1_P1.mos

Field No. 409 | .... | MASOL Nr.: 000062

Plate Epoch: 1976.8800 | RASS Info: | ROSAT Source Name: RX J00074-2809

Equinox: J2000.0 | Error radii: 1 sigma = 19.2" ; plotted: 90% conf. = 1.645 sigma = 31.5" | ROSAT Position (2000.0): 00 07 24.3 -28 09 27

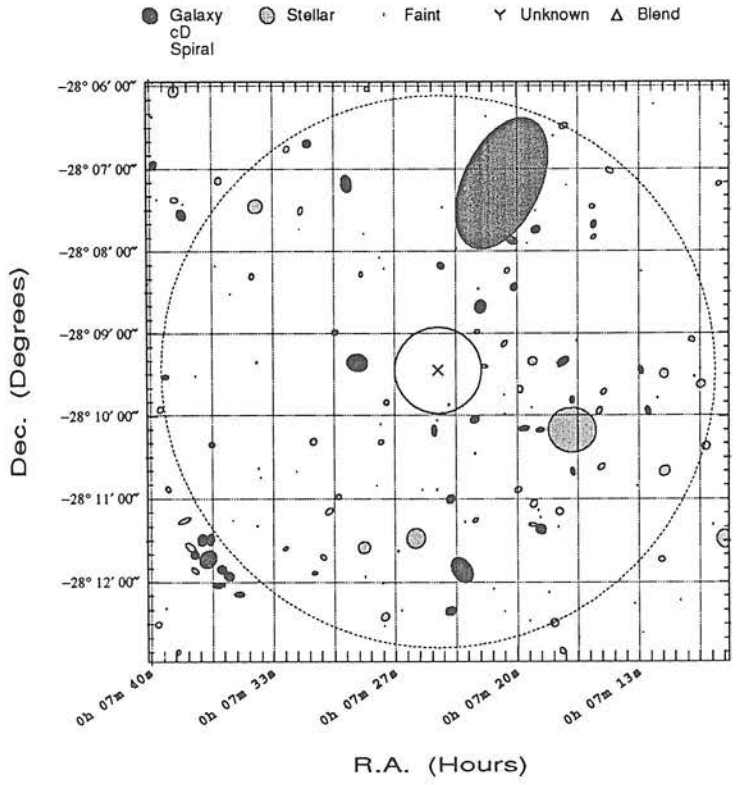

(1950.0): 00 04 51.6 -28 26 08

Galactic II (l,b): 24.36603 -80.19784

#	CLASS	B	R.A.	Dec.	DIST.
01	Faint	23.77	00 07 23.7	-28 09 52	26.3
02	Stellar	22.36	00 07 21.8	-28 09 24	33.8
03	Faint	23.59	00 07 24.4	-28 10 03	36.4
04	Stellar	22.13	00 07 22.2	-28 08 59	39.7
05	Galaxy	21.23	00 07 24.5	-28 10 10	43.7
06	Galaxy	19.55	00 07 22.3	-28 10 02	44.3
07	Stellar	21.06	00 07 27.2	-28 09 50	44.4
08	Faint	22.96	00 07 20.7	-28 09 44	50.6
09	Stellar	21.96	00 07 20.7	-28 09 07	51.8
10	Galaxy	17.33	00 07 22.0	-28 08 41	55.4
11	Faint	23.93	00 07 27.5	-28 10 06	57.3
12	Faint	23.61	00 07 20.7	-28 09 59	57.8
13	Galaxy	15.20	00 07 28.7	-28 09 21	58.8
14	Stellar	20.47	00 07 19.8	-28 09 41	60.7
15	Faint	24.33	00 07 22.3	-28 10 27	65.9
16	Faint	23.66	00 07 22.1	-28 08 27	66.4
17	Stellar	21.37	00 07 27.4	-28 10 19	66.7
18	Stellar	18.50	00 07 19.1	-28 09 20	68.6
19	Faint	22.63	00 07 19.2	-28 09 54	72.7
20	Galaxy	20.52	00 07 19.6	-28 10 09	75.3
21	Galaxy	21.14	00 07 24.1	-28 08 10	76.4
22	Galaxy	21.87	00 07 29.9	-28 08 59	79.6
23	Galaxy	20.45	00 07 20.1	-28 08 26	82.1
24	Faint	23.61	00 07 27.2	-28 08 12	83.9
25	Galaxy	21.95	00 07 18.7	-28 10 10	85.7
26	Faint	22.94	00 07 24.4	-28 10 53	86.5
27	Faint	22.88	00 07 25.2	-28 10 53	87.4
28	Stellar	21.48	00 07 20.5	-28 08 14	88.2
29	Stellar	22.33	00 07 28.5	-28 08 17	89.7
30	Faint	22.60	00 07 23.3	-28 07 58	89.9

Selection criterion: distance
Galaxy Density = 844 per sq. deg.
Sample Radius = 200.0 arc sec

Stars	=	39
Total galaxies	=	25 (cDs = 0, spirals = 1)
Blend objects	=	0
Faint objects	=	52
Unknown objects	=	0
Sum	=	116

Figure C.31: CUOC Finding chart of candidate 0853062

ROSAT Identification | **ROSAT / MPE / RSDC | 28-JUN-94 09:05:07 | RGC** | Page: 1

UKST IIIaJ (blue) | **ROE/NRL COSMOS Finding Chart** | MASOS file: roe_disk:[roedat.masos]086_N1_SI03_N1_P1.mos

Field No. 606 | MASOL Nr.: 000043

Plate Epoch: 1976.8770 | RASS Info: | ROSAT Source Name: RX J23564-2102

Equinox: J2000.0 | Error radii: 1 sigma = 17.9" ; plotted: 90% conf. = 1.645 sigma = 29.4" | ROSAT Position (2000.0): 23 56 28.7 -21 02 08

(1950.0): 23 53 54.5 -21 18 50

Galactic II (l,b): 55.90175 -76.06788

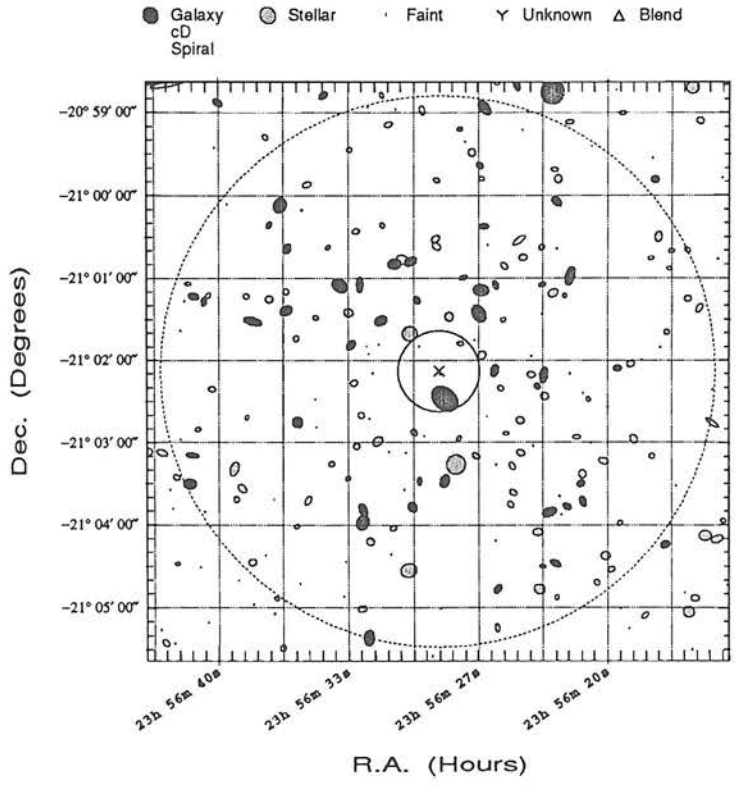

#	CLASS	B	R.A.	Dec.	DIST.
01	Faint	24.89	23 56 28.7	-21 02 10	2.6
02	Galaxy	15.52	23 56 28.4	-21 02 28	20.5
03	Faint	24.55	23 56 29.8	-21 01 50	23.3
04	Stellar	21.64	23 56 27.6	-21 01 48	25.1
05	Stellar	19.78	23 56 26.5	-21 01 56	33.1
06	Faint	25.05	23 56 26.9	-21 01 45	33.9
07	Stellar	16.28	23 56 30.2	-21 01 40	34.8
08	Galaxy	19.51	23 56 25.8	-21 02 08	40.1
09	Stellar	19.40	23 56 28.2	-21 01 28	40.4
10	Stellar	20.83	23 56 25.5	-21 02 20	46.3
11	Faint	24.35	23 56 31.8	-21 01 49	47.7
12	Faint	25.05	23 56 26.2	-21 02 41	47.9
13	Faint	23.70	23 56 32.1	-21 02 10	48.0
14	Stellar	21.41	23 56 30.0	-21 02 53	48.1
15	Faint	23.15	23 56 29.5	-21 02 55	48.5
16	Stellar	22.50	23 56 27.7	-21 02 57	50.8
17	Galaxy	16.38	23 56 26.6	-21 01 26	51.1
18	Faint	22.65	23 56 32.3	-21 01 55	52.5
19	Galaxy	20.83	23 56 29.9	-21 01 16	54.5
20	Faint	24.19	23 56 32.4	-21 01 50	55.5
21	Galaxy	19.24	23 56 31.7	-21 01 31	55.9
22	Stellar	22.05	23 56 25.4	-21 01 30	59.7
23	Faint	23.15	23 56 32.3	-21 02 42	61.2
24	Stellar	20.47	23 56 33.1	-21 02 17	61.8
25	Stellar	21.16	23 56 32.7	-21 02 40	64.4
26	Faint	23.13	23 56 30.4	-21 03 08	64.4
27	Stellar	22.29	23 56 25.3	-21 02 53	66.1
28	Galaxy	19.40	23 56 33.2	-21 01 49	66.2
29	Galaxy	17.82	23 56 26.5	-21 01 09	66.3
30	Stellar	19.79	23 56 24.0	-21 02 10	66.4

Selection criterion: distance
Galaxy Density = 1052 per sq. deg.
Sample Radius = 200.0 arc sec

Stars	=	88
Total galaxies	=	45 (cDs = 0, spirals = 0)
Blend objects	=	0
Faint objects	=	50
Unknown objects	=	0
Sum	=	183

Figure C.32: CUOC Finding chart of candidate 0863043

ROSAT Identification | **ROSAT / MPE / RSDC | 28-JUN-94 09:05:22 | RGC** | Page: 2

UKST IIIaJ (blue) | **ROE/NRL COSMOS Finding Chart** | MASOS file: roe_disk:[roedat.masos]086_N1_SI03_N1_P1.mos

Field No. 606 | .... | MASOL Nr.: 000044

Plate Epoch: 1976.8770 | RASS Info: | ROSAT Source Name: RX J23593-2047

Equinox: J2000.0 | Error radii: 1 sigma = 8.6" ; plotted: 90% conf. = 1.645 sigma = 14.2" | ROSAT Position (2000.0): 23 59 18.9 -20 47 51

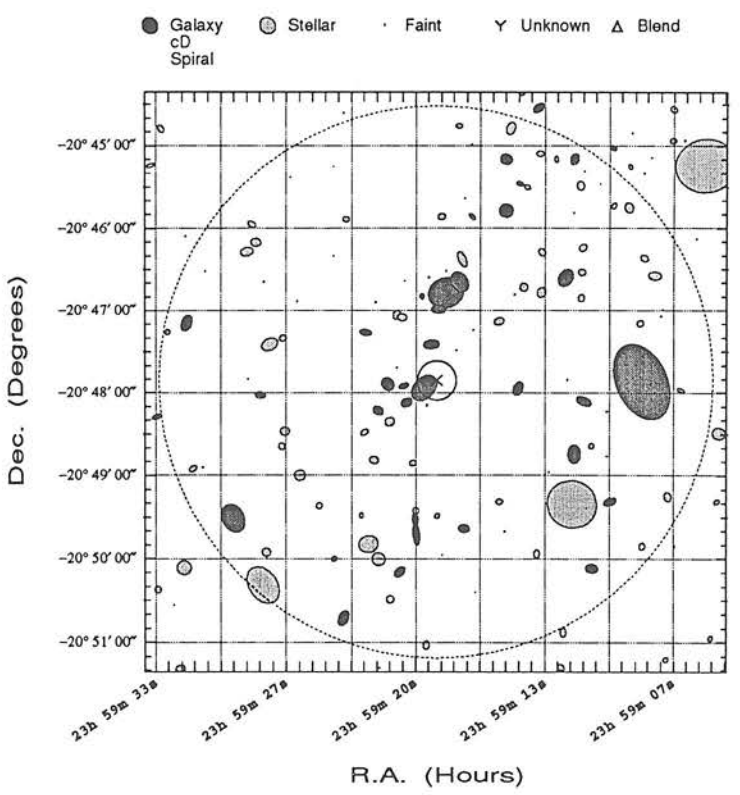

(1950.0): 23 56 45.0 -21 04 33

Galactic II (l,b): 58.15579 -76.52664

#	CLASS	B	R.A.	Dec.	DIST.
01	Galaxy	15.22	23 59 19.5	-20 47 57	10.5
02	Faint	25.07	23 59 19.4	-20 48 09	19.6
03	Galaxy	21.28	23 59 20.6	-20 47 55	24.5
04	Faint	23.56	23 59 17.9	-20 47 29	26.1
05	Galaxy	18.02	23 59 19.2	-20 47 25	26.4
06	Galaxy	19.15	23 59 20.5	-20 48 07	27.1
07	Faint	23.69	23 59 21.0	-20 47 42	30.7
08	Galaxy	17.57	23 59 21.5	-20 47 54	35.9
09	Faint	23.02	23 59 17.0	-20 47 14	45.2
10	Stellar	19.11	23 59 21.4	-20 48 21	45.5
11	Galaxy	18.81	23 59 22.0	-20 48 13	48.1
12	Galaxy	19.78	23 59 18.8	-20 46 59	51.9
13	Stellar	19.33	23 59 20.7	-20 47 05	52.5
14	Stellar	19.09	23 59 21.0	-20 47 03	56.1
15	Galaxy	17.69	23 59 14.7	-20 47 57	58.9
16	Stellar	19.97	23 59 15.7	-20 47 08	62.1
17	Galaxy	22.52	23 59 19.7	-20 46 50	62.3
18	Stellar	21.26	23 59 20.2	-20 48 51	62.4
19	Galaxy	19.78	23 59 22.6	-20 47 16	62.5
20	Galaxy	13.89	23 59 18.4	-20 46 47	64.4
21	Stellar	20.19	23 59 22.6	-20 48 29	64.5
22	Faint	22.97	23 59 22.1	-20 46 54	72.3
23	Stellar	19.18	23 59 22.2	-20 48 49	73.7
24	Galaxy	16.28	23 59 17.7	-20 46 39	73.8
25	Faint	24.57	23 59 19.3	-20 46 36	75.6
26	Faint	22.86	23 59 20.6	-20 46 39	76.2
27	Faint	22.83	23 59 18.4	-20 46 31	80.1
28	Faint	25.09	23 59 14.9	-20 46 49	84.2
29	Stellar	19.78	23 59 17.6	-20 46 23	90.3
30	Stellar	19.29	23 59 14.4	-20 46 43	92.4

Selection criterion: distance
Galaxy Density = 1052 per sq. deg.
Sample Radius = 200.0 arc sec

Stars	=	55
Total galaxies	=	31 (cDs = 0, spirals = 1)
Blend objects	=	0
Faint objects	=	31
Unknown objects	=	0
Sum	=	117

Figure C.33: CUOC Finding chart of candidate 0863044

ROSAT Identification
UKST IIIaJ (blue)
Field No. 350
Plate Epoch: 1978.8140
Equinox: J2000.0

ROSAT / MPE / RSDC | 28-JUN-94 09:05:31 | RGC
ROE/NRL COSMOS Finding Chart
....
RASS Info:
Error radii: 1 sigma = 9.2" ; plotted: 90% conf. = 1.645 sigma = 15.2"

Page: 1
MASOS file: roe_disk:[roedat.masos]087_N1_SI03_N1_P1.mos
MASOL Nr.: 000078
ROSAT Source Name: RX J00340-3354
ROSAT Position (2000.0): 00 34 00.3 -33 54 24

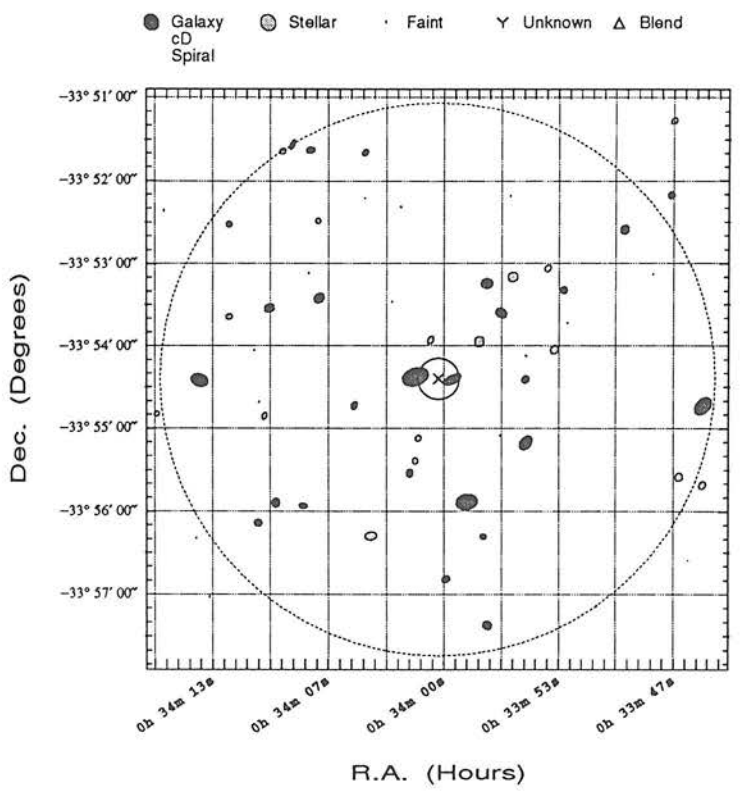

(1950.0): 00 31 33.0 -34 10 56
Galactic II (l,b): 330.82917 -82.25367

#	CLASS	B	R.A.	Dec.	DIST.
01	Galaxy	16.12	00 33 59.5	-33 54 24	10.3
02	Galaxy	14.76	00 34 01.7	-33 54 23	17.0
03	Stellar	18.77	00 34 00.8	-33 53 56	28.6
04	Stellar	16.83	00 33 57.9	-33 53 57	40.1
05	Stellar	19.75	00 34 01.5	-33 55 07	45.3
06	Faint	21.92	00 33 56.8	-33 55 05	60.3
07	Stellar	19.99	00 34 01.7	-33 55 24	61.9
08	Galaxy	18.83	00 33 55.3	-33 54 24	62.7
09	Galaxy	19.39	00 34 05.2	-33 54 43	63.7
10	Faint	22.77	00 33 55.2	-33 54 07	65.1
11	Faint	22.72	00 34 03.0	-33 53 28	65.7
12	Galaxy	17.03	00 33 56.7	-33 53 36	66.0
13	Galaxy	18.95	00 34 02.0	-33 55 33	71.6
14	Galaxy	17.26	00 33 57.5	-33 53 15	77.9
15	Galaxy	16.86	00 33 55.2	-33 55 11	78.5
16	Stellar	17.65	00 33 53.6	-33 54 03	86.1
17	Galaxy	14.93	00 33 58.6	-33 55 53	91.3
18	Stellar	17.12	00 33 56.0	-33 53 10	91.4
19	Faint	21.04	00 33 52.8	-33 53 44	101.4
20	Galaxy	17.95	00 34 07.2	-33 53 25	103.9
21	Galaxy	19.09	00 33 53.0	-33 53 20	111.1
22	Stellar	19.45	00 33 54.0	-33 53 04	112.6
23	Galaxy	20.04	00 33 57.7	-33 56 18	118.7
24	Faint	21.08	00 34 07.8	-33 53 07	121.4
25	Stellar	17.00	00 34 04.2	-33 56 18	124.1
26	Stellar	20.21	00 34 10.3	-33 54 51	127.8
27	Faint	20.87	00 34 02.5	-33 52 19	128.1
28	Faint	22.30	00 34 10.7	-33 54 41	130.0
29	Galaxy	17.88	00 34 10.1	-33 53 33	131.9
30	Galaxy	20.04	00 34 08.1	-33 55 56	133.8

Selection criterion: distance
Galaxy Density = 844 per sq. deg.
Sample Radius = 200.0 arc sec
Stars = 13
Total galaxies = 25 (cDs = 0, spirals = 0)
Blend objects = 0
Faint objects = 13
Unknown objects = 0
Sum = 51

Figure C.34: CUOC Finding chart of candidate 0873078

ROSAT Identification
UKST IIIaJ (blue)
Field No. 196
Plate Epoch: 1979.8790
Equinox: J2000.0

ROSAT / MPE / RSDC | 28-JUN-94 09:05:39 | RGC
ROE/NRL COSMOS Finding Chart
RASS Info:
Error radii: 1 sigma = 30.0" ; plotted: 90% conf. = 1.645 sigma = 49.4"

Page: 1
MASOS file: roe_disk:[roedat.masos]088_N1_SI03_N1_P2.mos
MASOL Nr.: 000087
ROSAT Source Name: RX J01342-4722
ROSAT Position (2000.0): 01 34 15.8 -47 22 05

(1950.0): 01 32 10.9 -47 37 25
Galactic II (l,b): 283.22694 -68.08831

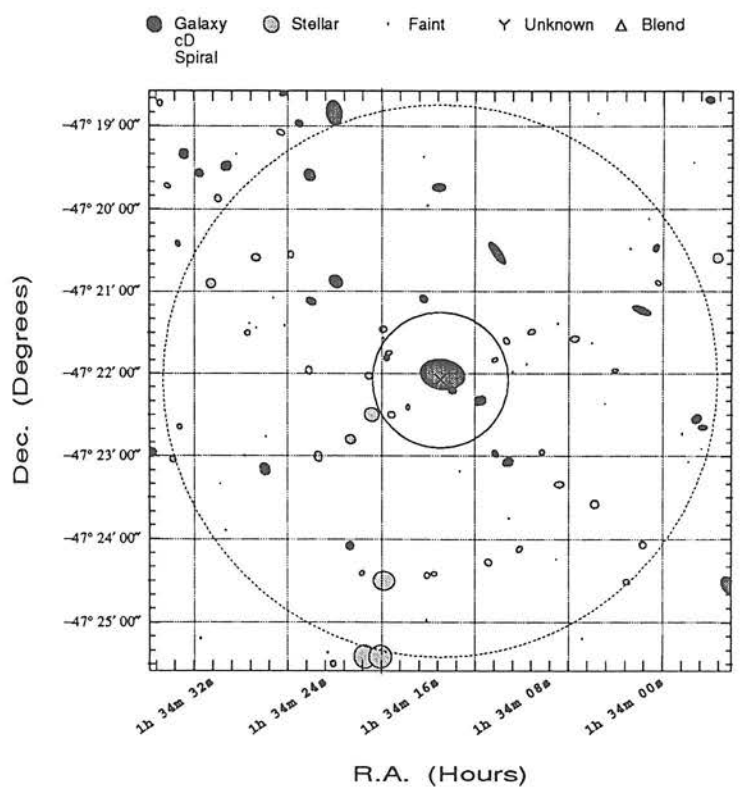

#	CLASS	B	R.A.	Dec.	DIST.
01	Galaxy	13.44	01 34 15.7	-47 22 01	4.2
02	Galaxy	19.97	01 34 14.9	-47 22 12	11.5
03	Stellar	21.02	01 34 18.1	-47 22 25	30.7
04	Galaxy	17.65	01 34 13.0	-47 22 20	32.4
05	Galaxy	20.81	01 34 19.6	-47 21 49	41.9
06	Stellar	20.99	01 34 11.9	-47 21 50	42.0
07	Stellar	20.96	01 34 19.5	-47 21 45	42.2
08	Stellar	19.59	01 34 19.3	-47 22 30	43.4
09	Faint	22.70	01 34 19.9	-47 21 34	51.2
10	Stellar	19.13	01 34 20.9	-47 22 02	52.0
11	Faint	23.05	01 34 10.7	-47 21 59	52.6
12	Stellar	19.26	01 34 19.9	-47 21 28	55.2
13	Stellar	15.79	01 34 20.7	-47 22 30	55.7
14	Stellar	20.37	01 34 11.1	-47 21 36	55.8
15	Galaxy	18.63	01 34 17.0	-47 21 06	60.3
16	Faint	21.19	01 34 09.7	-47 21 53	63.3
17	Galaxy	20.52	01 34 11.9	-47 22 58	66.5
18	Faint	21.55	01 34 14.4	-47 23 11	67.6
19	Stellar	19.91	01 34 09.3	-47 21 30	74.8
20	Galaxy	18.23	01 34 11.0	-47 23 04	77.2
21	Stellar	16.87	01 34 22.2	-47 22 48	78.0
22	Stellar	20.69	01 34 08.5	-47 22 57	90.4
23	Faint	21.20	01 34 07.4	-47 21 24	94.6
24	Stellar	19.28	01 34 25.1	-47 21 58	95.1
25	Galaxy	15.74	01 34 11.8	-47 20 32	101.3
26	Stellar	18.55	01 34 06.2	-47 21 35	101.9
27	Galaxy	16.58	01 34 23.2	-47 20 53	104.4
28	Stellar	18.05	01 34 24.5	-47 23 00	104.4
29	Galaxy	18.51	01 34 25.0	-47 21 07	109.7
30	Faint	21.40	01 34 10.9	-47 23 45	111.9

Selection criterion: distance
Galaxy Density = 685 per sq. deg.
Sample Radius = 200.0 arc sec
Stars = 31
Total galaxies = 18 (cDs = 0, spirals = 0)
Blend objects = 0
Faint objects = 25
Unknown objects = 0
Sum = 74

Figure C.35: CUOC Finding chart of candidate 0883087

ROSAT Identification | **ROSAT / MPE / RSDC | 28-JUN-94 09:05:55 | RGC** | Page: 1

UKST IIIaJ (blue) | **ROE/NRL COSMOS Finding Chart** | MASOS file: roe_disk:[roedat.masos]089_N1_SI03_N1_P1.mos

Field No. 296 | .... | MASOL Nr.: 000097

Plate Epoch: 1977.6331 | RASS Info: | ROSAT Source Name: RX J01086-4020

Equinox: J2000.0 | Error radii: 1 sigma = 32.7" ; plotted: 90% conf. = 1.645 sigma = 53.8" | ROSAT Position (2000.0): 01 08 38.2 -40 20 26

(1950.0): 01 06 21.1 -40 36 25

Galactic II (l,b): 288.95104 -76.31722

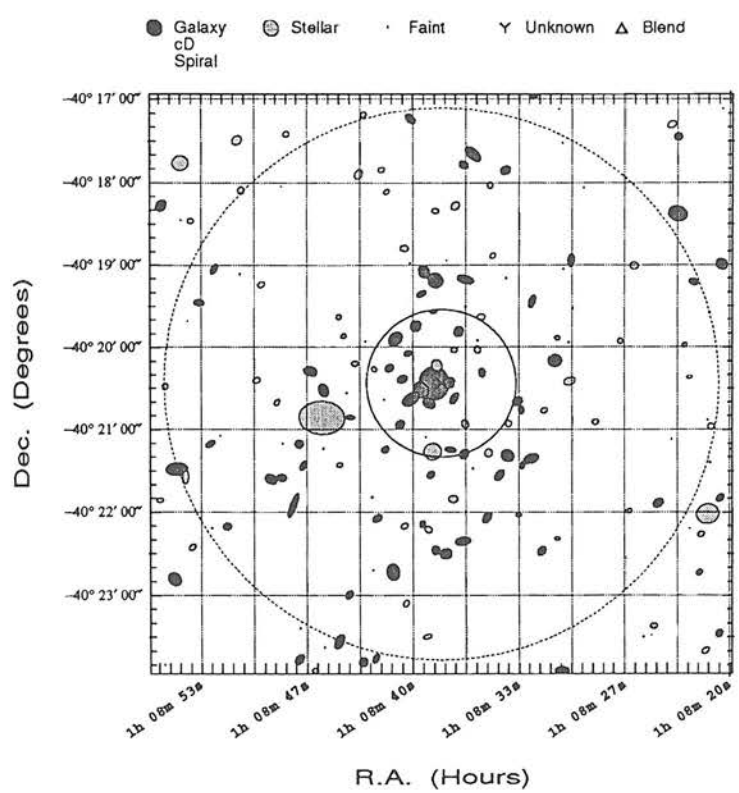

#	CLASS	B	R.A.	Dec.	DIST.
01	Galaxy	13.80	01 08 38.6	-40 20 26	5.0
02	Galaxy	19.06	01 08 37.7	-40 20 26	5.8
03	Stellar	19.60	01 08 38.5	-40 20 13	13.7
04	Galaxy	19.39	01 08 37.4	-40 20 37	14.1
05	Galaxy	16.39	01 08 39.5	-40 20 31	15.5
06	Galaxy	18.72	01 08 39.0	-40 20 41	17.2
07	Galaxy	16.54	01 08 40.1	-40 20 38	25.0
08	Stellar	21.66	01 08 37.4	-40 20 02	25.8
09	Galaxy	19.71	01 08 40.7	-40 20 23	28.2
10	Galaxy	19.62	01 08 35.7	-40 20 19	30.1
11	Galaxy	20.78	01 08 40.3	-40 20 05	32.3
12	Stellar	19.30	01 08 36.7	-40 20 56	34.1
13	Stellar	20.26	01 08 35.9	-40 20 02	35.7
14	Galaxy	19.15	01 08 41.5	-40 20 15	38.9
15	Galaxy	18.08	01 08 37.1	-40 19 49	39.5
16	Faint	22.54	01 08 35.9	-40 19 55	40.6
17	Faint	22.58	01 08 39.2	-40 21 05	40.7
18	Galaxy	18.97	01 08 40.8	-40 20 56	42.3
19	Faint	23.09	01 08 41.8	-40 20 38	43.1
20	Galaxy	17.95	01 08 39.8	-40 19 45	45.5
21	Galaxy	17.04	01 08 41.1	-40 19 54	46.0
22	Galaxy	20.26	01 08 37.6	-40 21 15	48.8
23	Stellar	21.50	01 08 42.4	-40 20 16	49.2
24	Stellar	15.14	01 08 38.7	-40 21 16	49.9
25	Galaxy	21.39	01 08 38.7	-40 19 34	52.4
26	Galaxy	18.33	01 08 36.8	-40 21 18	53.9
27	Stellar	19.48	01 08 35.7	-40 19 38	56.0
28	Galaxy	18.56	01 08 33.4	-40 20 39	56.2
29	Stellar	20.26	01 08 34.0	-40 20 56	56.5
30	Faint	22.72	01 08 36.7	-40 19 30	58.6

Selection criterion: distance
Galaxy Density = 956 per sq. deg.
Sample Radius = 200.0 arc sec
Stars = 44
Total galaxies = 59 (cDs = 0, spirals = 0)
Blend objects = 0
Faint objects = 26
Unknown objects = 0
Sum = 129

Figure C.36: CUOC Finding chart of candidate 0893097

ROSAT Identification
UKST IIIaJ (blue)
Field No. 539
Plate Epoch: 1977.7640
Equinox: J2000.0

ROSAT / MPE / RSDC | 28-JUN-94 09:06:14 | RGC
ROE/NRL COSMOS Finding Chart
RASS Info:
Error radii: 1 sigma = 9.9" ; plotted: 90% conf. = 1.645 sigma = 16.2"

Page: 1
MASOS file: roe_disk:[roedat.masos]090_N1_SI03_N1_P1.mos
MASOL Nr.: 000046
ROSAT Source Name: RX J00260-1855
ROSAT Position (2000.0): 00 26 04.4 -18 55 06

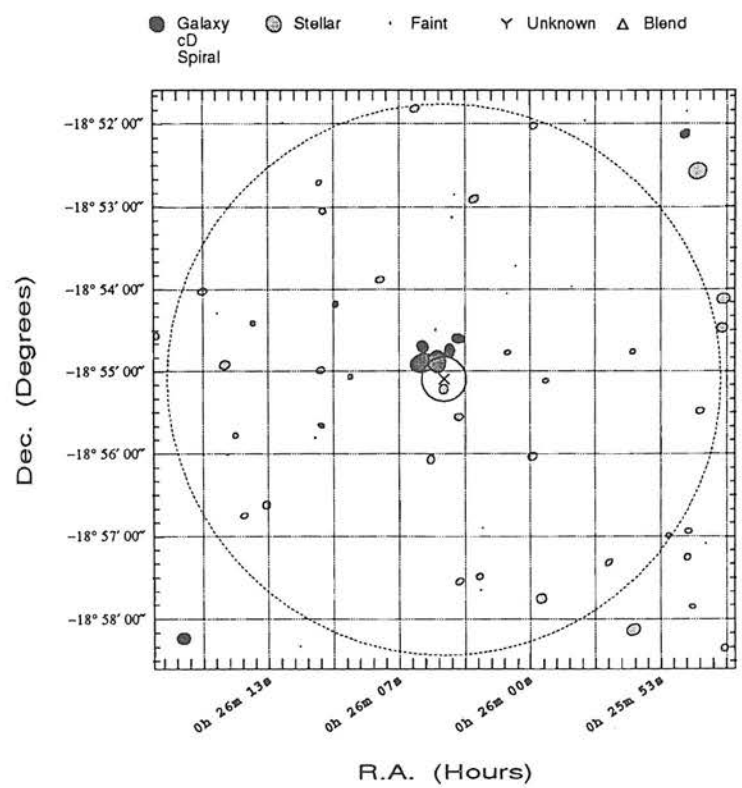

(1950.0): 00 23 33.2 -19 11 42
Galactic II (l,b): 86.23114 -79.93196

#	CLASS	B	R.A.	Dec.	DIST.
01	Stellar	20.02	00 26 04.4	-18 55 13	7.3
02	Galaxy	16.26	00 26 04.7	-18 54 53	13.7
03	Galaxy	15.31	00 26 05.5	-18 54 54	19.3
04	Galaxy	19.44	00 26 04.1	-18 54 45	21.1
05	Galaxy	19.71	00 26 05.5	-18 54 42	28.2
06	Stellar	20.95	00 26 03.7	-18 55 33	29.3
07	Galaxy	18.86	00 26 03.7	-18 54 36	31.3
08	Faint	25.15	00 26 04.8	-18 54 30	36.6
09	Stellar	23.12	00 26 01.2	-18 54 46	49.9
10	Stellar	21.01	00 26 05.1	-18 56 04	59.3
11	Stellar	22.61	00 26 09.2	-18 55 04	67.7
12	Stellar	23.04	00 25 59.2	-18 55 07	73.5
13	Faint	24.61	00 26 01.2	-18 54 03	77.6
14	Stellar	20.50	00 25 59.9	-18 56 02	85.2
15	Stellar	21.20	00 26 07.6	-18 53 53	86.0
16	Stellar	20.46	00 26 10.7	-18 54 59	89.4
17	Galaxy	23.14	00 26 10.7	-18 55 39	94.8
18	Galaxy	22.98	00 26 09.9	-18 54 11	95.5
19	Faint	26.06	00 26 00.7	-18 53 43	97.7
20	Faint	24.71	00 26 10.9	-18 55 48	102.0
21	Faint	23.66	00 26 02.4	-18 56 53	111.1
22	Faint	23.97	00 25 57.9	-18 53 58	114.6
23	Faint	26.04	00 26 04.0	-18 53 07	118.6
24	Stellar	20.02	00 26 02.9	-18 52 54	133.2
25	Faint	25.00	00 26 03.9	-18 52 51	135.1
26	Stellar	23.23	00 25 54.8	-18 54 46	138.0
27	Stellar	23.41	00 26 14.2	-18 54 25	144.5
28	Stellar	21.38	00 26 02.6	-18 57 29	145.3
29	Stellar	20.66	00 26 03.6	-18 57 33	147.3
30	Stellar	22.17	00 26 10.6	-18 53 03	150.9

Selection criterion: distance
Galaxy Density = 733 per sq. deg.
Sample Radius = 200.0 arc sec
Stars = 27
Total galaxies = 7 (cDs = 0, spirals = 0)
Blend objects = 0
Faint objects = 11
Unknown objects = 0
Sum = 45

Figure C.37: CUOC Finding chart of candidate 0903046

ROSAT Identification | **ROSAT / MPE / RSDC | 28-JUN-94 09:06:24 | RGC** | Page: 1

UKST IIIaJ (blue) | **ROE/NRL COSMOS Finding Chart** | MASOS file: roe_disk:[roedat.masos]090_N1_SI03_N1_P1.mos

Field No. 540 | .... | MASOL Nr.: 000060

Plate Epoch: 1982.8600 | RASS Info: | ROSAT Source Name: RX J00391-2219

Equinox: J2000.0 | Error radii: 1 sigma = 7.3" ; plotted: 90% conf. = 1.645 sigma = 12.0" | ROSAT Position (2000.0): 00 39 07.5 -22 19 59

(1950.0): 00 36 38.4 -22 36 27

Galactic II (l,b): 92.03206 -84.44996

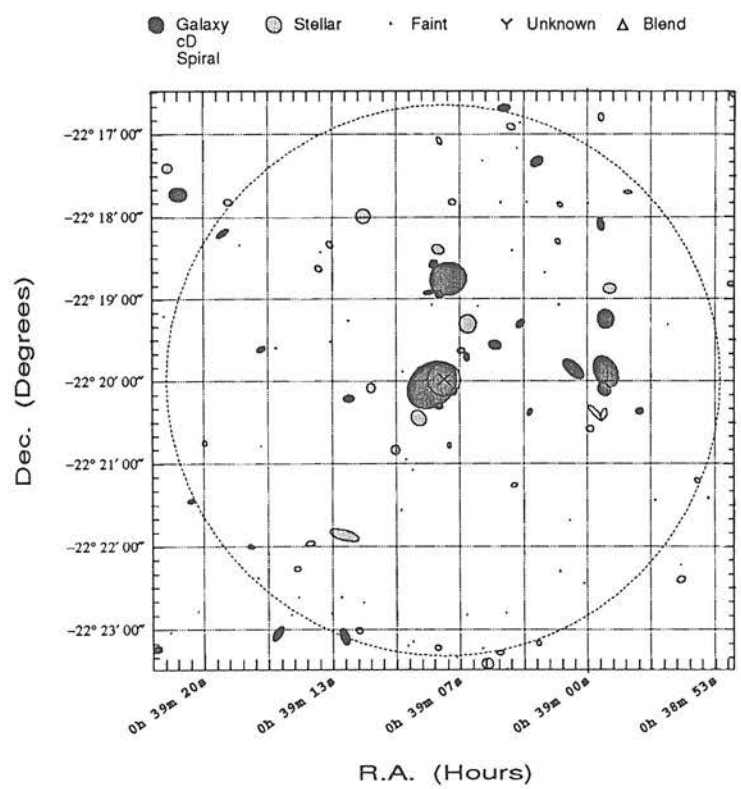

#	CLASS	B	R.A.	Dec.	DIST.
01	Galaxy	11.81	00 39 08.1	-22 20 03	9.8
02	Galaxy	21.29	00 39 07.0	-22 20 08	11.6
03	Galaxy	21.76	00 39 08.8	-22 19 52	19.0
04	Galaxy	21.35	00 39 07.8	-22 20 18	19.9
05	Galaxy	20.92	00 39 06.3	-22 19 42	23.2
06	Stellar	21.04	00 39 06.6	-22 19 38	24.3
07	Faint	24.27	00 39 09.7	-22 19 53	30.8
08	Stellar	18.14	00 39 08.8	-22 20 27	33.5
09	Stellar	14.48	00 39 06.3	-22 19 18	44.1
10	Galaxy	18.18	00 39 04.8	-22 19 34	44.7
11	Stellar	22.23	00 39 07.2	-22 20 47	47.9
12	Stellar	18.39	00 39 11.3	-22 20 05	53.2
13	Faint	24.83	00 39 08.1	-22 19 04	55.1
14	Faint	22.42	00 39 05.7	-22 19 05	59.0
15	Galaxy	20.10	00 39 07.7	-22 18 57	61.9
16	Stellar	18.61	00 39 10.1	-22 20 50	62.1
17	Faint	23.02	00 39 09.5	-22 20 57	64.5
18	Galaxy	21.08	00 39 08.3	-22 18 55	64.5
19	Galaxy	21.97	00 39 03.0	-22 20 23	66.6
20	Galaxy	19.38	00 39 03.5	-22 19 18	68.7
21	Faint	22.32	00 39 09.2	-22 21 05	69.9
22	Galaxy	19.48	00 39 12.5	-22 20 13	70.5
23	Galaxy	12.53	00 39 07.3	-22 18 45	73.4
24	Faint	23.98	00 39 12.5	-22 19 16	81.6
25	Galaxy	20.07	00 39 08.1	-22 18 35	84.6
26	Faint	24.27	00 39 13.4	-22 19 31	86.8
27	Stellar	21.93	00 39 03.8	-22 21 15	91.8
28	Galaxy	14.91	00 39 00.7	-22 19 51	94.1
29	Stellar	16.93	00 39 07.8	-22 18 24	95.0
30	Faint	22.87	00 39 01.5	-22 19 04	99.5

Selection criterion: distance
Galaxy Density = 557 per sq. deg.
Sample Radius = 200.0 arc sec

Stars	=	29
Total galaxies	=	23 (cDs = 0, spirals = 0)
Blend objects	=	0
Faint objects	=	36
Unknown objects	=	0
Sum	=	88

Figure C.38: CUOC Finding chart of candidate 0903060

ROSAT Identification | **ROSAT / MPE / RSDC | 28-JUN-94 09:06:43 | RGC** | Page: 1

UKST IIIaJ (blue) | **ROE/NRL COSMOS Finding Chart** | MASOS file: roe_disk:[roedat.masos]104_N2_SI04_N1_P1.mos

Field No. 825 | .... | MASOL Nr.: 000097

Plate Epoch: 1982.8521 | RASS Info: | ROSAT Source Name: RX J00341-0209

Equinox: J2000.0 | Error radii: 1 sigma = 34.2" ; plotted: 90% conf. = 1.645 sigma = 56.3" | ROSAT Position (2000.0): 00 34 08.5 -02 09 27

(1950.0): 00 31 35.2 -02 25 58

Galactic II (l,b): 112.78281 -64.68772

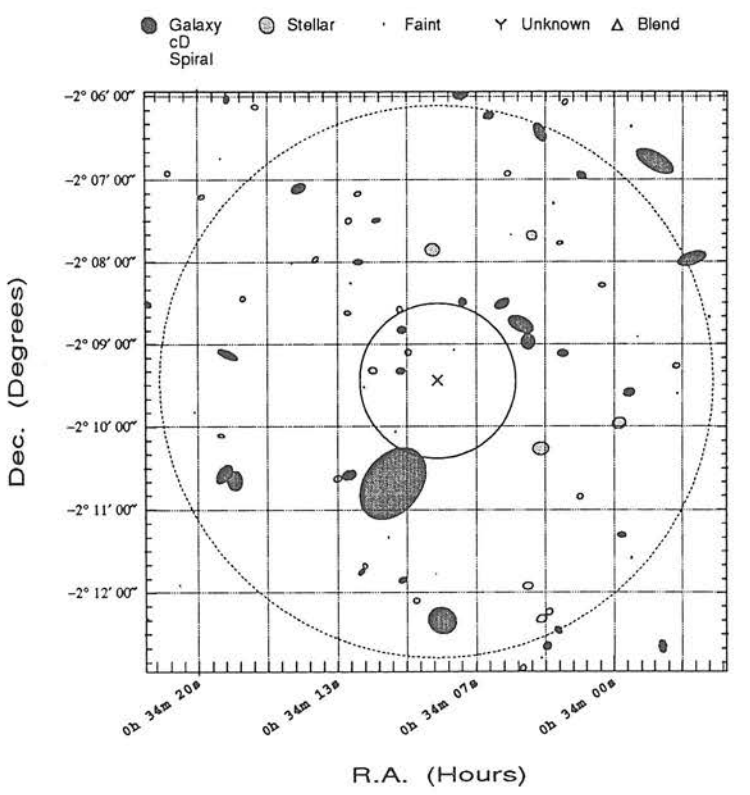

#	CLASS	B	R.A.	Dec.	DIST.
01	Faint	21.88	00 34 07.7	-02 09 05	24.7
02	Galaxy	20.33	00 34 10.3	-02 09 20	27.5
03	Stellar	20.27	00 34 09.9	-02 09 06	29.5
04	Galaxy	19.20	00 34 10.2	-02 08 50	45.1
05	Stellar	20.02	00 34 11.6	-02 09 19	47.2
06	Faint	22.79	00 34 10.5	-02 10 04	48.1
07	Faint	22.05	00 34 12.0	-02 09 31	53.3
08	Stellar	21.14	00 34 10.3	-02 08 35	58.8
09	Galaxy	18.84	00 34 07.3	-02 08 29	60.3
10	Galaxy	16.45	00 34 04.2	-02 08 59	70.9
11	Galaxy	15.22	00 34 04.5	-02 08 46	72.5
12	Galaxy	16.58	00 34 05.4	-02 08 31	72.5
13	Spiral	10.36	00 34 10.7	-02 10 41	81.1
14	Stellar	21.20	00 34 12.8	-02 08 37	81.5
15	Stellar	15.25	00 34 03.6	-02 10 16	89.1
16	Galaxy	18.80	00 34 02.5	-02 09 07	92.4
17	Galaxy	17.08	00 34 12.8	-02 10 35	93.5
18	Faint	21.85	00 34 12.7	-02 08 15	94.9
19	Stellar	15.40	00 34 08.7	-02 07 51	95.3
20	Stellar	18.90	00 34 13.3	-02 10 37	101.4
21	Galaxy	19.64	00 34 12.3	-02 08 00	104.0
22	Faint	23.66	00 34 05.0	-02 07 40	118.3
23	Faint	22.17	00 34 10.9	-02 11 20	119.1
24	Stellar	21.16	00 34 14.4	-02 07 58	124.9
25	Galaxy	21.34	00 34 11.5	-02 07 30	125.1
26	Stellar	16.99	00 34 04.0	-02 07 41	125.3
27	Stellar	20.34	00 34 01.7	-02 10 51	132.5
28	Stellar	20.05	00 34 12.8	-02 07 30	133.0
29	Stellar	21.34	00 34 02.6	-02 07 47	133.1
30	Stellar	16.25	00 33 59.8	-02 09 58	134.7

Selection criterion: distance
Galaxy Density = 1084 per sq. deg.
Sample Radius = 200.0 arc sec
Stars = 24
Total galaxies = 23 (cDs = 0, spirals = 1)
Blend objects = 0
Faint objects = 13
Unknown objects = 0
Sum = 60

Figure C.39: CUOC Finding chart of candidate 1044097

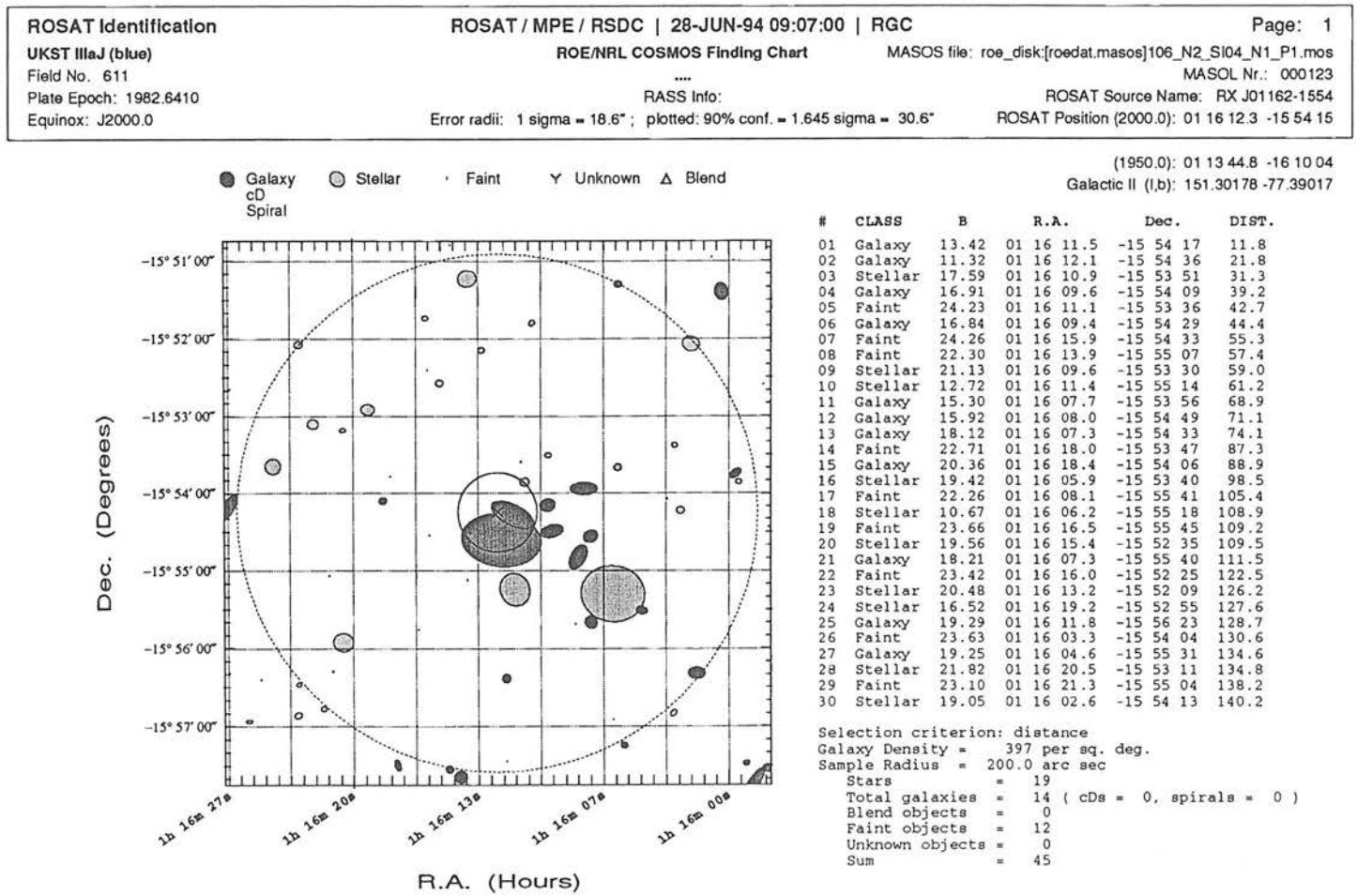

#	CLASS	B	R.A.	Dec.	DIST.
01	Galaxy	13.42	01 16 11.5	-15 54 17	11.8
02	Galaxy	11.32	01 16 12.1	-15 54 36	21.8
03	Stellar	17.59	01 16 10.9	-15 53 51	31.3
04	Galaxy	16.91	01 16 09.6	-15 54 09	39.2
05	Faint	24.23	01 16 11.1	-15 53 36	42.7
06	Galaxy	16.84	01 16 09.4	-15 54 29	44.4
07	Faint	24.26	01 16 15.9	-15 54 33	55.3
08	Faint	22.30	01 16 13.9	-15 55 07	57.4
09	Stellar	21.13	01 16 09.6	-15 53 30	59.0
10	Stellar	12.72	01 16 11.4	-15 55 14	61.2
11	Galaxy	15.30	01 16 07.7	-15 53 56	68.9
12	Galaxy	15.92	01 16 08.0	-15 54 49	71.1
13	Galaxy	18.12	01 16 07.3	-15 54 33	74.1
14	Faint	22.71	01 16 18.0	-15 53 47	87.3
15	Galaxy	20.36	01 16 18.4	-15 54 06	88.9
16	Stellar	19.42	01 16 05.9	-15 53 40	98.5
17	Faint	22.26	01 16 08.1	-15 55 41	105.4
18	Stellar	10.67	01 16 06.2	-15 55 18	108.9
19	Faint	23.66	01 16 16.5	-15 55 45	109.2
20	Stellar	19.56	01 16 15.4	-15 52 35	109.5
21	Galaxy	18.21	01 16 07.3	-15 55 40	111.5
22	Faint	23.42	01 16 16.0	-15 52 25	122.5
23	Stellar	20.48	01 16 13.2	-15 52 09	126.2
24	Stellar	16.52	01 16 19.2	-15 52 55	127.6
25	Galaxy	19.29	01 16 11.8	-15 56 23	128.7
26	Faint	23.63	01 16 03.3	-15 54 04	130.6
27	Galaxy	19.25	01 16 04.6	-15 55 31	134.6
28	Stellar	21.82	01 16 20.5	-15 53 11	134.8
29	Faint	23.10	01 16 21.3	-15 55 04	138.2
30	Stellar	19.05	01 16 02.6	-15 54 13	140.2

Selection criterion: distance
Galaxy Density = 397 per sq. deg.
Sample Radius = 200.0 arc sec
Stars = 19
Total galaxies = 14 (cDs = 0, spirals = 0)
Blend objects = 0
Faint objects = 12
Unknown objects = 0
Sum = 45

Figure C.40: CUOC Finding chart of candidate 1064123